Determination of the stress field in polycrystalline materials by Laue microdiffraction

Fengguo Zhang

2015–ENAM–0020

École doctorale n° 432 : Science des Métiers de l'ingénieur

Doctorat ParisTech

T H È S E

pour obtenir le grade de docteur délivré par

l'École Nationale Supérieure d'Arts et Métiers

Spécialité " Science des Matériaux "

présentée et soutenue publiquement par

Fengguo ZHANG

07/07/2015

Determination of the stress field in crystalline materials by Laue microdiffraction

Détermination du champ de contraintes dans les matériaux cristallins par microdiffraction Laue

Directeur de thèse : **Olivier CASTELNAU**
Co-encadrement de la thèse : **Michel BORNERT, Johann PETIT**

Jury

M. Wolfgang LUDWIG, Directeur de Recherche au CNRS, INSA Lyon	Président
M. Pierre-Olivier RENAULT, Professeur, Université de Poitiers	Rapporteur
M. Alexander KORSUNSKY, Professeur, University of Oxford	Rapporteur
M. Jean-Luc BECHADE, Ingénieur, CEA Scalay	Examinateur
M. Michel BORNERT, Ingénieur, Ecole des Ponts ParisTech	Examinateur
M. Johann PETIT, Maître de conférences, Université Paris-Ouest	Examinateur
M. Olivier CASTELNAU, Directeur de Recherche au CNRS, Arts et Métiers ParisTech	Examinateur

Arts et Métiers ParisTech - Centre de Paris
Procédés et Ingénierie en Mécanique et Matériaux - UMR CNRS 8006
151 Boulevard de l'Hôpital, 75013 Paris, France

T H È S E

Acknowledgment

This work is supported by ANR project MICROSTRESS and China Scholarship Council (CSC) (grant 2011623166). I want to thank all the academic and industrial partners of this project. It has been a great honor for me to work with them. I am very grateful to the laboratory Procédés et Ingénierie en Mécanique et Matériaux (PIMM), Arts et Métiers ParisTech, for providing me the perfect environment to complete this thesis work. I would also like to thank Shanghai Jiao Tong University for recommending me to enter PIMM. This work would not have been possible though, without the different kinds of contributions of a lot of people.

First of all, I would like to express my deepest sense of gratitude to my Ph.D thesis advisors, Dr. Olivier Castelnau, Dr. Michel Bornert, and Dr. Johann Petit, for providing me the opportunity to achieve this work. They give me many invaluable advices and encouragements so that I could find a way to overcome the difficulties. I would like to thank the members of the jury of this thesis. Many thanks to Prof. Pierre-Olivier Renault, Prof. Alexander Korsunsky, Dr. Jean-Luc Béchade, and Dr. Wolfgang Ludwig for their great work on my thesis committee.

I would express great thanks to Dr. Odile Robache and Dr. Jean-Sébastien Micha, two energetic scientists, who have always been very helpful throughout my PhD life. I would like to thank Dr. Eva Héripré and Emeric Plancher, who helped me with the sample preparation. My colleagues, Jean-Baptiste Marijon and Tang Gu, gave me great encouragement and countless help, and I would also like to express my deepest gratitude to them. I would like to thank all the PIMM staff. Special thanks to Ines Mkacher, Sophie Versavaud, Tétiana Salivon, Nada Bou-Malhab, Odile Angèle, Alain Gaudy, Christophe Canu, Ngoc Lam Phung, and Fabrice Detrez.

I would also like to thank Prof. Xianghuai Dong of Shanghai Jiao Tong University, who taught me the fundamentals of continuum mechanics and finite element method.

Let me express my deepest gratitude to my friends, Mengxing Li, Xiguang Li, Kaikai Liu, Youlong Wu, Lili Wang, Tian Ban, Chen Lu, and Lijun Wei. You have made me feel at home in Paris. I would also like to thank l'Eglise Alliance Chinoise de Paris, where I have made many friends, like the Lings, Liang Xue, Wenli Huang, Fu Ji, Yahui Guang, Menglin Wu, Lihua Zhuang, Xing Wang, etc. You have given me much comfort and consolation in the last year of my PhD life.

Most importantly, I would like to express my sincere thanks to my family. My parents always provide relentless love and support to me. I say I would never finish PhD without their love.

Résumé

La microdiffraction Laue permet l'estimation des déformations élastiques à l'échelle du micron. La procédure d'analyse standard, bien établie, utilisée pour extraire les déformations élastiques des images de Laue est limitée par deux sources d'erreurs : la détermination de la positions des taches de Laue sur le détecteur, et la sensibilité aux paramétres de calibration du montage. Pour améliorer la procédure, nous avons développé une procédure appelée Laue-DIC qui utilise la très bonne résolution de la technique de corrélation d'images numériques (DIC). Cette méthode utilise, pour la détermination de l'incrément de déformation élastique et de rotation, le déplacement des pics entre deux configurations mécaniques, estimé par DIC, au lieu de leur position. Nous montrons que cette méthode donne un profil de contrainte en meilleur accord avec les solutions analytiques et numériques, pour des échantillons monocristallins déformés en flexion 4-points. Nous proposons également une méthode Laue-DIC améliorée, dans laquelle les paramètres de calibration sont estimés à chaque point de mesure, simultanément à la déformation élastique.

En paralléle à la formulation de la méthode Laue-DIC (améliorée), nos efforts ont porté sur l'estimation de l'incertitude obtenue sur les déformations élastiques. Nous avons développé un modèle de bruit pour les images de Laue mesurées en rayonnement synchrotron, qui a été validé sur des séries de données, et qui nous a permis d'estimer les erreurs statistiques de la DIC, à partir d'images de Laue synthétiques. Ces erreurs ont ensuite été propagées dans la méthode Laue-DIC afin d'estimer les incertitudes sur les déformations élastiques, que l'on trouve en bon accord avec la fluctuation des contraintes locales estimées

Mots clés : Microdiffraction Laue, corrélation d'images numériques, rayonnement synchrotron, analyse d'erreurs, essai mécanique in situ

Abstract

Laue microdiffraction is a powerful technique to characterize the intragranular elastic strain field at the scale of micrometer. Although a standard procedure extracting elastic strain and crystal orientation from Laue image has been well-established, it can suffer from two sources of uncertainties: the determination of peaks' positions and the sensitivity to calibration parameters. In light of the high accuracy of digital image correlation (DIC), we developed the so-called Laue-DIC method which used the peaks' displacements measured by DIC instead of peaks' positions to determine the elastic strain increment and rotation between two mechanical configurations. This method has been proved more efficient than the standard procedure in terms of stress profiles of bended beam. We also developed the enhanced version of Laue-DIC. By using the term "enhanced", we mean that we attempt to obtain both lattice matrices and calibration parameters of two configurations rather than solely the elastic strain increment and rotation from peaks' displacements.

Aside from the formulation of Laue-DIC, we also developed a procedure of statistically estimating the errors of elastic strain/stress resulted from DIC errors and calibration accuracy. We have first validated a classical noise model, Poissonian-Gaussian model, from diffraction images acquired at synchrotron radiation facility. With the noise model, we could statistically estimate the DIC errors by synthesizing artificial spots. The estimated DIC errors were further transmitted into the errors of Laue-DIC through statistical tests.

Keywords : Laue microdiffraction, digital image correlation, synchrotron radiation, error analysis, *in situ* mechanical test

Contents

Introduction

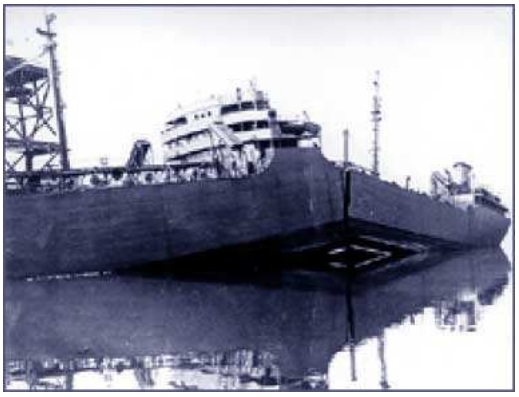

Figure 1: The crush of Schenectady tanker

On 16 January 1943, a tanker called Schenectady was docking quietly at Swan Island, US, in calm weather. Suddenly, without warning, a earsplitting, audible for at least a mile, sound came, and the bulk of the tanker cracked almost by half. This was not the first of the merchant fleet to fracture in this way in World War II - there had been ten other major incidents before, and several more would follow - but it was perhaps the most influential; it happened right under the noses of Portland's citizens, and was widely reported by the press even during the war.

Although later research inferred that the steel of the tanker became highly brittle due to low ambient temperature, exacerbating any existing faults and becoming more vulnerable to fracture, the cause of such accident within service life was not fully understood at that time. Because material fatigue or fracture, unlike other materials' properties, e.g. stiffness, strength, thermal conductivity, yield strength, depends heavily on the local characteristics of microstructure (lattice distortion, void, impurities, grain boundary), rather than average

attributes of microstructure such as mean grain size, phase volume fractions, impurity ratio, etc [McDowell 2010].

Nowadays, when large machines (airplanes, rockets, submarine) and megastructures are increasingly emerging in our life, engineers have to be cautious with designing and manufacturing them in order to avoid an accident as aforementioned and economize the cost as well. Traditional paradigms of material selection based on macroscopic strength theory needs to be revolutionized, because an increase in a machine/structure size introduces new complexities, and it is not simply scaling up an existing machine/structure but redesigning with new material, new manufacturing to some degree. Sometimes, it may be more demanding if a machine/structure has to work under extreme conditions, for example, a satellite must function in vacuum, and the structure of submarine must withstand high pressure deep under the sea. These urgent needs from industry and engineering have fostered a new subject - "material design" aiming at tailoring materials' properties to meet the requirements of materials' application [McDowell 2001].

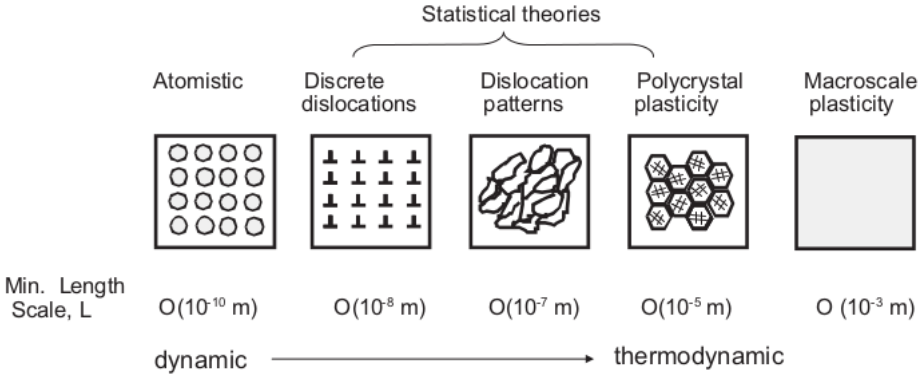

Figure 2: The hierarchy of structure in polycrystalline material [McDowell 2010]

For polycrystalline materials, there exist three intermediate levels in the hierarchy from atomistic level ($\sim 10^{-10}$ m) to macroscopic level ($\sim 10^{-3}$ m) [McDowell 2010]: discrete dislocation level ($\sim 10^{-8}$ m), dislocation pattern level ($\sim 10^{-7}$ m), polycrystal level ($\sim 10^{-5}$ m) (see Fig. 2). While it sounds possible to employ first principle to simulate materials' behavior at each level, and there have been some efforts towards this direction [Gonze et al. 2002], this approach is impracticable and costly when dealing with levels

higher than atomistic level, not only due to the huge amount of calculation involved, but also due to the tremendous amount of degree-of-freedoms and boundary conditions to be fed in. Therefore, it is very compelling if we could develop a multiscale modeling method to bridge the gap from atomistic scale to macroscopic scale [Liu et al. 2006]. Thanks to the advancement of computer's performance and numerical methods, material scientists have developed corresponding methods for simulation at higher level: finite element method (FEM) [Li et al. 2008; Zhang et al. 2012], fast Fourier transformation (FFT) method [Suquet et al. 2012] and cellular automation (CA) [Jin and Cui 2012] for macroscopic level and polycrystal level, dislocation dynamics (DD) [Gaucherin et al. 2009] for dislocation pattern level, molecular dynamics (MD) [Raabe 2004] for discrete dislocation level, etc.

The improvements of these numerical methods need observations and validations from experiment, therefore it is imperative to have experimental tools probing materials' behavior at the corresponding scale, so that the results of numerical simulations and experimental measurements can be cross-checked and hence both numerical method and experimental measurements can be promoted. However, at present, one cannot bridge the gap between the simulation results and experimental observation when it comes to predicting material's behavior at microscale. In [Hoc et al. 2003], the comparison between calculated and measured strain field has been found to be highly influenced by local behavior of material, and in [Magid et al. 2009], the stress fluctuations within Cu monocrystal measured by X-ray diffraction is found to be of the order of GPa, a result which is unrealistic. This gap is either due to the inadequacy of simulation method, the flaws in experimental observation, or the limited knowledge of material's behavior at fine scale. Therefore, concerted efforts from experts of both numerical simulation and experimental characterization are needed in order to have a more reliable predictive methodology to have insight into material's properties at a fine scale.

This thesis is under the framework of ANR project "MICROSTRESS" aiming at improving the experimental characterization of material at the scale of micrometer. This project is dedicated to two experimental techniques: HR-EBSD (High angular Resolution Electron Back Scattered Diffraction) and Laue microdiffraction, both of which enable the measurement of elastic strain field and hence stress field. The stress field, along with the

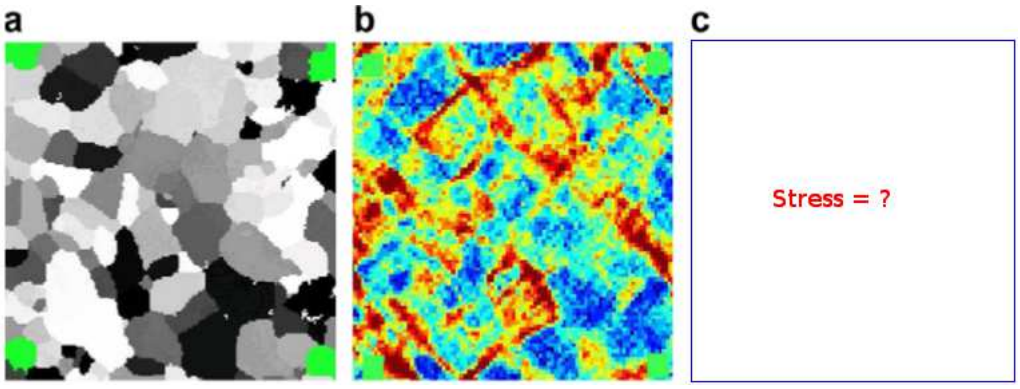

Figure 3: (a) Polycrystal's microstructure obtained by OIM; (b) The deformation field obtained by applying DIC to SEM images; (c) The stress of material is unknown. (a) and (b) are from [Héripré et al. 2007]

microstructure obtained by OIM (Orientation Image Microscopy) and the total strain field obtained by DIC (Digital Image Correlation), will provide insight into the constitutive behavior of material (see Fig. 3). In this project, one PhD student, Emeric Plancher, is working on the development of HR-EBSD, and this thesis is dedicated to improve the precision of stress characterization by Laue microdiffraction. The whole thesis is organized as follows:

1. Chapter I presents the background and fundamentals of this thesis, including the heterogeneity of stress, the diffraction technology, and the calculation of elastic strain from diffraction image.

2. Chapter II first presents the so-called Laue-DIC method, i.e. the application of DIC into diffraction image treatment, and the analysis of Laue-DIC uncertainty arising from image noise.

3. Chapter III presents an enhanced version of Laue-DIC, which enables the acquisition of both lattice matrices and geometrical parameters. And numerical tests will be given to test its efficiency and its robustness against DIC errors.

4. Chapter IV applies the standard method presented in Chapter II, Laue-DIC method presented in Chapter II, and enhanced Laue-DIC method presented in Chapter III, to diffraction images collected from Laue microdiffraction experiments, carried out

in beamline BM32 of ESRF during *in situ* mechanical tests. We will compare the results with analytical solution and discuss their discrepancies.

Chapter 1

Bibliography

1.1 Motivation

It is well-known that homogeneous strain/stress fields at the macroscopic scale might exhibit heterogeneities at a finer scale, and such heterogeneities may give rise to microplasticity [Tatschl and Kolednik 2003; Zhang et al. 2005] and crack initiation [Sangid 2013; Bach et al. 2014]. The ignorance of the heterogeneity of strain/stress field may lead to the failure of mechanical components (for example, the crush of Schenectady tanker, see Fig. 1). The heterogeneity of strain/stress field usually arises from the heterogeneity of the microstructure. Thanks to recent developments of experimental techniques and data treatment, scientists now have various technologies available to characterize materials' morphology at various scale: at atomic scale, for example, we have scanning tunneling microscopy (STM), transmission electron microscopy (TEM) and atomic force microscopy (AFM), and at polycrystal and macroscopic scale, we have diffraction contrast tomography (DCT), scanning electron microscopy (SEM), orientation imaging microscopy (OIM), and optic microscopy. The images acquired by these techniques, together with image processing algorithm such as DIC (Digital Image Correlation) [Sutton et al. 2009b], reveal the kinematics of materials at different scale [Doumalin and Bornert 2000; Hild and Roux 2006; Héripré et al. 2007; St-Pierre et al. 2008].

To fully explore the constitutive model of materials, stress of materials is also required aside from morphology and kinematics of materials. Stress can be considered as the tendency to push material back to its equilibrium state. For crystalline material, stress arise

from the distortion of lattice, therefore diffraction methods, such as X-ray diffraction, neutron diffraction, or electron diffraction, offer non-destructive ways to detect the lattice distortion and hence the stress at the scale of lattice. For non-crystalline material such as rubber, the characterization of stress can be accomplished by thermal analysis, such as TSA (thermographic stress analysis) [Zhang et al. 1990]. One can gain an insight into material's constitutive model by superimposing stress map to strain map.

This thesis will be dedicated to the development of Laue microdiffraction aiming at measuring elastic strain, and this chapter will lay the scientific foundations relevant to this thesis. The whole chapter is structured in the following sequence: (i) in §1.2, we introduce the concept of evaluation of stress by diffraction and compare three mainstream of stress evaluation method based on diffraction (X-ray diffraction, neutron diffraction, and electron diffraction); (ii) in §1.3, we will present the basic concepts in X-ray diffraction; (iii) in §1.4, we will discuss the commonly used X-ray diffraction technique and introduce Laue microdiffraction; (iv) and in §1.5, we introduce the standard Laue treatment to obtain elastic strain from Laue microdiffraction data.

1.2 Evaluation of elastic strain by diffraction method

Evaluation of elastic strain by diffraction falls into the category of non-destructive analysis of material. When electromagnetic wave propagate through crystal, both constructive interference and destructive interference of waves would occur when the incident electromagnetic wave and atoms spacing meet certain conditions. This phenomenon is called diffraction. Given the actual inter-atom spacing in real matters, the electromagnetic wave chosen to probe material is usually X-ray, whose spectrum is within the range of $0.01 - 100\,\text{Å}$. Due to the wave-particle duality, the interaction of matters with neutrons or electrons can also produce visible diffraction pattern at certain conditions, hence electron diffraction and neutron diffraction are used to analyse material properties as well. Bear in mind that all the three method do not directly measure stress but the distortion of lattice from its equilibrium state.

1.2.1 Neutron diffraction

For neutron diffraction, the most appealing feature is that neutrons carries no charge therefore neutron diffraction has the deepest penetration depth compared to electrons and X-ray as the propagation of neutron is rarely impeded by electromagnetic forces inside material. Moreover, neutron diffraction is widely used in studying magnetic materials and organic materials. For magnetic material, this is due to the fact that neutrons carry magnetic moments and can be scattered magnetically. For organic materials, X-ray diffraction image will be strongly blurred by Compton effect (see §1.3.1), because Compton effect is very pronounced when photons are diffracted by light elements, e.g. carbon, oxygen, and hydrogen, which constitute the majority of organic materials [Cullity 1956b]. In contrast, neutrons, which interact with nucleus of atoms, demonstrate less Compton effect. However, the bottleneck of neutron diffraction at present is the availability of neutron source, which can be either a radioactive material, a nuclear reactor, e.g. LLB in Saclay or ILL in Grenoble, or a spallation source, e.g. ISIS in UK or the future ESS in Sweden. Low flux of neutron sources is also a factor hindering the usage of neutron diffraction.

1.2.2 Electron diffraction

Electron diffraction works in either transmission mode or backscatter mode. The former is mentioned as TEM (transmission electron diffraction) and the latter is mentioned as EBSD (electron backscatter diffraction, available in a SEM device). Due to the superficial penetration depth of electron into matters, TEM is only limited to study thin films with a thickness of $\sim 100\,\text{nm}$ and EBSD is only limited to surface characterization of materials.

Aside from the limited penetration of electrons, electron diffraction is also limited by the following factors:

1. The sample must be put in a vacuum, otherwise electron beam's energy would dissipate in the air. Usually the size of vacuum chamber limits the size of sample and experimental equipment in case of *in situ* tests.

2. The surface of sample must be extremely smooth and clean. For non-conductive materials, its surface must be coated with conductive materials, otherwise too much

charges will accumulate on the surface and repel the incident electrons.

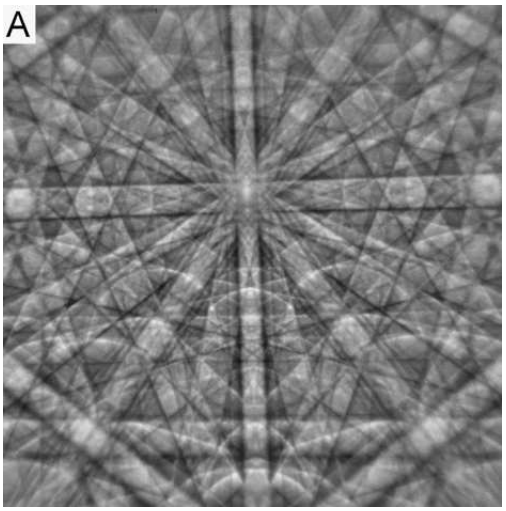

Figure 1.1: Kikuchi pattern from a Ge sample [Britton et al. 2010]

However, the most obvious advantage of electron diffraction is its fine spatial resolution, as its beam size is merely of the order of 30 nm in EBSD, therefore it is often used to analyze the intragranular misorientation [Maurice et al. 2012]. The spatial resolution can be ~ 1 Åin TEM, which is suitable to study interatomic behavior of material. The electron/matter interaction is a rich source of information concerning the crystal's orientation, chemical composition, surface morphology, etc:

backscattered electrons Due to wave-particle duality, electrons could be scattered by all sets of lattice planes which satisfy the diffraction condition, and form Kikuchi pattern (see Fig. 1.1).

secondary electrons The incident electron beam could ionize the atoms on the material's surface. The ionized atoms will release electrons. These electrons are called "secondary electrons", and the amount of electrons is related to the surface morphology.

characteristic X-ray The incident beam may strike a bound electron in an atom. After the electron has been ejected, the atom is left with a vacant energy level, and an outer-shell electron then falls into the inner shell, releasing characteristic X-ray with

a certain wavelength. The released characteristic X-rays may be scattered by all sets of lattice planes which satisfy the diffraction condition, and form a Kossel pattern (see Fig. 1.2).

Kossel pattern suffers from a poor signal-to-noise ratio, though some work has been done to analyze Kossel line [Bouscaud et al. 2014]. The material characterization by EBSD is mainly accomplished by analyzing Kikuchi pattern, which is actually the gnomonic projection of the crystal lattice plane.

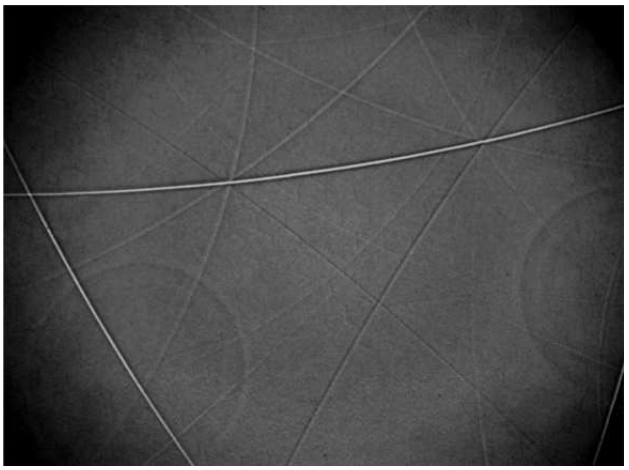

Figure 1.2: Kossel pattern from a Cu alloy [Maurice and Fortunier 2008]

1.2.3 X-ray diffraction

Unlike neutrons, X-ray photons are mainly scattered by electrons in matter instead of nucli. The penetration of X-ray beam in matter depends strongly on the photons' energy - higher energy gives deeper penetration depth except at X-ray absorption edges, where the X-ray photons will be absorbed entirely and trigger fluorescence of material.

The X-ray can be generated either from the characteristic radiation of atoms, as we have mentioned in the formation of Kossel pattern in §1.2.2, or from the acceleration/deceleration of any charged particle. Therefore the X-ray source can be very versatile. The simplest X-ray source involves sealed X-ray tube and rotating anode generator, in which electrons are emitted from the cathode and are accelerated by high voltages (typ-

ically 40 kV) between the cathode and anode. When the electrons reach the anode made by a selected metal, they stop instantaneously and radiate X-ray at all directions with a broad spectrum. This kind of radiation is called Bremsstrahlung radiation. Aside from Bremsstrahlung radiation, the interaction between electrons and anode material will also emit characteristic radiation, which is monochromatic unlike Bremsstrahlung radiation. The wavelength of the characteristic radiation depends on the element of anode material. The most frequently used characteristic radiations include K_α line and K_β line of copper. [He 2009a].

More advanced X-ray source is synchrotron radiation source. Like Bremsstrahlung radiation, synchrotron radiation comes from the acceleration/deceleration of any charged particle. The resulted electric field by the acceleration/deceleration of a charged particle is given as [Jackson 1999]:

$$\underline{E} = \frac{Q}{4\pi\epsilon_0 c^2 \|\underline{r}\|} \frac{\hat{\underline{r}} \times [(\hat{\underline{r}} - \underline{v}/c) \times \dot{\underline{v}}]}{(1 - \underline{v} \cdot \hat{\underline{r}}/c)^3}, \tag{1.1}$$

where Q is the amount of electric charge of the particle, $\underline{r}$ is the position vector originated from the particle, $\hat{\underline{r}}$ is its unit vector, and $\underline{v}$ is the speed of particle. If the particle moves periodically, the consequent electric field will vary periodically and produce electromagnetic waves.

In the beginning, synchrotron radiation was just a byproduct of particle accelerator in the experiment of high-energy physics. Soon, it found its application in material science, since it offered incomparable high intensity and high energy X-ray beam, well suited for probing into the interior of materials non-destructively. The demand of spectrum more concentrated in certain wavelength led to the development of magnetic insertion devices called wigglers and undulators regulating the motion of the charged particles (see Fig. 1.3). Together with optical equipments adapted to synchrotron radiation, e.g. Kirkpatrick-Baez mirror, monochromator, etc [Ice 1997; Ice et al. 2000; Liu et al. 2005; Ice 2007], researchers can have X-ray beam whose sizes are just of the order of nm. Thanks to these advantages of synchrotron radiation, a powerful material characterization technology, Laue microdiffraction, was developed during the past decades, and we will elaborate this technology in §1.4.

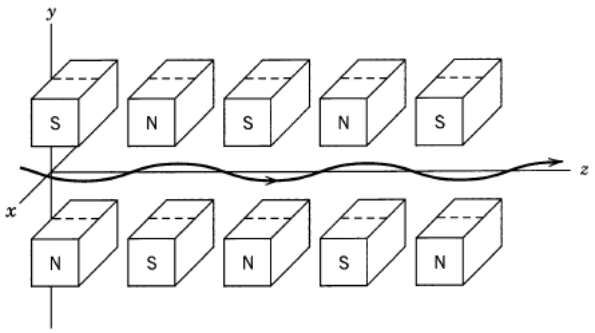

Figure 1.3: Bending magnets in a wiggler or undulator in a synchrotron radiation source [Jackson 1999]

To sum up, X-ray diffraction excels in availability compared to neutron diffraction, and in versatility compared to electron diffraction. Thanks to the development of synchrotron radiation and optical technology, material scientists can have X-ray beam of high brilliance at micrometer scale. We will detail the principle and technology of X-ray diffraction hereinafter.

1.3 Principle of X-ray diffraction

1.3.1 The X-ray/matter interaction

X-rays belong to a portion of the electromagnetic spectrum encompassing longer wavelengths than γ rays and shorter wavelengths than ultraviolet. Material scientists should choose the spectrum of X-ray in vicinity of the interatomic spacing in crystals so as to generate detectable diffraction.

The X-ray/matter interactions are listed in Fig. 1.4. The scattered X-rays include coherently scattered (Thomson scattering) and incoherently scattered (Compton scattering). In Thomson scattering, the photons retain their energies after scattered while in Compton scattering, there are energy transfers between photons and electrons. Most of time, Compton scattering would increase the wavelength of X-ray (corresponding to lower energy). Compton scattering cannot be explained by classical electromagnetism, which consider X-ray merely as a wave, because it is due to the particle nature of X-ray (see Fig. 1.5).

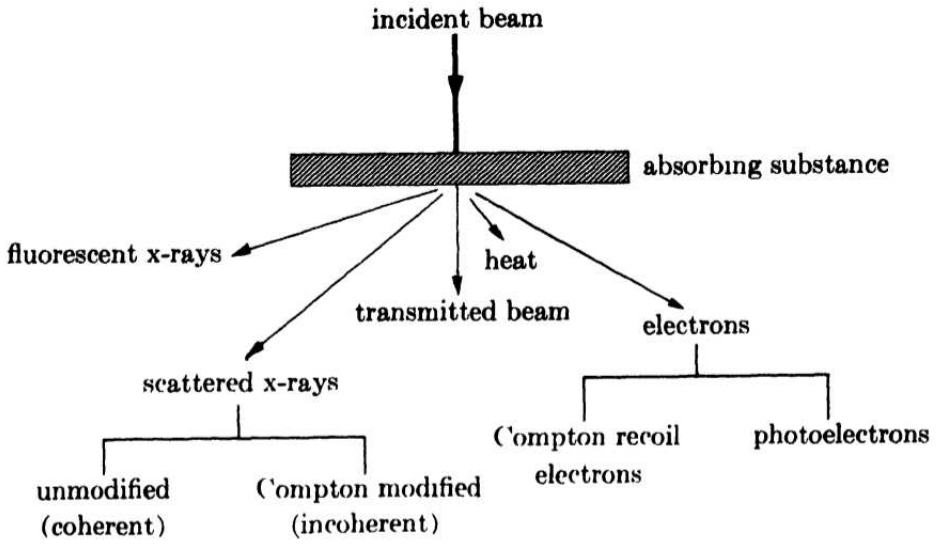

Figure 1.4: The X-ray/matter interaction [Cullity 1956b]

From the theory of quantum mechanics, the relation between photon's energy E and wavelength λ can be expressed as:

$$E = \frac{hc}{\lambda}, \tag{1.2}$$

where h is Planck's constant, c is the light speed. If E is expressed in the unit of keV, and λ is expressed in the unit of Å, their relation is:

$$E = \frac{12.398}{\lambda}.$$

The difference between the incident wavelength λ_0 and scattered wavelength λ in Compton scattering follows the following relation:

$$\Delta\lambda = \lambda - \lambda_0 = \frac{h}{mc}(1 - \cos 2\theta), \tag{1.3}$$

where m is the electron mass, and c is the light speed. $\frac{h}{mc} \approx 2.43 \times 10^{-3}\,\text{nm}$ is called "Compton wavelength".

In general, tightly bounded electrons tend to scatter photons coherently, and loosely bounded electrons tend to scatter photons incoherently. However, when X-rays interact with crystals, where the atoms are spaced periodically, coherently scattered X-ray undergoes reinforcement in certain directions and cancellation in other directions, whereas

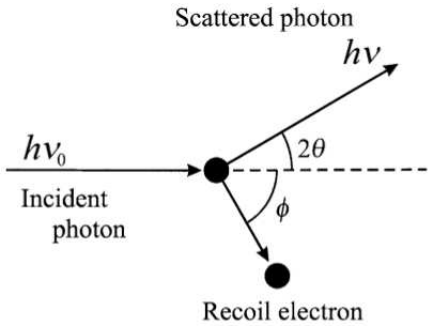

Figure 1.5: Compton scattering [Waseda et al. 2011]

incoherently scattered X-rays are not direction-dependent. Thus when we consider the diffraction of X-ray by crystals, incoherent scattering is usually ignored [Woolfson 1997].

1.3.2 Bragg's Law

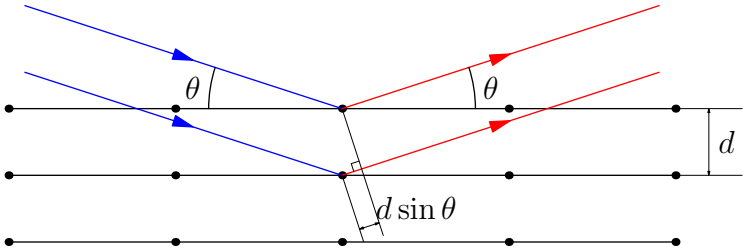

Figure 1.6: The incident X-ray and reflected X-ray make an angle of θ symmetric to the normal of crystal plane.

Of all the models describing diffraction phenomenon, Bragg's law is the simplest and most intuitive (see Fig. 1.6). Suppose that a monochromatic plane wave of X-ray impinges on aligned planes of lattice points at angle θ, and the lattice plane reflects the X-ray like a mirror. There will be a phase difference between the rays that are reflected by two adjacent lattice planes whose Miller indexes are denoted as (hkl). The phase difference of the two diffracted rays, say $\Delta\phi$, is

$$\Delta\phi = 2\pi\frac{2d_{hkl}\sin\theta}{\lambda},$$

where λ is the wavelength, d is the distance between each adjacent lattice plane (d-spacing). Only when the phase difference $\Delta\phi$ is an integer, say n, times 2π, is the interference of two

rays constructive. Therefore, the condition of diffraction is

$$n\lambda = 2d_{hkl}\sin\theta.$$

When diffraction occurs, θ is called the Bragg angle. Waves with various wavelengths can satisfy Bragg's condition given the same d-spacing and Bragg angle according to the integer n, and these waves corresponding to different n are called harmonic waves. For brevity, we designate n to be 1. For the nth order harmonic wave diffracted by (hkl) lattice plane, we regard the beam diffracted by the $(nh\,nk\,nl)$ lattice plane. In that case, Bragg's law is written into

$$\lambda = 2d_{hkl}\sin\theta. \tag{1.4}$$

Although Bragg's law successfully reveals the relation between crystal structure and diffraction pattern, it is just a phenomenological model describing the kinematics of diffraction. For example, in Bragg's model, X-rays appear to be diffracted by nuclei of atoms. In fact X-rays are diffracted by electrons of atoms. Nevertheless, Bragg's law earns its applications due to its simplicity. The complete diffraction theory is described by the "dynamic" theory, which aims at solving Maxwell's equations given certain boundary conditions [Schwartz and Cohen 1987b].

1.3.3 Reciprocal lattice

Despite the brevity of Bragg's law, it is more convenient to describe diffraction phenomenon in the reciprocal lattice. The Ewald's sphere provides a graphical interpretation useful in some applications of diffraction. We introduce the concept of reciprocal lattice below. For the sake of brevity, we will use Einstein summation convention in the following expressions.

We first denote vectors starting from the origin of lattice to [100], [010], and [001] lattice point as $\underline{l}_1$, $\underline{l}_2$, and $\underline{l}_3$ respectively, e.g.

$$\underline{l}_1 \doteq \begin{bmatrix} l_{11} \\ l_{12} \\ l_{13} \end{bmatrix}, \quad \underline{l}_2 \doteq \begin{bmatrix} l_{21} \\ l_{22} \\ l_{23} \end{bmatrix}, \quad \text{and} \quad \underline{l}_3 \doteq \begin{bmatrix} l_{31} \\ l_{32} \\ l_{33} \end{bmatrix}.$$

And we can assemble the three vectors into a 3×3 matrix, $\underset{\sim}{l}$:

$$\underset{\sim}{l} \doteq [l_1, l_2, l_3]^{\mathrm{T}} = \begin{bmatrix} l_{11} & l_{12} & l_{13} \\ l_{21} & l_{22} & l_{23} \\ l_{31} & l_{32} & l_{33} \end{bmatrix},$$

and we call this matrix as lattice matrix.

The lattice vectors of reciprocal lattice is defined as below:

$$\begin{aligned} \underline{l}_1^* &\doteq \frac{\underline{l}_2 \times \underline{l}_3}{\det \underset{\sim}{l}}, \\ \underline{l}_2^* &\doteq \frac{\underline{l}_3 \times \underline{l}_1}{\det \underset{\sim}{l}}, \\ \underline{l}_3^* &\doteq \frac{\underline{l}_1 \times \underline{l}_2}{\det \underset{\sim}{l}}, \end{aligned},$$

or, more specifically,

$$\begin{aligned} l_{1i}^* &\doteq \frac{\epsilon_{ijk} l_{2j} l_{3k}}{\det \underset{\sim}{l}}, \\ l_{2i}^* &\doteq \frac{\epsilon_{ijk} l_{3j} l_{1k}}{\det \underset{\sim}{l}}, \\ l_{3i}^* &\doteq \frac{\epsilon_{ijk} l_{j1} l_{2k}}{\det \underset{\sim}{l}}, \end{aligned} \tag{1.5}$$

where $i = 1, 2, 3$, ϵ_{ijk} is the Levi-Civita symbol defined as follows:

$$\epsilon_{ijk} \doteq \begin{cases} +1, & \text{if } (ijk) \text{ is (123), (231), or (312)} \\ -1, & \text{if } (ijk) \text{ is (132), (213), or (321)} \\ 0, & \text{otherwise.} \end{cases}$$

and $\det \underset{\sim}{l}$ is the determinant of $\underset{\sim}{l}$ defined as:

$$\det \underset{\sim}{l} \doteq \epsilon_{ijk} l_{1i} l_{2j} l_{3k}. \tag{1.6}$$

From Eqns. 1.5 and 1.6, we can conclude that:

$$\underline{l}_i \cdot \underline{l}_j^* = l_{ik} l_{jk}^* = \delta_{ij}, \tag{1.7}$$

where δ_{ij} is the Kronecker symbol defined as:

$$\delta_{ij} \doteq \begin{cases} 1, & \text{if } i = j \\ 0, & \text{if } i \neq j \end{cases}.$$

Eqn. 1.7 is equivalent to

$$\underset{\sim}{l} \cdot \underset{\sim}{l}^{*\mathrm{T}} = \underset{\sim}{1},$$

Therefore, the relation between the direct lattice and the reciprocal lattice is expressed as,

$$\underset{\sim}{l}^{-\mathrm{T}} = \underset{\sim}{l}^{*}. \tag{1.8}$$

Fig. 1.7 gives a visual contrast between the direct lattice and the reciprocal lattice. Direct lattice is drawn with solid lines, and reciprocal lattice is drawn with dotted lines. Except the origin, each lattice point in direct space is denoted by a set of integers u, v, w within brackets, i.e. $[uvw]$, whilst each reciprocal lattice point is denoted by a set of integer h, k, l within brackets marked by a star, i.e. $[hkl]^*$.

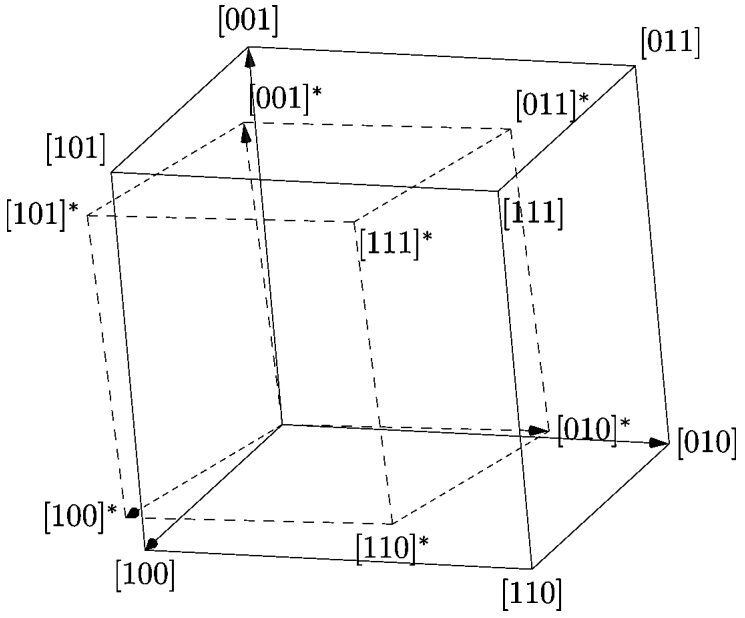

Figure 1.7: The relationship between the direct lattice and the reciprocal lattice. Direct lattice is drawn with solid lines, and reciprocal lattice is drawn with dotted lines.

A reciprocal lattice vector $\underline{r}^*_{hkl}$ drawn from the origin to the reciprocal lattice point $[hkl]^*$ is given by

$$\underline{r}^*_{hkl} \doteq h\underline{l}^*_1 + k\underline{l}^*_2 + l\underline{l}^*_3. \tag{1.9}$$

If we take the dot product of this vector with vectors in the (hkl) plane, say $\underline{l}_2/k - \underline{l}_1/h$ and $\underline{l}_3/l - \underline{l}_1/h$, according to Eqn. 1.7 we have

$$\begin{aligned} (\underline{l}_2/k - \underline{l}_1/h) \cdot \underline{r}^*_{hkl} &= 0 \\ (\underline{l}_3/l - \underline{l}_1/h) \cdot \underline{r}^*_{hkl} &= 0. \end{aligned}$$

As $\underline{r}^*_{hkl}$ is perpendicular to two vectors in the plane (hkl), it is perpendicular to the plane. Hence, we can represent the vector perpendicular to a lattice plane in terms of reciprocal lattice vectors.

As for the magnitude of $\underline{r}^*_{hkl}$, $\underline{r}^*_{hkl}/\|\underline{r}^*_{hkl}\|$ is the unit vector perpendicular to the plane (hkl). And the projection of the vector $\underline{l}_1/h$ onto $\underline{r}^*_{hkl}/\|\underline{r}^*_{hkl}\|$ is the d-spacing of (hkl) plane, i.e.

$$d_{hkl} = \frac{\underline{r}^*_{hkl}}{\|\underline{r}^*_{hkl}\|} \cdot \frac{\underline{l}_1}{h}.$$

Expanding the equation above with Eqn. 1.7, we have

$$\|\underline{r}^*_{hkl}\| = \frac{1}{d_{hkl}}. \tag{1.10}$$

Then the magnitude of $\underline{r}^*_{hkl}$ is equal to the reciprocal of d-spacing of the (hkl) space. Therefore, each reciprocal lattice point $[hkl]^*$ corresponds a set of lattice planes (hkl) in lattice of direct space. The position of the point in the reciprocal lattice defines the orientation and d-spacing of the lattice planes in the direct lattice. The more distant a reciprocal lattice point is from the origin, the smaller is the d-spacing of the corresponding lattice planes.

1.3.4 Laue's Equation and Ewald's Sphere

With the concept of reciprocal lattice, the Bragg's law can be equivalently transformed in Laue's equation. For diffraction by the (hkl) lattice plane, the Bragg's law (Eqn. 1.4) can be equivalently written as:

$$\frac{1}{d_{hkl}} = \frac{2\sin\theta}{\lambda}. \tag{1.11}$$

From Eqn. 1.10, we can see that the left hand side of Eqn. 1.11 equals the magnitude of reciprocal lattice vector $\underline{r}^*_{hkl}$, i.e. $\|\underline{r}^*_{hkl}\|$. And the right-hand side of Eqn. 1.11 equals to magnitude of difference between incident- and diffracted wavevectors from Fig. 1.8, $\underline{k}^{\mathrm{f}}$ and $\underline{k}^{\mathrm{i}}$, whose lengths are both $1/\lambda$ in case of coherent diffraction, i.e. $\frac{2\sin\theta}{\lambda} = \|\underline{k}^{\mathrm{f}} - \underline{k}^{\mathrm{i}}\|$, therefore, we have

$$\|\underline{r}^*_{hkl}\| = \|\underline{k}^{\mathrm{f}} - \underline{k}^{\mathrm{i}}\|.$$

On the other hand, Bragg's law implicitly implies that the direction of $\underline{k}^{\mathrm{f}} - \underline{k}^{\mathrm{i}}$ is perpendicular to the lattice plane (hkl), which is the same as that of $\underline{r}^*_{hkl}$. Thus, by defining the

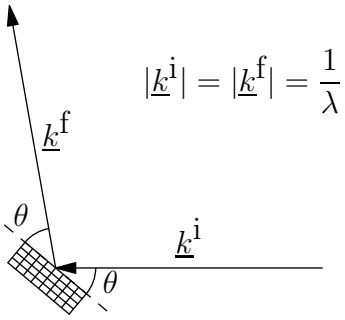

Figure 1.8: Incident and diffracted beams at a Bragg angle of θ.

diffraction vector $\underline{q}$ as:

$$\underline{q} \doteq \underline{k}^{\mathrm{f}} - \underline{k}^{\mathrm{i}}, \tag{1.12}$$

we have Laue's equation equivalent to Bragg's law,

$$\underline{r}^{*}_{hkl} = \underline{q}. \tag{1.13}$$

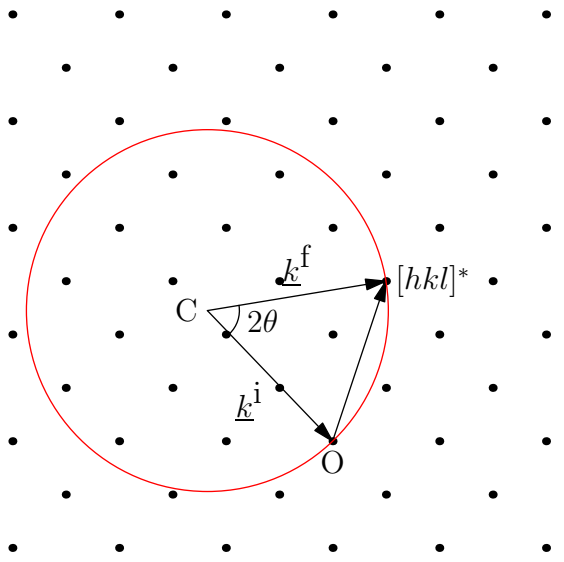

Figure 1.9: Ewald's sphere, the points all belong to the reciprocal lattice.

Laue's equation can be visually illustrated by Ewald's sphere. In Fig. 1.9, the monochromatic incident beam, with a wavelength of λ, impinges upon a crystal. The magnitude of the incident wavevector, $\underline{k}^{\mathrm{i}}$, is $1/\lambda$. We translate $\underline{k}^{\mathrm{i}}$ so that its endpoint lies at the origin of reciprocal lattice, O, and its startpoint is moved to a point, say C. In case of coherent

diffraction, the diffracted wavevector must also have a magnitude of $1/\lambda$, therefore we draw a sphere with a radius of $1/\lambda$ and with its center at C, and this sphere is called Ewald's sphere. The surface of Ewald's sphere represents all possible diffraction direction. Only when a reciprocal lattice point $[hkl]^*$ lies upon Ewald's sphere can the incident beam be diffracted by the (hkl) lattice plane in direct space.

1.3.5 Structure Factor

The Bragg's law (Eqn. 1.4), or Laue's equation (Eqn. 1.13) is the necessary condition for diffraction to occur. However, the occurrence of diffraction is also governed by a so-called *structure factor*, and we will elaborate it in this section.

Let us first define *atomic scattering factor* f: the amplitude of the wave diffracted by a single atom relative to that diffracted by a single electron:

$$f = \frac{\text{Amplitude of the wave diffracted by a single atom}}{\text{Amplitude of the wave diffracted by a single electron}},$$

where f is a complex number with imaginary part which corresponds to the phase difference between the incident and diffracted wave.

For a crystal, the diffraction is the collective effect of diffraction from all unit cells within crystal. And the net effect of diffraction by a unit cell can be expressed as a summation of diffraction from all atoms in a unit cell:

$$F \doteq \sum_{1}^{N} f_n e^{2\pi \mathrm{i} \underline{q} \cdot \underline{r}_n},$$

where N is the total number of atoms within the unit cell, f_n is the atomic scattering factor of the nth atom, $\underline{r}_n$ is the radius vector of the nth atom, and $\underline{q}$ is the diffraction vector. If the diffraction comes from the (hkl) lattice plane, then from Eqn. 1.13, we define the *structure factor* of (hkl) lattice plane, F_{hkl}:

$$F_{hkl} \doteq \sum_{1}^{N} f_n e^{2\pi \mathrm{i} \underline{r}^*_{hkl} \cdot \underline{r}_n}, \tag{1.14}$$

For the occurrence of the diffraction by (hkl) lattice plane, it must be satisfied that $F_{hkl} \neq 0$, otherwise, the diffracted waves by all the atoms with a unit cell will cancel out. For example, for a *bcc* cell containing two atoms, one of them is located at a certain

position, say the origin, and the other is distanced by a vector $\frac{1}{2}\underline{l}_1 + \frac{1}{2}\underline{l}_2 + \frac{1}{2}\underline{l}_3$. hence Eqn. 1.14 become:

$$F_{hkl} = f[1 + e^{\pi \mathrm{i}(h+k+l)}].$$

If $h+k+l$ is odd, then $F_{hkl} = 0$ and we will not detect any diffraction by the (hkl) lattice plane, even if Bragg's law or Laue's equation is met.

1.4 Laue Microdiffraction

1.4.1 The principle of Laue microdiffraction

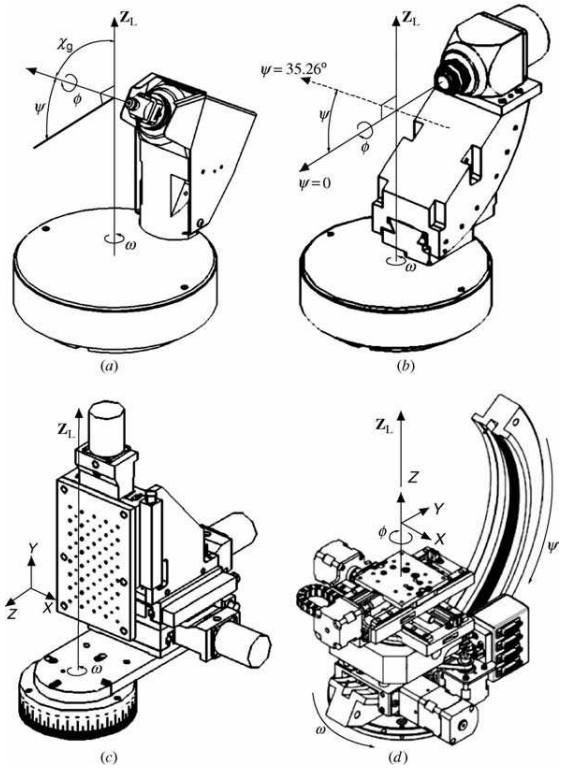

Figure 1.10: Various sample stages of Bruker AXS [He 2009c].

The diffraction will occur if and only if Bragg's law (Eqn. 1.4) or Laue's equation (Eqn. 1.13) is satisfied. The occurrence of diffraction depends on both the incident angle θ impinging lattice plane and the wavelength λ. The essence of any diffraction technique is by varying either the incident angle or the wavelength to meet Bragg/Laue condition.

Therefore, existing diffraction techniques can be classified into two categories according to which quantities are fixed or varied (see Tab. 1.1).

	λ	θ
Rotating method	Fixed	Varied
Laue method	Varied	Fixed

Table 1.1: Two mainstreams of diffraction techniques

In rotating method, the wavelength of monochromatic beam usually corresponds to the characteristic radiation lines of a certain anode, and the unwanted white radiations and characteristic lines are further filtered out by a monochromator, therefore the monochromality of incident beam is well guaranteed [He 2009a]. A sample is first mounted onto the sample stage of diffractometer(see Fig. 1.10). Then user can position and rotate the sample by manipulating the stage to trigger diffraction with incident monochromatic beam. The diffracted beam is recorded either by a point detector or area detector. A typical example of the rotating method is the $\sin^2\psi$ method [Macherauch 1966], adapted for macroscopic stress analysis.

In Laue method, the incident beam is a white beam with a given spectrum, and the incident angle is fixed. The idea of using white beam to probe crystals was first proposed by Max von Laue in order to answer two fundamental questions: (i) What is the nature of X-rays and (ii) does a crystal really consist of periodically spaced atoms. Max von Laue then won the Nobel Prize of Physics in 1914 due to this pioneering work.

Compared to Laue method, experimenters using the rotating method have to take pain to rotate sample, detector, or incident beam to capture diffraction's peak, because, as demonstrated in Fig. 1.9, the chance for a reciprocal lattice point to lie on Ewald's sphere is very small. By contrast, Laue method uses white beam with a certain energy band pass, thus each Ewald sphere of a certain photon energy is superimposed to form a finite volume (see the red area of Fig. 1.11). Every reciprocal lattice points located within this volume will trigger diffraction as long as its structure factor is not zero. And the volume is decided by maximum wavelength and the minimum wavelength in the incident beam, $\lambda_{\max}$ and $\lambda_{\min}$. Therefore, Laue method can economize the time required for rotation.

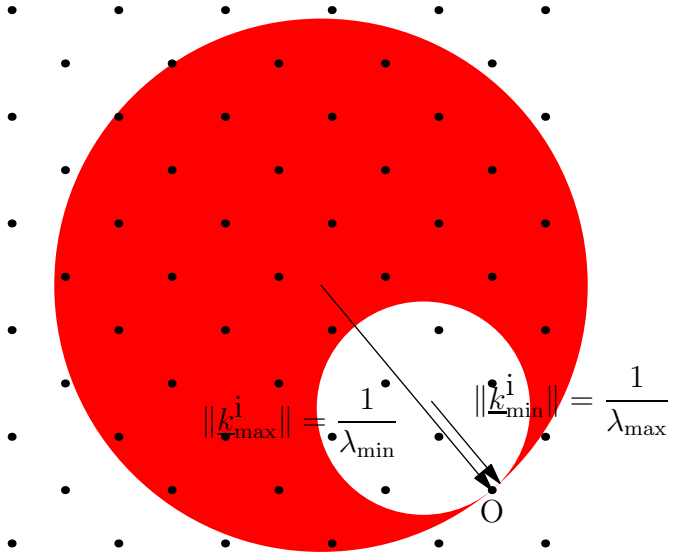

Figure 1.11: Volume for possible diffraction

Moreover, a disadvantage of rotating method is the uncertainty of rotating center (see Fig. 1.12), because in rotating method, it is very hard to ensure that the center of rotation of the goniometer coincides with the region of interest, otherwise the illumination will drift away from the region of interest after rotation. Besides, a goniometer may have multi-axis of rotation, and it is difficult to ensure that they intersect at one point. The uncertainty of their intersection is called sphere of confusion. In practice, the sphere of confusion of goniometer is at best 20 μm. Furthermore, due to the penetration of X-ray, it is impossible to maintain a constant illuminated volume at different incident angle except for the case that the entire sample is smaller than the beam size so that the sample can be bathed in the beam. By contrast, these difficulties do not exit in Laue method. Like electron

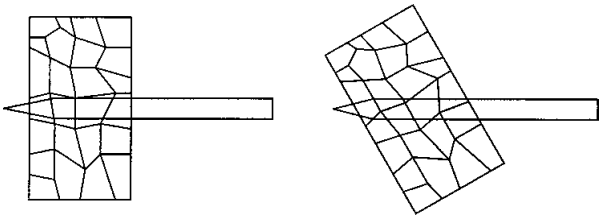

Figure 1.12: Variation of illumination volume introduced by rotation [Chung and Ice 1999]

diffraction mentioned in §1.2.2, Laue diffraction also works in either transmission mode or

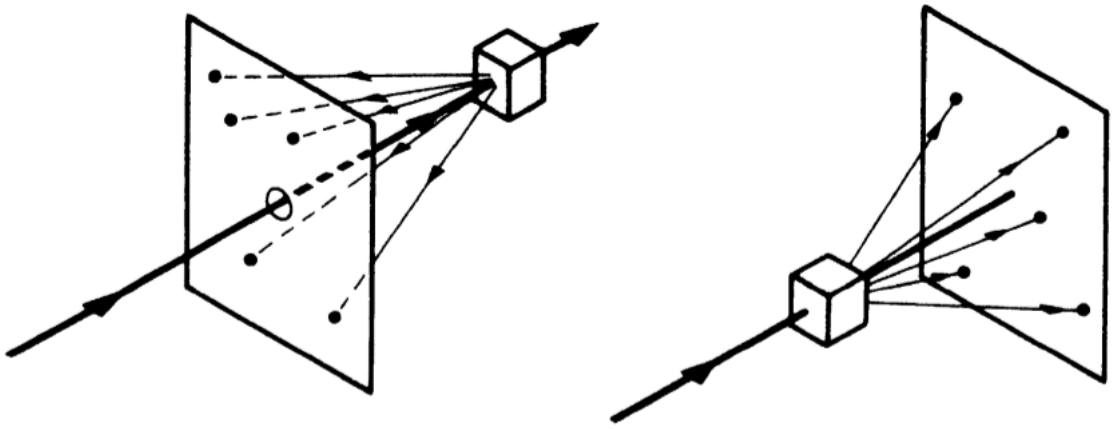

(a) Backscatter Laue diffraction (b) Transmission Laue diffraction

Figure 1.13: Two modes of Laue microdiffraction [Cullity 1956a]

backscatter mode (see Fig. 1.13). Unlike TEM, Laue transmission allows for the analysis of bulk material when using high energy photon [Hofmann et al. 2012].

Both transmission and backscatter Laue diffraction will generate Laue spots on an area detector. The main difference is that the spots of transmission Laue diffraction seem to lie on ellipses while those of backscatter Laue diffraction seem to lie on hyperbolas (see Fig. 1.14).

It is worth noting that Laue method is incapable of measuring the volume of a unit lattice cell, as an isotropic dilatation will not change the Bragg angle. This shortage can be overcome by inserting an energy dispersive detector into experimental setup [Robach et al. 2011] or by switching to monochromatic mode, in that case, at least the energy of one spot, say (hkl), is known, say E_{hkl}. From Eqn. 1.2, the wavelength of spot (hkl) is hc/E. From Eqn. 1.2 and 1.4, we have:

$$d_{hkl} = \frac{hc}{2\sin\theta_{hkl} E_{hkl}}, \tag{1.15}$$

hence, with the energy of at least one spot, we can obtain the d-spacing of direct lattice plane (hkl), and consequently the volume of lattice.

Nowadays with the development of optical technology and synchrotron radiation technology, Laue methods have experienced a renaissance as researchers can scale down the beam size to the order of tens of nm with a brilliance (energy passing through a unit area

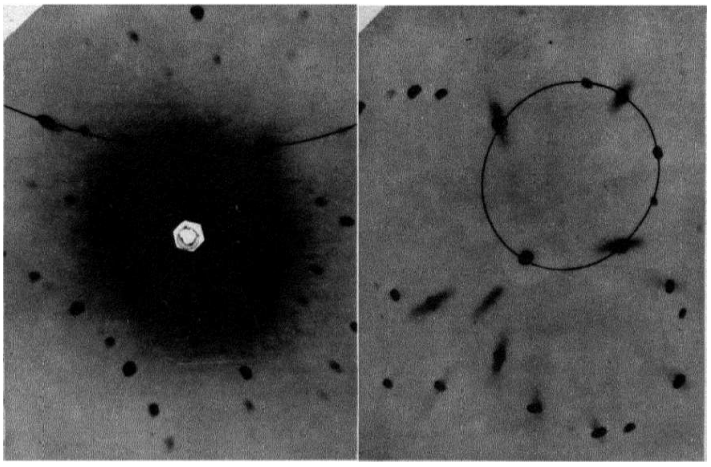

(a) Spots of backscatter Laue diffraction

(b) Spots of transmission Laue diffraction

Figure 1.14: Spots of backscatter and transmission Laue diffraction [Cullity 1956a]

of surface within a unit solid angle in unit time and for a unit bandwidth) which is about 10^4 times that from an X-ray tube [Schwartz and Cohen 1987a]. To distinguish the Laue method with beams produced by X-ray tube, we call the Laue method with micrometric (or even sub-micrometric) beam size Laue microdiffraction. Laue microdiffraction is very suitable for studying intragranular material behavior, as its beam size is smaller than grain size. And also thanks to its penetration, it also enable researchers to gain an in-depth insight into the material by developing a technique called DAXM (Differential Aperture X-ray Microscopy) [Yang et al. 2004; Ice et al. 2006].

There are a number of synchrotron radiation facilities worldwide that can perform Laue microdiffraction, such as ESRF (Grenoble, France), SLS (Villingen, Switzerland), ALS (Berkeley, CA, USA), APS (Chicago, IL, USA), etc. We will introduce BM32 at ESRF as an example to further elaborate Laue microdiffraction technology in §4.2.1.

However, given the high brilliance of synchrotron radiation, we also need to bear in mind that such dosage of radiation might damage the sample [Ice et al. 2009; Holton 2009], or at least, elevate the thermal vibration of atoms within materials, giving rise to *temperature-diffuse scattering* [Cullity 1956b].

1.4.2 Laue microdiffraction vs. HR-EBSD

As we have mentioned in the introduction of this thesis, this thesis is under the framework of ANR project "MICROSTRESS" which targets the developments of HR-EBSD (High angular Resolution EBSD) and Laue microdiffraction. HR-EBSD is a technology initiated by [Troost et al. 1993], and further developed in [Wilkinson 1996; Wilkinson et al. 2006; Villert et al. 2009]. HR-EBSD allows for an angular resolution of 0.01° and hence elastic strain of 10^{-4}. Such improved resolution compared to traditional EBSD is thanks to a current image processing technique called cross-correlation technique. The principle of HR-EBSD can be generalized in the following two steps: (i) use cross-correlation technique to compare the Kikuchi pattern under scrutiny to a reference pattern, which can either be a simulated pattern or originated from a known lattice (ii) calculate the relative deformation gradient with respect to the reference pattern. Another PhD student in "MICROSTRESS" project is working on HR-EBSD.

Both HR-EBSD and Laue microdiffraction are very promising material characterization methods at the scale of micrometer and complementary to each other (see Tab. 1.2).

	Laue microdiffraction	HR-EBSD
spatial resolution	μm	nm
in-depth resolution	Yes	No
accessibility	requires synchrotron beamline, less accessible	requires electron microscopy, more accessible
versatility	more versatile	must be in vacuum environment, less versatile
sample preparation	less laborious	requires surface polishing, more laborious

Table 1.2: Laue microdiffraction vs. HR-EBSD

1.5 Standard Laue Treatment to Obtain Elastic Strain

1.5.1 General Procedure

The elastic strain of crystal arises from lattice distortion, therefore measurement of elastic strain is actually measurement of lattice matrix $\underset{\sim}{l}$. With Laue diffraction, we do not directly measure the lattice matrix in direct space but in reciprocal space. The lattice

matrix in reciprocal space can be transferred to the one in direct space with Eqn. 1.8. From the acquired Laue images, e.g. Fig. 1.18, the sequence of determining lattice matrix can be summarized as following:

1. Locate the Laue peaks on the 2D image, and get their position precisely.

2. Translate the peaks' rectangular positions on the area detector into their angular positions.

3. Index these peaks, i.e. find which (hkl) lattice plane they correspond to.

4. Get the lattice matrix.

The procedure mentioned above has been standarized and implemented in several academic software, such as LaueTools [LaueTools], LaueGo, Xmas, etc. In their implementation, the positions of Laue peaks are usually determined by fitting the intensity distribution of gray level with some analytical function, e.g. Gaussian function, Lorentzian function. Fig. 1.15 shows the panel of fitting a Laue spot from XMAS.

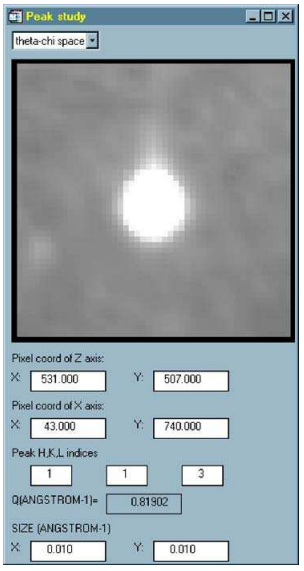

Figure 1.15: The panel of peak study from XMAS [Valek 2003]

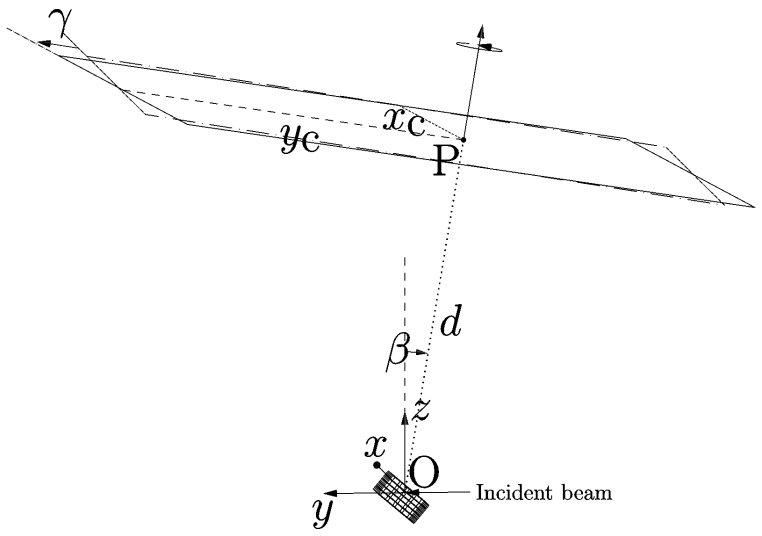

Figure 1.16: Description of calibration parameters of experimental setup

1.5.2 Formulation

We acquire from the area detector the rectangular coordinates of Laue peaks, i.e. the xy coordinates of peaks on the detector screen. However, we actually use angular coordinates of Laue peaks to calculate elastic strain and orientation of lattice. Therefore, it is important to transfer the rectangular coordinates of Laue peaks into the corresponding angular coordinates. In the following, we will define five calibration parameters which associate 2D position of Laue peaks with their angular positions.

The relative spatial relation between incident beam and area detector can be characterized by two angles. Let us first establish an absolute coordinate system (referred to as $\Re$ hereinafter) upon which we will base our calculation (see Fig. 1.16), and a detector frame that lies parallel to the x- and y- axis of $\Re$ when the angle β and γ defined below are zero. The y axis of $\Re$ is collimated with the incident beam. O is the illuminated point at the specimen surface, and P is the orthogonal projection of O onto the detector plane, then x axis is defined as

$$\underline{e}_x \doteq \frac{\underline{e}_y \times \overrightarrow{\mathrm{OP}}}{\|\underline{e}_y \times \overrightarrow{\mathrm{OP}}\|},$$

and z axis is defined as

$$\underline{e}_z \doteq \underline{e}_x \times \underline{e}_y.$$

We characterize the experimental setup with five parameters: x_c, y_c, β, γ, and d [Robach et al. 2011]. d is the distance between illuminated point O and detector plane, i.e. $d = \|\overrightarrow{\mathrm{OP}}\|$. β and γ characterize the spatial relation between $\Re$ and the detector plane: the first angle β is around $x-$ axis, and the second one γ is around the detector's normal $\overline{\mathrm{OP}}$. x_c, y_c are the coordinates of P on the detector plane. These parameters are crucial in translating the peak representation from rectangular coordinate system to angular coordinate system.

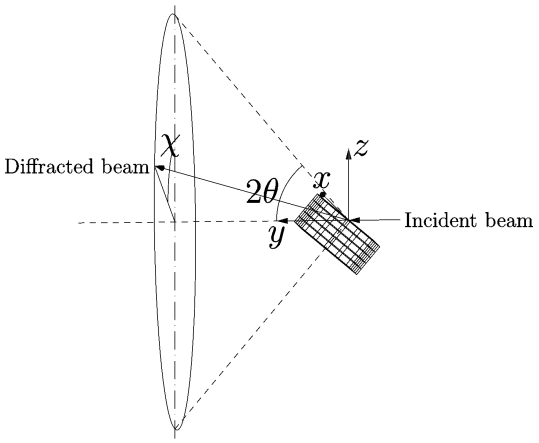

Figure 1.17: Angular coordinate system

The calculation of strain/stress is actually carried upon using the angular position of peak position, $2\theta, \chi$ (see figure 1.17), where 2θ is the apex angle twice the Bragg angle θ, and χ is the azimuthal angle. Here we establish the mathematical formulation translating between peak's angular coordinate $(2\theta, \chi)$ and rectangular coordinates on the detector plane (x, y). Let $\underline{k}^{\mathrm{f}}$ denote the wavevector of the diffracted beam. The unit vector of $\underline{k}^{\mathrm{f}}$, $\hat{\underline{k}}^{\mathrm{f}}$, expressed by the angular position $(2\theta, \chi)$, is

$$[\hat{\underline{k}}^{\mathrm{f}}] = [-\sin 2\theta \sin\chi, \cos 2\theta, \sin 2\theta \cos\chi]^{\mathrm{T}}. \tag{1.16}$$

The superscript $\hat{}$ represents unit vector. Then, we have,

$$[\hat{\underline{k}}^{\mathrm{f}}] = \begin{bmatrix} -\sin 2\theta \sin\chi \\ \cos 2\theta \\ \sin 2\theta \cos\chi \end{bmatrix} = \frac{1}{r} \begin{bmatrix} \cos\gamma & \sin\gamma & 0 \\ -\cos\beta \sin\gamma & \cos\beta \cos\gamma & \sin\beta \\ \sin\beta \sin\gamma & -\sin\beta \cos\gamma & \cos\beta \end{bmatrix} \begin{bmatrix} x - x_c \\ y - y_c \\ d \end{bmatrix}, \tag{1.17}$$

where

$$r \doteq \sqrt{(x - x_c)^2 + (y - y_c)^2 + d^2}. \tag{1.18}$$

The matrix on the right hand of Eqn. 1.17 represents the translation from detector coordinate system to the absolute coordinate system, we represent its transpose by $[\underset{\sim}{g}]$,

$$[\underset{\sim}{g}] \doteq \begin{bmatrix} \cos\gamma & -\cos\beta\sin\gamma & \sin\beta\sin\gamma \\ \sin\gamma & \cos\beta\cos\gamma & -\sin\beta\cos\gamma \\ 0 & \sin\beta & \cos\beta \end{bmatrix}. \tag{1.19}$$

Therefore, Eqn. 1.17 can be written into:

$$[\underset{\sim}{g}] \cdot [\hat{\underline{k}}^{\mathrm{f}}] = \frac{1}{r}[x - x_{\mathrm{c}}, y - y_{\mathrm{c}}, d]^{\mathrm{T}},$$

hence $r = d/(k_i^{\mathrm{f}} g_{3i})$ and

$$\begin{aligned} x &= d\frac{\hat{k}_i^{\mathrm{f}} g_{1i}}{\hat{k}_i^{\mathrm{f}} g_{3i}} + x_{\mathrm{c}}, \\ y &= d\frac{\hat{k}_i^{\mathrm{f}} g_{2i}}{\hat{k}_i^{\mathrm{f}} g_{3i}} + y_{\mathrm{c}}. \end{aligned} \tag{1.20}$$

The equation above can be equivalently written as:

$$\begin{aligned} x &= d\frac{k_i^{\mathrm{f}} g_{1i}}{k_i^{\mathrm{f}} g_{3i}} + x_{\mathrm{c}}, \\ y &= d\frac{k_i^{\mathrm{f}} g_{2i}}{k_i^{\mathrm{f}} g_{3i}} + y_{\mathrm{c}}. \end{aligned} \tag{1.21}$$

From figure (1.8), it is found out that the relation between the unit diffraction vector $\hat{\underline{q}}$ and Bragg angle θ is

$$\hat{\underline{q}} = (\hat{\underline{k}}^{\mathrm{f}} - \hat{\underline{k}}^{\mathrm{i}})/(2\sin\theta), \tag{1.22}$$

$$\sin\theta = -\hat{\underline{q}} \cdot \hat{\underline{k}}^{\mathrm{i}}. \tag{1.23}$$

Because $\hat{\underline{k}}^{\mathrm{i}} \doteq [0, 1, 0]^{\mathrm{T}}$ according to the definition of absolute coordinate system, $\Re$, Eqn. 1.23 can be written as:

$$\sin\theta = -\hat{q}_2. \tag{1.24}$$

From Eqn. 1.9 and 1.13, we have:

$$\underline{q} = \underset{\sim}{l}^* \cdot \underline{h},$$

where $\underline{h}$ is defined as:

$$[\underline{h}] \doteq [h, k, l]^{\mathrm{T}}.$$

Then, the unit vector of $\underline{q}$, $\hat{\underline{q}}$ is:

$$\hat{\underline{q}} = \frac{\underset{\sim}{l}^* \cdot \underline{h}}{\|\underset{\sim}{l}^* \cdot \underline{h}\|}.$$

or,

$$\hat{q}_i = \frac{l^*_{ij} h_j}{\sqrt{l^*_{pm} h_m l^*_{pn} h_n}}. \tag{1.25}$$

Combining the equation above with Eqn. 1.24, we have:

$$\sin\theta = -\frac{l^*_{2j} h_j}{\sqrt{l^*_{pm} h_m l^*_{pn} h_n}}, \tag{1.26}$$

Substituting Eqn. 1.25 and 1.26 into Eqn. 1.22, we have,

$$\hat{k}^{\mathrm{f}}_i = \frac{l^*_{pm} h_m l^*_{pn} h_n \delta_{2i} - 2 l^*_{2j} h_j l^*_{is} h_s}{l^*_{pm} h_m l^*_{pn} h_n}. \tag{1.27}$$

Let's define a new vector, $\underline{\xi}$ whose components are just the numerator of the right hand side of Eqn. 1.27:

$$\xi_i \doteq l^*_{pm} h_m l^*_{pn} h_n \delta_{2i} - 2 l^*_{2j} h_j l^*_{is} h_s. \tag{1.28}$$

Then, Eqn. 1.21 can be written as:

$$\begin{array}{rcl} x & = & d\dfrac{\xi_i g_{1i}}{\xi_i g_{3i}} + x_{\mathrm{c}} \\ y & = & d\dfrac{\xi_i g_{2i}}{\xi_i g_{3i}} + y_{\mathrm{c}} \end{array}. \tag{1.29}$$

ξ only depends on the reciprocal lattice matrix and the hkl index of lattice plane, whereas $[\underset{\sim}{g}]$, x_{c}, y_{c}, and d define the calibration of the experiment.

1.5.2.1 Determination of calibration parameters

In order to determine the five parameters d, x_{c}, y_{c}, β, and γ described previously, it is mandatory to obtain a Laue pattern from a well known strain-free monocrystal, for example Ge monocrystal, located exactly at the same position as the region of interest to be analyzed. Then the diffraction peaks' positions are determined by analytical fitting. With a first estimation of the five parameters and a rough understanding of the orientation of the calibration monocrystal, we index each Laue peak to find the (hkl) index of each spot. This calibration monocrystal is usually glued on the sample (see Fig. 4.7).

With indexations of Laue spots, the procedure used in LaueTool to determine precisely the calibration parameters is as follows [Labat et al. 2011]:

1. First, the ratio of distances between Laue peaks on the area detector are used to determine the β angle.

2. Second, d, the distance between the region of interest and area detector, is deduced from the distances among the Laue peaks and the pixel size of the camera.

3. Adjust the coordinate (x_c, y_c) and the γ angle to minimize the simulated peaks' positions and fitted peaks' position.

The experimental diffraction peak's position is obtained by an analytical fit of the measured spots on the area detector. Usually, the calculated peak's position deviates a little bit (about 0.2 pix in average) from the fitting peaks' position. This is usually due to the imperfect pixel grid permutation on the area detector, errors in estimating peak's position or the simplified model in which the scattering volume is viewed as a point [Labat et al. 2011].

1.5.3 Indexation of peaks

There are a wealth of literature dedicated to peaks' indexation, indexation e.g. by Hough transformation [Wenk et al. 1997], by template matching [Gupta and Agnew 2009; Labat et al. 2011]. Here we present the method by template matching. The basic idea is to compare the experimental angular distances among normals of lattice planes and the theoretical ones. With the unit vector pointing to a peak, $\underline{k}^f$, we can calculate the vector normal to the corresponding lattice planes by:

$$\underline{n} = \frac{\underline{k}^f - \underline{k}^i}{\|\underline{k}^f - \underline{k}^i\|}.$$

The experimental angles between different normals of lattice plane are determined from the scalar product of different $\underline{k}$. With N Laue spots, we have $N(N-1)/2$ angles among each pair of Laue spots. Then, a list of theoretical angles is calculated according to the crystal structure under investigation and the energy band pass of the incident white X-ray beam. Finally, for a triplet of experimental angles, the indexation code will search for the matches among the triplets of theoretical angles so as to give index to each spots among the triplet. Note that it is important to set a angular tolerance between experimental angle and theoretical angle, because lattice distortion, fitting errors, calibration errors, etc may contribute to the discrepancy of experimental angle and theoretical angle. After a match of experimental triplet and theoretical triplet is found, the indexation code will

proceed to calculate a full list of theoretical angular positions of each index, and compare the calculated angular positions to the experimental ones. The match which gives the least discrepancy among the theoretical angular positions and theoretical positions is the best match. It is worth noting that, due to the symmetry of crystal, the indexation of spots is not unique, i.e. the numbers in the indexation can be permuted arbitrarily as long as the angular distances among spots remain constant.

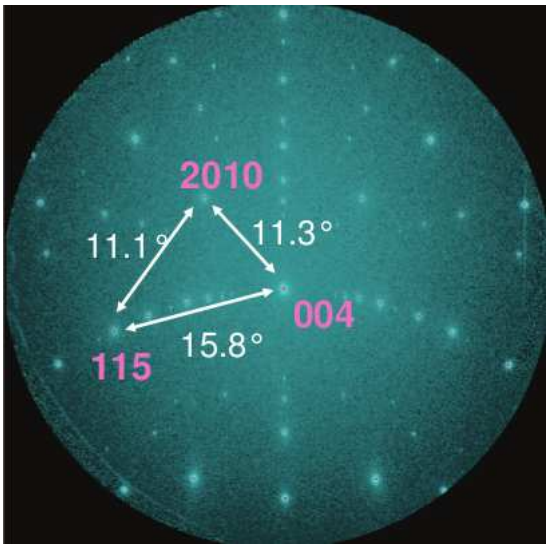

Figure 1.18: For a triplet of Laue spots, we can calculate the angular distances among each spot, and find matches of theoretical angular distances within a given angular tolerance.

If the Laue image contains spots coming from $1 \sim 10$ grains due to, for example, penetration of X-ray or small grain size, [Chung and Ice 1999] have presented an automated routine to find the pertained crystal of each spots and index them. However, we will not elaborate this algorithm here because our treatment is confined to Laue images from monocrystal.

1.5.4 The determination of elastic strain and orientation

After the spots are indexed, it is possible to calculate the lattice matrix and hence the corresponding elastic strain and orientation. Here we present the procedure of [Chung and Ice 1999]. Without any information about the volume of a unit cell, it is only possible to calculate the ratios among components of reciprocal lattice matrix, hence there are eight

degrees of freedom (x and y) in terms of lattice matrix in case of ignorance of lattice volume. Because each spot has two degrees of freedom, at least four spots are needed to calculate the lattice matrix.

Suppose the directions of four Laue spots are measured and denoted as $\underline{n}_i$, $(i = 1, 2, 3, 4)$. And the reciprocal lattice vectors associated to the four Laue spots are denoted as $\underline{r}_i^*$. Here $\hat{\underline{n}}_i$ are related to $\underline{r}_i^*$ through scale factors s_i, which are defined as

$$\begin{aligned} \underline{r}_1^* &= s_1 s_3 \underline{n}_1, \\ \underline{r}_2^* &= s_2 s_3 \underline{n}_2, \\ \underline{r}_3^* &= s_3 \underline{n}_3, \\ \underline{r}_4^* &= c_1 \underline{r}_1^* + c_2 \underline{r}_2^* + c_3 \underline{r}_3^*, \end{aligned}$$

where c_i are determined by the indexes of spots, and s_3 is the overall unit-cell scale factor which cannot be determined without energy measurements. To find s_1 and s_2, we use

$$\begin{cases} \dfrac{\underline{e}_x \cdot \underline{r}_4^*}{\underline{e}_z \cdot \underline{r}_4^*} = \dfrac{(c_1 s_1 \underline{n}_1 + c_2 s_2 \underline{n}_2 + c_3 \underline{n}_3) \cdot \underline{e}_x}{(c_1 s_1 \underline{n}_1 + c_2 s_2 \underline{n}_2 + c_3 \underline{n}_3) \cdot \underline{e}_z} \\ \dfrac{\underline{e}_y \cdot \underline{r}_4^*}{\underline{e}_z \cdot \underline{r}_4^*} = \dfrac{(c_1 s_1 \underline{n}_1 + c_2 s_2 \underline{n}_2 + c_3 \underline{n}_3) \cdot \underline{e}_y}{(c_1 s_1 \underline{n}_1 + c_2 s_2 \underline{n}_2 + c_3 \underline{n}_3) \cdot \underline{e}_z} \end{cases}.$$

The two equations above are used to solve for the two unknown ratios $s_1 = \frac{\|\underline{r}_1^*\|}{\|\underline{r}_3^*\|}$ and $s_2 = \frac{\|\underline{r}_2^*\|}{\|\underline{r}_3^*\|}$. Once s_1 and s_2 are known, the direction and magnitudes (represented in the

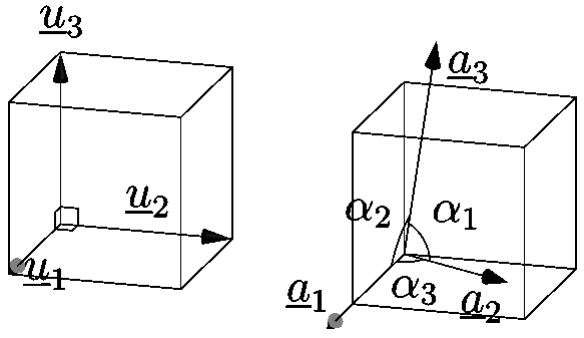

Figure 1.19: Unit cell of lattice and a Cartesian coordinate system attached, used by [Chung and Ice 1999]

unit of s_3) of any reciprocal lattice vector can be determined in the laboratory reference frame, and consequently the reciprocal lattice matrix. And with Eqn. 1.8, we can obtain the lattice matrix $\underset{\sim}{l}$ in direct space, we proceed to extract strain from lattice parameters.

The essence of calculating strain is isolating lattice distortion from lattice rotation. There are many methods of handling this matter, and the convention method [Chung

and Ice 1999] is given below. Consider, for example, a unit cell with lattice parameters $\|\underline{l}_i\|, i = 1, 2, 3$ and $\alpha_i, i = 1, 2, 3$ and a Cartesian coordinate system $\underline{u}_i, i = 1, 2, 3$, which is attached to the lattice (see figure 1.19). Their relations are given as: the vector $\underline{l}_1$ coincides with the $\underline{u}_1$ axis, $\underline{l}_2$ is in the $\underline{u}_1 \otimes \underline{u}_2$ plane, and $\underline{u}_3$ is perpendicular to the $\underline{u}_1 \otimes \underline{u}_2$ plane:

$$\begin{array}{rcl} \underline{u}_1 & \doteq & \dfrac{\underline{l}_1}{\|\underline{l}_1\|}, \\ \underline{u}_3 & \doteq & \dfrac{\underline{l}_1 \times \underline{l}_2}{\|\underline{l}_1 \times \underline{l}_2\|}, \\ \underline{u}_2 & \doteq & \dfrac{\underline{l}_3 \times \underline{l}_1}{\|\underline{l}_3 \times \underline{l}_1\|}. \end{array} \tag{1.30}$$

In this manner, a lattice direction $[uvw]$ can be expressed in the attached Cartesian coordinate system as well:

$$\underline{r}_{uvw} = u\underline{l}_1 + v\underline{l}_2 + w\underline{l}_3 = uB_{1i}\underline{u}_i + vB_{2j}\underline{u}_j + wB_{3k}\underline{u}_k, \tag{1.31}$$

where B_{ij} is the component of the matrix $\underset{\sim}{B}$:

$$[\underset{\sim}{B}] \doteq [\underline{u}_1, \underline{u}_2, \underline{u}_3]^{\mathrm{T}} \cdot [\underline{l}_1, \underline{l}_2, \underline{l}_3] = \begin{bmatrix} \|\underline{l}_1\| & \|\underline{l}_2\| \cos\alpha_3 & \|\underline{l}_3\| \cos\alpha_2 \\ 0 & \|\underline{l}_2\| \sin\alpha_3 & -\|\underline{l}_3\| \sin\alpha_2 \cos\alpha_1^* \\ 0 & 0 & 1/\|\underline{l}_3^*\| \end{bmatrix}. \tag{1.32}$$

Here, $\underline{l}_i^*$ and $\alpha_i^*, i = 1, 2, 3$ $(i = 1, 2, 3)$ are the reciprocal lattice vectors and their angles. Denote $\underset{\sim}{U}$ as:

$$[\underset{\sim}{U}] \doteq [\underline{u}_1, \underline{u}_2, \underline{u}_3].$$

Obviously, $\underset{\sim}{U}$ is an orthogonal matrix, therefore Eqn. 1.32 can be written into

$$\underset{\sim}{U} \cdot \underset{\sim}{B} = \underset{\sim}{l}, \tag{1.33}$$

where $\underset{\sim}{U}$ represents the orientation of the lattice, and $\underset{\sim}{B}$ represents the shape and volume of the lattice. Since the lattices of the materials under scrutiny are all cubic lattice, for lattice without distortion, the lattice parameters should be:

$$\begin{array}{l} |\underline{B}_1| = |\underline{B}_2| = |\underline{B}_3|; \\ \alpha_1 = \alpha_2 = \alpha_3 = \pi/2. \end{array} \tag{1.34}$$

As we are ignorant of the lattice's volume without measuring Laue spots' energy, we only get the shape of the lattice:

$$\hat{\underset{\sim}{B}} = \frac{\underset{\sim}{B}}{\sqrt[3]{\det \underset{\sim}{B}}}.$$

In this manner, the elastic strain of the lattice, represented in lattice frame, should be expressed as:

$$\underset{\sim}{\varepsilon}^{\text{lattice}} \doteq c\frac{\hat{\underset{\sim}{B}} + \hat{\underset{\sim}{B}}^{\text{T}}}{2} - \underset{\sim}{1},$$

where c is a constant relating to the dilatation of lattice. With $\underset{\sim}{\varepsilon}$, we are able to calculate the stress in lattice frame,

$$\underset{\sim}{\sigma}^{\text{lattice}} = \underset{\sim}{\underset{\sim}{C}} : \underset{\sim}{\varepsilon}^{\text{lattice}}.$$

where $\underset{\sim}{\underset{\sim}{C}}$ is the elastic tensor expressed in the lattice frame.

The stress in the lattice frame needs to be further rotated into laboratory frame by,

$$\underset{\sim}{\sigma} = \underset{\sim}{U} \cdot \underset{\sim}{\sigma}^{\text{lattice}} \cdot \underset{\sim}{U}^{\text{T}}.$$

However, it is worth noting that in practice, Laue microdiffraction cannot measure the c, therefore we can only get the deviatoric part of $\underset{\sim}{\varepsilon}^{\text{lattice}}$, say $\underset{\sim}{\varepsilon}'$, whose trace is designated to be zero, i.e. $\underset{\sim}{\varepsilon}' : \underset{\sim}{1} = 0$. Will the absence of volumetric strain, say $\underset{\sim}{\varepsilon}^{\text{vol}}$, contribute to errors to the evaluation of deviatoric stress, say $\underset{\sim}{\sigma}'$? That depends on the values of $\underset{\sim}{\underset{\sim}{C}}$, if

$$\underset{\sim}{\underset{\sim}{C}} : \underset{\sim}{1} = \lambda \underset{\sim}{1}, \tag{1.35}$$

where λ is a certain constant, then it is safe to declare that:

$$\underset{\sim}{\sigma}' = \underset{\sim}{\underset{\sim}{C}} : \underset{\sim}{\varepsilon}'. \tag{1.36}$$

1.6 Summary

In the beginning of this chapter, we have presented the context of the thesis, three commonly used diffraction method (neutron diffraction, electron diffraction, and X-ray diffraction), their advantages and disadvantages. Under the framework of ANR project "MICROSTRESS", two diffraction techniques: HR-EBSD and Laue microdiffraction will be developed, not only because they are well adapted to material characterization at microscale, but also because they are complementary in terms of spatial resolution, in-depth resolution, accessibility, versatility, and readiness of sample preparation. This thesis is dedicated to the development of Laue microdiffraction.

Then we have introduced the principle of Laue microdiffraction, including the kinematic theory of X-ray diffraction, advantages of Laue diffraction by using white beam rather than monochromatic beam, and the renaissance of Laue diffraction thanks to the developments in synchrotron radiation and optics.

Finally, we have narrated the standard Laue Treatment of obtaining the elastic strain and orientation from Laue microdiffraction image. We will improve the procedure with the aid of DIC (Digital Image Correlation), which will be presented in the next chapter.

Chapter 2

Laue-DIC and its Precision

2.1 Motivation

From the previous chapter, we can conclude that the determination of elastic strain and crystal orientation basically rests upon locating the positions of peaks on the area detector. For example, for a steel sample undergoing a tensile test (see Fig. 2.1), reaching an accuracy

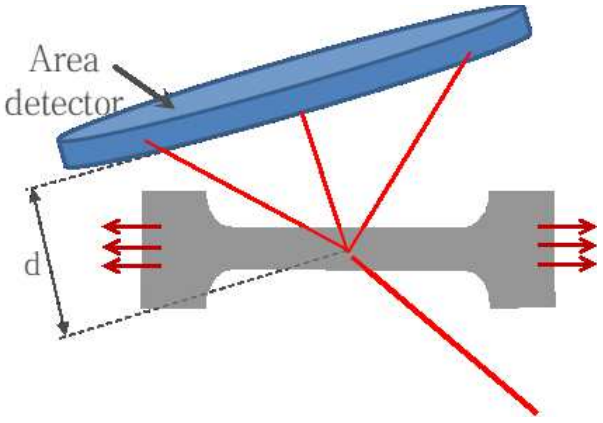

Figure 2.1: A steel monocrystal sample undergoes a tensile test.

of 10 MPa on the tensile stress (equivalent to an accuracy of 5×10^{-5} on the elastic strain) typically requires determining diffracted beam directions with an angular resolution of the order of 0.05 mrad. That angular resolution further corresponds to an accuracy of ~ 0.1 pix in locating peak's position if the sample-detector distance $d = 165$ mm and the pixel size $1\,\text{pix} = 80.6\,\mu\text{m}$. That is to say, it is imperative to locate peaks' positions with a subpixel resolution if we wish to attain an accuracy of 10 MPa on the stress, or an accuracy of

5×10^{-5} on the elastic strain.

The standard Laue treatment described in the previous chapter, although plausible, suffers from the following approximations:

1. as described in §1.5.2, the calibration parameters are obtained by matching the Laue pattern obtained from a calibration monocrystal. In this process, the distortions of the area detector grid may give rise to the inaccuracies of measurements of diffraction peaks.

2. Moreover, the diffraction peaks are usually obtained by fitting the spots with an analytical function, e.g. Gaussian function, Lorentz function, etc. Typically, the theoretical peaks' positions deviate on average about 0.1 pix from the fitted peaks' position [Poshadel et al. 2012].

3. Shifting the illumination from the calibration monocrystal to the region of interest would introduce some errors due to the inaccuracies of motor's motion, no matter how careful the experimenter shifts the illumination. Moreover, the difference in the penetration depth between the calibration monocrystal and the sample of interest would contribute to the uncertainties of calibration parameters as well.

4. The diffraction peaks from the region of interest on the sample is determined by analytical fitting as well. The mainstream codes of treating Laue diffraction image requires the ellipticity of spots, because the analytical functions employed, either Gaussian function or Lorentzian function, are elliptically shaped. Although there exist Laue spots which take on elliptical shapes (see Fig. 1.15), some spots exhibit irregular shapes and can hardly be described by an analytical function (see Fig. 2.2). These deviations from ellipticity can be attributed to various reasons, for example, the existence of geometrical necessary dislocations (GND) would streak the Laue spots [Barabash et al. 2001]; for pure crystal undergoing bending each Laue spot would be accompanied by a satellite spot due to dynamic effect [Yan and Noyan 2006].

These error sources mentioned above will eventually accumulated into the evaluation of

elastic strain, and hence stress. For example, it is found that stress fluctuations of the order of 1 GPa in a single crystal of pure Cu [Magid et al. 2009], a result which might not be physically relevant as it far exceeds the yield limit of Cu.

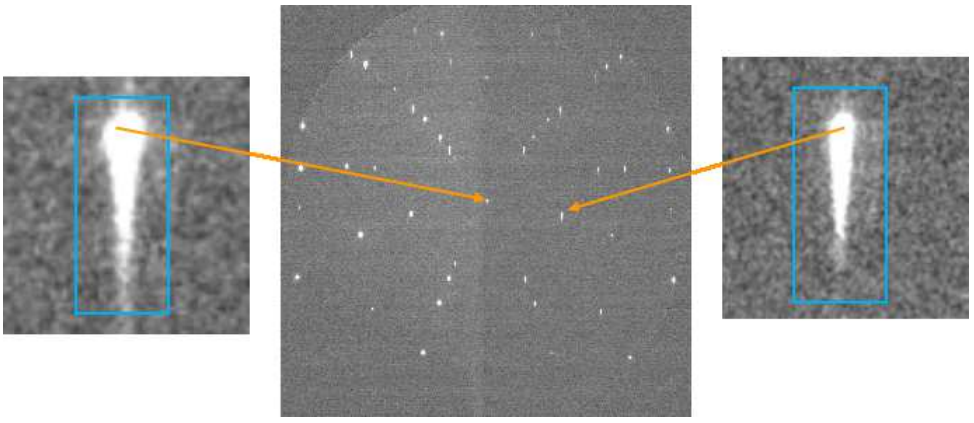

Figure 2.2: Irregular spots in diffraction image of Si.

To solve these problems, J. Petit introduced digital image correlation (DIC) technology into the treatment of Laue diffraction image [Petit et al. 2012, 2015]. The new treatment will be denoted as Laue-DIC hereinafter. The basic idea behind Laue-DIC is borrowed from HR-EBSD (see §1.4), i.e. use the peaks' displacements between two images (see Fig. 2.3), instead of peaks' absolute positions, to obtain relative deformation gradient. This requires that the spots of two diffraction images carry some resemblance. The idea of using peaks' displacements is superior to using peaks' absolute positions in the following way:

1. The uncertainty of DIC is of the order of 0.01 pix [Bornert et al. 2009; Amiot et al. 2013], much less than that of analytical fitting, which is of the order of 0.1 pix [Poshadel et al. 2012].

2. DIC is insensitive to spots' shapes, as long as the two correlated spots carry resemblance. The resemblance can be quantified by a parameter called correlation coefficient, which will be mentioned in §2.2.1. Thanks to the concept of correlation coefficient, we can *a posteriori* verify the resemblance of spots by investigating the correlation coefficient.

To give a visual impression about the improved accuracy with DIC compared to ana-

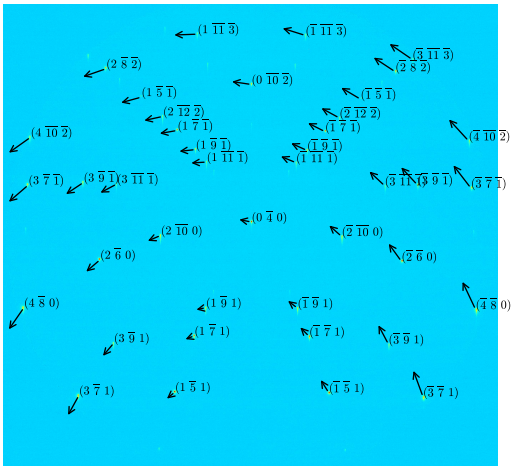

Figure 2.3: Displacement field of Laue spots on the area detector, for a specimen undergoing deformation.

lytical fitting, we present an experimental investigation done by acquiring successive Laue patterns on a Ge monocrystal translating in a direction almost parallel to the incoming beam, i.e. almost parallel to the area detector (see Fig. 2.4) [Petit et al. 2012, 2015]. The detector used in the test was MarCCD detector. The distance that the Ge monocrystal traveled matches approximately the size of one pixel of the detector screen (80.5 μm), and 100 Laue patterns were recorded at regular intervals in course of the translation of Ge monocrystal. The Laue patterns are expected to be displaced rigidly by an amount equal to the imposed translation of the specimen. Therefore, the DIC's accuracy can be expected by comparing the spots displacements measured by DIC and the one prescribed to the specimen.

This analysis enables the investigation of both systematic error and random error of spots' displacements. The systematic error is expressed as the discrepancy of the average displacements of all Laue spots and the prescribed displacements, and provides a measure of the overall displacement error resulting from the DIC technique. The random error is the standard deviation of the displacements measured for all Laue spots and provides an estimation of the displacement fluctuation as DIC does not guarantee the uniformity of measurements of spots' displacements when they are measured independently. In this analysis, 75 spots were taken into consideration and biquintic gray level interpolation was

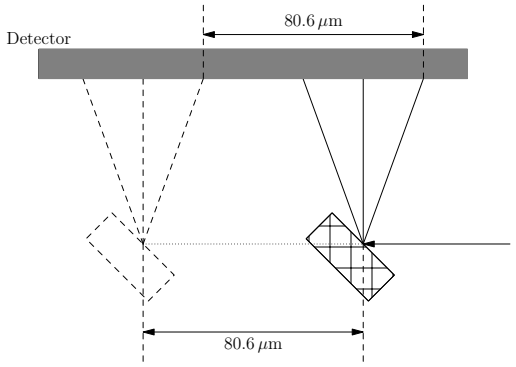

Figure 2.4: A Ge monocrystal is translated along the incident X-ray for evaluating DIC accuracy of Laue spots' displacements

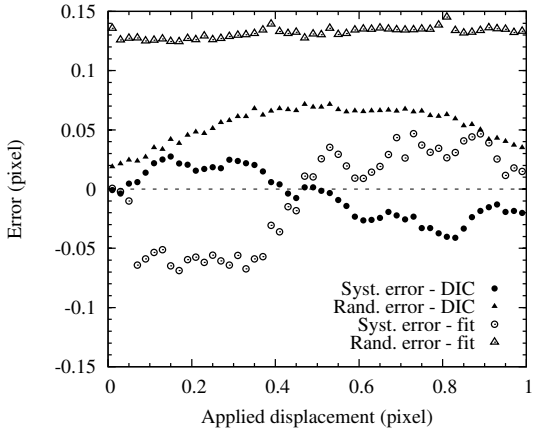

Figure 2.5: Systematic and random errors of DIC over 85 spots with subpixel translation. Both applied displacements and errors are expressed in pixel unit.

used (see §2.2.1 for more details of DIC).

Fig. 2.5 shows the results of systematic and random errors of spots' displacements. The systematic error recovered an S-shape curve as indicated by [Bornert et al. 2009; Amiot et al. 2013] with a maximum values of ~ 0.03 pix and an average (of the absolute value of errors) of 0.018 pix. The random error is slightly larger with a maximum error of 0.07 pix and an average of 0.054 pix. For comparison, we also gave the systematic error and random error when the displacements were obtained by analytical fitting of the absolute positions (Fig. 2.5). Obviously, both systematic and random errors are larger than those by DIC.

Now that we have presented the improved accuracy of peaks' displacements acquired

by DIC than peaks' absolute position acquired by analytical fitting,in the following, we will first introduce the principle of DIC and the calculation of Laue-DIC. To go one step further, one needs to evaluate the accuracy of DIC when applying it to Laue images. As this accuracy is largely influenced by the image noise, we will introduce the classical Poissonian-Gaussian model for describing image noise and test it with experimental images in order to validate this model and estimate the parameters of the model as well. Then, we investigate the error of DIC with synthetic spots' images. Finally, we study how the DIC errors is culminated into the errors of elastic strain using Laue-DIC by numerical tests.

2.2 Laue-DIC

2.2.1 Principle of DIC

Digital image correlation (DIC) belongs to the category of optical full-field measurement techniques. Compared to other optical technique, e.g. photoelasticity, moiré, holographic, speckle interferometry, grid method, etc, the procedure of DIC is more straightforward and simple.It originates from the research activities in artificial intelligence and robotic to develop vision-based algorithms and stereo-vision methodologies in parallel with photogrammetry applications for aerial photographs [Sutton et al. 2009a]. However, gradually, it lent its application to the realm of mechanics, because it offers a non-contact and non-destructive method to measure material's displacement/deformation field [Peters and Ranson 1982; Wattrisse et al. 2001; Abanto-Bueno and Lambros 2002; Wang and Cuitiño 2002; Bergonnier et al. 2005].

The procedure of DIC consists in recording some digital images of a specimen in course of its deformation with a camera and treating these images with an image correlation code. The image correlation code will match the subsets in a series of images to provide a measurement of the displacement field. Thanks to the constant shrinkage of costs of digital cameras and computers, this technology is becoming more and more available to both industry and academic society. We will elaborate on this technique by introducing several vital concept in DIC.

Correlation Window Correlation window is a region within the whole image, usually a rectangle. It is the displacement field of the correlation window that DIC code will track.

Correlation Coefficient Correlation coefficient is a quantification of subset resemblance. DIC code tracks the displacement field of one correlation window in a sequence of images by seeking an extremum of correlation coefficient. Various forms of correlation coefficients are available Amiot et al. [2013]: zero mean normalised cross-correlation (ZNCC), normalised sum of squared difference (NSSD), sum of squared differences (SSD), and normalised cross-correlation (NCC). The simplest form of correlation coefficient is SSD and NCC:

$$\begin{aligned} C_{\mathrm{SSD}} &= \sum (f_i - g_i)^2, \\ C_{\mathrm{NCC}} &= \sum f_i g_i, \end{aligned}$$

where f_i and g_i are the gray levels at the ith pixel of the two investigated images. The smaller C_{SSD} is, the more resemblance exists between two compared correlation windows, while it is opposite with C_{NCC}.

In practice, though ZNCC is much more complex than SSD and NCC, it is insensitive to the uniform offset and scale changes in the gray level of image, and gives the best results compared to other correlation coefficient in terms of displacement measurement Tong [2005]. Its expression is:

$$C_{\mathrm{ZNCC}} = 1 - \frac{\sum (f_i - \overline{f})(g_i - \overline{g})}{\sqrt{\sum (f_i - \overline{f})^2 \sum (g_i - \overline{g})^2}}. \tag{2.1}$$

Shape Function The displacement field within the correlation window is usually approximated by a linear combination of several analytical expression, usually polynomial. These analytical functions are called shape function. The most used shape function is second order polynomial, given by

$$\left\{ \begin{array}{rcl} u(X,Y) &=& a_{u1} + a_{u2}\Delta X + a_{u3}\Delta Y + a_{u4}\Delta X \Delta Y \\ & & + a_{u5}\Delta X^2 + a_{u6}\Delta Y^2 + a_{u7}\Delta X^2 \Delta Y \cdots \\ & & \cdots + a_{u8}\Delta X \Delta Y^2 + a_{u9}\Delta X^2 \Delta Y^2 \\ v(X,Y) &=& a_{v1} + a_{v2}\Delta X + a_{v3}\Delta Y + a_{v4}\Delta X \Delta Y \\ & & + a_{v5}\Delta X^2 + a_{v6}\Delta Y^2 + a_{v7}\Delta X^2 \Delta Y \cdots \\ & & \cdots + a_{v8}\Delta X \Delta Y^2 + a_{v9}\Delta X^2 \Delta Y^2 \end{array} \right. \tag{2.2}$$

where $\Delta X = X - X_0$, $\Delta Y = Y - Y_0$, (X_0, Y_0) being the center of correlation window. The order of shape function reflects its capability to describe complex deformation mode. The simplest shape function is zero order polynomial associated with pure translation, i.e. only a_{u1}, $a_{v1} \neq 0$.

Gray Level Interpolation Correlation computations often needs evaluation of gray levels at non-integer pixel location in order to get a subpixel resolution. For that end, correlation code will interpolate adjacent integer pixel to estimate the gray level at non-integer location. Interpolation methods used by DIC include: polynomial interpolation, B-spline interpolation, Fourier or wavelet transforms.

The principle of DIC can also be extended to explore out-plane motion (3D-DIC [Sutton et al. 2009c]) and motion underneath surface (Volumetric-DIC [Sutton et al. 2009d]). These extensions often require additional image acquisition equipment.

2.2.2 Calculation of Relative Deformation Gradient

Like in HR-EBSD (see §1.4), we use the displacements of Laue spots to evaluate the relative deformation gradient from one lattice whose matrix, $\underset{\sim}{L}$, is supposed to be known, to another lattice whose matrix, $\underset{\sim}{l}$, is to be determined. We refer to the lattice whose matrix is known as reference lattice, and the configuration whose lattice is to be determined as current configuration. Once we have determined the reciprocal relative deformation gradient between two configurations, $\underset{\sim}{F}^*$, the reciprocal lattice matrix in current configuration, $\underset{\sim}{l}^*$, can be calculated by:

$$\underset{\sim}{l}^* = \underset{\sim}{F}^* \cdot \underset{\sim}{L}^*,$$

where $\underset{\sim}{L}^*$ represents the reciprocal lattice matrix of reference configuration.

Although in [Petit et al. 2012, 2015] $\underset{\sim}{F}$ was calculated by minimizing the dicrepancy between the simulated displacements of spots and those measured by DIC, i.e.

$$\sum_{hkl} \|\Delta \underline{X}_{\mathrm{sim}}(\underset{\sim}{F}|\underset{\sim}{l}_0, hkl) - \Delta \underline{X}^{hkl}_{\mathrm{dic}}\|^2,$$

it is more straightforward to use linear regression to calculate a least-square solution of $\underset{\sim}{F}^*$, and we will demonstrate this method in the following. Since we can not determine the

absolute value of lattice matrix, we can impose arbitrarily any component of lattice matrix to be 1, as long as this component is not zero in laboratory system. Here, with no loss of generality, we prescribe the xx component of reciprocal relative deformation gradient, F^*_{11}, to be one, and determine the least square solution of the reciprocal lattice matrix.

For reference configuration, since its lattice matrix is known *a priori*, the unit vector of the normal of lattice plane (hkl) can be calculated as:

$$\underline{n}^{\mathrm{ref}}_{hkl} = \frac{\begin{bmatrix} L^*_{11} & L^*_{21} & L^*_{31} \\ L^*_{12} & L^*_{22} & L^*_{32} \\ L^*_{13} & L^*_{23} & L^*_{33} \end{bmatrix} \begin{bmatrix} h \\ k \\ l \end{bmatrix}}{\left\| \begin{bmatrix} L^*_{11} & L^*_{21} & L^*_{31} \\ L^*_{12} & L^*_{22} & L^*_{32} \\ L^*_{13} & L^*_{23} & L^*_{33} \end{bmatrix} \begin{bmatrix} h \\ k \\ l \end{bmatrix} \right\|}.$$

Then, with Eqn. 1.20 and 1.22 (note that $\underline{n}^{\mathrm{ref}}_{hkl} = \hat{q}$ as the diffraction vector must be normal to the diffraction plane), we can transform the unit vector $\underline{n}^{\mathrm{ref}}_{hkl}$ into Laue spot's position $(x^{\mathrm{ref}}_{hkl}, y^{\mathrm{ref}}_{hkl})$. And we can further get the spot's position at current configuration with the spot's displacement $(\Delta x^{\mathrm{dic}}_{hkl}, \Delta y^{\mathrm{dic}}_{hkl})$, measured by DIC from reference configuration to current configuration:

$$\begin{aligned} x^{\mathrm{cur}}_{hkl} &= x^{\mathrm{ref}}_{hkl} + \Delta x^{\mathrm{dic}}_{hkl} \\ y^{\mathrm{cur}}_{hkl} &= y^{\mathrm{ref}}_{hkl} + \Delta y^{\mathrm{dic}}_{hkl}. \end{aligned}$$

Laue spot's position $(x^{\mathrm{cur}}_{hkl}, y^{\mathrm{cur}}_{hkl})$ in current configuration can be transformed into unit vector $\underline{n}^{\mathrm{cur}}_{hkl}$ by Eqn. 1.17. In this way, we get the unit vectors of Laue spots in reference and current configuration, the relation are given as:

$$\begin{bmatrix} (\underline{n}^{\mathrm{cur}}_i)_1 \\ (\underline{n}^{\mathrm{cur}}_i)_2 \\ (\underline{n}^{\mathrm{cur}}_i)_3 \end{bmatrix} = \frac{1}{\rho_i} \begin{bmatrix} 1 & F^*_{21} & F^*_{31} \\ F^*_{12} & F^*_{22} & F^*_{32} \\ F^*_{13} & F^*_{23} & F^*_{33} \end{bmatrix} \begin{bmatrix} (\underline{n}^{\mathrm{ref}}_i)_1 \\ (\underline{n}^{\mathrm{ref}}_i)_2 \\ (\underline{n}^{\mathrm{ref}}_i)_3 \end{bmatrix}, \tag{2.3}$$

where the subscript $_i$ represents the ordering of Laue spots, and ρ_i is the normalization

factor to ensure both sides of Eqn. 2.3 to be unit vectors. Eqn. 2.3 can also be written as:

$$\begin{bmatrix} (\underline{n}_i^{\mathrm{ref}})_2 & (\underline{n}_i^{\mathrm{ref}})_3 & 0 & 0 & 0 & 0 & 0 & 0 & -(\underline{n}_i^{\mathrm{cur}})_1 \\ 0 & 0 & (\underline{n}_i^{\mathrm{ref}})_1 & (\underline{n}_i^{\mathrm{ref}})_2 & (\underline{n}_i^{\mathrm{ref}})_3 & 0 & 0 & 0 & -(\underline{n}_i^{\mathrm{cur}})_2 \\ 0 & 0 & 0 & 0 & 0 & (\underline{n}_i^{\mathrm{ref}})_1 & (\underline{n}_i^{\mathrm{ref}})_2 & (\underline{n}_i^{\mathrm{ref}})_3 & -(\underline{n}_i^{\mathrm{cur}})_3 \end{bmatrix} \begin{bmatrix} F_{12}^* \\ F_{13}^* \\ F_{21}^* \\ F_{22}^* \\ F_{23}^* \\ F_{31}^* \\ F_{32}^* \\ F_{33}^* \\ \rho_i \end{bmatrix}$$

$$= \begin{bmatrix} -(\underline{n}_i^{\mathrm{ref}})_1 \\ 0 \\ 0 \end{bmatrix}. \tag{2.4}$$

If there are N Laue spots taken into account, Eqn. 2.4 can be assembled into:

$$\begin{bmatrix} \underset{\sim}{P}_1 & \underline{Q}_1 \\ \vdots & \vdots \\ \underset{\sim}{P}_n & \underline{Q}_n \end{bmatrix} \begin{bmatrix} F_{12}^* \\ F_{13}^* \\ F_{21}^* \\ F_{22}^* \\ F_{23}^* \\ F_{31}^* \\ F_{32}^* \\ F_{33}^* \\ \rho_1 \\ \vdots \\ \rho_N \end{bmatrix} = \begin{bmatrix} \underline{R}_1 \\ \vdots \\ \underline{R}_n \end{bmatrix} \tag{2.5}$$

where

$$[\underset{\sim}{P}_i] = \begin{bmatrix} (\underline{n}_i^{\mathrm{ref}})_2 & (\underline{n}_i^{\mathrm{ref}})_3 & 0 & 0 & 0 & 0 & 0 & 0 \\ 0 & 0 & (\underline{n}_i^{\mathrm{ref}})_1 & (\underline{n}_i^{\mathrm{ref}})_2 & (\underline{n}_i^{\mathrm{ref}})_3 & 0 & 0 & 0 \\ 0 & 0 & 0 & 0 & 0 & (\underline{n}_i^{\mathrm{ref}})_1 & (\underline{n}_i^{\mathrm{ref}})_2 & (\underline{n}_i^{\mathrm{ref}})_3 \end{bmatrix},$$

$$[\underline{Q}_i] = \begin{bmatrix} 0 & \cdots & 0 & -(n_i^{\mathrm{cur}})_1 & 0 & \cdots & 0 \\ 0 & \cdots & 0 & -(n_i^{\mathrm{cur}})_2 & 0 & \cdots & 0 \\ \underbrace{0}_{1} & \cdots & \underbrace{0}_{i-1} & \underbrace{-(n_i^{\mathrm{cur}})_3}_{i} & \underbrace{0}_{i+1} & \cdots & \underbrace{0}_{N} \end{bmatrix},$$

and

$$[\underline{R}_i] = \begin{bmatrix} -(\underline{n}_i^{\mathrm{ref}})_1 \\ 0 \\ 0 \end{bmatrix}.$$

With N reciprocal points, there are totally $3N$ equations and $8 + N$ variables, so at least 4 reciprocal points are needed to get the deformation gradient.

If $N \geq 4$, a least-square solution can be obtained. More specifically,

$$[\underset{\sim}{S}] = \begin{bmatrix} F^*_{12} \\ F^*_{13} \\ F^*_{21} \\ F^*_{22} \\ F^*_{23} \\ F^*_{31} \\ F^*_{32} \\ F^*_{33} \\ \rho_1 \\ \vdots \\ \rho_N \end{bmatrix} = ([\underset{\sim}{C}]^{\mathrm{T}}[\underset{\sim}{C}])^{-1}[\underset{\sim}{C}]^{\mathrm{T}}[\underset{\sim}{R}] \tag{2.6}$$

where

$$[\underset{\sim}{C}] = \begin{bmatrix} \underset{\sim}{P}_1 & \underset{\sim}{Q}_1 \\ \vdots & \vdots \\ \underset{\sim}{P}_N & \underset{\sim}{Q}_N \end{bmatrix} \quad \text{and} \quad [\underset{\sim}{R}] = \begin{bmatrix} \underline{R}_1 \\ \vdots \\ \underline{R}_N \end{bmatrix}$$

Only the first eight terms of the solution $[\underset{\sim}{S}]$ is of our concern, which is just the rest eight component of the reciprocal relative deformation gradient $\underset{\sim}{F}^*$. $\underset{\sim}{F}^*$ can be conveniently transformed into relative deformation gradient in real space by

$$\underset{\sim}{F} = (\underset{\sim}{F}^*)^{-\mathrm{T}}, \tag{2.7}$$

and together with the reference lattice matrix, which is supposed to be known, we can calculate the current lattice matrix.

The introduction of DIC is supposed to have improved the precision of elastic strain measurement. To have a visual idea of the difference of original Laue-DIC and standard Laue treatment, we scanned the Si monocrystal in four-point bending test (see Fig. 4.5) along x-axis to get a sequence of Laue microdiffraction images, and plotted in Fig. 2.6 the trajectories of spots with indexes of (371) and $(1\bar{1}7)$ of the sequence. We compared the trajectories by analytical peak fitting and DIC: the blue trajectory was determined entirely by analytical fitting of the absolute position of spot, and the green trajectory was determined by first obtaining absolute position of spot in one image by analytical fitting and then measuring the displacements of the spots in other images of the same sequence by DIC. It is obvious that the green trajectory, which is determined with the aide of DIC, displays less fluctuation that the blue one.

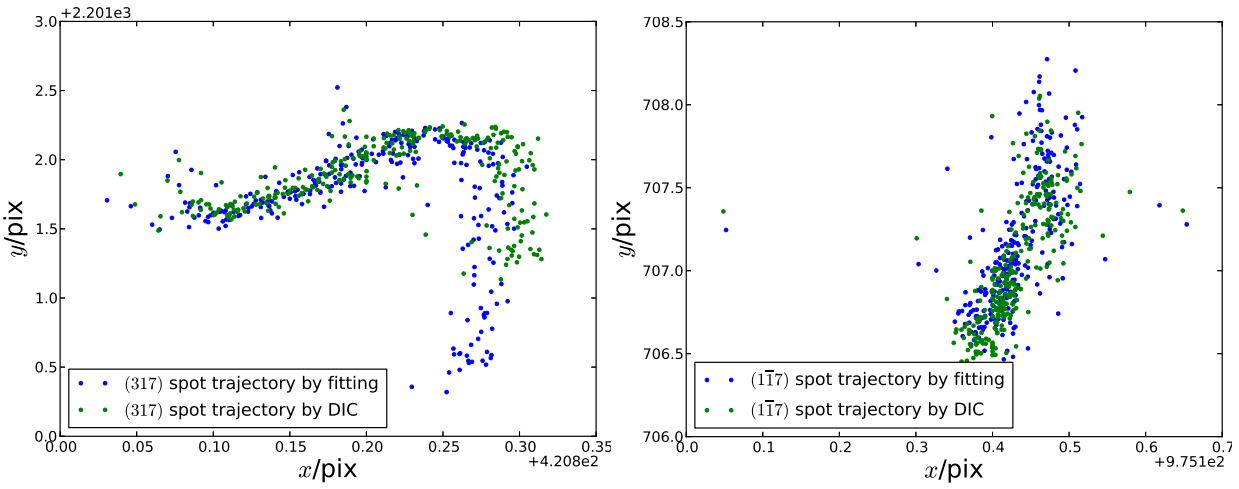

(a) (317) spot (b) (1$\bar{1}$7) spot

Figure 2.6: Comparison between trajectories on the detector screen determined by fitting and DIC

In the bending test mentioned above, the strain profile along the scanning line (see Fig. 4.5) is supposed to vary linearly along x-axis [Rand and Rovenski 2005]. Fig. 2.7a and 2.7b are the results of ε_{yy} profile obtained from the same series of diffraction images, which are taken along the central line of the sample, but are treated differently, i.e. Fig. 2.7a is the result of Laue-DIC, while Fig. 2.7b is the result of standard Laue treatment elaborated in §1.5. It is obvious that the strain profile obtained by Laue-DIC exhibits much less fluctuation than its counterpart obtained by standard Laue treatment.

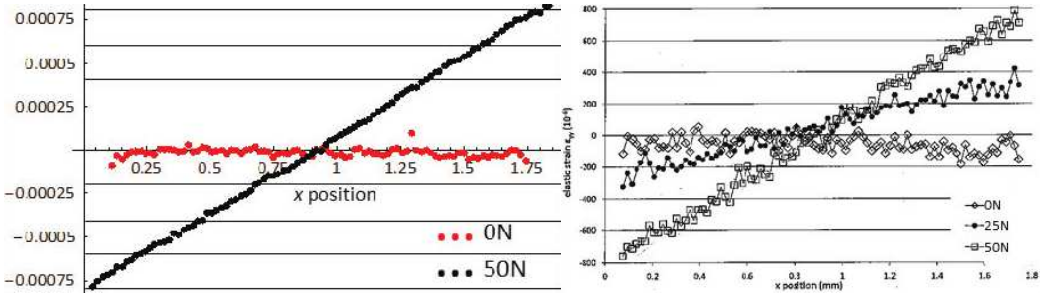

(a) [Petit et al. 2012] (b) [Hofmann 2011]

Figure 2.7: The ε_{yy} profile obtained by (a) Laue-DIC and (b) standard Laue treatment (see §1.5).

2.3 Introduction to Poissonian-Gaussian noise model in synchrotron radiation experiment

Laue-DIC, drawing on the relative displacements of Laue spots instead of the absolute positions of Laue spots, turns out to be a promising method to obtain local elastic strain. However, the precision of Laue-DIC method is limited by several factors: the noise of diffraction image, uncertainties of calibration parameters, etc. It is well-known that image noise, usually characterized by Poissonian-Gaussian model [Faraji and MacLean 2006; Boulanger et al. 2010; Foi et al. 2008], would give rise to random error [Wang et al. 2009] in DIC. In this section, we will first introduce Gauss-Poisson model to describe the noise property. Then, we will apply this model to diffraction images from Si, Ge, and Cu, and 316 stainless steel. In the end, we will analyze the accuracy of DIC measurements of spot displacement with artificial images and the impact of noise on the accuracy of elastic strain.

2.3.1 Terminologies characterizing the performance of a detector

Nowadays, electronic area detectors are overwhelmingly used in recording flux spatial distribution in replacement of photographic films. This is because the digital information recorded by electronic area detector is more convenient to process and to transmit than the analogue information recorded by photographic films. Various types of area detectors are emerging recently to cater for more demanding requirements of X-ray flux measurements, such as hybrid pixel array detectors [Ponchut et al. 2007; Henrich et al. 2009; Basolo et al. 2008; Teyssier et al. 2011; Le Bourlot et al. 2012], coupled-charged device (CCD) based area detector [Westbrook and Naday 1997], etc. Several common criteria, independent of the technology and the application, have been widely acknowledged by the scientific community to facilitating comparing and choosing a detector. These criteria will be introduced in the following.

Gain The gain g is usually defined as the output signal s_{o} per unit input signal s_{i},

$$g = \frac{s_{\mathrm{o}}}{s_{\mathrm{i}}}.$$

Relative variance, detective quantum efficiency, and energy range The *relative variance* R is defined as the ratio of variance of signal σ^2 to the square of signal s^2,

$$R = \sigma^2/s^2,$$

and *Detective quantum efficiency* (DQE) is referred to as the ratio of relative variance of input signal to that of output signal,

$$\mathrm{DQE} = \frac{R_\mathrm{i}}{R_\mathrm{o}} = \frac{(s_\mathrm{o}/\sigma_\mathrm{o})^2}{(s_\mathrm{i}/\sigma_\mathrm{i})^2} = \frac{(\sigma_\mathrm{i}/s_\mathrm{i})^2}{(\sigma_\mathrm{o}/s_\mathrm{o})^2}.$$

If the output signal were strictly proportional to input signal, the DQE would be 100%. Failure to detect certain signal and additional noise would decrease the DQE. A detector's DQE is affected by various factors, e.g. incident X-ray photon energy, transmission of the detector window, geometrical design, etc. The dependence of the DQE on the X-ray photon energy defines the *energy range* of a detector. The DQE drops significantly if the X-ray photons' energies are out of the energy range [He 2009b].

Dynamic range, encoding range The dynamic range is defined as the ratio of maximum signal within the linear range to the minimum detectable signal, and is generally expressed in bits (logarithm base 2).

The encoding range is generally referred to as the bits of output digital signal. Larger encoding ranges can be achieved at the expense of readout speed [Ponchut 2006].

Dark signal, dark signal non-uniformity, and read-out noise Dark signal is the non-zero signal at output when the input signal is zero. The cause of dark signal depends on the mechanism of the detector. The dark signal usually increases with integration time [Ponchut 2006], hence the dark signal can generally be quantified from the accumulation of gray levels without X-ray exposure.

The variance of fluctuation exhibited by dark signal, σ_d^2, is indicative of dark signal noise level, and consisted of random read-out noise σ_r^2 and non-random dark signal non-uniformity (DSNU) σ_DSNU^2:

$$\sigma_\mathrm{d}^2 = \sigma_\mathrm{r}^2 + \sigma_\mathrm{DSNU}^2.$$

Fortunately, most area detectors provide online dark-field subtraction, thereby only read-out noise is left in the corrected image with DSNU cancelled out.

2.3.2 Principle of charged-coupled device

The type of detector we used in our experiment is X-ray 11 megapixel VHR (Very High Resolution) CCD camera, especially customised for BM32 ESRF by Photonic Science. This is a coupled-charge device (CCD) based detector, and more than 90 % of the X-ray 2D detectors on ESRF beamlines are of this type [Ponchut 2006]. The hegemony of CCD-based area detector in ESRF is due to their extreme versatility, with spatial resolutions ranging from submicrometric to millimetric, and the high reliability of commercial CCD cameras and systems [Ponchut 2006].

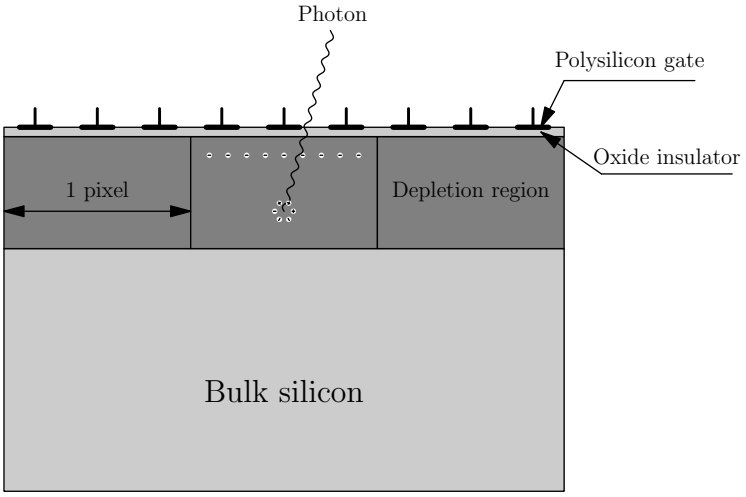

Figure 2.8: The mechanism of photon detection of CCD chip (schematic from [He 2009b])

Figure (2.8) explains the mechanism of photon detection by CCD chip. A photon passes through the polysilicon gate and oxide insulator, and reaches the depletion region of the chip, generating electron-hole pairs, which are then separated by the internal electric field. The electrons are stored in the potential wells at each pixel site, and then their voltages are read out.

However, in the practice of synchrotron radiation imaging, the fluence of synchrotron radiation is so high that CCD chips can hardly adapt to such high counting rate [Arndt, 1978]. Therefore, most of detectors used for X-ray imaging detect the fluorescence stimu-

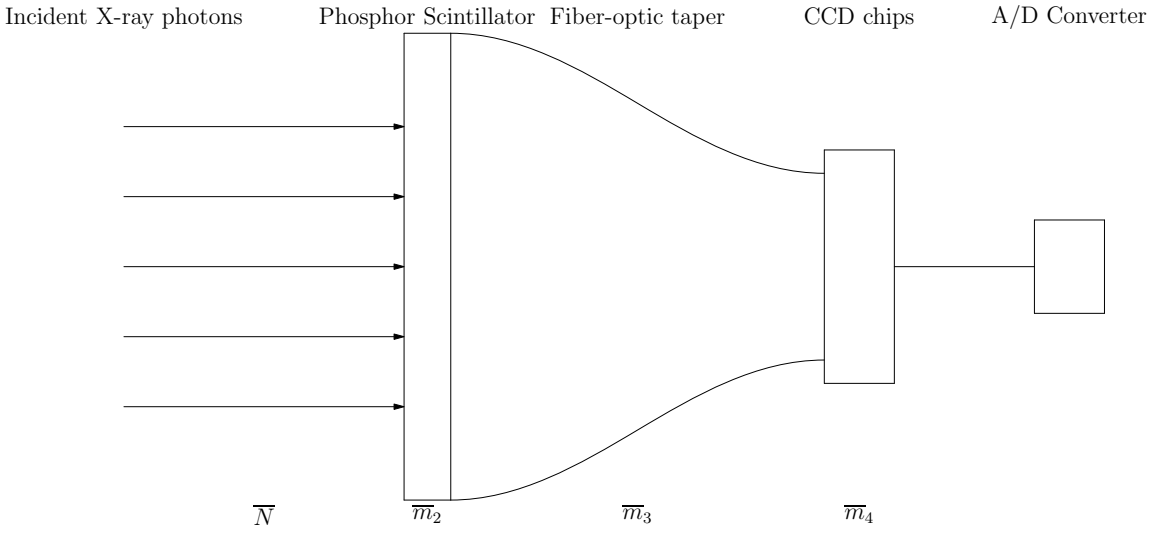

Figure 2.9: The cascading process of a detection event

lated by X-ray photons.

2.3.3 Cascading structure of X-ray photon detector

Fig. 2.9 is a schematic of the cascading structure of detector, indicating that a detection event is naturally described by a chain of signal transmission, with output at one stage feeding into the input of the next. The transmission of signal can be segmented into four stages:

1. The incident X-ray photons arrive at the screen of the detector.
2. The incident X-ray photons interact with the phosphor scintillator of the screen, and the scintillator will emit visible photons.
3. The visible photons travel through the fiber optic taper (FOT), which bridges the phosphor scintillator of the screen and the CCD chip.
4. The visible photons will trigger electron-hold pairs on the CCD chip.

Of course, each stage has its own source of uncertainty, that is subject to a probability distribution. Tab. 2.1 lists all parameters characterizing the stochastic nature of each stage.

Stage	Statistical distribution	Parameter(s)	Specifications
0	Poisson	$\overline{N}$	Mean number of incident X-ray photons
1	Binomial	$\overline{g}_1$	Fraction of incident X-ray photons that interact with phosphor
2	Normal	$\overline{g}_2$	Mean photon yield per X-ray photon on phosphor
		$\sigma^2_{g_2}$	Variance of photon yield
3	Binomial	$\overline{g}_3$	Fraction of photons traveling through FOT and absorbed by CCD chip
4	Normal	$\overline{g}_4$	Mean yield of electron-hole pairs per photon on CCD chip
		$\sigma^2_{g_4}$	Variance of yield of electron-hole pairs

Table 2.1: Signal transmission of a detection event [Waterman and Evans 2010].

The consequent mean electron-hole pairs deposited on a certain pixel due to the reaction chain is

$$\overline{m} = \overline{N}\overline{g}_1\overline{g}_2\overline{g}_3\overline{g}_4 + m_{\mathrm{d}}. \tag{2.8}$$

where m_{d} is the mean quantity of thermally accumulated electron-hole pairs, which give rise to the dark signal, and the meanings of $\overline{N}$, $\overline{g}_1$, $\overline{g}_2$, $\overline{g}_3$ and $\overline{g}_4$ are explained Tab. 2.1.

2.3.4 Errors involved in the cascading detection

The users of detector wishes that the output image honestly tells the distribution of incident X-ray flux. Unfortunately, every stage of the signal transmission is prone to errors due to its statistical nature, and the final error of the output signal is the accumulated result of all previous errors. Errors are mainly classified into systematic errors, which influence the accuracy of the results, and random error, which influence the precision of the results. It is important to distinguish between the terms *accuracy* and *precision*. The accuracy of a result refers to a measure of how close the result is to the true value. The precision refers to a measure of how well the result has been determined, without reference to its agreement with the true value. The precision is also indicative of the reproducibility of result [Bevington and Robinson 2003].

2.3.4.1 Systematic errors

The effect of systematic errors manifests itself by biasing the result from the true value unilaterally with certain degree of fluctuations. Since the true value is never known, systematic errors cannot be detected by statistical analysis. The systematic errors with CCD-based detectors are mainly:

Gain inhomogeneity The gains of the whole pixels of a detector surface varies one by one. A map of gain variations is usually obtained by either exposing the detection area to a perfectly homogeneous beam, which may be unpractical for a large-area system, or performing a time-consuming detector surface scanning with a perfectly stable or precisely monitored beam. For diffraction systems a gain inhomogeneity of $\pm 1\%$ with respect to the average value is deemed acceptable [Ponchut 2006].

Geometric distortion of FOT The FOT serves to transport the photons released from the phosphor scintillator to the much smaller CCD chip. The ideal FOT should be a zooming optical device, evenly scaling down the image on the phosphor side. However, due to the errors in manufacturing and assembling FOT, the demagnification ratio is not uniform, thereby distortions occur on the CCD side, so-called "grid distortion".

The correction of distortion usually requires a mask with regular spaced nodes in front of the detector as a reference. Several algorithm are proposed to correct this distortion based on the distortion of the mask image [Paciorek et al. 1999].

Dark signal In CCD detector, the dark signal, mentioned in §2.3.1, is due to thermally produced electron-hole pairs, which accumulate in the potential well with time. The dark current now becomes the dominant error source for long exposures, and can be decreased by cooling the detector [He 2009b].

As mentioned before, systematic errors are difficult to detect by statistical method.

2.3.4.2 Random errors

The reproducibility of a result depends on the random errors. The fluctuation of the result is usually quantified by the variance or relative variance. In an image acquisition event, incident photons need to pass through 5 stages to reach at the A/D converter finally (see Tab. 2.1), and the relative variances of each stage, labeled as $R_i, i = 0, 1, 2, 3, 4$ are given according to their own statistical properties:

$$\begin{aligned} R_0 &= \frac{1}{\overline{N}}, \quad R_1 = \frac{1}{\overline{g}_1} - 1, \quad R_2 = \frac{\sigma_{g_2}^2}{\overline{g}_2^2}, \\ R_3 &= \frac{1}{\overline{g}_3} - 1, \quad R_4 = \frac{\sigma_{g_4}^2}{\overline{g}_4^2}. \end{aligned} \tag{2.9}$$

According to [Arndt and Gilmore 1979; Stanton et al. 1992; Waterman and Evans 2010], the relative variance of the induced electron-hole pairs can be evaluated by the following empirical formula:

$$\begin{aligned} R &= R_0 + \frac{R_1}{\overline{N}} + \frac{R_2}{\overline{N}\overline{g}_1} + \frac{R_3}{\overline{N}\overline{g}_1\overline{g}_2} + \frac{R_4}{\overline{N}\overline{g}_1\overline{g}_2\overline{g}_3} \\ &= \frac{1}{\overline{N}\overline{g}_1}\left(1 + \frac{\sigma_{g_2}^2}{\overline{g}_2^2} + \frac{1}{\overline{g}_2\overline{g}_3} - \frac{1}{\overline{g}_2} + \frac{\sigma_{g_4}^2}{\overline{g}_2\overline{g}_3\overline{g}_4^2}\right). \end{aligned} \tag{2.10}$$

The relative variance of the number of electron-hole pairs on the CCD chips is converted into the actual variance of this quantity, σ_{m}^2, by multiplying the squared output signal for the combined cascade stages, $(\overline{N}\overline{g}_1\overline{g}_2\overline{g}_3\overline{g}_4)^2$, and adding the dark current variance,

$$\sigma_m^2 = \overline{N}\overline{g}_1(\overline{g}_2\overline{g}_3\overline{g}_4)^2\left(1 + \frac{\sigma_{g_2}^2}{\overline{g}_2^2} + \frac{1}{\overline{g}_2\overline{g}_3} - \frac{1}{\overline{g}_2} + \frac{\sigma_{g_4}^2}{\overline{g}_2\overline{g}_3\overline{g}_4^2}\right) + \sigma_{m\mathrm{d}}^2. \tag{2.11}$$

The voltage triggered by the electron-hole pairs, $\overline{m}$, is converted into digital signal by multiplying by a coefficient, say, analogue-digital gain g_{AD}, and digitalizing the result,

$$\overline{p} = g_{\mathrm{AD}}\overline{m}, \tag{2.12a}$$

$$p = \overline{p} + d, \tag{2.12b}$$

where d is the error introduced by digitalization, p is the digitalized gray level, and $\overline{p}$ is the gray level before digitalization. Strictly speaking, the distribution of d should depend on the distribution of the number of electron-hole pairs. Nevertheless, it is customary to

assume it to be independent and obey uniform distribution with a range of 1 analogue-to-digital unit (ADU) [Widrow et al. 1996]. In that case, the variance of error of digitalization is 1/12.

The resulted variance of p, σ_p^2, by combining equation (2.11) and (2.12), should be

$$\begin{aligned}\sigma_p^2 &= g_{\mathrm{AD}}^2\sigma_m^2 + \frac{1}{12} \\ &= \overline{N}\overline{g}_1(\overline{g}_2\overline{g}_3\overline{g}_4 g_{\mathrm{AD}})^2\left(1 + \frac{\sigma_{g_2}^2}{\overline{g}_2^2} + \frac{1}{\overline{g}_2\overline{g}_3} - \frac{1}{\overline{g}_2} + \frac{\sigma_{g_4}^2}{\overline{g}_2\overline{g}_3\overline{g}_4^2}\right) + g_{\mathrm{AD}}^2\sigma_{m\mathrm{d}}^2 + \frac{1}{12}.\end{aligned} \tag{2.13}$$

The gain of the detector for each absorbed X-ray photon is given by $G = \overline{g}_2\overline{g}_3\overline{g}_4 g_{\mathrm{AD}}$ [Leslie 1999; Waterman and Evans 2010]. Using this definition of G given, the above expressions 2.12a, 2.12b, and 2.13 can be given as

$$\begin{aligned}\overline{p} &= \overline{N}\overline{g}_1 G + g_{\mathrm{AD}} m_{\mathrm{d}}, \\ \sigma_p^2 &= \overline{N}\overline{g}_1 G^2\left(1 + \frac{\sigma_{g_2}^2}{\overline{g}_2^2} + \frac{1}{\overline{g}_2\overline{g}_3} - \frac{1}{\overline{g}_2} + \frac{\sigma_{g_4}^2}{\overline{g}_2\overline{g}_3\overline{g}_4^2}\right) + g_{\mathrm{AD}}^2\sigma_{m\mathrm{d}}^2 + \frac{1}{12}.\end{aligned} \tag{2.14}$$

Generally, these parameters can hardly be measured individually, we prefer to fold the terms into a *cascade factor* γ and *pixel factor* ψ [Waterman and Evans 2010]. With equation 2.8, and denoting dark signal in unit of ADU as $p_{\mathrm{d}} = g_{\mathrm{AD}} m_{\mathrm{d}}$, we have

$$\sigma_p^2 = (\overline{p} - p_{\mathrm{d}})\gamma + \psi, \tag{2.15}$$

with

$$\gamma = G\left(1 + \frac{\sigma_{g_2}^2}{\overline{g}_2^2} + \frac{1}{\overline{g}_2\overline{g}_3} - \frac{1}{\overline{g}_2} + \frac{\sigma_{g_4}^2}{\overline{g}_2\overline{g}_3\overline{g}_4^2}\right), \tag{2.16a}$$

$$\psi = g_{\mathrm{AD}}^2\sigma_{m\mathrm{d}}^2 + \frac{1}{12}. \tag{2.16b}$$

2.4 Experimental study of the noise of diffraction images

2.4.1 Validation of Poissonian-Gaussian model and estimation of its parameters

In this section, we will test the validity of Poissonian-Gaussian model on the experimental data, and identify the parameters of the model, γ, ψ, and p_{d}. For doing this, we collect stacks of 100 Laue microdiffraction images from several specimens. During the

acquisition of each image stack, we should endeavor to maintain the experimental setup to ensure that the only factor leading to the variation of gray levels in the same stack is image noise. With each pixel of one stack, we calculate the average and standard deviation of its gray level to validate the presented noise model and estimate its parameters.

Although diffraction images, acquired from experiments, contains huge amount of pixels (in our case, there are $2\,594 \times 2\,774$ pixels), fortunately only a small portion of pixels where the diffracted X-rays intersect with the area detector are of our interests. Therefore, the primary step of data treatment is to extract the rectangular windows containing individual Laue spots from the background which contains nothing but noise. Since the sizes, the shapes of Laue spots vary according to the spots' energies, angular projection, defects of materials, etc, we need to adaptively select the windows' sizes, aspect ratio to best fit the spots. The algorithm we adopted in this work is shown in Fig. 2.10, and three realizations of this algorithm is shown in Fig. 2.11.

We first look at an image stack collected from a Si monocrystal sample. To analyze the relation between the gray levels and their variances, we plot pairs of the averages and standard variance of gray level for each pixel, $(\overline{p}, \sigma_p^2)$, of a subimage of a spot (Fig. 2.12).

Visual impression of the average-variance distributions indicates a linear relationship between the average and variance of gray level as revealed by Eqn. 2.15. To test the linearity of the distribution, we used the linear regression method, in which the linearity was quantified by linear correlation coefficient (LCC) r defined as:

$$r = \frac{n\sum_n x_i y_i - \sum_n x_i \sum_n y_i}{\sqrt{n\sum_n x_i^2 - \left(\sum_n x_i\right)^2}\sqrt{n\sum_n y_i^2 - \left(\sum_n y_i\right)^2}}. \tag{2.17}$$

The value of r is in the range $-1 \leq r \leq +1$. $r = \pm 1$ means that the data pairs are perfectly linearly related. The smaller $|r|$, the weaker the linear relationship between the data pairs.

In Fig. 2.13, we plotted the distribution of LCCs of all spots in the same image stack. Most of the LCCs are distributed within the range of 0.9 and 1.0, indicating a strong linear relationship between $\overline{p}$ and σ_p^2, thereby further confirming the soundness of equation 2.15.

Applying linear regression to every spot would give us a series of lines, whose slope is

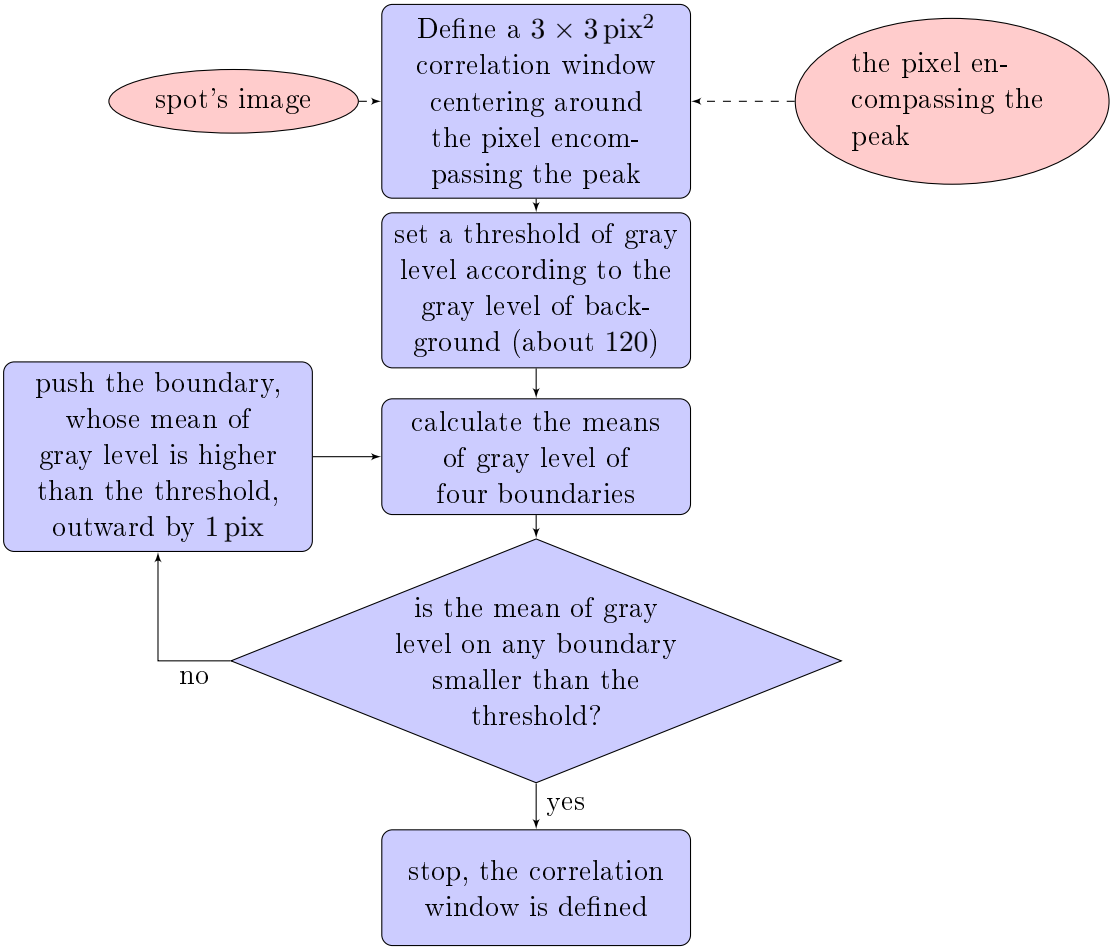

Figure 2.10: Algorithm for determining the optimum window containing a Laue spot

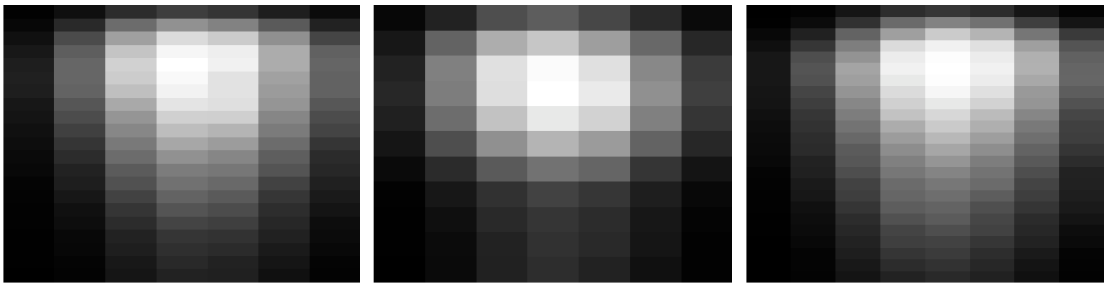

(a) (b) (c)

Figure 2.11: Three realizations of the algorithm in Fig. 2.10

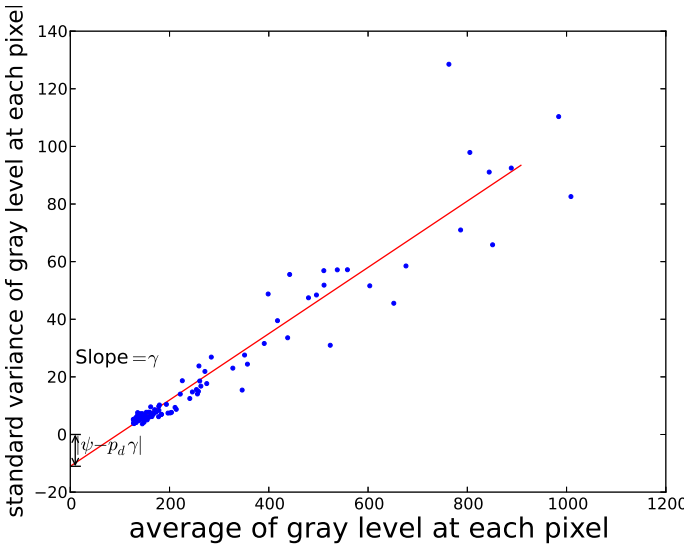

Figure 2.12: $\overline{p}$ vs. σ_p^2 of gray levels. Treat these spots with linear regression, we get a line with slope being the estimation of the cascade factor γ, and the interception with y axis being the estimation of $\psi - p_{\mathrm{d}}\gamma$

the estimation of γ, and whose interception on the y axis is the estimation of $\psi - p_{\mathrm{d}}\gamma$. Plotting all pairs of estimated $(\gamma, \psi - p_{\mathrm{d}}\gamma)$ for all Laue spots would enable us to estimate ψ and p_{d} by linear regression (Fig. 2.14).

From the results of linear regression, we find the linear correlation coefficient to be -0.94, indicating a high linear correlation. The rest parameter are found to be

$$p_{\mathrm{d}} = 118.7 \quad \text{and} \quad \psi = 4.3.$$

Note that the estimated p_{d} is slightly higher than the average gray level of background of the image (about 101.1), however we are not clear about this phenomenon. After all,

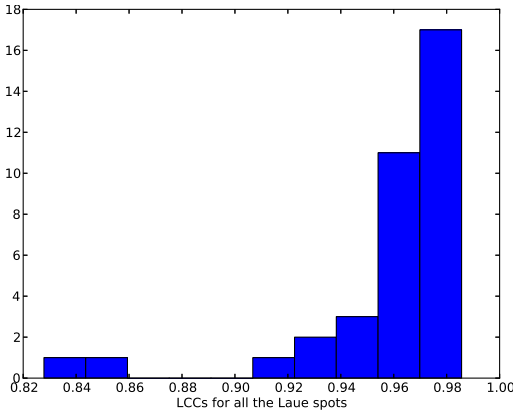

Figure 2.13: The distribution of LCCs for the spots of one Si diffraction image

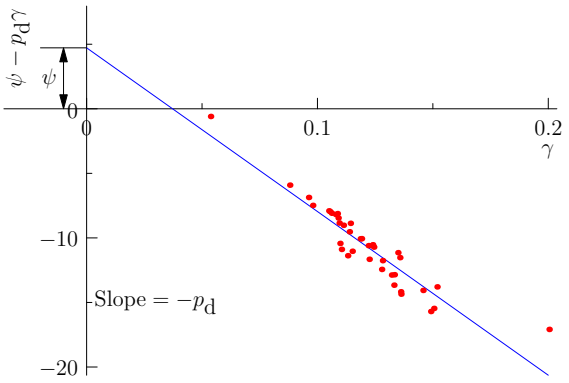

Figure 2.14: Plot of pairs $(\gamma, \psi - p_d\gamma)$ of each Laue spot. Obviously, the pairs are highly linearly correlated with LCCs $r = -0.94$.

the transmission of signal from incident photons to digital images is too complex to be fully described by Poissonian-Gaussian model. Fortunately, the precision of DIC is not affected by p_d as long as the correlation coefficient is zero-mean normalized cross-correlation (ZNCC) coefficient [Tong 2005].

We applied the same procedure to image stacks collected from other Si samples, Ge samples, Cu samples, and 316 steel samples, and we found that for most image stacks the averages of LCCs were above 0.9, showing a strong linear correlation between the variance and the average of gray levels. However, there were two exceptions: one came from Ge sample, and another came from 316 steel sample. We will talk about the two exceptions in §2.4.3.

Note that, in Fig. 2.14, we plotted all the $(\gamma, \psi - p_d\gamma)$ pairs collected in a single

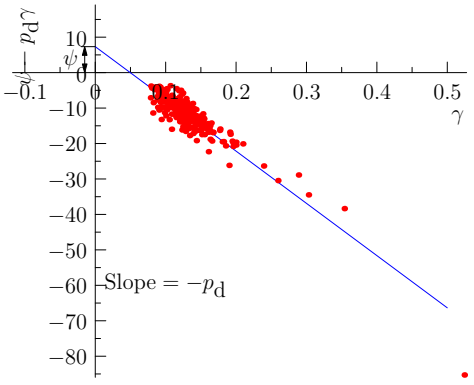

Figure 2.15: Plot of pairs $(\gamma, \psi - p_d\gamma)$ of each Laue spot. Obviously, the LCC of these pairs is -0.92.

diffraction image to estimate the background noise, each pair corresponding to a Laue spot. Of course, more pairs would give a better estimation of background noise parameters, i.e. p_d and ψ. On the other hand, the detector, as an apparatus to detect photons, should be ignorant of the diffracted material. Therefore, we will plot all the $(\gamma, \psi - p_d\gamma)$ pairs of different materials in a single XY-plot to estimate the background parameters. These pairs were collected from all the diffraction images that we had taken (each pair corresponds to a spot, and a total of 316 spots investigated), among which the spots with a LCC lower than an empirical threshold, 0.9, were excluded. The LCC for these pairs are -0.92, $p_d = 147.3$ and $\psi = 7.3$ in our estimation. The estimated p_d is much larger than the background of image, but this parameter is a trivial one since it would not influence neither the precision of pinpointing peak by analytical fitting nor the precision of displacement measurement by DIC. Moreover, the estimation of p_d is meaningless because in reality p_d is not uniformly distributed on the area detector due to the influence of diffuse X-ray.

2.4.2 The dependence of cascade factor γ on photons' energy

The performance of detector should be independent of the material under scrutiny. Likewise, the cascade factor γ should be function of incident photon's energy rather than the lattice parameters of the crystal diffracting. In order to reveal the relation between the cascade factor and incident photons' energy, we plotted all the (γ, E) pairs for all spots under consideration in Fig. 2.16, where E is the energy of the energy of incident spot. E

can be calculated from Eqn. 1.15:

$$E_{hkl} = \frac{\mathbb{h}c}{2d_{hkl}\sin\theta},$$

where the subscript $_{hkl}$ represent the index of lattice plane from which the spot is diffracted, and d_{hkl} is the d-spacing of the lattice plane, c is the light speed, and $\mathbb{h}$ is the Planck's constant (we used a different font of h so as not to be confused with the index of lattice plane hkl). From Eqn. 1.10, for cubic lattice, d_{hkl} is given as:

$$d_{hkl} = \frac{1}{\|r^*_{hkl}\|} = \frac{1}{\frac{1}{a}\sqrt{h^2+k^2+l^2}} = \frac{a}{\sqrt{h^2+k^2+l^2}},$$

where a is the side length of the cubic lattice. Therefore, for cubic lattice, the energy of photon diffracted by (hkl) lattice plane is:

$$E = \frac{\mathbb{h}c\sqrt{h^2+k^2+l^2}}{2a\sin\theta}.$$

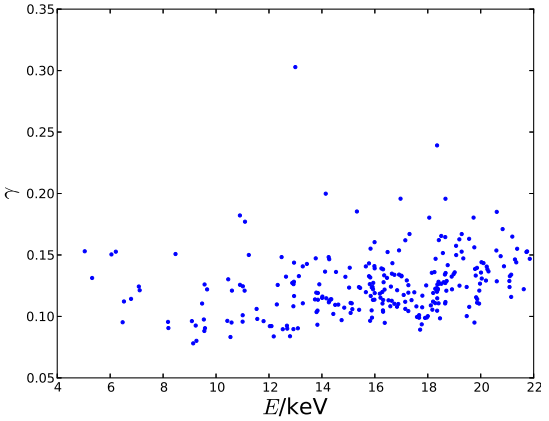

Figure 2.16: γ vs. E

From Fig. 2.16, we do not see any clear relation between spot energy E and cascade factor γ, and therefore we could only estimate the range of cascade factor from this figure. We will implicitly assume $\gamma = 0.125$ if there is no further specification hereinafter.

2.4.3 Issues with the Same Dataset

Poissonian-Gaussian noise model applies for most image stack collected in our experiment. However, in §2.4.1 we mentioned that there were two exceptions: one came from a 316 steel sample, and another came from a Ge sample.

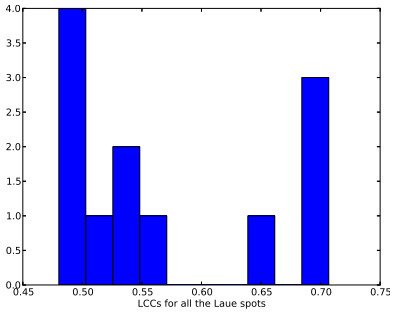

Figure 2.17: The distribution of LCCs of spots of the exception from a 316 steel sample.

We first talked about the exception from the 316 steel sample. We plotted its LCCs in Fig. 2.17, and we observed that most LCCs were below 0.7, indicating a poor linear relationship between $\overline{p}$ and σ_p^2. To further investigate the origin of this failure of the linearity implicated in Eqn. 2.15, we plotted the three different images of one spot in Fig. 2.18, we observed an intense fluctuation of spot intensity distribution. The causes of this fluctuation is not known yet. One possible explanation is the occurrence of instabilities during the experiment, e.g. like external vibration, thermal expansion of the equipment, instability of beam, etc.

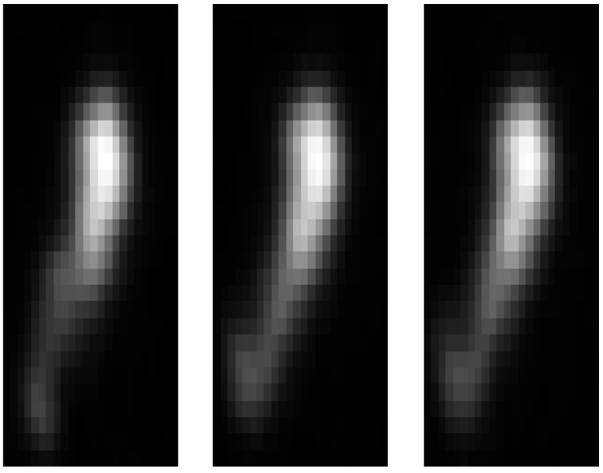

Figure 2.18: The fluctuation of one spot in a stack of diffraction images of 316 steel sample.

We then talked about the exception from the Ge sample. For this Ge sample, we had collected image stacks at three different sample-detector distance to investigate the influence of spot's resolution upon the image noise, and we plotted their histograms of

LCCs in Fig. 2.19.

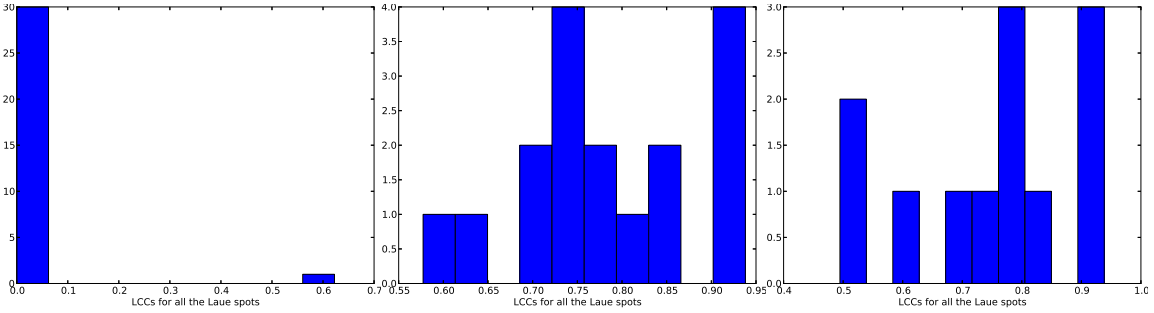

(a) LLCs at the distance of 59.824 mm (b) LLCs at the distance of 101.763 mm (c) LLCs at the distance of 143.892 mm

Figure 2.19: The distribution of LCCs of spots of the exception from a Ge sample.

The LCCs of the exception from Ge sample were larger than those of exception from 316 steel sample. We also plotted three different images of one spot in Fig. 2.20, but we did not observed any strong fluctuation of spot intensity distribution.

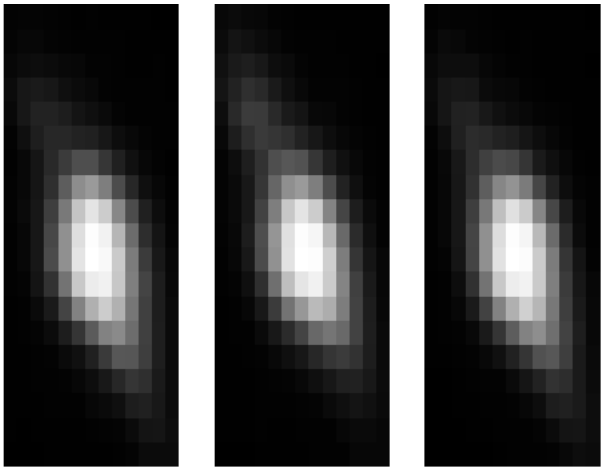

Figure 2.20: The fluctuation of one spot in a stack of diffraction images of a Ge sample.

When we plot the pairs of the averages and standard variance of gray level of each pixel of the spot in Fig. 2.21, we found that the trend of spot distribution tended to split at some point. The split of distribution may indicate a heterogeneous distribution of cascade factor γ among the region of spot. The reason for this heterogeneous distribution is not known yet.

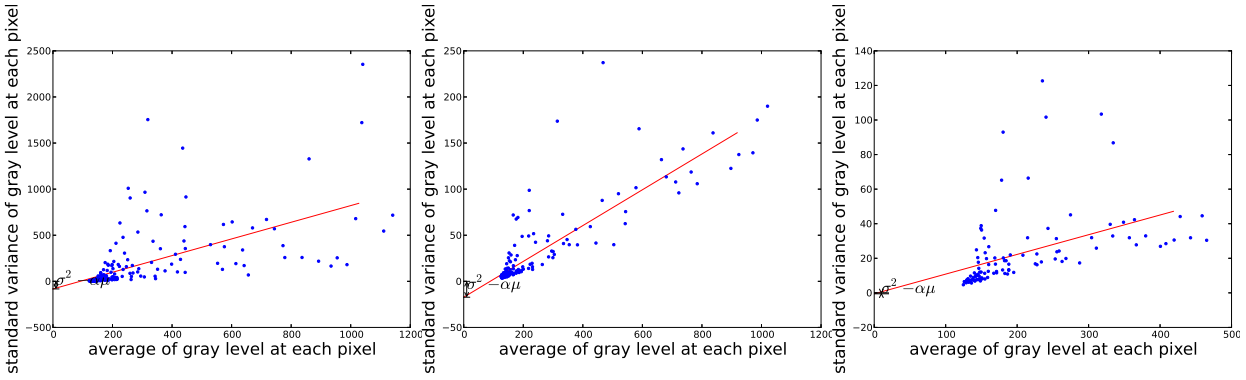

(a) (b) (c)

Figure 2.21: The pairs of the averages and standard variance of gray level of each pixel for three spots from Ge sample I

2.5 Numerical Tests of Laue-DIC

The uncertainties on DIC will be ultimately transmitted to the calculation of relative deformation gradient $\underset{\sim}{F}$. Alongside the uncertainties from DIC are the uncertainties of calibration parameters (see §1.5.2). It is difficult to derive an analytical formula to generalize the influence of each parameters onto the final accuracy of $\underset{\sim}{F}$, therefore here we used numerical tests to achieve this. Similar work has been done by [Hofmann et al. 2011; Poshadel et al. 2012].

2.5.1 The Accuracy of Displacement by DIC

The principle of Laue-DIC is acquiring the precise relative displacement of Laue spots on the area detector thanks to DIC technique. Therefore, the accuracy of displacement measurement by DIC is crucial to obtain highly reliable results. Although it is relatively straightforward to compare the mechanical imposed displacements with those measured by DIC, as presented in §2.1, it is difficult to experimentally prescribe well-controlled displacement field whose precision must be of at least one order of magnitude better than the one of DIC, as the imposed displacements field also depends on motor's precision, alignment of detector, stability of experimental setup, etc.

One possible approach to impose a displacement field between two images of Laue spots

can be taking a real image from real experiment and to numerically transform it by a know displacement field. The transformation is accomplished either in the frequency domain by applying Fourier transformation according to the shift theorem, or in the space domain by interpolating at subpixel positions. Although this approach can retain all characteristics of images taken under experimental circumstances, the numerical transformation itself would introduce some error to the transformed images [Amiot et al. 2013], depending on the specific algorithm under usage.

In this section, we attempt to estimate the error of DIC and the influence of image noise by fabricating and operating on artificial images by a multi-resolution approach [Doumalin and Bornert 2000] in order to evade both the uncertainties of experimental equipment and the errors introduced by numerical transformation of images.

2.5.1.1 Fabrication of noiseless artificial spots

It is customary to characterize the intensity distribution of a Laue spot by an analytical function, e.g. 2D Gaussian, Lorentzian, or Pearson function. It was said that a 2D Lorentzian function typically gives the best fit of peak position [Valek 2003], but in treating the image sequences of Chapter 4, it was found that the residual error resulted from Gaussian fitting was smaller than that resulted from Lorentzian fitting. Therefore spots were described by a Gaussian function in my study.

The analytical function of 2D Gaussian distribution is given as:

$$\begin{aligned} I(x,y) &= A\exp\left\{-\left[C_1(x-x_0)^2 + C_2(x-x_0)(y-y_0) + C_3(y-y_0)^2\right]\right\} + p_\mathrm{d}, \\ C_1 &= \frac{1}{2}\left(\frac{\cos^2\theta}{r_X^2} + \frac{\sin^2\theta}{r_Y^2}\right), \\ C_2 &= \sin\theta\cos\theta\left(-\frac{1}{r_X^2} + \frac{1}{r_Y^2}\right), \\ C_3 &= \frac{1}{2}\left(\frac{\sin^2\theta}{r_X^2} + \frac{\cos^2\theta}{r_Y^2}\right) \end{aligned} \tag{2.18}$$

where A represents the amplitude of the spot, x_0 and y_0 represent the center of the spot, r_X and r_Y are the width of spot along two main axis at the $1/\sqrt{e}$ of the maximum height, θ represent the rotation angle of main axis of Gaussian function with respect to the pixel grid, and p_d is the dark signal as mentioned in §2.3. Note that as the value of p_d does not influence the result of DIC when ZNCC (see Eqn. 2.1) is used [Tong 2005], therefore it

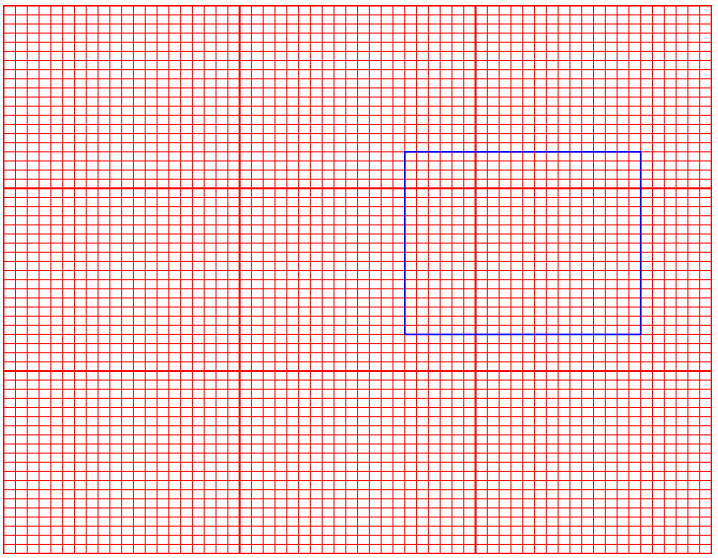

Figure 2.22: The red rectangulars represent the original pixels subdivided into $N \times N$ subpixels, and the blue pixel represents the pixel after being moved by a subpixel displacement. In my study, $N = 100$.

can be set arbitrarily. Here we set it to be 100.

The essence of the multi-resolution approach consist in the following steps:

1. Subdivide each pixel into $N \times N$ subpixels. N represents the resolution of subpixel step. The larger N is, the finer the resolution is.

2. Calculate the gray level for each subpixel by performing the integration of Eqn. 2.18 within each subpixel.

3. To obtain the gray level of each pixel after a displacement of $(\frac{n_x}{N}, \frac{n_y}{N})$ (n_x and n_y are integers), we only have to move the pixel in two dimensions by n_x and n_y substeps (see Fig. 2.22, the blue rectangular represent the pixel after displacements). Then, we bin together subpixels within the moved pixel, and have its gray level.

In this manner, the only source of error in constructing the displaced image is digitalization. Here, we choose N to be 100, then the resolution of subpixel displacement is 0.01. Fig. 2.23a and 2.23b depict the spots before and after a subpixel displacement of 0.5 pix along both x and y direction.

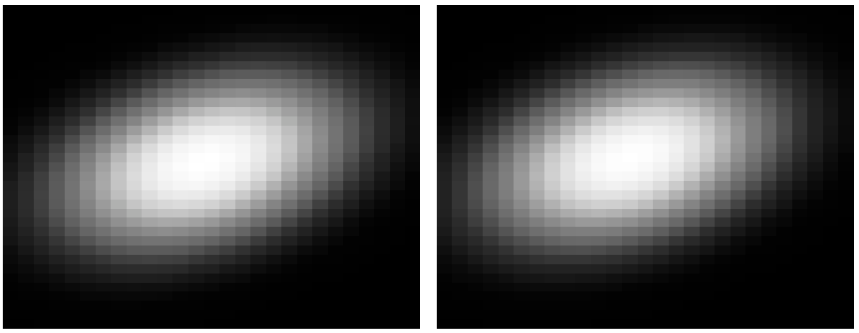

(a) Initial spot (b) After moved by 0.5 pixel in each dimension

Figure 2.23: Spots before and after displacement

2.5.1.2 Precision of displacement measurements of noiseless spot

We used in-house DIC software CMV [Doumalin and Bornert 2000] to study the precision of displacement acquisition with noiseless spot. By "noiseless", we meant that the spot and background were not polluted by random fluctuation, and the only source of error was digitalization. CMV uses ZNCC (see Eqn. 2.1) as its correlation coefficient so that it is robust against the uniform offset and scale changes in the gray level of image. We tested the performance of the lowest and the highest orders of interpolations in CMV, i.e. bilinear interpolation and biquintic interpolation respectively. The parameters characterizing the spot used for this study are tabulated in Tab 2.2 which come from analytical fitting a real spot. The meaning of these parameters are given in Eqn. 2.18.

A	r_X	r_Y	θ
572.65	2.54	1.75	173.18°

Table 2.2: Parameters characterizing a spot

Because spots are just rigidly displaced in two images, therefore there would be no errors in mismatch of shape functions if we use zero order shape function, the only error of DIC we will encounter is the "ultimate error" of DIC [Bornert et al. 2009; Amiot et al. 2013]. Note that because the spot that we fabricated was central symmetrical, a subpixel translation along x or y axis with the distance u is equivalent to a translation opposite to

x or y axis with distance u, which is itself equivalent to a translation along x or y axis with distance $1-u$. Therefore, the error curves without noise should be central symmetrical with respect to the point $(0.5, 0.5)$.

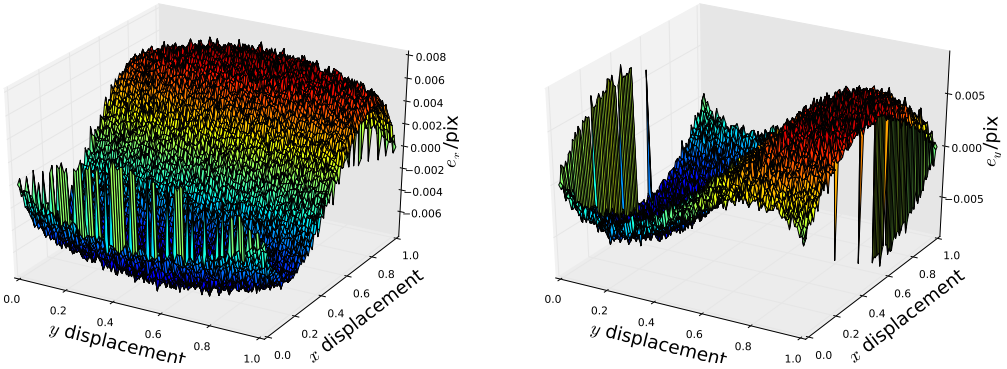

(a) x displacement error (b) y displacement error

Figure 2.24: Error distribution with bilinear interpolation as the function of x and y displacement

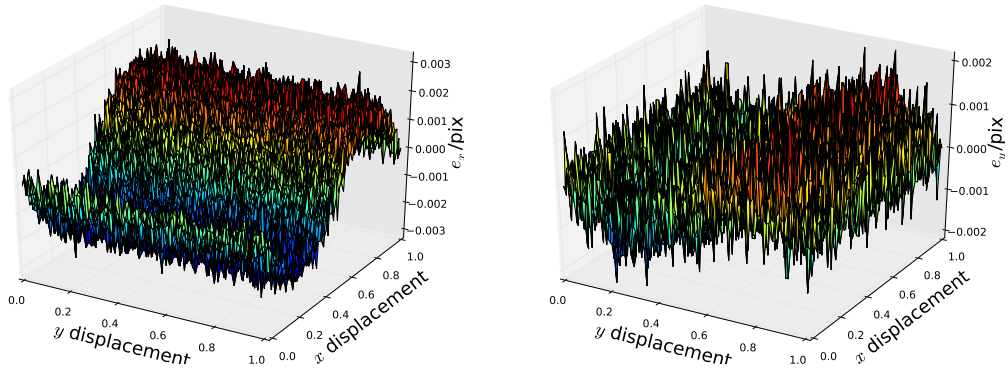

(a) x displacement error (b) y displacement error

Figure 2.25: Error distribution with biquintic interpolation as the function of x and y displacement

To obtain the dependence of displacements' error upon the imposed displacements, we first translated the spot's image by a certain amount (fraction of a pixel size), then we performed DIC between the initial and the translated spots' images, with which we could have the measured displacements and compare them with the imposed ones. Fig. 2.24 and 2.25 are the distribution of errors in x and y directions with bilinear and biquintic

interpolation respectively. In these figures, the (x, y) coordinate represents the imposed displacements, and the z coordinate represent the error in x or y directions, which is defined as the measured x or y displacement minus the imposed x or y displacements respectively:

$$e_x = x_{\text{dic}} - x_{\text{imposed}}, \quad e_y = y_{\text{dic}} - y_{\text{imposed}}.$$

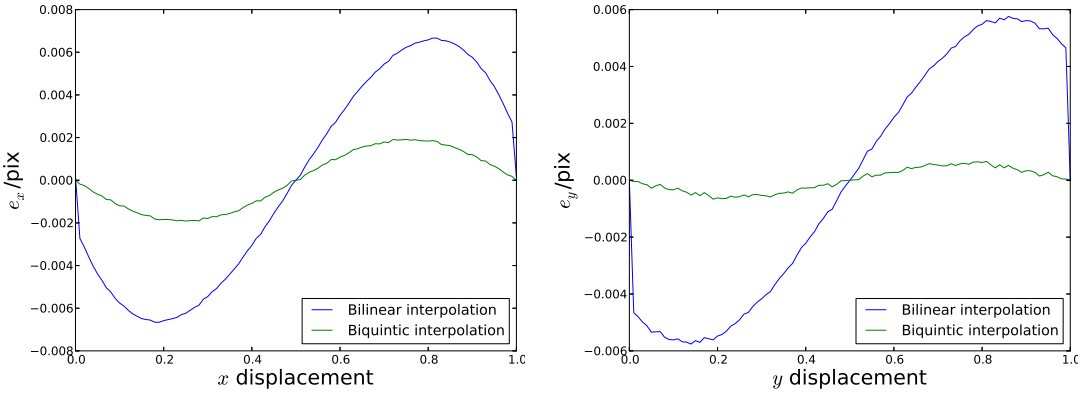

(a) Average x displacement error

(b) Average y displacement error

Figure 2.26: Average x (or y) displacement error over different y (or x) displacements

It was shown that:

- The coupled dependence of errors on x and y subpixel displacement turned out to be weak, i.e. the e_x (or e_y) displacement depends mainly on x(or y) displacement and poorly on y (or x) displacement. Therefore, we can turn Fig. 2.24 and Fig. 2.25, which are 3D plots, into 2D plots by plotting the average of e_x (or e_y) with the same x (or y) displacement but different y (or x) displacement in Fig. 2.26.
- Either from the 3D plots Fig. 2.24 and Fig. 2.25 or from the 2D plot Fig. 2.26, we found that the amplitude of error curve of biquintic interpolation was smaller than that of bilinear interpolation. This means that biquintic interpolation gives better results that bilinear interpolation.
- In Fig. 2.26, the error curves are all S-shaped, with their minimum located at 0 pix, 0.5 pix, and 1 pix.
- The amplitude of error curve for y displacement was smaller than that for x displacement in both biquintic case and bilinear case. This was because the spot was

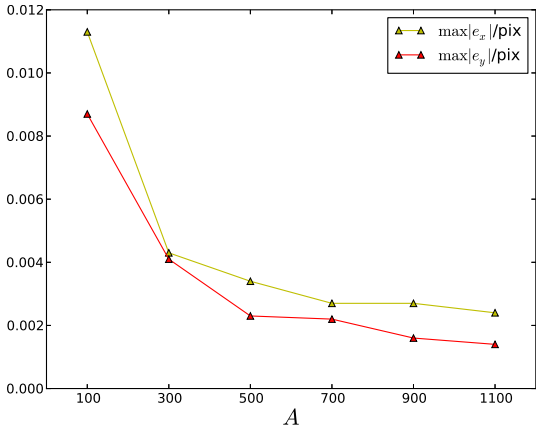

Figure 2.27: $\max|e_x|$ and $\max|e_y|$ for spots with different amplitudes A.

more streaked in x direction, therefore the gray level was more evenly distributed in x direction, resulting less contrast in x direction. There is a simple formula to demonstrate in 1D DIC and with linear interpolation of gray level how the contrasts of gray level influence affect the error of DIC [Sutton et al. 2009b]:

$$e = -\frac{\sum(\overline{g}_i - f_i)\nabla f_i}{\sum(\nabla f_i)^2},$$

where f_i represents the gray level of the ith pixel on the current image, ∇f_i represents its gradient of gray level, and $\overline{g}_i$ represents the interpolated gray level of of the ith pixel on the translated reference image. It is obvious from this equation that the error of 1D DIC decreases with the gradient of gray level. For the case of 2D DIC with images polluted by Gaussian noise, the formulas are much more complex [Wang et al. 2009].

- The minimum error level occurs at around 0, 0.5, and 1 displacements, while the maximum error level occurs at around 0.25 and 0.75 displacements.

To investigate the influence of amplitude A on the accuracy of DIC, we fabricated spots with six different amplitudes: 100, 300, 500, 700, 900, and 1100. The accuracy of DIC was characterized by the maximum absolute value of errors, $\max|e_x|$ and $\max|e_y|$. The results of $\max|e_x|$ and $\max|e_y|$ with different A are given in Fig. 2.27.

It was shown that the error level will decrease as the spot's amplitude increase both for x displacement and y displacement. This is because that increasing the spot's amplitude

will increase the gradient of gray level in Eqn. 2.18, and hence the contrast of gray levels with respect to neighboring pixels after digitalization. Another factor is that the error introduced by digitalization of gray level will become less significant compared to the increased contrasts of gray level.

2.5.1.3 Fabrication of noisy artificial spots

The real experimental spots are more or less fluctuated due to the image noise introduced in §2.3.4. We formulated a normal distribution to describe the fluctuation of gray level, and confirmed the distribution with several samples in §2.4. We fabricated the noisy spot in the following procedure:

1. Calculate the noise-free, non-digitalized gray level $\overline{p}$ with the procedure stated in §2.5.1.2.

2. Add noise to the gray level by generating a normally distributed random number $\overline{p}'$ with its mean being $\overline{p}$, and variance being $\gamma(\overline{p} - p_{\mathrm{d}}) + \psi$, where γ is cascade factor and ψ is pixel factor.

3. Digitalize the random number $\overline{p}'$ to get the final gray level p.

2.5.1.4 Precision of displacement measurements of noisy spot

To study the fluctuation of DIC errors due to the fluctuation of gray levels, we generated 100 random Laue spots for each displacement. We only studied the error distributions with biquintic interpolation because the study in §2.5.1.2 had demonstrated that biquintic interpolation gave the best results in terms of maximum error. The pixel factor ψ we chose to fabricate these noisy pixels was 7.3 according to §2.4.1, and the cascade factor γ was set to be 0.125. The rest of spot parameters were listed in Tab. 2.2

Fig. 2.28 and 2.29 depict the averages and standard deviations of errors at all the displacements, representing the systematic errors and random errors respectively. Again, we see that the coupled dependence of systematic errors on x and y subpixel displacement turns out to be weak. The amplitude of systematic error curve for y displacement, 0.008,

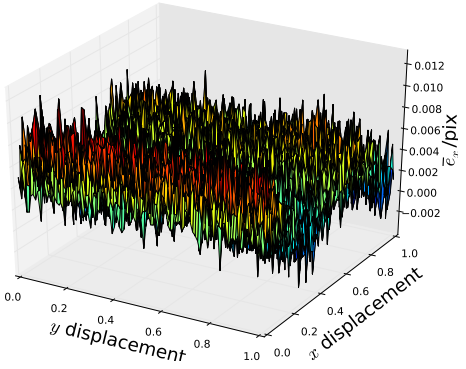

(a) Average x displacement errors with biquintic interpolation

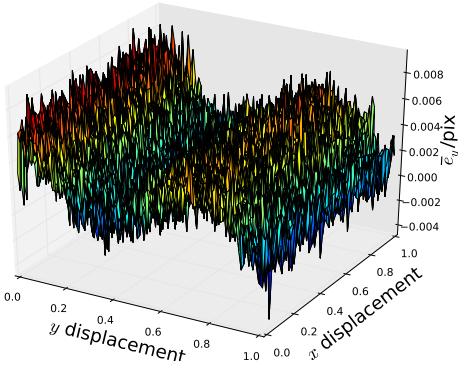

(b) Average y displacement errors with biquintic interpolation

Figure 2.28: Average displacement errors with biquintic interpolation

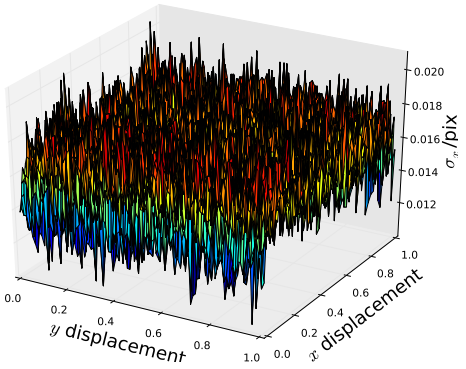

(a) Standard deviation of x displacement errors with biquintic interpolation

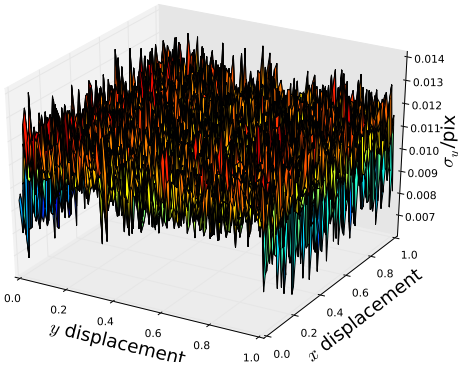

(b) Standard deviation of y displacement errors with biquintic interpolation

Figure 2.29: Standard deviation of displacement errors with biquintic interpolation

is smaller than that for x displacement, 0.012. But compared to the case of noiseless spots (see §2.5.1.2), the levels of errors increased significantly due to the introduction of noise.

In terms of random errors, the coupling between x and y subpixel still turned out to be weak. The amplitude of random error curve for y displacement, 0.014, is smaller than that for x displacement, 0.02 as there is more contrast in y direction rendering measurements on y direction more robust against noise. Similar to the curve of systematic errors, the minimum error level occurs at around 0, 0.5, and 1 displacements, while the maximum error level occurs at around 0.25 and 0.75 displacements. Compared to Fig. 2.24 and 2.25, the errors increase significantly with the introduction of image noise, therefore, image noise

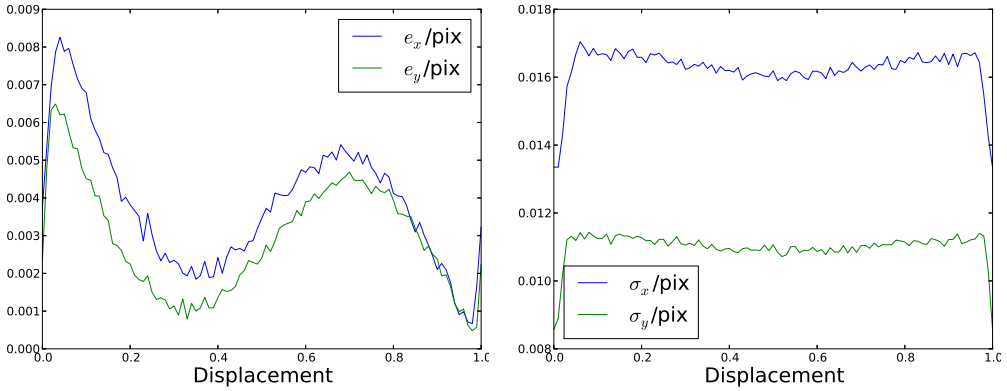

(a) Average systematic errors in x and y dimensions.

(b) Average random errors in x and y dimensions.

Figure 2.30: Average errors in x and y dimensions.

is one limiting factor of DIC.

Because the coupling between the errors in x and y dimension is very weak, it is possible to turn Fig. 2.28 and 2.29 into 2D plots, i.e. Fig. 2.30, as we have plotted Fig. 2.26 to facilitate . In Fig. 2.30a, it is found that the error curves appear much noisy than those of Fig. 2.26, and they deviate from S-shape curve, the reason for such deviation is not known yet. In Fig. 2.30b, it is found that the random errors are smaller near integer pixel displacement, and they quickly reach a plateau as the imposed displacement deviate from integer pixel.

To study the collective influence of cascade factor γ and spots' peak A, we studies the systematic errors and random errors of spots with different combinations of γ and A. The range of A was 100, 300, 500, 700, 900, and 1100, while the range of γ, according to Fig. 2.15, was set to 0.075, 0.1, 0.125, 0.15, 0.175, 0.2. The level of errors were quantified by the maximum values with various displacements. The results of systematic errors and random errors were given in Fig. 2.31 and 2.32 respectively.

From Fig. 2.31 and 2.32 we could draw several conclusions:

1. The systematic error is mainly governed by the amplitudes of spots, i.e. spots with larger amplitudes give lower systematic error. The systematic error slightly increases with the cascade factor γ.

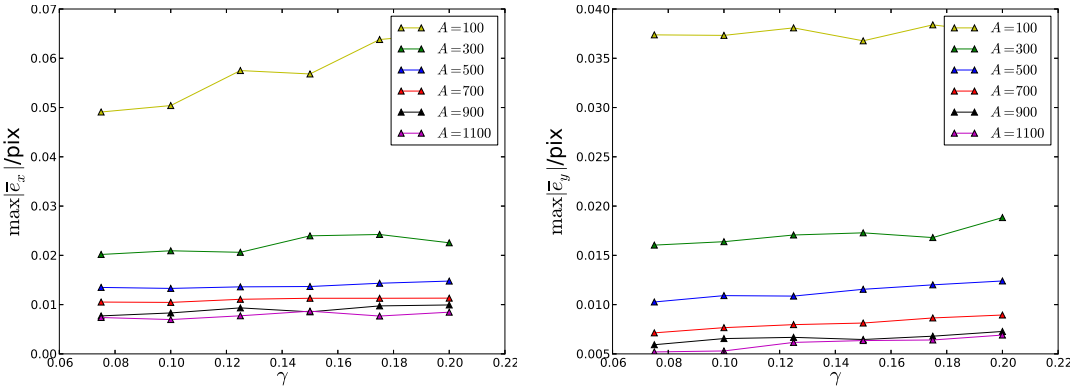

(a) Maximum systematic errors in x direction (b) Maximum systematic errors in y direction

Figure 2.31: Maximum systematic errors with with biquintic interpolation

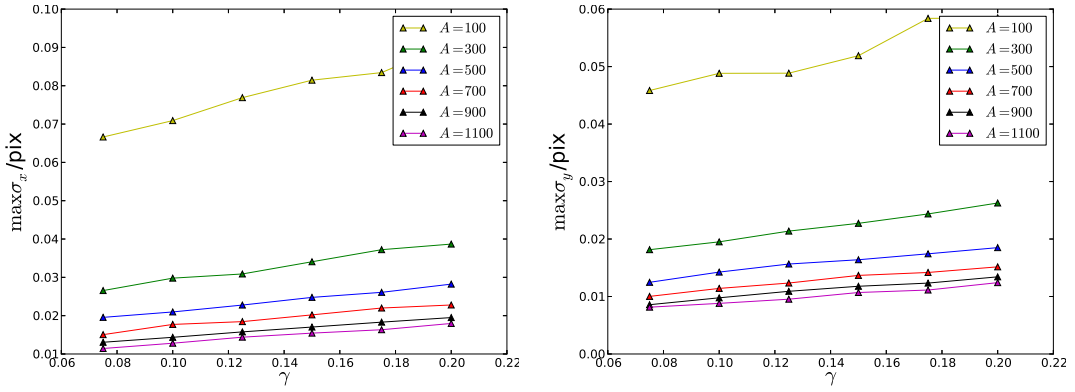

(a) Maximum random errors in x direction (b) Maximum random errors in y direction

Figure 2.32: Maximum random errors with with biquintic interpolation

2. For random error, the error level is governed by both the amplitude of spot and cascade factor. Random error will increase with decreasing the amplitude of spot or increasing the cascade factor γ.

3. Both systematic error and random error in y direction are lower than their counterparts in x direction. There is due to the fact that there is more gray level gradient in y direction.

4. The level of random error is larger than that of systematic error. This may be related to the value of cascade factor — lower cascade factor will render random error smaller than systematic error. For intense peak, errors are of the order of 0.01 pix, and it

can increase up to ~ 0.05 pix for peaks with small amplitudes. Such accuracy is well adapted for our application.

2.5.2 Laue-DIC's Uncertainties

From §2.5.1, we gained a quantitative idea about the errors of DIC. Now we proceed to investigate the collective influence of uncertainties by DIC and by calibration parameters. It is difficult to quantify the errors on the deformation gradient $\underset{\sim}{F}$ because it has nine components and is influenced by volumeric changes which is beyond the capability of Laue diffraction. Therefore we use the following steps to define the errors on $\underset{\sim}{F}$:

1. rescale each component of $\underset{\sim}{F}$ by the cube root of the determinant of $\underset{\sim}{F}$ in order to get rid of the uncertainty on the volume of crystal lattice, i.e.

$$\hat{\underset{\sim}{F}} \doteq \frac{\underset{\sim}{F}}{\sqrt[3]{\det \underset{\sim}{F}}},$$

2. the error on $\underset{\sim}{F}$ is defined as

$$\epsilon_F \doteq \frac{\sum_{i=1}^{3}\sum_{j=1}^{3}|\hat{F}_{ij}^{\text{cal}} - \hat{F}_{ij}^{\text{exa}}|}{9},$$

where the superscript $^{\text{cal}}$ represents the calculated value, and the superscript $^{\text{exa}}$ represents the exact value.

In case of statistical tests where multi random cases are treated, we define the systematic error $\bar{\epsilon}_F$ and random error σ_{ϵ_F} of $\underset{\sim}{F}$ as:

$$\begin{aligned} \bar{\epsilon}_F &\doteq \frac{\sum_{i=1}^{3}\sum_{j=1}^{3}|\overline{\hat{F}}_{ij}^{\text{cal}} - \hat{F}_{ij}^{\text{exa}}|}{9}, \\ \sigma_{\epsilon_F} &\doteq \frac{\sum_{i=1}^{3}\sum_{j=1}^{3}\sigma_{\hat{F}_{ij}^{\text{cal}}}}{9}, \end{aligned}$$

where the overline on the right hand of equations means the average, and the σ on the right hand of equations means the standard deviation.

The procedure of numerical tests goes as following (see Fig. 2.33, where the superscript $^{\text{dis}}$ means the values disturbed by noise):

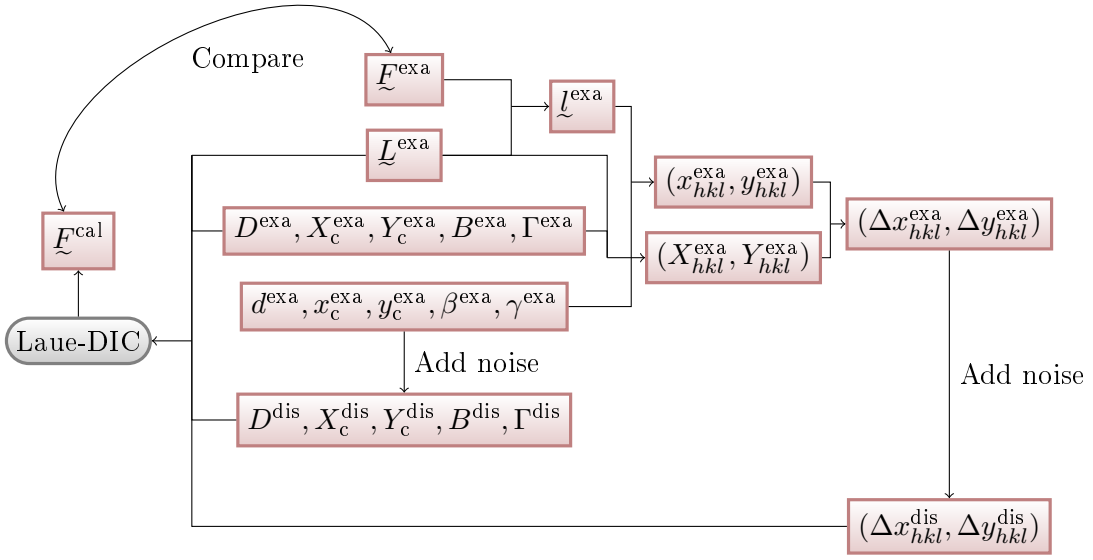

Figure 2.33: Flowchart of numerical tests

1. Give the lattice matrices and calibration parameters of both reference and current configurations.

2. Deviate the calibration parameters of current configuration a little bit from their values according to normal distribution with given deviations,

3. Simulate the spots' displacements, and add noise to the spots' displacements to represent to DIC errors.

4. Use the spots' displacements to calculate the relative deformation gradient, and compare it to the exact value.

In our numerical test, we use the real data from one of our experiment as the exact values to make our tests more realistic. The exact values for geometrical parameters are listed in Tab. 2.3, and the exact values for $\underset{\sim}{L}^{*}$ is

$$[\underset{\sim}{L}^{*}] = \begin{bmatrix} 1 & -7.74 \times 10^{-3} & 1.66 \times 10^{-2} \\ 8.03 \times 10^{-3} & -0.654 & -0.758 \\ 1.61 \times 10^{-2} & 0.758 & -0.653 \end{bmatrix} \tag{2.19}$$

We considered three cases, in which the relative deformation gradients are given by $\underset{\sim}{F}^{*}$,

d/mm	x_c/pix	y_c/pix	β	γ
59.799	1365.75	943.97	0.344°	0.517°

Table 2.3: Exact values of calibration parameters in Fig. 2.33

σ_d/mm	σ_{x_c}/pix	σ_{y_c}/pix	σ_β	σ_γ
0.004	0.16	0.26	0.005°	0.005°

Table 2.4: Uncertainties of calibration parameters [Poshadel et al. 2012] (pixel size: 31 μm)

$(\underset{\sim}{F}^*)^2$, and $(\underset{\sim}{F}^*)^3$ respectively, and the exact value for $\underset{\sim}{F}^*$ is

$$[\underset{\sim}{F}^*] = \begin{bmatrix} 1 & 3.33 \times 10^{-4} & -3.55 \times 10^{-4} \\ 9.15 \times 10^{-6} & 1 & -4.49 \times 10^{-4} \\ -3.36 \times 10^{-4} & 2.42 \times 10^{-4} & 1 \end{bmatrix} \tag{2.20}$$

The three cases, namely case I, II, and III, represent increasing deformations in a row. For each cases, we tested three subcases, in which the numbers of Laue spots captured by the area detector were 40, 25, and 10, respectively.

We will perform the numerical tests in two aspects:

Variation of uncertainties with the level of DIC errors From §2.5.1, we know that the maximum error is usually of the order of 0.1 pix, the average of error would be of the order of 0.05 pix. In this section, we will add zero-mean Gaussian errors to the spots' displacements to investigate the influence of noise upon the precision of strain and geometrical parameters. We will impose all the input displacements of spots in the same Laue image with zero-mean Gaussian errors whose deviations are 0.005 pix, 0.01 pix, 0.015 pix, 0.02 pix, 0.025 pix, 0.03 pix, 0.035 pix, 0.04 pix, 0.045 pix, 0.05 pix.

In terms of the level of calibration parameter, they are tabulated in Tab. 2.4. The reason for why there is more uncertainty in y_c than in x_c is that the penetration depth in y-axis contributes to the uncertainty (remember that the incident beam is always parallel to the y-axis according to the definition of absolute coordinate system). For each deviation level, we generated 500 random cases and then calculate the average errors of lattice matrices.

Variation of uncertainties with the level of calibration errors We vary the level of calibration error by uniformly scaling the deviations of calibration parameters tabulated in Tab. 2.4 by a scaling factor, say, α. The scaling factor α we set are 0, 0.25, 0.5, 0.75, 1, 1.25, 1.5, 1.75, 2, 2.25, 2.5. For the sake of brevity, we only consider the case where the deviations of spots' displacements are 0.01 pix for both x and y directions of all the spots. The rest settings of tests are the same as in the previous aspect of tests.

The variations of systematic and random errors with imposed zero-mean Gaussian noise are displayed in Fig. 2.34, and those with the level of calibration errors are displayed in Fig. 2.35. We can draw several conclusions:

- Both systematic and random errors of $\underset{\sim}{F}$ decreases with increasing the number of Laue spots. This justifies the strategy of using as many spots as possible to perform Laue-DIC.

- Systematic errors of $\underset{\sim}{F}$ increases abruptly with instilling the zero-mean Gaussian errors either to the spots' displacements or to the calibration parameters. However, the systematic errors become stable with further increasing the deviation of errors.

- The random errors slightly increases with increasing the deviation of errors on the spots' displacements despite fluctuations. By contrast, the increments of random errors with the deviation of errors on the calibration parameters are very obvious, and they depend almost linearly on the scaling factor α.

- The curves of random error seem to be insensitive to the imposed relative deformation gradient, while the systematic error decreases with larger imposed deformation (the imposed deformation gradients of case I, II, and III are $\underset{\sim}{F}$, $\underset{\sim}{F}^2$, and $\underset{\sim}{F}^3$ respectively). This is probably due to the fact that larger amplitude of deformation will engender larger spots' displacements, and hence reduce the relative errors of spots' displacement.

- The systematic and random errors of $\underset{\sim}{F}$ are of the order of $\sim 10^{-4}$, well adapted for our study.

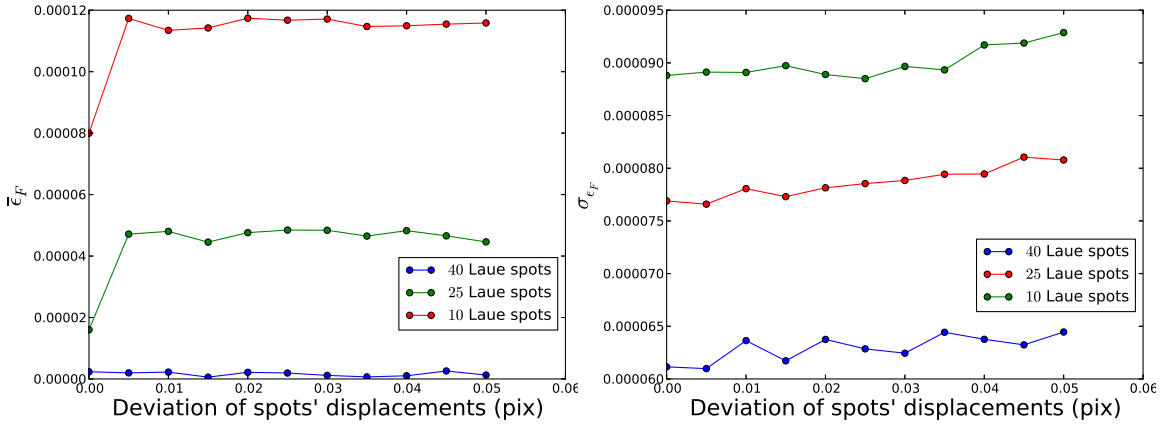

(a) Systematic error in case I

(b) Random error in case I

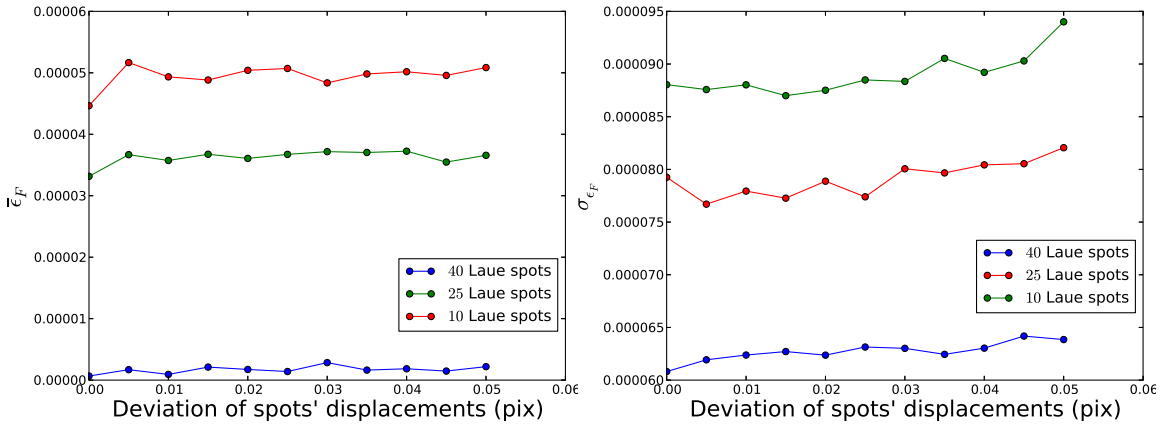

(c) Systematic error in case II

(d) Random error in case II

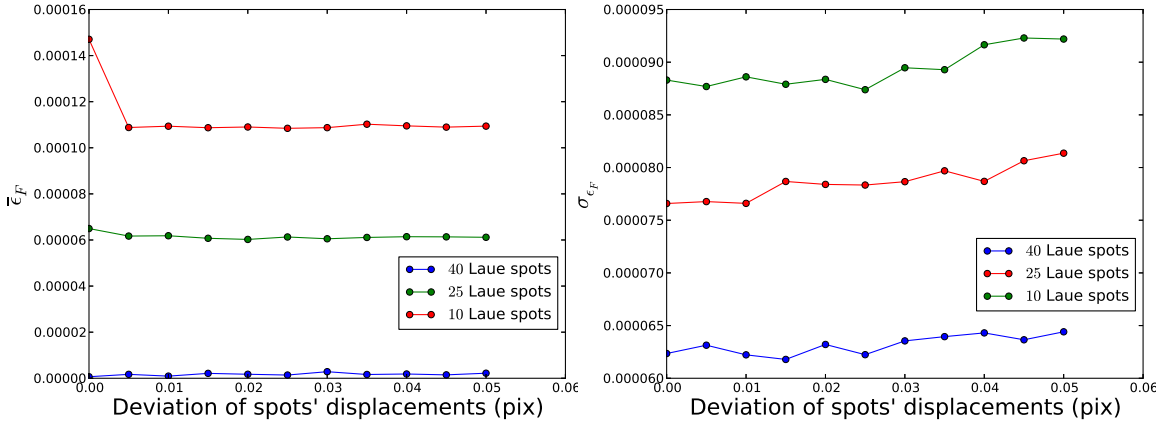

(e) Systematic error in case III

(f) Random error in case III

Figure 2.34: Influence of imposed zero-mean Gaussian error to the measurements

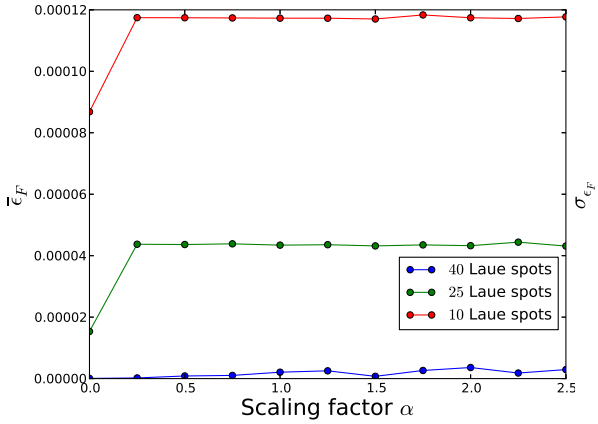

(a) Systematic error in case I

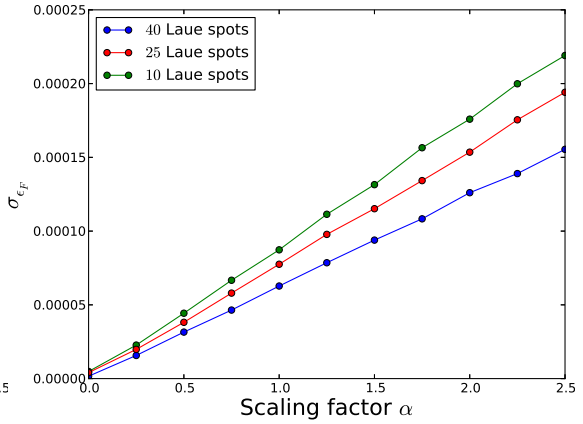

(b) Random error in case I

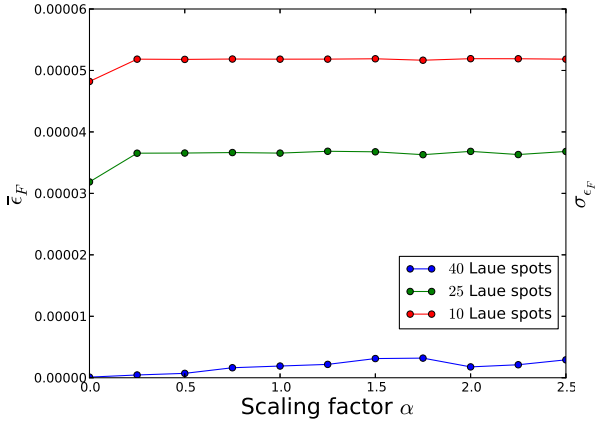

(c) Systematic error in case II

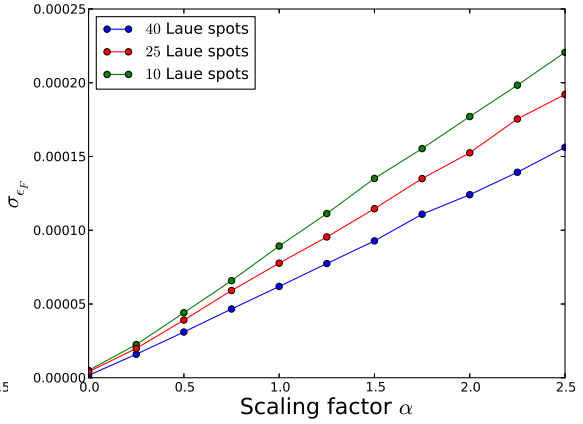

(d) Random error in case II

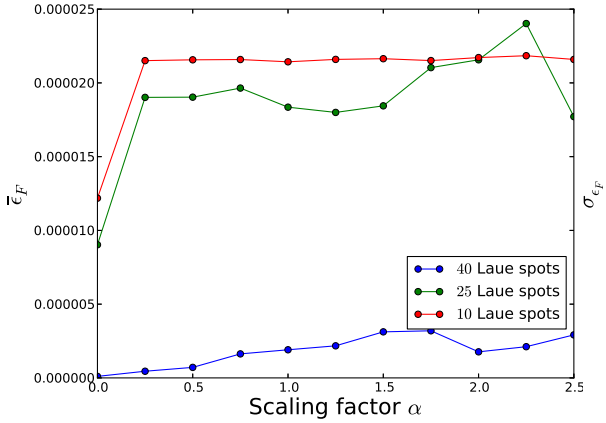

(e) Systematic error in case III

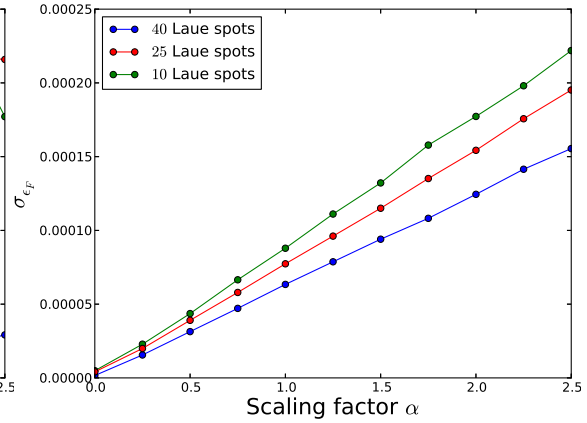

(f) Random error in case III

Figure 2.35: Influence of perturbations of calibration parameters to the measurements

As we have mentioned above, the random errors seem to increase linearly with the scaling factor α, while they seem more stable with the deviations of the displacement errors. This may indicate that at present the dominant factor governing the random errors should be the scaling factor α. This may lead us postulate that the deviations of displacement errors may become the dominant one if they are further increased. To prove this point, we further extend the range of the abscissa of Fig. 2.34b, 2.34d, and 2.34f to 0.16 pix, and plot the variation of error curves with multiple αs in Fig. 2.36. To save space, here we only consider the case with the deformation gradient $\underset{\sim}{F}^2$ and 25 spots considered.

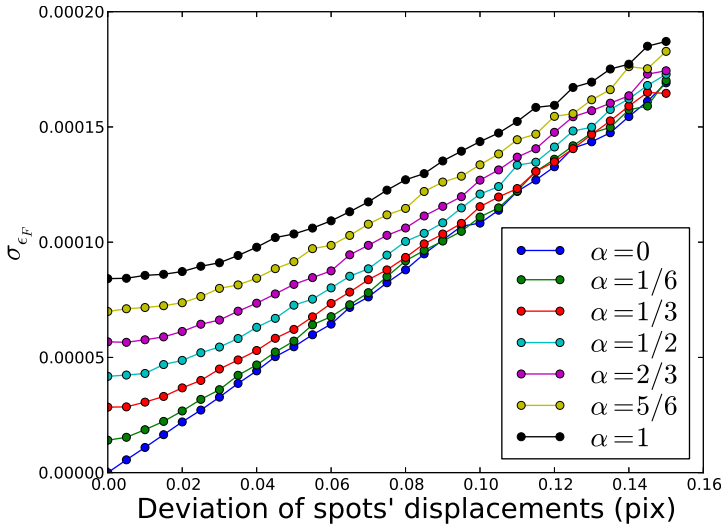

Figure 2.36: Variation of error curves with the scaling factor α

In Fig. 2.36, it is obvious that all curves asymptotically converge to certain curves if we further increase the deviations of displacement errors. When $\alpha = 0$, i.e. the calibration parameters are exactly given, the errors increases almost linear with the deviations of errors. As we increase α, a basin in which the errors increase slightly with the deviation of displacement errors is formed, and the range of the basin increases with α. This implies that the errors of calibration parameters influence the error of deformation gradient as well as the displacement errors.

2.6 Summary

In this chapter, we have introduced the principle of Laue-DIC, and analyzed its uncertainty by numerical tests. The originality of Laue-DIC, compared to standard Laue treatment (see §1.5), is: (i) that Laue-DIC uses peaks' displacements measured by DIC rather than peaks' absolute positions; (ii) that Laue-DIC calculates the relative deformation gradient between two configurations. However, it is worth to mention that Laue-DIC shares the same limitation with HR-EBSD: both need reference configurations which has been known *a priori*. This limitation will be discussed in the next chapter.

The error of Laue-DIC originates from the errors of calibration parameters and the errors of displacements measured by DIC. The errors of calibration parameters depends on the stability of experimental equipment, the precision of motor's movement, and the accuracy of the acquisition of calibration parameters. Errors of DIC can be classified into two categories: systematic error and random error. Systematic error originates from the "ultimate error" of DIC [Bornert et al. 2009; Amiot et al. 2013], and random error originates from the noise of diffraction images, which is usually characterized by a simple but efficient noise model - Poissonian-Gaussian model (see §2.3). We have collected image stacks, each of which contains 100 images, in our experiment to check the validity of Poissonian-Gaussian model and to fit the parameters of this model, and found that most image stacks confirm this model despite several exceptions. We postulate that the incident beams or experimental equipments underwent stabilities when we were collecting these image stacks. In future, it is always a good idea to check regularly the stabilities of beam or equipments before any image acquisition by a similar process of image noise evaluation.

Considering the complexity of errors involved in Laue-DIC, we performed numerical tests to estimate the uncertainties of Laue-DIC in two steps:

1. estimate the uncertainties of displacements by operating upon the artificial spots with imposed displacements. In our case, the simulated error of displacement is of the order of 0.05 pix;

2. estimate the uncertainty of relative deformation gradient by randomly perturbing

the spots' displacements and calibration parameters. To this end, we impose zero-mean Gaussian error to simulated spots' displacements and pre-known calibration parameters to investigate their influence upon relative deformation gradient, and the simulated error of relative deformation gradient is of the order of 10^{-5} when 25 Laue spot are considered.

Chapter 3

Enhanced Laue-DIC and its Precision

3.1 Motivation

In §2.2.2, we have presented the principle of Laue-DIC and have demonstrated that Laue-DIC method is capable of improving the accuracy of elastic strain measurement, because it draws on a more reliable source of information — the displacements of spots rather than the absolute positions of spots. Although this is a good start point towards improving the evaluation of orientation and elastic strain from Laue microdiffraction, it suffers from several drawbacks:

- The evaluation of elastic strain needs a reference configuration whose lattice matrix is known. This ignorance of lattice matrix of reference configuration would add up to the uncertainty of the evaluation of elastic strain, or limit the application of Laue-DIC to circumstances where the elastic strain and orientation of reference configuration is straightforward, e.g. the neutral fiber in bending test, in which the normal stress in the direction of longitude is supposed to be zero.

- Aside from lattice rotation and distortion, any perturbation of calibration parameters from reference configuration to current configuration may contribute to the spot displacements, which may be confused with the displacements caused by lattice distortion/rotation.

- Even the acquisition of relative deformation gradient requires the lattice matrix and calibration parameters to be known accurately, as shown in Eqn. 2.4, where the

calculation of $\underline{n}_i^{\text{ref}}$ needs the lattice matrix and calibration parameters of reference configuration.

This chapter is dedicated to provide an enhanced version of Laue-DIC to solve the problems mentioned above. We will present the formulation of enhanced Laue-DIC in the first place, and then we will run numerical tests in order to: (i) investigate the proper optimization algorithm, (ii) the performance of enhanced Laue-DIC.

3.2 Enhanced Laue-DIC

We will refer to the Laue-DIC mentioned in the previous chapter as original Laue-DIC hereinafter in order to distinguish it from the enhanced version which will be presented in this chapter. Like its original version, enhanced Laue-DIC still needs two diffraction images and to treat them by DIC. The novelty of enhanced Laue-DIC compared with the original one rests in treating both the lattice matrices of reference configuration and calibration parameters as unknowns. For brevity, we use lowercase letter to represent parameters in current configuration, and uppercase letter to represent parameters in reference configuration. Tab. 3.1 tabulates the symbols for the parameters. The spots' displacements in

Configuration	Current	Reference
Reciprocal lattice matrix	$\underline{\underline{l}}$	$\underline{\underline{L}}$
Sample-detector distance	d	D
The nearest point on the area detector to the illumination	$(x_{\text{c}}, y_{\text{c}})$	$(X_{\text{c}}, Y_{\text{c}})$
Pitch angle of detector	β	B
Yaw angle of detector	γ	Γ
Detector orientation matrix (Eqn. 1.19)	$\underline{\underline{g}}$	$\underline{\underline{G}}$
Scaled diffraction vector (Eqn. 1.28)	$\underline{\xi}$	$\underline{\Xi}$

Table 3.1: Symbols for parameters

different configuration are mainly due to: (i) the lattice distortion and (ii) perturbation of experimental setup. In real practice, the two causes happen simultaneously, therefore a sound evaluation of lattice distortion must take perturbation of experimental setup into consideration. For a spots with a given index hkl, its displacement is a function of recip-

rocal lattice parameters and calibration parameters:

$$\begin{cases} x(\underset{\sim}{l}^*, d, x_c, \beta, \gamma, hkl) - x(\underset{\sim}{L}^*, D, X_c, B, \Gamma, hkl) &= \Delta x^{hkl} \\ y(\underset{\sim}{l}^*, d, y_c, \beta, \gamma, hkl) - y(\underset{\sim}{L}^*, D, Y_c, B, \Gamma, hkl) &= \Delta y^{hkl} \end{cases} \tag{3.1}$$

Substitute Eqn. 1.29 into Eqn. 3.1, we have:

$$\begin{cases} d\dfrac{\xi_i^{hkl} g_{1i}}{\xi_i^{hkl} g_{3i}} + x_c - D\dfrac{\Xi_i^{hkl} G_{1i}}{\Xi_i^{hkl} G_{3i}} - X_c &= \Delta x^{hkl} \\ d\dfrac{\xi_i^{hkl} g_{2i}}{\xi_i^{hkl} g_{3i}} + y_c - D\dfrac{\Xi_i^{hkl} G_{2i}}{\Xi_i^{hkl} G_{3i}} - Y_c &= \Delta y^{hkl} \end{cases}$$

Denote $\Delta x_c = x_c - X_c$ and $\Delta y_c = y_c - Y_c$, we have

$$\begin{cases} d\dfrac{\xi_i^{hkl} g_{1i}}{\xi_i^{hkl} g_{3i}} - D\dfrac{\Xi_i^{hkl} G_{1i}}{\Xi_i^{hkl} G_{3i}} + \Delta x_c &= \Delta x^{hkl} \\ d\dfrac{\xi_i^{hkl} g_{2i}}{\xi_i^{hkl} g_{3i}} - D\dfrac{\Xi_i^{hkl} G_{2i}}{\Xi_i^{hkl} G_{3i}} + \Delta y_c &= \Delta y^{hkl} \end{cases} \tag{3.2}$$

Notice that Laue diffraction will not resolve isotropic dilation of lattice without additional information, e.g. spot's energy [Robach et al. 2011], we can therefore resolve only eight degrees of freedom of lattice from Laue diffraction. Without loss of generality, we exclude the component of reciprocal lattice matrix, whose index is $_{11}$, from our optimization, in other words, we keep it fixed throughout the optimization. Therefore if we are provided a series of spots' displacements by DIC, there are totally 24 unknowns to be solved from Eqn. 3.2: 8 parameters for $\underset{\sim}{l}^*$, 8 parameters for $\underset{\sim}{L}^*$, and calibration parameters d, D, Δx_c, Δy_c, β, γ, B, Γ. We denote the parameters to be optimized by $\mathcal{P}$. Note that it is impossible to determine x_c, y_c, X_c, or Y_c from Eqn. 3.2, because the left hand side of Eqn. 3.2 is irrelevant to the any of them, only Δx_c and Δy_c can be determined.

If the lattice parameters and calibration parameters are given, we can uniquely determine any spot's displacement with equation 3.2. Now the question is, given twelve spots' displacements, can we determine the sixteen lattice matrix components and eight calibration parameters? The answer is, according to implicit function theorem, as long as the Jacobian matrix of Eqn. 3.2 has full rank, we can determine the 24 parameters (denoted as $\mathcal{P}$ hereinafter) from at least 12 spots' displacements, i.e.:

$$\det[\underset{\sim}{J}] = \det\left[\frac{\partial(\Delta x_1, \Delta y_1, \Delta x_2, \Delta y_2, \cdots, \Delta x_{12}, \Delta y_{12})}{\partial \mathcal{P}}\right] \neq 0, \tag{3.3}$$

To illustrate the role of Jacobian matrix $[\mathcal{J}]$, we raise an examples in which different sets of 24 parameters give the same displacements of spots. If the parameters of current configuration are the same with their counterparts in reference configurations except d, then for any spot we have from Eqn. 3.2:

$$\frac{\partial \Delta x}{\partial d} = \frac{\xi_i g_{1i}}{\xi_i g_{3i}} = \frac{\Xi_i G_{1i}}{\Xi_i G_{3i}} = -\frac{\partial \Delta x}{\partial D}, \quad \frac{\partial \Delta y}{\partial d} = \frac{\xi_i g_{2i}}{\xi_i g_{3i}} = \frac{\Xi_i G_{2i}}{\Xi_i G_{3i}} = -\frac{\partial \Delta y}{\partial D}.$$

From the equation above, we see that the column of the Jacobian matrix $[\mathcal{J}]$ corresponding to the partial derivatives with respect to d is opposite to the column corresponding to the partial derivatives with respect to D, hence $\det[\mathcal{J}] = 0$. Therefore, even if we were able to get more than 12 displacements, we could obtain nothing from these data if the Jacobian matrix were not full ranked. In fact, we can arbitrarily increase or decrease d and D by the same amount without changing the resulted displacement field, as long as $d - D$ is kept constant.

In real practice, we can obtain more than 12 spots' displacements, our problem becomes minimizing an objective function:

$$\begin{aligned} \Pi = & \sum_{hkl} W_x^{hkl} \left(d\frac{\xi_i^{hkl} g_{1i}}{\xi_i^{hkl} g_{3i}} - D\frac{\Xi_i^{hkl} G_{1i}}{\Xi_i^{hkl} G_{3i}} + \Delta x_{\mathrm{c}} - \Delta x_{\mathrm{dic}}^{hkl} \right)^2 \\ & + \sum_{hkl} W_y^{hkl} \left(d\frac{\xi_i^{hkl} g_{2i}}{\xi_i^{hkl} g_{3i}} - D\frac{\Xi_i^{hkl} G_{2i}}{\Xi_i^{hkl} G_{3i}} + \Delta y_{\mathrm{c}} - \Delta y_{\mathrm{dic}}^{hkl} \right)^2, \end{aligned} \tag{3.4}$$

where W_x^{hkl} and W_x^{hkl} are the weight for x- and y- displacements of the (hkl) spots respectively (in §4.4, we will give one definition of weights), the subscript $_{\mathrm{dic}}$ represents that the spots' displacements are measured by DIC, and the unit of Π is pix^2.

In order to save CPU time of minimization, we do not optimize β, γ, B, and Γ directly, we rather optimize $\tan\frac{\beta}{2}$, $\tan\frac{\gamma}{2}$, $\tan\frac{B}{2}$, and $\tan\frac{\Gamma}{2}$, in that case, the parameters to be optimized become

$$\mathcal{P} = \{\underset{\sim}{U}^*, \underset{\sim}{L}^*, d, D, \Delta x_{\mathrm{c}}, \Delta y_{\mathrm{c}}, \tan\frac{\beta}{2}, \tan\frac{\gamma}{2}, \tan\frac{B}{2}, \tan\frac{\Gamma}{2}\}. \tag{3.5}$$

The original formulation of cost function, Eqn. 3.4, becomes

$$\begin{aligned} \Pi = & \sum_{hkl} W_x^{hkl} \left(d\frac{\xi_i^{hkl} t_{1i}}{\xi_i^{hkl} t_{3i}} - D\frac{\Xi_i^{hkl} T_{1i}}{\Xi_i^{hkl} T_{3i}} + \Delta x_{\mathrm{c}} - \Delta x_{\mathrm{DIC}}^{hkl} \right)^2 \\ & + \sum_{hkl} W_y^{hkl} \left(d\frac{\xi_i^{hkl} t_{2i}}{\xi_i^{hkl} t_{3i}} - D\frac{\Xi_i^{hkl} T_{2i}}{\Xi_i^{hkl} T_{3i}} + \Delta y_{\mathrm{c}} - \Delta y_{\mathrm{DIC}}^{hkl} \right)^2, \end{aligned} \tag{3.6}$$

where

$$
\begin{aligned}
[t] &= [g] \cdot (1+\tan^2\tfrac{\beta}{2})(1+\tan^2\tfrac{\gamma}{2}) \\
&= \begin{bmatrix} (1+\tan^2\frac{\beta}{2})(1-\tan^2\frac{\gamma}{2}) & -(1-\tan^2\frac{\beta}{2})\tan\frac{\gamma}{2} & 4\tan\frac{\beta}{2}\tan\frac{\gamma}{2} \\ 2(1+\tan^2\frac{\beta}{2})\tan\frac{\gamma}{2} & (1-\tan^2\frac{\beta}{2})(1-\tan^2\frac{\gamma}{2}) & -2\tan\frac{\beta}{2}(1-\tan^2\frac{\gamma}{2}) \\ 0 & 2\tan\frac{\beta}{2}(1+\tan^2\frac{\gamma}{2}) & (1-\tan^2\frac{\beta}{2})(1+\tan^2\frac{\gamma}{2}) \end{bmatrix},
\end{aligned}
$$

and

$$
\begin{aligned}
[T] &= [G] \cdot (1+\tan^2\tfrac{B}{2})(1+\tan^2\tfrac{\Gamma}{2}) \\
&= \begin{bmatrix} (1+\tan^2\frac{B}{2})(1-\tan^2\frac{\Gamma}{2}) & -(1-\tan^2\frac{B}{2})\tan\frac{\Gamma}{2} & 4\tan\frac{B}{2}\tan\frac{\Gamma}{2} \\ 2(1+\tan^2\frac{B}{2})\tan\frac{\Gamma}{2} & (1-\tan^2\frac{B}{2})(1-\tan^2\frac{\Gamma}{2}) & -2\tan\frac{B}{2}(1-\tan^2\frac{\Gamma}{2}) \\ 0 & 2\tan\frac{B}{2}(1+\tan^2\frac{\Gamma}{2}) & (1-\tan^2\frac{B}{2})(1+\tan^2\frac{\Gamma}{2}) \end{bmatrix},
\end{aligned}
$$

In this manner, we manage to avoid trigonometric calculations in each iteration of optimization.

Although we usually provide the initial guess of $\mathcal{P}$ by standard Laue treatment, enhanced Laue-DIC essentially uses spots' displacements as input. The flowchart of enhanced Laue-DIC is given in Fig. 3.1: image enhanced Laue-DIC as a black box, the inputs of the black box are spots' displacements measured by DIC and spots' indexes (for example, obtained by LaueTools [LaueTools]), and the outputs are lattice matrices and calibration parameters of both current and reference configurations; to facilitate the calculation, an initial estimation of lattice matrices and calibration parameters are provided by other means, e.g. standard Laue treatment (see §1.5).

The original Laue-DIC, introduced in the previous chapter, is actually a special case of enhanced Laue-DIC, and it corresponds to the case in which the lattice matrix of reference configuration, the calibration parameters of both reference and current configurations are known, only the relative deformation gradient, or more precisely, the lattice matrix of current configuration, will be calculated. As we have shown in §2.2.2, solving a system of linear equations of Eqn. 2.6 would suffice to obtain the relative deformation gradient. However, in enhanced Laue-DIC, $\mathcal{P}$, the set of unknowns to be inquired, is more complex than in original Laue-DIC. Therefore, we need to employ some more advanced numerical methods, and we will cover the topic in the next section.

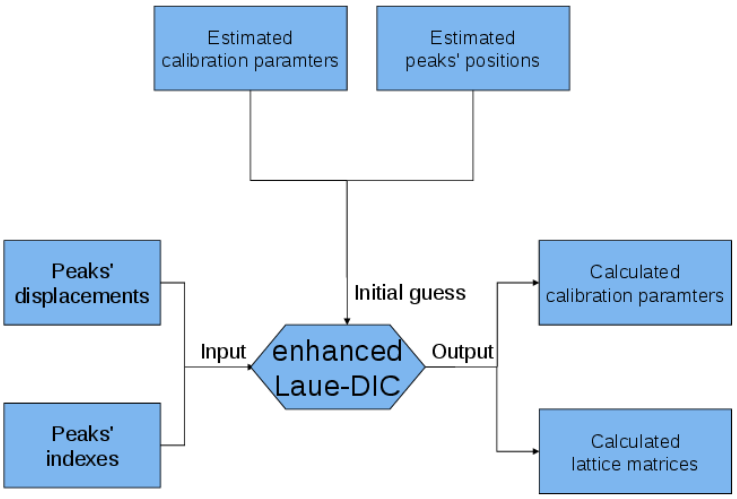

Figure 3.1: Flowchart of enhanced Laue-DIC

3.3 Numerical Tests of Enhanced Laue-DIC

Now our problem is to minimizing $\Pi(\mathcal{P})$ by manipulating $\mathcal{P}$. Prior to dealing with experimental data, we first run some numerical tests with simulated data for the following purpose:

- investigating the variation of $\Pi(\mathcal{P})$ with its variables.
- finding the most efficient optimization algorithm.
- investigating how the uncertainties of DIC influence the minimization of $\Pi(\mathcal{P})$.

The procedure of numerical test goes as following (see Fig. 3.2):

1. Given the exact values of lattice matrices and calibration parameters for two configurations, generate theoretical peak positions on detector plane with Eqn. 1.29 and subsequently their displacements.
2. Deviate the simulated peaks' positions and calibration parameters a little bit from their exact values according to normal distribution. The deviation of peak's position

is 0.1 pix in both x and y direction to represent the uncertainties of fitting Laue spot [Poshadel et al. 2012], and the deviation of calibration parameters are tabulated in Tab. 2.4.

3. Use, for example, the standard Laue treatment to calculate lattice matrices for the two configurations with the deviated peaks' positions and deviated calibration parameters as estimation of lattice matrices.

4. If we wish to study the influence of errors on spots' displacements, deviate the input displacements a little bit from their theoretical values.

5. Run the optimization to investigate whether we can recover the exact values of lattice matrices and calibration parameters using the simulated displacements as input and deviated parameters as initial guess.

For calibration parameters, their errors are quantified by their discrepancies between calculated values and the exact ones:

$$\epsilon_x = |x^{\mathrm{cal}} - x^{\mathrm{exa}}|, \quad x \in \{d, D, \Delta x_{\mathrm{c}}, \Delta y_{\mathrm{c}}, \beta, B, \gamma, \Gamma\},$$

where the superscript $^{\mathrm{cal}}$ represents the result after optimization, and the superscript $^{\mathrm{exa}}$ represents the exact value which is known in advance. As for the quantification of the errors on lattice matrices, $\underset{\sim}{l}$ and $\underset{\sim}{L}$, we use similar definition of errors as that of relative deformation gradient in §2.5.2:

1. dividing each component of lattice matrix by the cube root of the determinant of the lattice matrix in order to get rid of the uncertainty on the volume of unit lattice, i.e.

$$\begin{aligned} \hat{\underset{\sim}{l}} &\doteq \frac{\underset{\sim}{l}}{\sqrt[3]{\det \underset{\sim}{l}}}, \\ \hat{\underset{\sim}{L}} &\doteq \frac{\underset{\sim}{L}}{\sqrt[3]{\det \underset{\sim}{L}}} \end{aligned} \tag{3.7}$$

2. the errors on $\underset{\sim}{l}$ and $\underset{\sim}{L}$ are defined as

$$\begin{aligned} \epsilon_l &\doteq \frac{\sum_{i=1}^{3}\sum_{j=1}^{3}|\hat{l}_{ij}^{\mathrm{cal}} - \hat{l}_{ij}^{\mathrm{exa}}|}{9}, \\ \epsilon_L &\doteq \frac{\sum_{i=1}^{3}\sum_{j=1}^{3}|\hat{L}_{ij}^{\mathrm{cal}} - \hat{L}_{ij}^{\mathrm{exa}}|}{9}. \end{aligned}$$

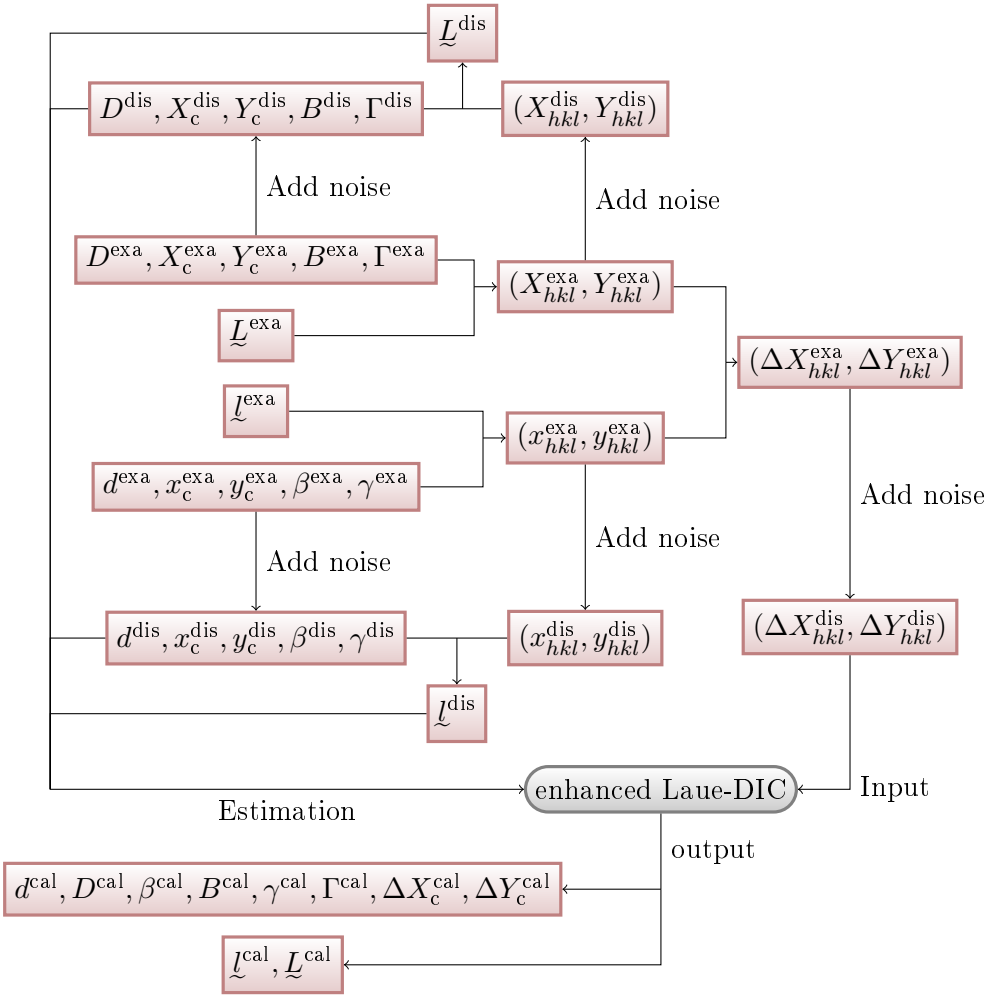

Figure 3.2: Flowchart of numerical tests

In case of statistical tests where multi random cases are treated, we define the systematic and random errors of $\underset{\sim}{l}$ and $\underset{\sim}{L}$ as:

$$\begin{aligned}
\bar{\epsilon}_l &\doteq \frac{\sum_{i=1}^{3}\sum_{j=1}^{3}|\bar{\hat{l}}_{ij}^{\mathrm{cal}} - \hat{l}_{ij}^{\mathrm{exa}}|}{9}, \\
\sigma_{\epsilon_l} &\doteq \frac{\sum_{i=1}^{3}\sum_{j=1}^{3}\sigma_{\hat{l}_{ij}^{\mathrm{cal}}}}{9}, \\
\bar{\epsilon}_L &\doteq \frac{\sum_{i=1}^{3}\sum_{j=1}^{3}|\bar{\hat{L}}_{ij}^{\mathrm{cal}} - \hat{L}_{ij}^{\mathrm{exa}}|}{9}, \\
\sigma_{\epsilon_L} &\doteq \frac{\sum_{i=1}^{3}\sum_{j=1}^{3}\sigma_{\hat{L}_{ij}^{\mathrm{cal}}}}{9}.
\end{aligned} \tag{3.8}$$

where the overline on the right hand of equations means the average, and the σ on the right hand of equations means the standard deviation.

We will perform two types of numerical tests in the following: the first type uses the peaks' displacements which are accurately given, and the purpose of this type is to find out an efficient optimization algorithm; and the second types uses displacements which are polluted by zero-mean Gaussian noise, and the purpose of this type is to evaluate the systematic and random errors of enhanced Laue-DIC. As for the exact values of lattice matrices, we deal with case I of §2.5.2 with the first type of tests; and we deal with all three cases of §2.5.2 with the second type of tests. In both types of tests, the calibration parameters and their uncertainties are given in Tab. 2.3 and 2.4 respectively.

3.3.1 Numerical tests with accurate spots' displacements as input

Let us first grasp some visual impression about the properties of the cost function $\Pi(\mathcal{P})$ (see Eqn. 3.6). Because $\Pi(\mathcal{P})$ contains 24 parameters, it is difficult to plot $\Pi(\mathcal{P})$ on paper. What we do is to investigate the variation of $\Pi(\mathcal{P})$ by altering one parameter of $\mathcal{P}$ while keeping the rest fixed. The lattice matrices used in this program is the same as those in the case I of §2.5.2.

Fig. 3.3 depicts the variation of $\Pi(\mathcal{P})$ with lattice parameters. For brevity, we only plotted the dependence on one diagonal and one off-diagonal components of lattice matrix $\underset{\sim}{l}$ and $\underset{\sim}{L}$, i.e. L_{22}, L_{23}, l_{22}, and l_{23}. Fig. 3.4 depicts the variation of $\Pi(\mathcal{P})$ with calibration parameters. In the two figures, the black curves represent the case where the rest parame-

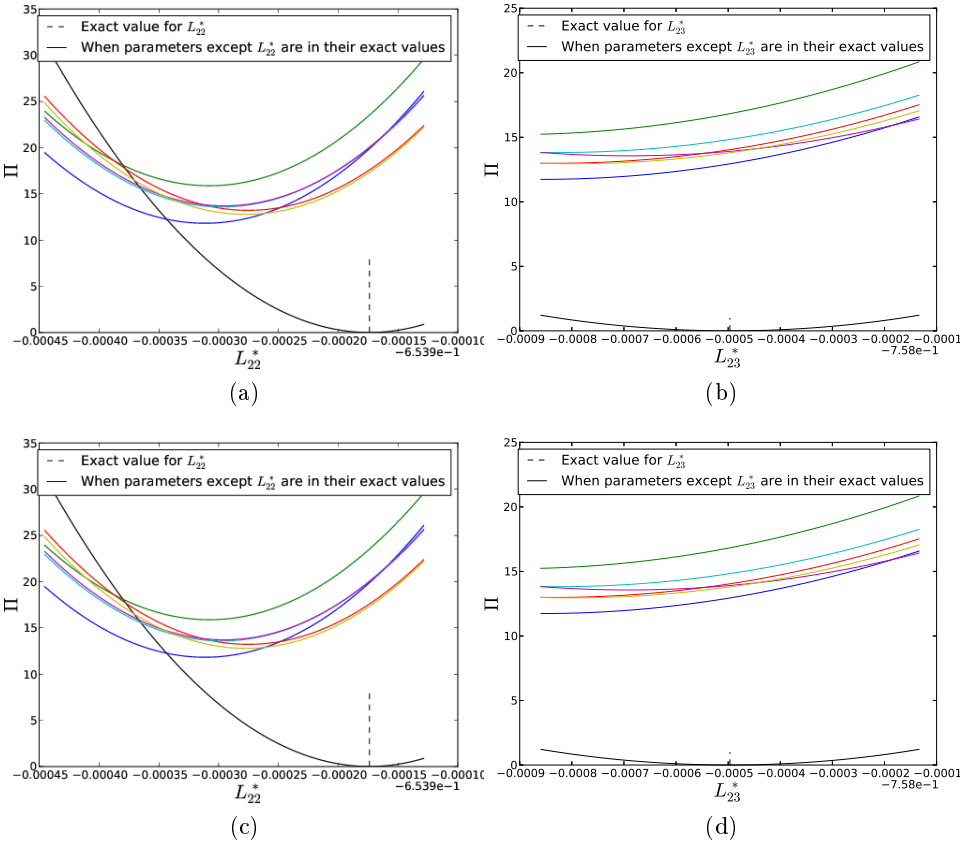

Figure 3.3: Variation of $\Pi(\mathcal{P})$ by altering L_{22}, L_{23}, l_{22}, and l_{23} while keeping the rest fixed

ters are kept in their exact values, while the colored curves represents the cases where the rest parameters are deviated from their exact values but kept fixed. We can see that:

1. If we only varied one parameter, we could find only one minimum point.

2. The position of the minimum point is influenced by other parameters, specifically, any deviation of other parameters from their exact values would deviate the minimum point from its exact value.

Since there is only one minimum if we vary one parameter while keeping the rest constant, it is straightforward for us to minimize each parameters one by one, and then iterate the process. After each minimization of one parameter, the cost function $\Pi(\mathcal{P})$ will decrease, and will eventually converge to zero if we keep on iterating the process. Although it sounds plausible, in practice, it requires a lot of CPU time. In my case, it requires 20 000

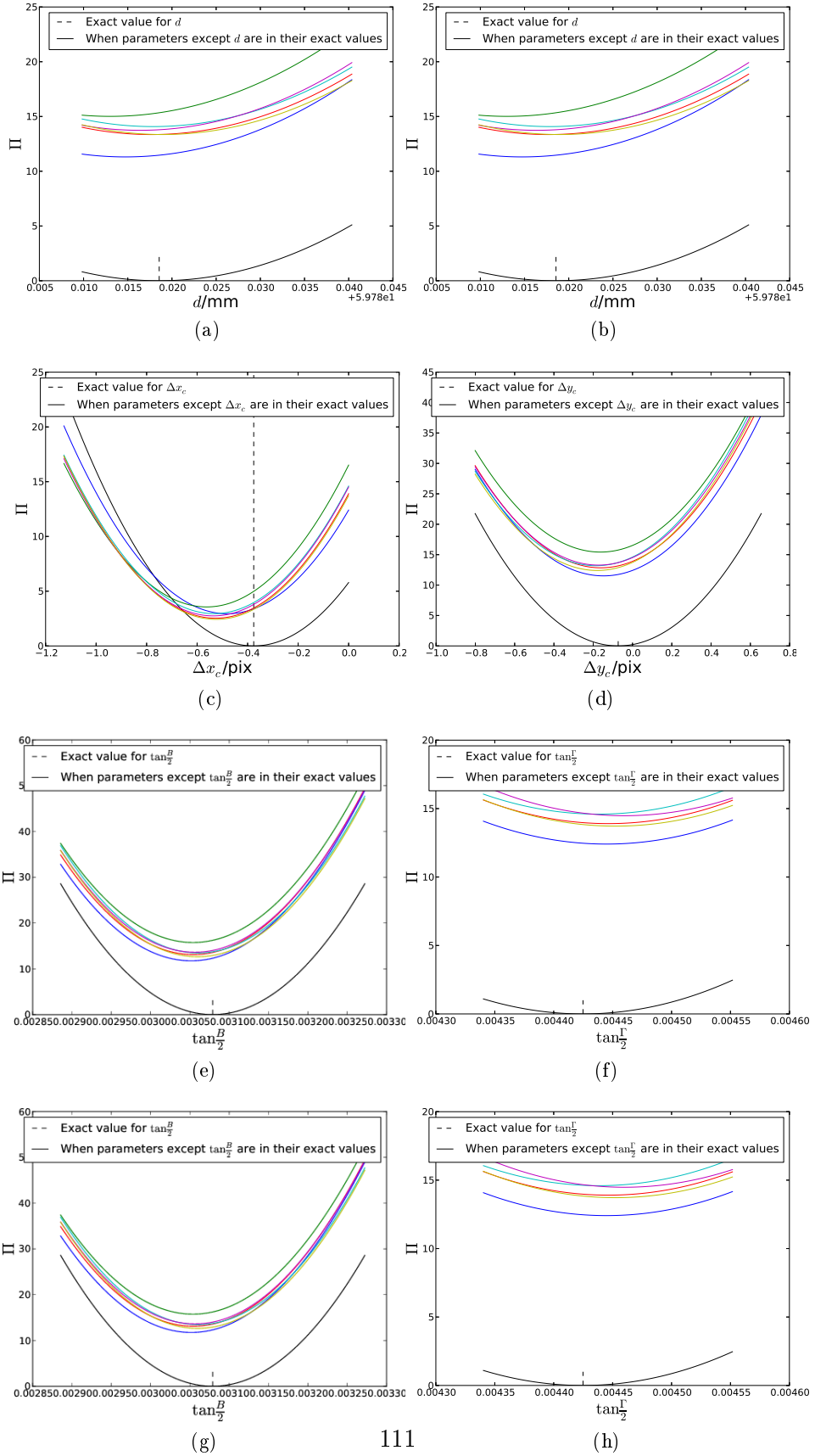

Figure 3.4: Variation of $\Pi(\mathcal{P})$ by altering one calibration parameter while keeping the rest fixed

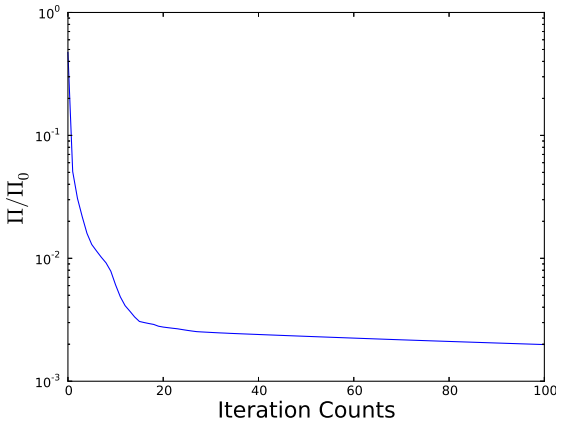

Figure 3.5: Π/Π_0 vs. iteration counts using L-BFGS-B algorithm, the peaks' displacements are accurately given.

iterations (about five minutes on a standard laptop) to reach an order of error of 10^{-6} in lattice matrices (see Eqn. 3.7 for the definition of error). Therefore, it is worthwhile to use some more advanced optimization methods to find the minimum of $\Pi(\mathcal{P})$.

The candidate algorithms in our test were: Powell's algorithm (requires no derivatives of Π, see [Powell 1964]), L-BFGS-B algorithm (requires the gradient of Π, see [Byrd et al. 1995]), and Trust-Region algorithm (requires both the gradient and Hessian matrix of Π, see [Byrd et al. 1987]). The analytical expressions of gradient and Hessian matrix of Π are given in Appendix A.2 and A.3 respectively. The halts of these algorithms are controlled by the iteration counts.

Of course, increasing the iteration counts would asymptotically decrease the value of Π to zero if the peaks' displacements were free of errors. Fig. 3.5 depicts the decrease of cost function Π with the iterations of the implementation of L-BFGS-B algorithm, in which Π_0 represents the initial value of cost function. It can be seen that the value of Π decreases significantly with increasing the iteration; however, when the iteration count exceeds 20, further iteration will not significantly reduce the cost function Π. Similar trend is also observed in other algorithms investigated. Therefore, for each algorithm, we will stop the iteration when the decrease of the cost function is less than 5% of its previous value. Tab. 3.2 lists the performances of the mentioned algorithms.

It is evident from Tab. 3.2 that though Trust-Region and L-BFGS-B algorithms can

	Trust-Region	L-BFGS-B	Powell	Initial value
ϵ_l	0.05	5.40×10^{-5}	9.57×10^{-5}	6.77×10^{-5}
ϵ_L	0.05	6.03×10^{-5}	9.60×10^{-5}	8.58×10^{-5}
ϵ_d/mm	2.9×10^{-3}	3.33×10^{-3}	1.44×10^{-3}	4.22×10^{-3}
ϵ_D/mm	1.3×10^{-3}	1.41×10^{-3}	1.46×10^{-3}	3.95×10^{-3}
$\epsilon_{\Delta x_c}$/pix	6.6×10^{-2}	0.17	2.38×10^{-4}	0.23
$\epsilon_{\Delta y_c}$/pix	3.7×10^{-2}	0.03	2.20×10^{-3}	0.38
$\epsilon_\beta/^\circ$	5.5×10^{-2}	1.24×10^{-3}	6.42×10^{-4}	5.12×10^{-3}
$\epsilon_B/^\circ$	5.4×10^{-2}	2.06×10^{-3}	4.09×10^{-3}	5.12×10^{-3}
$\epsilon_\gamma/^\circ$	0.51	6.45×10^{-4}	6.52×10^{-4}	4.90×10^{-3}
$\epsilon_\Gamma/^\circ$	0.51	6.25×10^{-4}	4.10×10^{-3}	5.07×10^{-3}
$\frac{\Pi}{\Pi_0} \times 100\%$	7.7%	12.1%	20.2%	100%

Table 3.2: Performance of each individual algorithm, Π_0 being the initial value of cost function

reduce the objective function Π, several indexes indicating the deviation from real value increase significantly after optimization. This phenomenon may signify that we have attained local minimum rather than global minimum. And Powell algorithm is very time-consuming (about 45 sec per iteration), perhaps due to the fact that Powell algorithm does not use any derivative of cost function. Though there are global minimization algorithm available, e.g. simulated annealing algorithm, genetic algorithm. These algorithms entail large mount of calculation, but in this work we do not have sufficient time to dig into them. Here, we tried to use partial optimization rather than full optimization.

To improve the procdure, we first subdivided all parameters $\mathcal{P}$ into lattice matrices $\mathcal{L} = \{\underline{l}, \underline{L}\}$, and calibration parameters, denoted as $\mathcal{C} = \{d, D, \Delta x_c, \Delta y_c, \beta, B, \gamma, \Gamma\}$. Because there is more uncertainty in $\mathcal{L}$ than in $\mathcal{C}$ (the uncertainty in lattice matrices comes from uncertainties in calibration parameters plus those in peaks' positions), we first optimize $\mathcal{L}$ while keeping $\mathcal{C}$ fixed. Once the optimization of $\mathcal{L}$ is finished, we optimize $\mathcal{C}$ while keeping $\mathcal{L}$ fixed. We iterate this procedure until the decrease of the cost function is less than 5% of its previous value.

We tested all the combinations of optimization algorithms to investigate which combination gave the best results in terms of $\epsilon_x, x \in \{l, L, d, D, \Delta x_c, \Delta y_c, \beta, B, \gamma, \Gamma\}$. As the calibration parameters are randomly deviated, we optimized 500 random cases for each

combination to make the results statistically significant. The statistical performance of each combination was evaluated by the average of $\epsilon_x, x \in \{l, L, d, D, \Delta x_c, \Delta y_c, \beta, B, \gamma, \Gamma\}$ of all cases (the average is denoted as $\bar{\epsilon}$). The results of numerical test were given in Tab. 3.3, we found that the result of the combination "L-BFGS-B"-"Powell" approached the real values of $\mathcal{L}$ most: the accuracies of $\mathcal{L}$ and $\mathcal{C}$ are one order magnitude better than simply using Powell's algorithm. The calculation of enhanced Laue-DIC hereinafter will use this combination if there were no other specification, which will cost $\sim 30\,\text{sec}$ for a single optimization.

3.3.2 Numerical tests with erroneous spots' displacements as input

We discussed the minimization of $\Pi(\mathcal{P})$ when the spots' displacements are accurately given as input in the previous section. However, in real case, the spots' displacements are prone to errors as demonstrated in the previous chapter. Just as in §2.5.2, we will perform the numerical tests in two aspects:

- Varying the deviations of spots' displacements while maintaining the deviations of calibration parameters. The deviations imposed to spots' displacements are 0.005 pix, 0.01 pix, 0.015 pix, 0.02 pix, 0.025 pix, 0.03 pix, 0.035 pix, 0.04 pix, 0.045 pix, 0.05 pix, while the deviations of calibration parameters are tabulated in Tab. 2.4.

- Vary the deviations of calibration parameters while maintaining the deviations of spots' displacements. The deviations of calibration parameters are obtained by uniformly scaling the deviations tabulated in Tab. 2.4, and the scaling factors are 0, 0.25, 0.5, 0.75, 1, 1.25, 1.5, 1.75, 2, 2.25, 2.5. The deviations of spots' displacements are 0.01 pix for both x and y directions of all the spots.

For each setting of deviations of spots' displacement and calibration parameters, we generate 500 random cases and then calculate the average errors of lattice matrices and calibration parameters. We applied the test to the case I, II, and III of §2.5.2, and the three cases represent increasing deformation in a row. Besides, in §2.5.2 we have also demonstrated that the number of spots considered will also affect the accuracy. Therefore we will also run the numerical tests with three different numbers of spots: 12, 25, and 45.

Algorithm for $\mathcal{L}$ Algorithm for $\mathcal{C}$	Trust-Region Trust-Region	Trust-Region L-BFGS-B	Trust-Region Powell	Initial value
$\overline{\epsilon}_l$	0.14	6.8×10^{-2}	0.17	Same as in Tab. 3.2
$\overline{\epsilon}_L$	0.14	6.8×10^{-2}	0.17	
$\overline{\epsilon}_d$/mm	4.4×10^{-3}	1.9×10^{-3}	4.4×10^{-3}	
$\overline{\epsilon}_D$/mm	3.3×10^{-3}	6.0×10^{-3}	3.8×10^{-2}	
$\overline{\epsilon}_{\Delta x_c}$/pix	0.60	0.33	7.9×10^{-2}	
$\overline{\epsilon}_{\Delta y_c}$/pix	0.76	0.41	0.85	
$\overline{\epsilon}_\beta/^\circ$	0.36	7.3×10^{-3}	7.0×10^{-4}	
$\overline{\epsilon}_B/^\circ$	1.33	1.4×10^{-2}	5.4×10^{-4}	
$\overline{\epsilon}_\gamma/^\circ$	0.36	1.2×10^{-2}	7.4×10^{-3}	
$\overline{\epsilon}_\Gamma/^\circ$	1.34	1.5×10^{-2}	8.2×10^{-3}	
$\frac{\overline{\Pi}}{\Pi_0} \times 100\%$	5.9%	10.1%	18.2%	100%

Algorithm for $\mathcal{L}$ Algorithm for $\mathcal{C}$	L-BFGS-B Trust-Region	L-BFGS-B L-BFGS-B	L-BFGS-B Powell	Initial value
$\overline{\epsilon}_l$	1.4×10^{-4}	2.4×10^{-3}	6.1×10^{-6}	Same as in Tab. 3.2
$\overline{\epsilon}_L$	2.2×10^{-5}	2.4×10^{-3}	8.4×10^{-6}	
$\overline{\epsilon}_d$/mm	1.1	3.1×10^{-3}	1.9×10^{-4}	
$\overline{\epsilon}_D$/mm	1.1	1.8×10^{-3}	1.6×10^{-4}	
$\overline{\epsilon}_{\Delta x_c}$/pix	0.30	0.16	9.1×10^{-3}	
$\overline{\epsilon}_{\Delta y_c}$/pix	0.22	0.25	1.5×10^{-2}	
$\overline{\epsilon}_\beta/^\circ$	6.1×10^{-3}	3.6×10^{-2}	4.3×10^{-4}	
$\overline{\epsilon}_B/^\circ$	3.4	5.5×10^{-3}	6.3×10^{-4}	
$\overline{\epsilon}_\gamma/^\circ$	5.6×10^{-2}	4.8×10^{-2}	2.5×10^{-4}	
$\overline{\epsilon}_\Gamma/^\circ$	3.4	6.7×10^{-3}	1.2×10^{-4}	
$\frac{\overline{\Pi}}{\Pi_0} \times 100\%$	7.2%	9.0%	8.0%	100%

Algorithm for $\mathcal{L}$ Algorithm for $\mathcal{C}$	Powell Trust-Region	Powell L-BFGS-B	Powell Powell	Initial value
$\overline{\epsilon}_l$	7.7×10^{-5}	1.0×10^{-4}	1.2×10^{-4}	Same as in Tab. 3.2
$\overline{\epsilon}_L$	5.3×10^{-5}	6.8×10^{-5}	3.4×10^{-5}	
$\overline{\epsilon}_d$	5.6×10^{-3}	1.3×10^{-3}	1.6×10^{-3}	
$\overline{\epsilon}_D$	1.1×10^{-3}	8.1×10^{-4}	3.6×10^{-3}	
$\overline{\epsilon}_{\Delta x_c}$/pix	0.14	5.7×10^{-2}	6.9×10^{-2}	
$\overline{\epsilon}_{\Delta y_c}$/pix	0.07	0.18	1.10	
$\overline{\epsilon}_\beta/^\circ$	0.11	9.0×10^{-2}	7.0×10^{-3}	
$\overline{\epsilon}_B/^\circ$	3.10	2.2×10^{-2}	6.7×10^{-3}	
$\overline{\epsilon}_\gamma/^\circ$	0.11	9.6×10^{-2}	8.5×10^{-4}	
$\overline{\epsilon}_\Gamma/^\circ$	3.10	4.0×10^{-2}	9.5×10^{-4}	
$\frac{\overline{\Pi}}{\Pi_0} \times 100\%$	13.9%	17.2%	23.6%	100%

Table 3.3: Performance of algorithm combinations

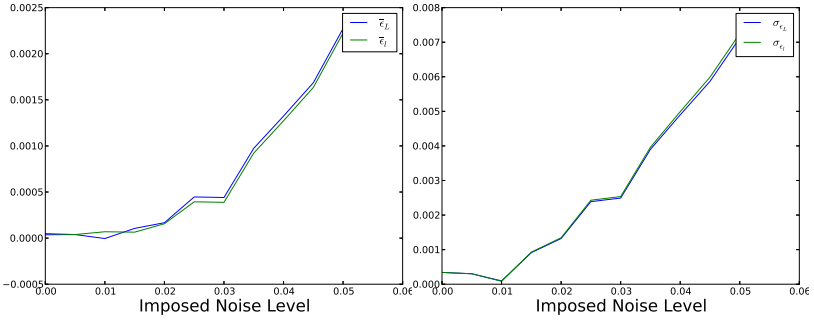

(a) Systematic error with 40 spots (b) Random error with 40 spots

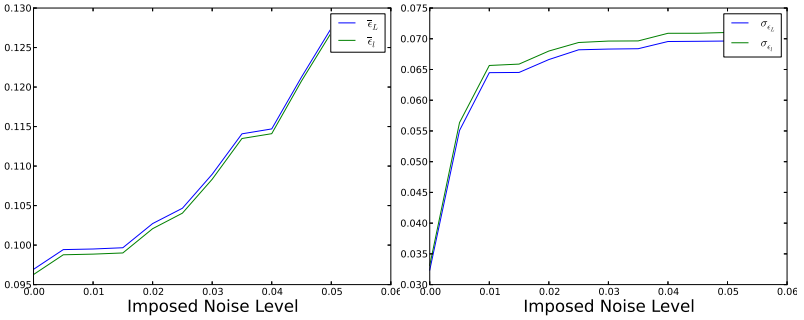

(c) Systematic error with 25 spots (d) Random error with 25 spots

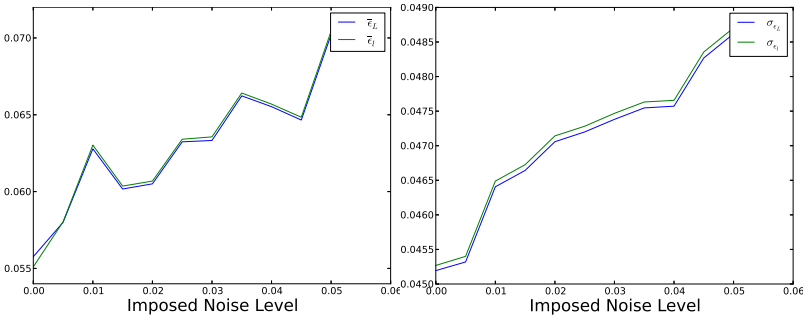

(e) Systematic error with 12 spots (f) Random error with 12 spots

Figure 3.6: Variations of systematic and random errors of lattice matrices with the deviations of displacements in case I.

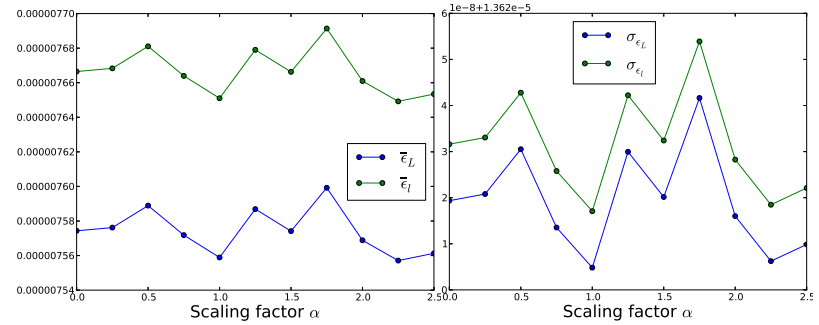

(a) Systematic error with 40 spots (b) Random error with 40 spots

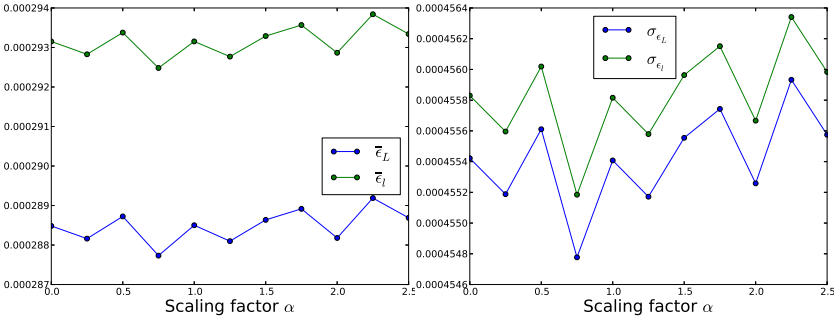

(c) Systematic error with 25 spots (d) Random error with 25 spots

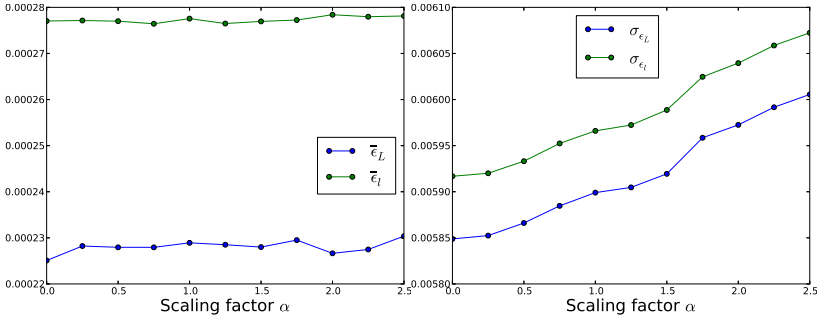

(e) Systematic error with 12 spots (f) Random error with 12 spots

Figure 3.7: Variations of systematic and random errors of lattice matrices with the deviations of calibration parameters in case I.

We first investigate the systematic and random errors on $\underset{\sim}{l}$ and $\underset{\sim}{L}$ of case I, with 40 spots, 25 spots, and 12 spots taken into account. In Fig. 3.6 and 3.7 we plot the variations of $\underset{\sim}{l}$ and $\underset{\sim}{L}$ relative to the errors of displacements and calibration parameters respectively, and we have the following conclusions:

- Both systematic and random errors of lattice matrices and calibration parameters increase with the deviations of spots' displacements.
- The systematic and random errors of $\underset{\sim}{l}$ and $\underset{\sim}{L}$ increase if the number of spots considered is reduced.
- The systematic errors seem more stable with the deviations of calibration parameters; this may be due to the fact that enhanced Laue-DIC has taken calibration parameters into consideration and become more robust against the errors in initial calibration parameters.
- When 12 spots are considered, the random error seems to increase linearly with the deviations of calibration parameters, while the random errors seem more stable with the deviations of calibration parameters when 40 or 25 spots are considered. This may be explained by the fact that the random error is also a function of number of spots considered, the influence of deviations of calibration parameters may be mitigated by increasing the number of spots considered. With less spots, the results of enhanced Laue-DIC are more prone to the errors of displacements and more likely to converge to wrong values.
- The random errors in lattice matrices are much higher than the corresponding systematic errors.
- Both systematic and random errors in lattice matrices increases with decreasing the number of spots taken into account.
- Despite the discrepancies between $\underset{\sim}{l}$'s and $\underset{\sim}{L}$'s systematic or random errors, the error curves of $\underset{\sim}{l}$ and $\underset{\sim}{L}$ are almost identical, that is to say, the errors of $\underset{\sim}{l}$ and $\underset{\sim}{L}$ increase almost at the same pace when increasing the deviations of displacements or calibration parameters.

- By comparing the evolution of the curves of random errors with the number of spots, we find that the curves of random errors appear to be more linearly shaped. When only 12 spots are considered, the curve loses the linearity.

The same trend has been observed in case II and case III.

Let us investigate the influence of deformation levels upon systematic and random errors of $\underset{\sim}{l}$ and $\underset{\sim}{L}$. For the sake of brevity, we only plotted the results with 25 spots taken into consideration to illustrate this point, and we found that the curves of both systematic and random errors of $\underset{\sim}{l}$ and $\underset{\sim}{L}$ do not vary significantly among the three cases corresponding to three levels of deformation $\underset{\sim}{F}$, $\underset{\sim}{F}^2$, and $\underset{\sim}{F}^3$: compare the systematic and random errors of case II and III in Fig. 3.8 with Fig. 3.6c and 3.6d, corresponding to the systematic and random errors of case I. The similar feature has also been found with other numbers of spots.

Now, we study the variations of systematic and random errors of calibration parameters with the deviations of displacements. We plotted the systematic and random errors of calibration parameters in case I with 25 spots considered in Fig. 3.9. We investigate two factors influencing the error curves:

numbers of spots considered In Fig. 3.10, we plotted the the variations of systematic and random errors of d and D with the deviations of displacements, with 12 and 40 spots considered in case I, and we found that it was not obvious that the errors of d and D would decrease as the number of spots increased unlike those of $\underset{\sim}{l}$ and $\underset{\sim}{L}$. The same feature has also been identified with other calibration parameters. Therefore, we concluded that the systematic and random errors on calibration parameters were less sensitive to the number of spots considered than those on lattice matrices.

levels of deformation To investigate the influence of deformation level, we plotted systematic and random errors of d and D in case II and III with 25 spots considered in Fig. 3.11. Again, we found that the relations between errors and levels of deformation did not seem obvious in d and D, nor in the rest of the parameters.

We also plotted the variation of systematic and random errors of calibration parameters

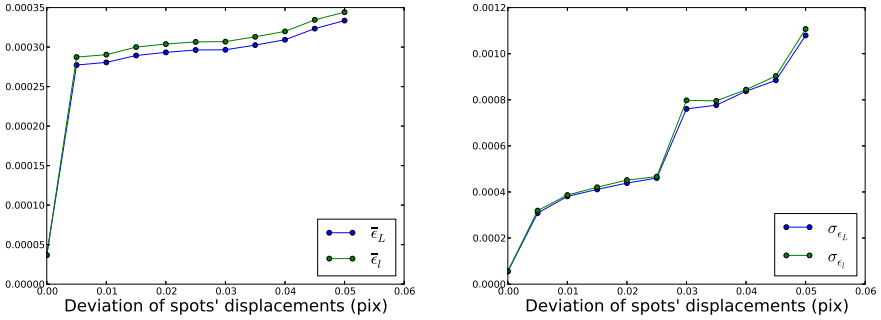

(a) Systematic errors of case II

(b) Random errors of case II

(c) Systematic errors of case III

(d) Random errors of case III

Figure 3.8: Variations of systematic and random errors of lattice matrices with the deviations of displacements in case II and III with 25 spots considered.

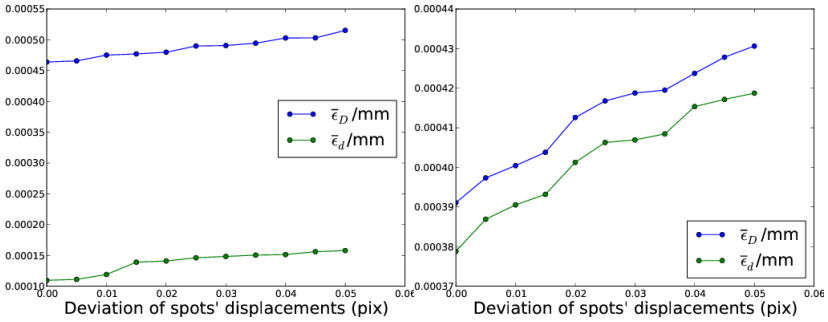

(a) Systematic error (b) Random error

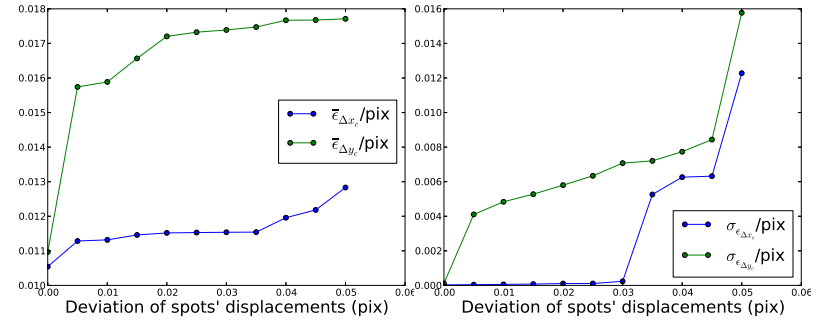

(c) Systematic error (d) Random error

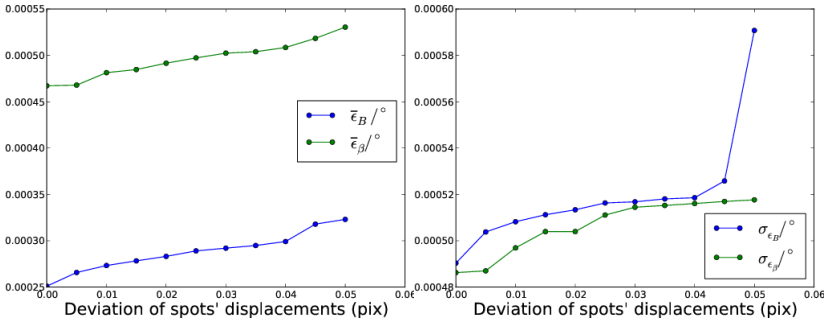

(e) Systematic error (f) Random error

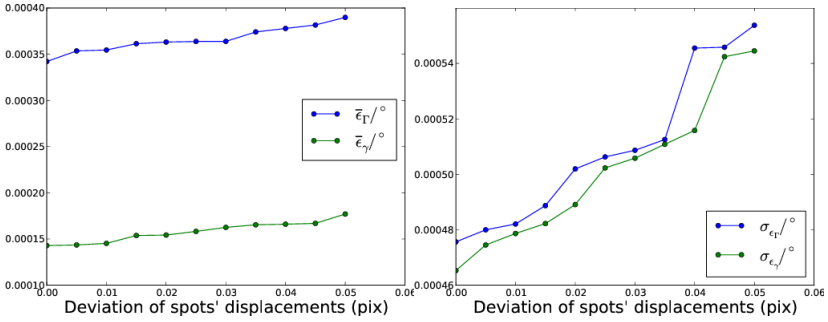

(g) Systematic error (h) Random error

Figure 3.9: Variations of systematic and random errors of calibration parameters with the deviations of displacements in case I with 25 spots considered.

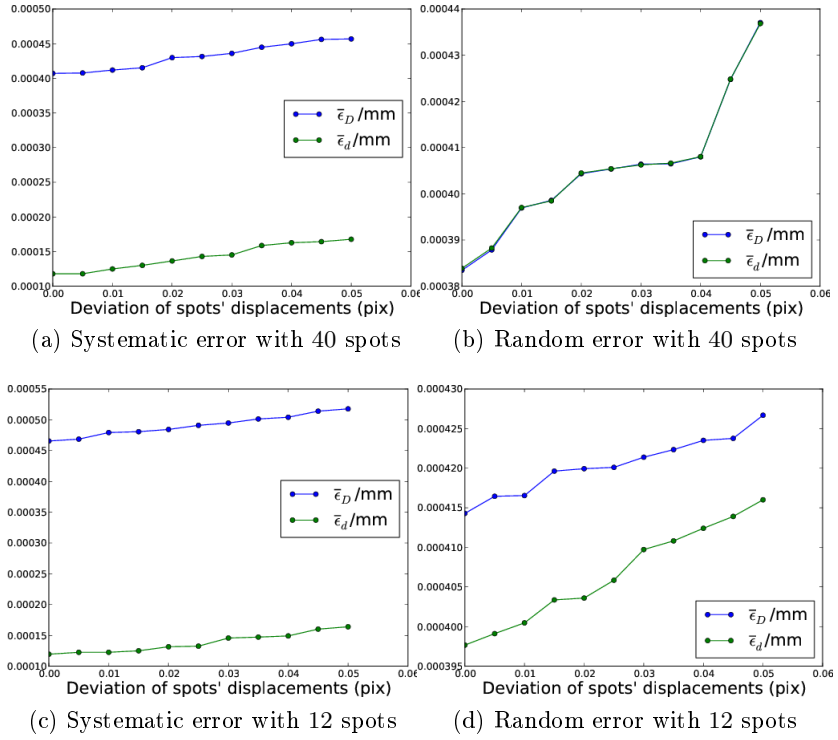

(a) Systematic error with 40 spots (b) Random error with 40 spots

(c) Systematic error with 12 spots (d) Random error with 12 spots

Figure 3.10: Variations of systematic and random errors of d and D with the deviations of displacements in case I.

with the deviations of calibration parameters in case I with 25 spots considered in Fig. 3.12. Like the errors of $\underset{\sim}{l}$ and $\underset{\sim}{L}$ in Fig. 3.7, the systematic errors seem stable with the deviations of calibration parameters, and the random errors seem to increase linearly with deviations of calibration parameters except the random errors of Δx_c and Δy_c. This may probably indicate that only Δx_c and Δy_c are accurately calculated since they appear insensitive to the variations of calibration parameters. Similar trend has also been found in cases II and III with other number of spots.

3.4 Summary

In this chapter, we have come up with an enhanced version of Laue-DIC. We first presented the limitation of the original Laue-DIC (see §3.1), which: (i) requires a reference configuration with a known lattice matrix, and (ii) requires the knowledge of calibration parameters of both current and reference configurations. Then, we presented its enhanced

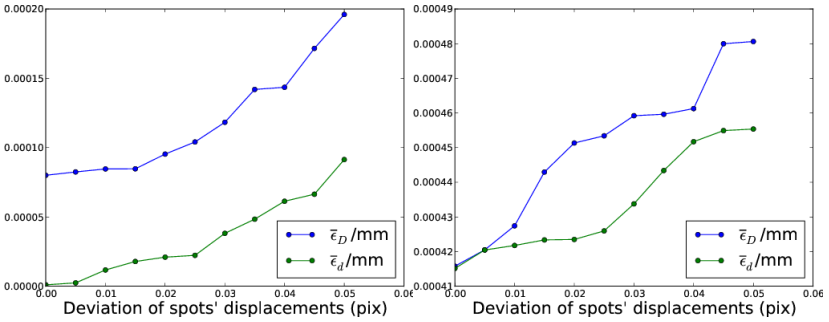

(a) Systematic error of case II (b) Random error of case II

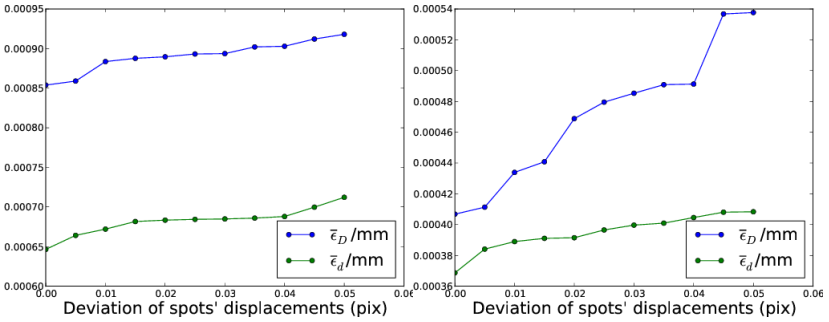

(c) Systematic error of case III (d) Random error of case III

Figure 3.11: Variations of systematic and random errors of d and D with the deviations of displacements in case II and III with 25 spots considered.

version, referred to as enhanced Laue-DIC (see §3.2). By "enhanced", we mean that the method uses solely spots' displacement measured by DIC as input, and the output includes not only the lattice matrices of two configurations but also the calibration parameters at two configurations. And this method is feasible as long as the Jacobian matrix (Eqn. 3.3) has full rank. In the end, we performed numerical tests with enhanced Laue-DIC in order to:

- try different optimization methods to find a proper optimization method; to this end, we first used accurate spots' displacements as input to check whether and how much we can recover the accurate lattice matrices and calibration parameters (see §3.3.1). So far the most efficient optimization algorithm among those we have tested is: optimizing the lattice matrices with L-BFGS-B method and optimizing the calibration parameters with Powell method.

- investigate the uncertainties of enhanced Laue-DIC from four dimensions: (i) the

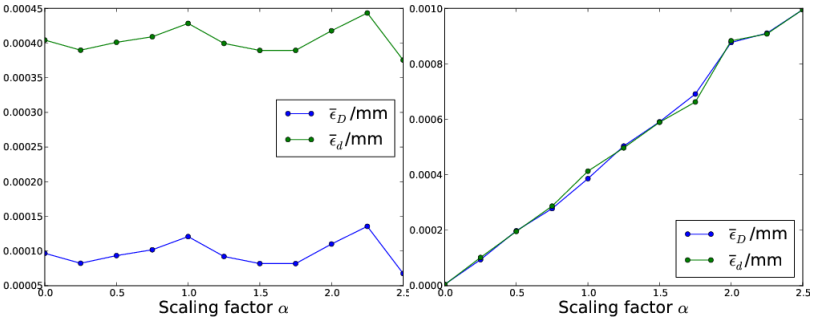

(a) Systematic error (b) Random error

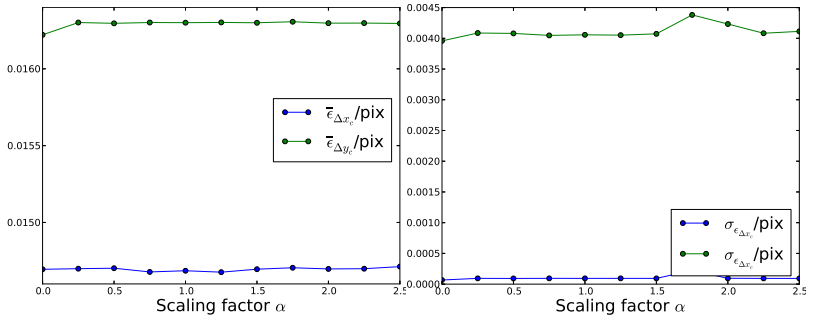

(c) Systematic error (d) Random error

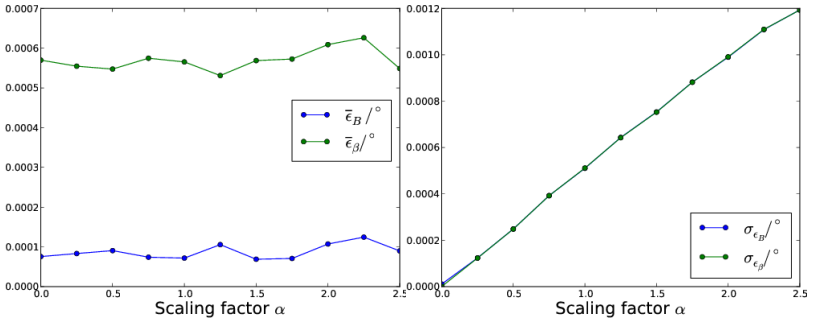

(e) Systematic error (f) Random error

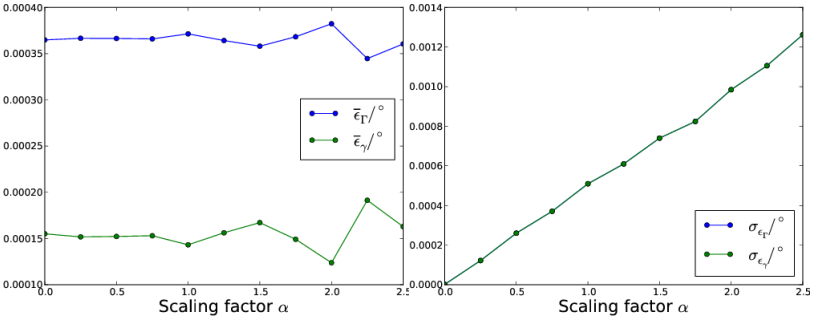

(g) Systematic error (h) Random error

Figure 3.12: Variations of systematic and random errors of calibration parameters with the deviations of calibration parameters in case I with 25 spots considered.

errors of spots' displacement, to this end, we added to spots' displacements with zero-mean Gaussian errors with incremental deviations from 0 to 0.05 pix; (ii) the errors of calibration parameters, to this end, we also added to the exact calibration parameters zero-mean Gaussian errors whose deviations came from scaling the deviations of Tab. 2.4 by a factor increasing from 0 to 2.5; (iii) the number of spots considered, 12, 25, and 40; (iv) the amplitude of deformation, $\underset{\sim}{F}$, $\underset{\sim}{F}^2$, and $\underset{\sim}{F}^3$ where $\underset{\sim}{F}$ is defined in Eqn. 2.20.

And the effects of the four aspects are summarized as following:

Errors of displacements Both systematic and random errors increase with the errors of displacements.

Errors of calibration parameters The systematic and random errors of lattice matrices seem more stable with the variation of calibration parameters, this may be due to the fact that enhanced Laue-DIC has taken the uncertainty of calibration parameters into account. The systematic errors of calibration parameters are also stable with the variation of calibration parameters, and the random errors of calibration parameters seem to increase linearly with the errors of calibration parameters except those of Δx_c and Δy_c, which appear stable.

Number of spots considered Both systematic and random errors of lattice matrices increases if the number of spots were reduced. However, the relationships between the errors of calibration parameters and number of spots is not very obvious.

Amplitude of deformation The relation between the errors and the amplitudes of deformation is not obvious in our study yet.

In the next chapter, we will use standard Laue treatment, original Laue-DIC, and enhanced Laue-DIC to treat experimental data collected from in-situ four point bending test.

Chapter 4

Applications

4.1 Introduction

In this chapter, we applied the standard Laue treatment mentioned in Chapter 1, the original Laue-DIC method mentioned in Chapter 2, and the enhanced Laue-DIC mentioned in Chapter 3 to experimental images, which were collected in BM32, ESRF. We will first present the context of the experiments, including an introduction of BM32, ESRF, and the processes of experiments. We will then compare the results by the three methods with analytical solutions or numerically simulated values and comment on that.

4.2 Description of Experiments

4.2.1 Introduction to Beamline BM32, ESRF

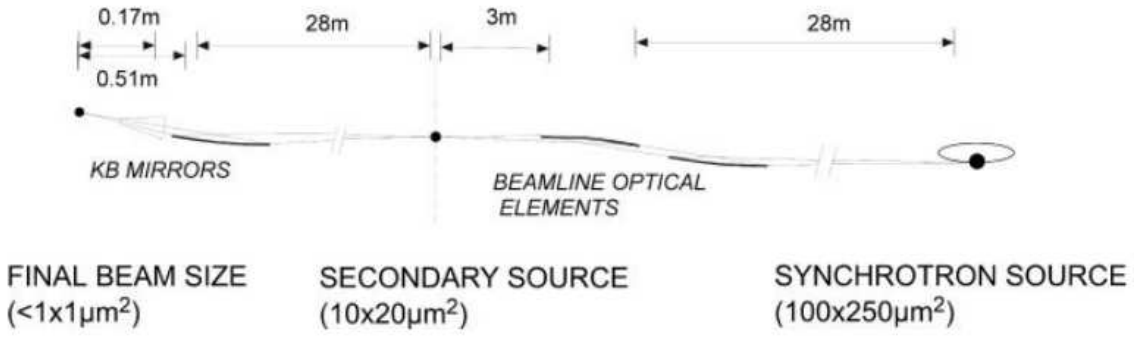

Figure 4.1: Sketch of the beamline [Ulrich et al. 2011]

In our experiments, we used the X-ray Laue microdiffraction equipments at beamline BM32 at ESRF, Grenoble. The full name of BM32 is Bending Magnet 32, and that of ESRF is European Synchrotron Radiation Facility. BM32 at ESRF is a Collaborative Research Group beamline by French institutes and specially dedicated to Surface X-ray Diffraction (SXRD), microdiffraction, and X-ray absorption spectroscopy (XAS). It fulfilled its duty in several experiments ([Villanova et al. 2010], [Desgranges et al. 2010], [Kirchlechner et al. 2011], [Hofmann et al. 2011]) and proved to be operational and fruitful.

BM32 consisted of optical hutch and experimental hutch as described in [Ulrich et al. 2011]. The optical hutch works in a $1:1$ mode where the synchrotron source-to-optics distance typically equals the optics-to-sample distance so as to keep an unitary demagnification ratio of synchrotron source at the sample position (see Fig. 4.1). Bending magnet source feeds the optical hutch with white beam, which will successively passes through entrance slit, first mirror, monochromator, second mirror, and finally exits the optical hutch through wide aperture micro-slit (figure 4.2). Before reaching the sample, the beam is further focused by Kirkpatrick-Baez mirror (hereinafter referred to as KB mirror) to achieve a size of $0.5 \times 0.5\,\mu\text{m}^2$ and to stabilize its position to better than $0.2\,\mu$m. The KB mirrors in BM32 ESRF has been changed from mechanically-bent mirrors into prefigured mirrors by the time we did our experiments, because prefigured mirrors including differentially profiled mirrors are lighter and less sensitive to thermal gradients than mechanically-bent mirrors. Actual issues to such state-of-art setup include the damage to the mirrors during the exposure to radiation and the aging of the mirrors can affect the long-term performance of the mirrors [Ice et al. 2009].

BM32 offers two modes: monochromatic beam and white beam, from which users can choose by adjusting the angle and distance of the two crystals of the monochromator. In the case of Laue microdiffraction, the mode of white beam should be chosen. The spectral band we used was $5 - 22\,\text{keV}$. However, the spectral brightness of synchrotron sources can hardly be characterized by single formula or diagram, since it depends on various factors, e.g., ring current, magnet field strength, beamline optics, etc (brightness is defined as the number of photons passing through a surface having unit solid angle per unit time [He 2009a]). We can have a general idea of spectral brightness from Fig. 4.3.

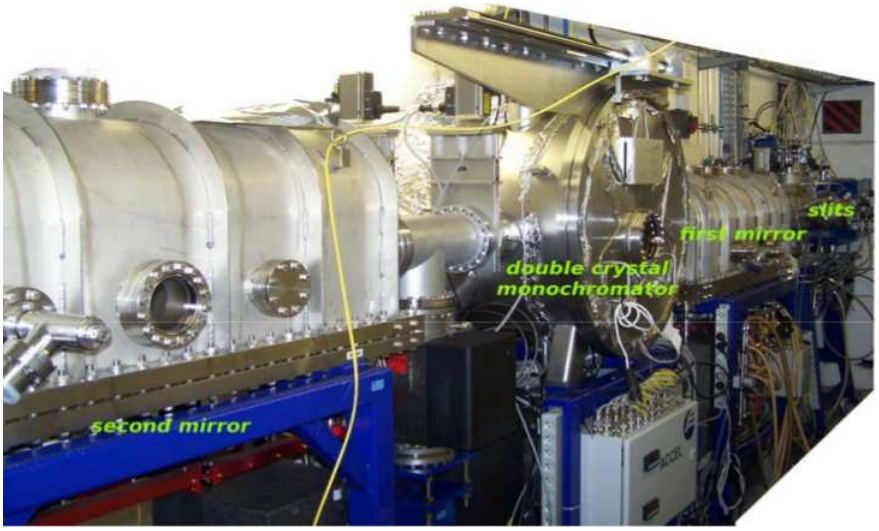

Figure 4.2: Optical system of BM32, ESRF

4.2.2 Specimens

In our experiments, we investigated three materials: Si, Ge, and 316 stainless steel (referred to as 316L hereinafter). Si and Ge are elastic material and do not deform plastically. Their difference lies in their penetration depth: Si has a larger penetration depth than Ge; for example, for X-ray photon generated by $K\beta_1$ line of Cu ($\sim 8\,\mathrm{keV}$), the absorption coefficient of Si is $110.7\,\mathrm{cm}^{-1}$, while that of Ge is $272.4\,\mathrm{cm}^{-1}$ [Maslen 2004]. 316L is a more industrial material than Si and Ge, and it will deform plastically.

4.2.2.1 Si specimens

We have prepared three Si monocrystals of different orientations to investigate the influence of orientation, namely Si sample I, Si sample II, and Si sample III. The sizes of the three samples are $2.42 \times 7.97 \times 35\,\mathrm{mm}^3$ (see Fig. 4.4), and the approximate orientation of three samples are tabulated in Tab. 4.1 The surfaces of the three Si samples were mechanically polished at ESRF to a mirror finish with negligible roughness.

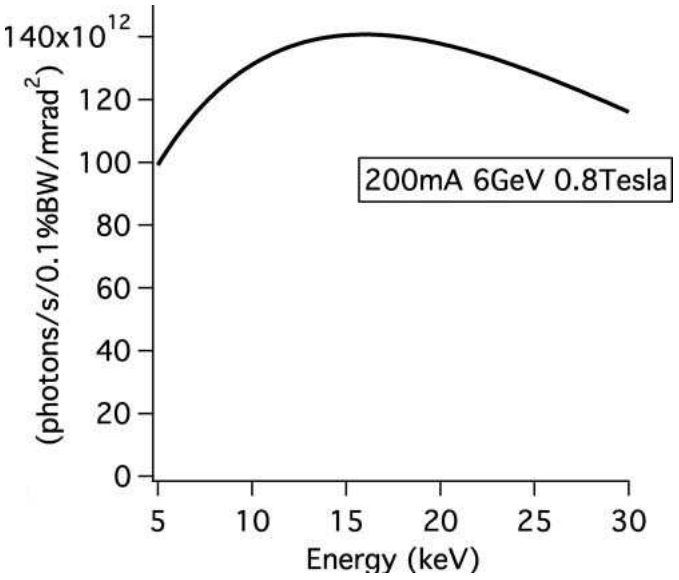

Figure 4.3: Spectral brightness distribution for the BM32, ERSF [Ulrich et al. 2011]

	(hkl)	$\langle uvw \rangle$
Sample I	[100]	[010]
Sample II	[110]	[001]
Sample III	[110]	$[1\bar{1}0]$

Table 4.1: Approximate orientations of three Si samples. The (hkl) and $\langle uvw \rangle$ are specified in Fig. 4.4.

4.2.2.2 Ge specimens

We have experimented on one Ge monocrystal, whose size is $2.42 \times 7.97 \times 35\,\mathrm{mm}^3$. The Ge sample was oriented so that its [100], [010], and [001] directions were aligned approximately parallel to the three edges of sample. The surfaces of the Ge sample was mechanically polished to a mirror finish with negligible roughness.

4.2.2.3 316L specimens

We have also experimented on a 316L monocrystalline sample, whose size is $0.52 \times 4.80 \times 30\,\mathrm{mm}^3$. The 316 sample was oriented so that its [100], [010], and [001] directions were aligned approximately parallel to the three edges of sample. 316 sample was first mechanically polished to a mirror finish with negligible roughness, and then chemically

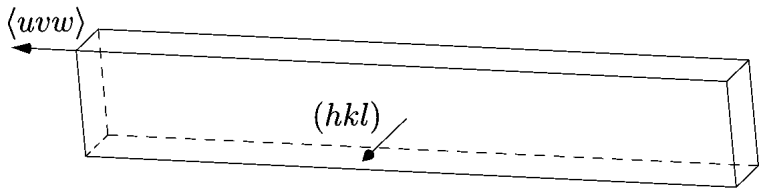

Figure 4.4: A sample's orientation

polished to remove the damaged surface layer.

4.2.3 Procedure of Experiments

The experiments we conducted were *in situ* four-point bending test (see Fig. 4.5). Four-point bending test (hereinafter referred to as FPB test) is a very classical test to explore the mechanical properties of materials, e.g. constitutive relation ([Hollenberg et al. 1971], [Belouettar et al. 2009]), crack growth ([Ma 1997], [Cuitiño and Ortiz 1996]), etc. FPB test wins its popularity in the community of solid mechanics because (i) the boundary conditions in FPB test are rather simple; (ii) the deformation modes in FPB test are multiple, including tension, compression, and sometimes shear, and the induced strain gradient within the beam is controllable, rendering it suitable for studying constitutive relation.

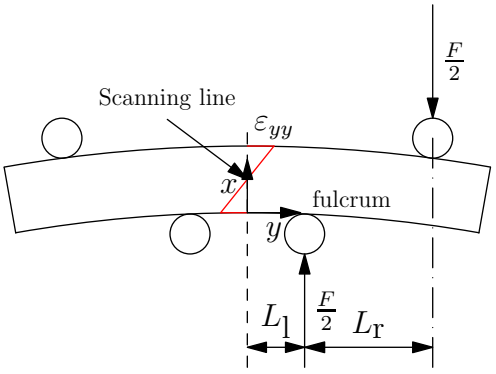

Figure 4.5: Four point bending test

The *in situ* test was carried out in the experimental hutch of BM32. Figure 4.7 is an example of the embedment of *in situ* test equipment into the beamline. Right above the experimental setup, there is an area detector to receive the diffraction pattern. In our experiment, we used X-ray Very High Resolution (VHR) CCD detector (see Fig. 4.8),

manufactured by Photonic Science Ltd. Some parameters of this detector are given in Tab. 4.2. A small Ge monocrystal with a known orientation is glued by wax on the surface of the sample to enable the calibration of the experimental setup. The calibration procedure runs as follow: (i) take diffraction image of Ge; (ii) manipulate the calibration parameters until the simulated Laue pattern coincide with the experimental one (see Fig. 4.6 for determining the calibration parameters in LaueTool).

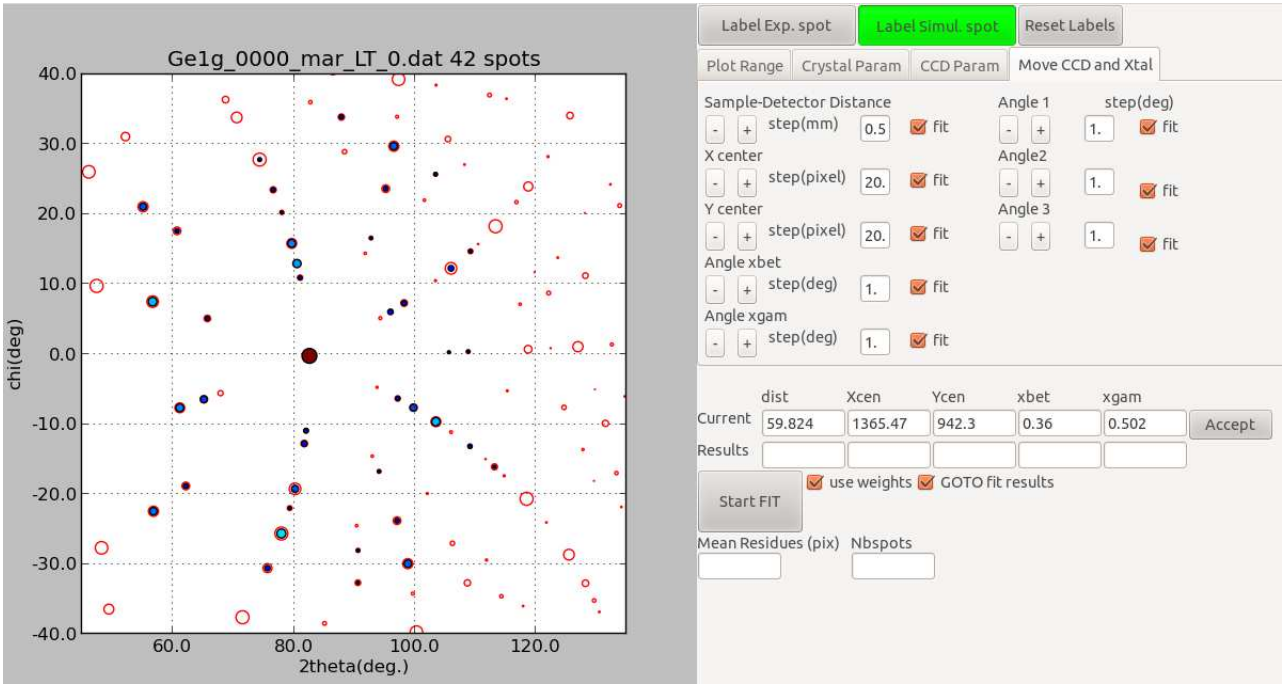

Figure 4.6: The panel of LaueTool to obtain the calibration parameters from diffraction image. The void circles represent the simulated spots, while the filled circles represent measured spots.

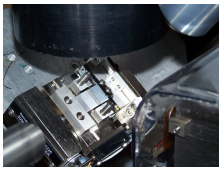

Figure 4.7: The embedment of FPB test into the beamline

For safety concerns, during experiment, when the beam entered the experimental hutch, people were not allowed to stay in the experimental hutch. The motion of experimental

Pixel size	Pixel array	Encoding range
$31 \times 31\,\mu\mathrm{m}^2$	4008×5344	12 bit

Table 4.2: Parameters of the VHR detector in our experiments

equipment was remotely controlled by SPEC, a software at ESRF. We used the DEBEN 300 N tensile machine (kindly lent by Damien Faurie of Lab LSPM) to perform FPB test by inserting four pins (see Fig. 4.9). As the FPB test proceeded, the four pins intermittently bent the sample (see Fig. 4.5, in which $L_\mathrm{r} = 8.5\,\mathrm{mm}$ and $L_\mathrm{l} = 3\,\mathrm{mm}$). During each interval of loading, we took diffraction images in the following sequence:

1. moved the sample so that the incident X-ray illuminated the Ge crystal glued on the sample to obtain the calibration parameters.

2. translated the sample to scan the middle line of the sample (the yellow line along the x-axis in Fig. 4.9) while maintaining the calibration parameters, and obtaining a sequence of images.

Figure 4.8: VHR CCD detector [VHR]

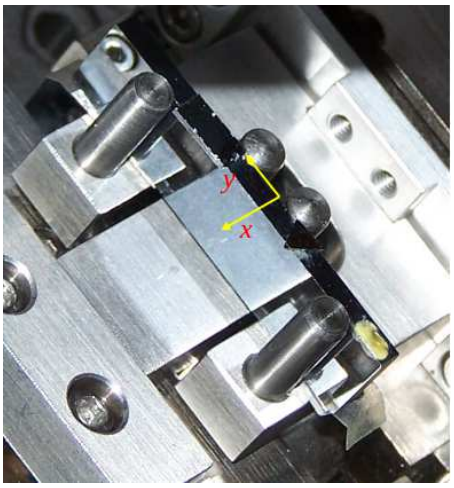

Figure 4.9: The *in situ* test carried out in BM32, ESRF

4.3 References for Results of Data Treatment

4.3.1 Analytical Solution of Elastic material

For Si and Ge, which deform elastically, the analytical solution [Rand and Rovenski 2005] of stress distribution in the central line of the beam under FPB test is independent from the sample's orientation and elastic constants if the sample is homogeneous:

$$\begin{cases} \sigma_{yy} = \dfrac{FL_{\mathrm{r}}}{2I_z}(x - \dfrac{X}{2}), \\ \sigma_{xx} = \sigma_{zz} = 0, \\ \tau_{xy} = \tau_{yz} = \tau_{zx} = 0, \end{cases} \tag{4.1}$$

where F and L_{r} are defined in Fig. 4.5, X is the sample size in x-axis of sample coordinate system (see Fig. 4.9 for the definition of x-axis), and I_y is the moment of inertia of the y-cross section defined as

$$I_y = \frac{ZX^3}{12},$$

where Z is the sample size in the direction parallel to pins. From the given analytical solution, we can conclude that the maximum normal stress will be attained at X edges and in y direction:

$$\max \sigma_{yy} = \frac{FL_{\mathrm{r}}X}{4I_z}. \tag{4.2}$$

For its deviatoric components, the analytic solution should be:

$$\begin{cases} \sigma'_{yy} = \dfrac{FL_{\mathrm{r}}}{3I_z}(x - \dfrac{X}{2}), \\ \sigma'_{xx} = \sigma'_{zz} = -\dfrac{FL_{\mathrm{r}}}{6I_z}(x - \dfrac{X}{2}), \\ \tau_{xy} = \tau_{yz} = \tau_{zx} = 0, \end{cases} \tag{4.3}$$

With the equation above, we can calculate a reference solution for the measurements. But in reality, due to the inaccuracy of force sensor, the calculated reference solution may not exactly match the true stress distribution. Here, given the linearity of stress distribution, we would rather apply linear regression to measured values to calculate a reference solution.

Although the stress profile is independent from material's elastic constants for a given prescribed moment and perfect geometry assumed, here we give the elastic constants of Si and Ge in Tab. 4.3 [Teodosiu 1982] because they relate elastic strain to stress.

	C_{11}/GPa	C_{12}/GPa	C_{44}/GPa
Si	165.8	63.9	79.6
Ge	128.5	48.3	66.8

Table 4.3: Elastic constants of Si and Ge

C_{11}, C_{12}, and C_{44} are defined in Eqn. 4.4, where σ and ε represent stress and elastic strain respectively, and the superscript $^{\mathrm{lattice}}$ represent component expressed in lattice coordinate system.

$$\begin{bmatrix} \sigma_{xx}^{\mathrm{lattice}} \\ \sigma_{yy}^{\mathrm{lattice}} \\ \sigma_{zz}^{\mathrm{lattice}} \\ \sigma_{yz}^{\mathrm{lattice}} \\ \sigma_{zx}^{\mathrm{lattice}} \\ \sigma_{yz}^{\mathrm{lattice}} \end{bmatrix} \doteq \begin{bmatrix} C_{11} & C_{12} & C_{12} & & & \\ C_{12} & C_{11} & C_{12} & & & \\ C_{12} & C_{12} & C_{11} & & & \\ & & & C_{44} & & \\ & & & & C_{44} & \\ & & & & & C_{44} \end{bmatrix} \begin{bmatrix} \varepsilon_{xx}^{\mathrm{lattice}} \\ \varepsilon_{yy}^{\mathrm{lattice}} \\ \varepsilon_{zz}^{\mathrm{lattice}} \\ 2\varepsilon_{yz}^{\mathrm{lattice}} \\ 2\varepsilon_{zx}^{\mathrm{lattice}} \\ 2\varepsilon_{yz}^{\mathrm{lattice}} \end{bmatrix} \tag{4.4}$$

It is obvious that the elastic constants of Si and Ge satisfy Eqn. 1.35. Therefore it is safe to calculate the deviatoric stress with merely deviatoric strain by Eqn. 1.36.

4.3.2 FEM Model for Elastoplastic Material

Because 316 stainless steel sample is an elastoplastic material, it is difficult to obtain the analytical solutions of stress distribution, therefore we use FEM simulation to provide references to measurements. The FEM simulation was performed by ABAQUS (see Fig. 4.10), we used the element C3D20 (second order full integration element), and we densified the mesh near the contacts between pins and beam to better handle the contact between the pins and sample. Due to the symmetrical nature of the FEM model, it is possible to model only one quarter of the sample while imposing boundary condition of symmetry to the symmetrical face. The pins were modeled as analytical rigid bodies. We used a simplified Johnson-Cook law to model the hardening of 316 stainless steel, in which the influences of temperature and strain rate are ignored:

$$\sigma_{\mathrm{Y}} = A + B\bar{\varepsilon}_{\mathrm{p}}^{n} \tag{4.5}$$

where σ_{Y} represents the yield stress, $\bar{\varepsilon}_{\mathrm{p}}$ represents the equivalent effective plastic strain, and A, B, n are material parameters. These parameters and elastic parameters are tabulated in Tab. 4.4 [Palengat et al. 2013].

Young's modulus (GPa)	Poisson's ratio	A (MPa)	B (MPa)	n
192	0.3	242	1295	0.61

Table 4.4: Parameters of 316 stainless steel

4.4 Image Treatment

After each scan, we obtained a series of diffraction images corresponding to different positions on the scanning line. We performed DIC to these images in two sequences adapting to original Laue-DIC and enhanced Laue-DIC. For original Laue-DIC, the sequence goes as below:

1. Obtain the calibration parameters from the diffraction image of Ge crystal.
2. Index and obtain the lattice parameters from the diffraction image taken at the center of the scanning line with standard Laue treatment.

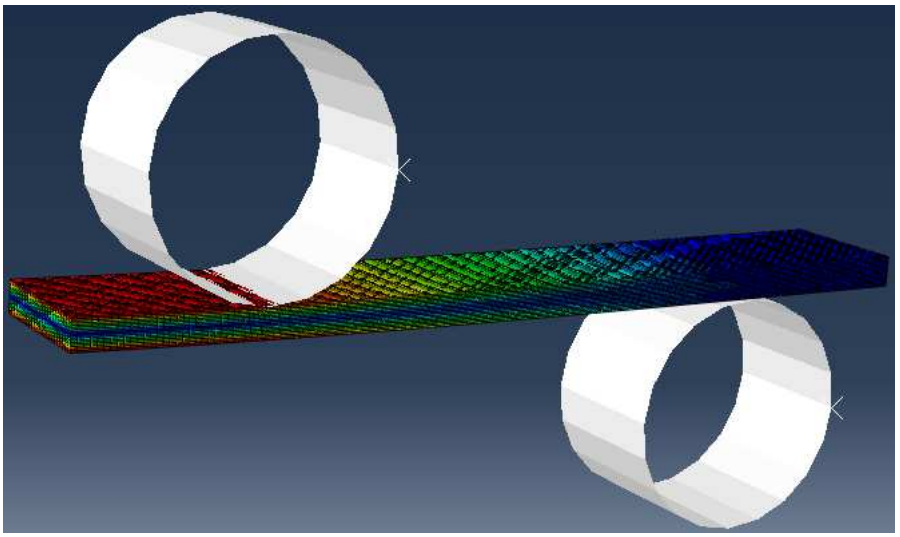

Figure 4.10: FEM model of ABAQUS, only one quarter of the sample was modeled thanks to the symmetry of model

3. Use DIC to obtain the displacements of spots between the image taken at the neutral fiber and all the other images (see Fig. 4.11).

4. Calculate the relative deformation gradient according to the procedure described in §2.2.2.

The sequence for enhanced Laue-DIC goes as below:

1. Obtain the calibration parameters as in original Laue-DIC.

2. Index and obtain the lattice parameters from the diffraction images taken at the scanning line either by standard Laue treatment, or original Laue-DIC.

3. Subdivide the diffraction images into several pairs. Use DIC to obtain the displacements of spots between images in the same pair. Fig. 4.12 gives several possible organizations of pairs, and here we use the first one: grouping two adjacent illumination sites (separated by about 0.01 mm) into one pair because (i) the spots collected from the two adjacent illumination sites usually coincide most in terms of spots' indexes; and (ii) two spots with the same index usually hold the largest resemblance if they come from two adjacent sites.

4. Refine the lattice parameters and calibration parameters using the displacements obtained in step 3 as input, and calibration parameters obtained in step 1 and lattice parameters obtained in step 2 as initial guess (see Fig. 3.1).

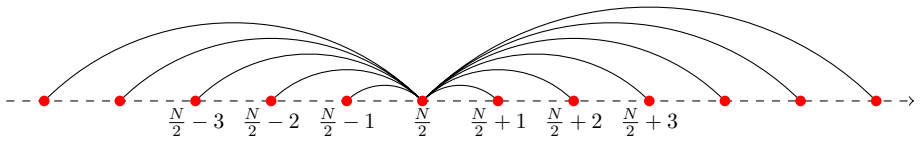

Figure 4.11: Correlation pairs of original Laue-DIC. N is the total number of illumination sites, and assumed even.

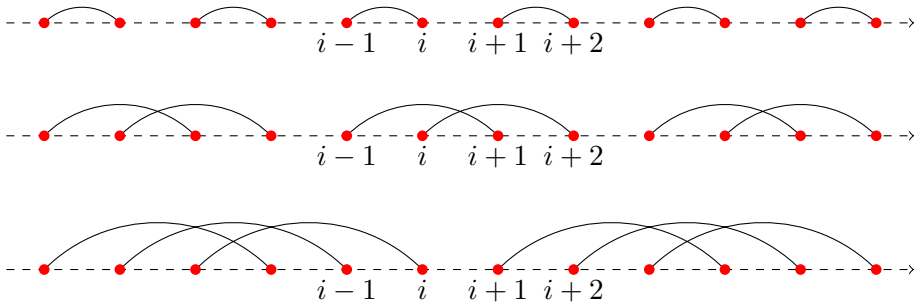

Figure 4.12: Correlation pairs of enhanced Laue-DIC

The DIC software we adopted here was CMV, as in §2.5.1.2. For the two images in the same pair, spots with the same index bore resemblance after the displacement, and these resemblances could be validated by the values of correlation coefficients, because correlation coefficient was a quantification of resemblance as shown in Eqn. 2.1. In the image correlations done in §4.5, the correlation coefficients are of the order of $10^{-3} \sim 10^{-2}$.

Fortunately, for pure crystals that we dealt with, there was few dislocations, and for metals, the loading was within the elastic range and spots' shape evolved little. Therefore the error arising from mismatch of shape function [Schreier and Sutton 2002] could be ignored even if we used zero order polynomial shape function associated with rigid 2D translation. The main source of DIC error that we encountered was the "ultimate error" [Amiot et al. 2013] which has been characterized in §2.5.1. The interpolation of gray level (see §2.2.1) that we chose was biquintic interpolation.

The size of correlation window (see §2.2.1) is an important issue affecting displace-

ment measurement. The information that DIC utilizes is the contrast of gray level within the correlation window. For ordinary DIC treatment (using DIC to analyze displacement/deformation of object's surface), if there were no mismatch of shape function, larger correlation window usually would mean more contrast was incorporated into the window, hence less random error. However, in treating Laue spots, the contrast of gray level would drop dramatically if the pixel were located in the background region of diffraction image. These pixel would introduce little information but noise into correlation window, increasing the random error. Therefore, DIC user should adapt the window closely to the spot's shape. We used the same algorithm demonstrated in Fig. 2.10 to determine the correlation window adapted to spot's shape.

In minimizing the cost function Eqn. 3.6, we need to assign weight to each spot. Here, we designated each spot the weight:

$$W_x^{hkl} = W_y^{hkl} = 1 - C^{hkl},$$

where C^{hkl} is the correlation coefficient of the spot with index (hkl) defined in Eqn. 2.1. Higher resemblance between spots usually means more credibility in the measurement of displacements. Other possible weight function could have been defined with respect to the peak's amplitude (for example, Fig. 2.31 and 2.32 show that peak with higher amplitude gives lower systematic and random errors.), but this has not been attempted yet.

We will present in the following section the results of image treatment of the specimens by standard Laue treatment, original Laue-DIC, and enhanced Laue-DIC, and comment on them.

4.5 Results of Image Treatment

4.5.1 Si samples

We first talk about the sample I. We scanned the sample at three different loadings: 3.92 N, 46.76 N, 88.57 N, and 199.43 N, and the corresponding maximum σ_{yy} are 2.14 MPa, 25.55 MPa, 48.39 MPa, and 108.95 MPa according to Eqn. 4.2. The number of spots considered in these analysis is $\sim$ 35. The approximate values of calibration parameters during these scanning was tabulated in Tab. 4.5.

d/mm	x_c/pix	y_c/pix	$\beta/^\circ$	$\gamma/^\circ$
59.8	1365.4	945.4	0.38	0.50

Table 4.5: Approximate calibration parameters when Si sample I was scanned.

The treatments of images of scanning sequence at the loading of 199.43 N by standard Laue treatment, original Laue-DIC, and enhanced Laue-DIC, are given in Fig. 4.13. We can see that the stress profiles by standard Laue treatment appear very noisy, specially for the shear components, while those by original and enhanced Laue-DIC exhibit much less fluctuation.

A more quantitative comparison lies in calculating the root mean square (RMS) of discrepancy between the measured values and the theoretical values, i.e. a linear fit:

$$\mathrm{RMS} = \sqrt{\frac{\sum_n (\sigma_{(i)}^{\mathrm{meas}} - \sigma_{(i)}^{\mathrm{theo}})^2}{n}}.$$

	σ'_x	σ'_y	σ'_z	τ_{yz}	τ_{zx}	τ_{xy}
Standard Method	3.22	2.02	2.67	13.71	9.79	11.82
Original Laue-DIC	1.83	1.19	1.30	8.74	4.54	4.78
Enhanced Laue-DIC	2.12	1.85	2.21	8.97	4.76	5.00

Table 4.6: RMSs of discrepancies of different components when Si sample I is bent at 199.43 N (unit: MPa)

We tabulated the RMS of different component in Tab. 4.6, and we found that both original and enhanced Laue-DIC had significantly reduce the RMS. However, the RMS of discrepancies by enhanced Laue-DIC is slightly higher than by original Laue-DIC. Aside from the loading of 199.43 N, we have also bent the sample at the loading of 88.57 N, 46.76 N, and 3.92 N while trying to maintain the same calibration parameters. Here for the sake of brevity, we only plotted their σ'_y components by the three methods in Fig. 4.14. We also tabulated the RMS of discrepancies at the loadings of 88.57 N and 46.76 N in Tab. 4.7 and 4.8, and found that the contrary to the case at the loading of 199.43 N, at the loading of 88.57 N and 46.76 N, the RMSs of discrepancies by enhanced Laue-DIC were slightly lower than those by original Laue-DIC. Moreover, we found that the RMSs of discrepancies in the shear components were larger than those in normal components of

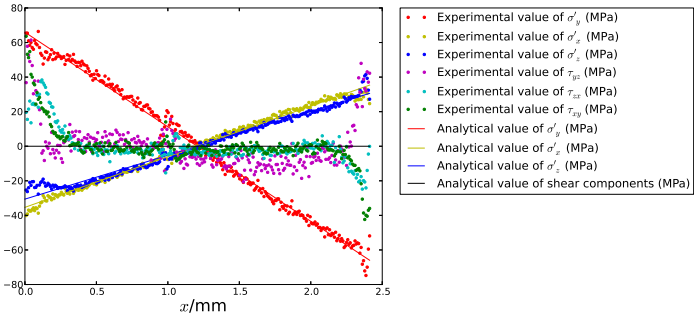

(a) Standard Laue treatment

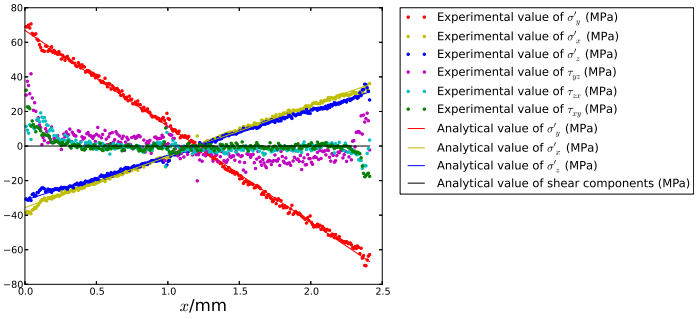

(b) Original Laue-DIC

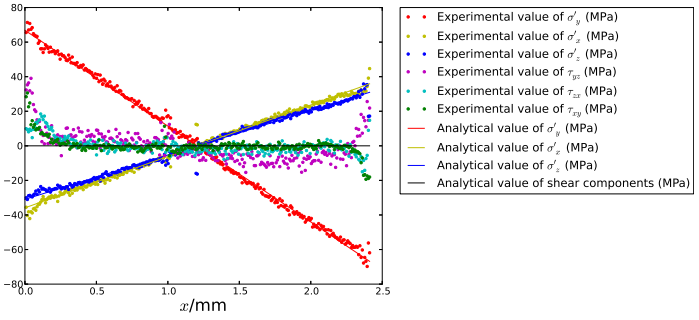

(c) Enhanced Laue-DIC

Figure 4.13: Stress profile of Si sample I at the loading of 199.43 N.

stress for all image sequences investigated.

	σ'_x	σ'_y	σ'_z	τ_{yz}	τ_{zx}	τ_{xy}
Standard Method	6.50	4.02	3.13	20.61	9.74	9.00
Original Laue-DIC	4.53	2.45	2.36	7.63	5.78	3.66
Enhanced Laue-DIC	3.94	2.13	2.21	7.66	5.41	3.59

Table 4.7: RMSs of discrepancies of different components when Si sample I is bent at 88.57 N (unit: MPa)

	σ'_x	σ'_y	σ'_z	τ_{yz}	τ_{zx}	τ_{xy}
Standard Method	5.42	3.20	2.58	17.09	11.16	10.63
Original Laue-DIC	3.29	1.95	1.53	6.40	6.58	3.86
Enhanced Laue-DIC	3.07	1.80	1.40	5.83	6.18	3.74

Table 4.8: RMSs of discrepancies of different components when Si sample I is bent at 46.76 N (unit: MPa)

To investigate the influence of orientation upon the stress profile, we treated the images of scanning sequence of Si sample II by standard Laue treatment, original Laue-DIC, and enhanced Laue-DIC, but only plotted the results of enhanced Laue-DIC in Fig. 4.15 for the sake of brevity. The sample was bent at the loading of 200.26 N and we tried to maintain the calibration parameters as in Si sample I. As we compare Fig. 4.15 with Fig. 4.13c, we found that the stress profiles were almost identical, and this has corroborated the statement of [Rand and Rovenski 2005] that the stress profiles are independent from sample's orientation when a homogeneous anisotropic material is bent.

For Si sample III, we have only scanned at the loading of 200.56 N, but at three different detector-sample distances, 59.84 mm, 101.73 mm, and 143.75 mm. At a higher distance, we will have a better resolution of individual spots, and hence better precision on spots' displacement. However, we will collect less spots on the detector, decreasing the coverage of pole figure. At the distance of 59.84 mm, $\sim$ 35 spots were considered, at the distance of 101.73 mm, $\sim$ 18 spots were considered, and at the distance of 143.75 mm, $\sim$ 9 spots were considered. For the distance of 59.84 mm and 101.73 mm, we treated the images with standard Laue treatment, original Laue-DIC, and enhanced Laue-DIC, and plotted the results in Fig. 4.16 and 4.17 respectively, while for the distance of 143.75 mm, we only

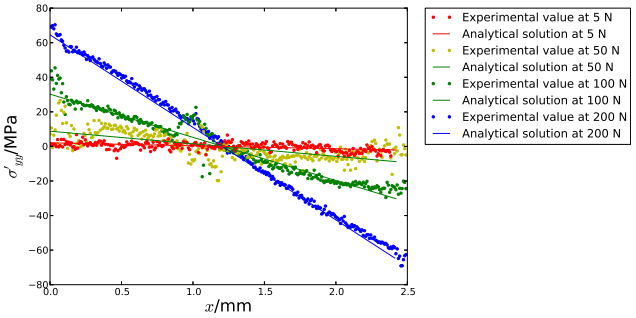

(a) Standard Laue treatment

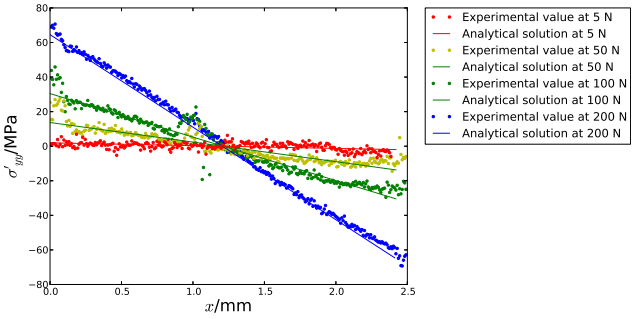

(b) Original Laue-DIC

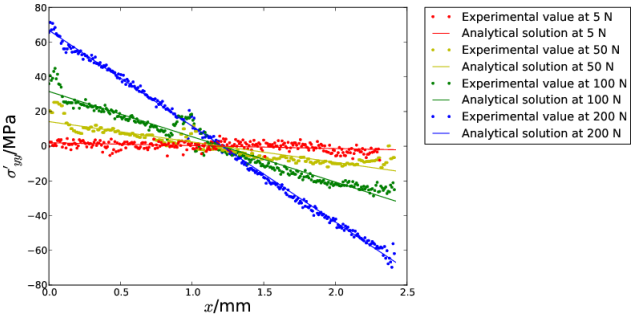

(c) Enhanced Laue-DIC

Figure 4.14: σ'_y component by different methods.

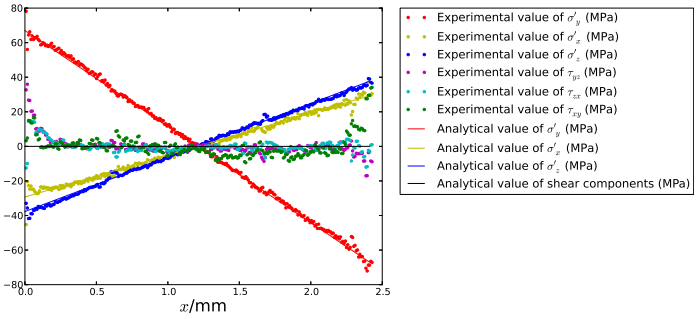

Figure 4.15: Stress profile of Si sample II at the loading of 200.26 N, treated by enhanced Laue-DIC.

treated the images with standard Laue treatment and original Laue-DIC, since enhanced Laue-DIC required no less than 12 spots considered, and we plotted the results in Fig. 4.18. It is obvious from visual impression that as we raise up the detector, the measured stress profiles by all methods become more and more fluctuated, that is to say, higher resolution for individual spot cannot compensate for the decrease of the number of spots considered.

Another important aspect of enhanced Laue-DIC is that it allows for the calculation of calibration parameters as well. We can also characterize the perturbation of calibration parameters in the course of scanning, and we use the superscript $^{\mathrm{cal}}$ to present the calculated calibration parameters. As we have mentioned in §4.2.3, we carefully glued a piece of Ge monocrystal on the sample to determine the calibration parameters of the experiment, say nominal calibration parameters, and use the superscript $^{\mathrm{nom}}$ to present them. The perturbations of calibration parameters are characterized by two terms: (i) mean deviation of calculated parameter from nominal one, i.e. $\overline{\epsilon}_x = |\overline{x}^{\mathrm{cal}} - x^{\mathrm{nom}}|$; (ii) standard deviation of calculated parameter, i.e. σ_x, where $x \in \{d, \Delta x_{\mathrm{c}}, \Delta y_{\mathrm{c}}, \beta, \gamma\}$. Note that $\Delta x_{\mathrm{c}}^{\mathrm{nom}}$ and $\Delta y_{\mathrm{c}}^{\mathrm{nom}}$ are supposed to be zero because the nominal $x_{\mathrm{c}}^{\mathrm{nom}}$ and $y_{\mathrm{c}}^{\mathrm{nom}}$ are assumed to be kept constant for all images in a series of scanning, therefore the their nominal increments from one configuration to another should be zero.

Here, we tabulated the $\overline{\epsilon}_x$ and σ_x of scanning Si sample I at the loading of 199.43 N in Tab. 4.9, corresponding to the stress profiles in Fig. 4.13, and those of other scanning are of similar values.

$\overline{\epsilon}_d$/mm	$\overline{\epsilon}_{\Delta x_{\mathrm{c}}}$/pix	$\overline{\epsilon}_{\Delta y_{\mathrm{c}}}$/pix	$\overline{\epsilon}_\beta/^\circ$	$\overline{\epsilon}_\gamma/^\circ$
2.8×10^{-3}	1.3×10^{-3}	4.6×10^{-3}	7.7×10^{-4}	2.6×10^{-3}
σ_d/mm	$\sigma_{\Delta x_{\mathrm{c}}}$/pix	$\sigma_{\Delta y_{\mathrm{c}}}$/pix	$\sigma_\beta/^\circ$	$\sigma_\gamma/^\circ$
4.9×10^{-3}	9.1×10^{-3}	1.5×10^{-3}	3.3×10^{-4}	4.2×10^{-3}

Table 4.9: The perturbation of calibration parameters in scanning Si sample I at the loading of 199.43 N

Comment From the figures and tables we listed above, we can draw several conclusions:

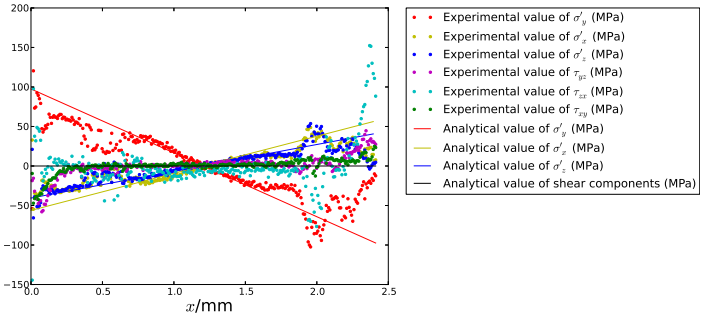

(a) Standard Laue treatment

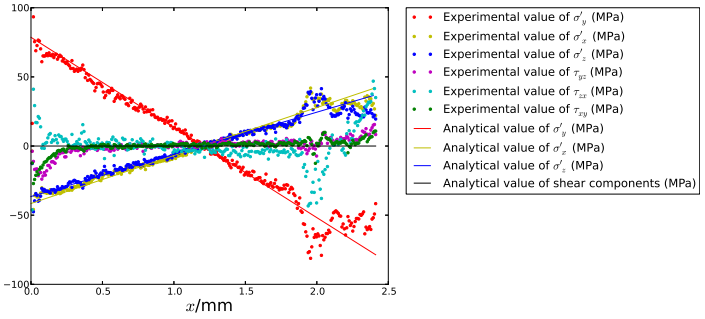

(b) Original Laue-DIC

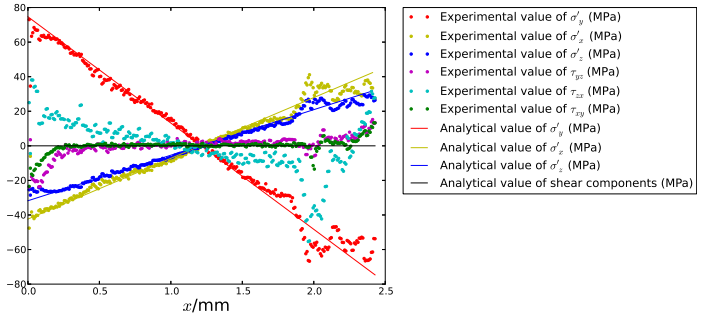

(c) Enhanced Laue-DIC

Figure 4.16: Stress profile of Si sample III at the distance of 59.84 mm.

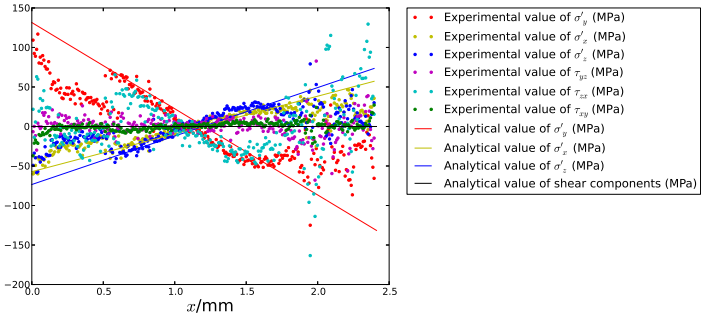

(a) Standard Laue treatment

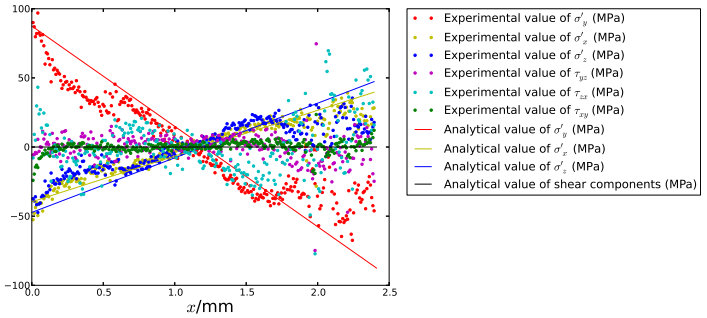

(b) Original Laue-DIC

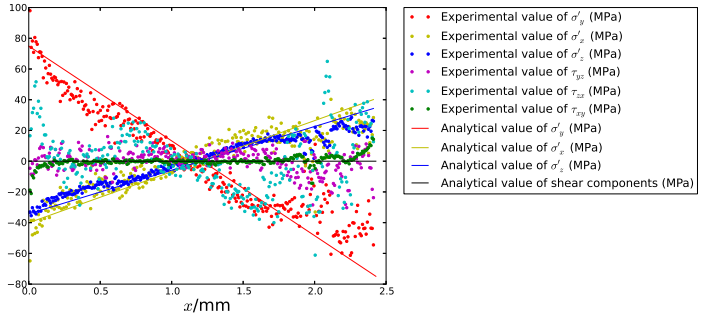

(c) Enhanced Laue-DIC

Figure 4.17: Stress profile of Si sample III at the distance of 101.73 mm.

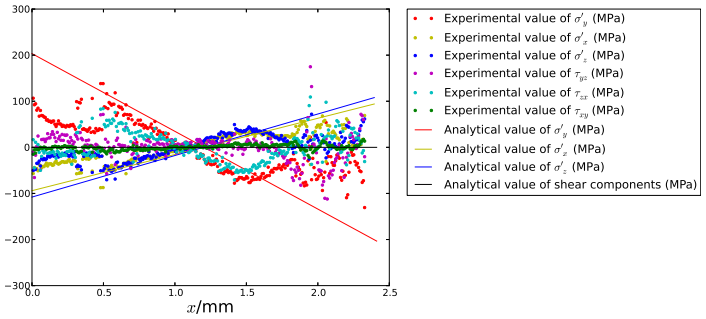

(a) Standard Laue treatment

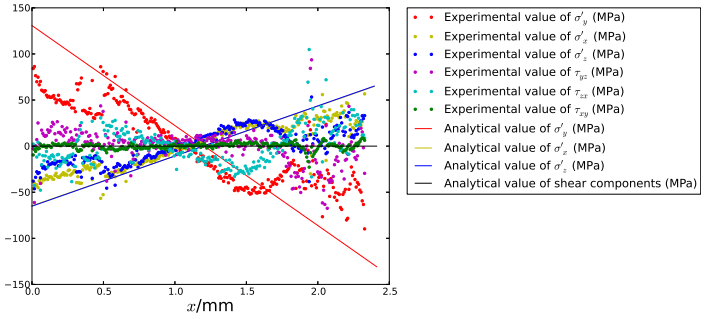

(b) Original Laue-DIC

Figure 4.18: Stress profile of Si sample III at the distance of 143.75 mm.

- Compared to the results of standard Laue treatment, both original and enhanced Laue-DIC can substantially reduce the fluctuation of profiles.

- At the loading level of 200 N, the RMS of discrepancies of enhanced Laue-DIC are slightly larger than those of original Laue-DIC, while at the loading level of 50 N and 100 N, the RMS of discrepancies of enhanced Laue-DIC were slightly lower than those of original Laue-DIC.

- Shear components of deviatoric stress exhibits more fluctuations than normal components.

- Though raising up a detector could increase the resolution of individual spot, this usually came at the cost of reducing the number of spots considered, and the cost outweighs the benefit.

- Comparing the uncertainties of calibration parameters listed in Tab. 4.9 with Tab. 2.4 which gives the uncertainties estimated by Poshadel et al. [2012], we find that we

have much better control over the perturbation of the experimental setup than the experiment of Poshadel.

4.5.2 Ge sample

We applied two loadings on the sample, 99.69 N and 140.35 N, and the corresponding maximum σ_{yy} are 54.5 MPa and 76.7 MPa respectively. For each loading, we scanned the central line at three different detector-sample distances: 59.83 mm, 101.97 mm, and 143.77 mm, and we collected ~ 40 spots, ~ 20 spots, and ~ 10 spots respectively. We plotted the stress profiles at the loading of 140.35 N with a detector-sample distance 59.83 mm in Fig. 4.19. A visual impression about Fig. 4.19 was that there was no significant distinction among the stress profiles by the three methods. We tabulated their RMSs of discrepancies in Tab. 4.10, and we also found quantitatively that the distinctions among the results by the three methods were very small. A possible explanation is that the Laue spots of Ge is more elliptically shaped thanks to the shallower penetration depth compared to Si, for example, Fig. 4.20 demonstrated two spots diffracted from Ge, and they appeared more elliptically shaped than those diffracted from Si in Fig. 2.2.

	σ'_x	σ'_y	σ'_z	τ_{yz}	τ_{zx}	τ_{xy}
Standard Method	1.72	2.01	0.88	3.56	1.97	3.11
Original Laue-DIC	1.95	2.25	1.05	3.80	1.76	3.21
Enhanced Laue-DIC	1.23	1.92	1.39	3.98	1.64	3.32

Table 4.10: RMSs of discrepancies of different components when Ge sample is bent at 140.35 N with a distance of 59.83 mm (unit: MPa).

Given the similarities of the results by the three methods, we will only plot the results by enhanced Laue-DIC for distance of 59.83 mm, 101.97 mm, and the results by original Laue-DIC for distance of 143.77 mm due to the scarcity of spots at such distance. We plotted the stress profiles at the loading of 140.35 N in Fig. 4.21, and stress profiles at the loading of 99.69 N in Fig. 4.22. It is obvious from the visual impressions of these figures that the stress profiles become more noised when the detector is elevated. However, the τ_{yz} component of Fig. 4.21b seems abnormally tilted, and we are unclear about such abnormality.

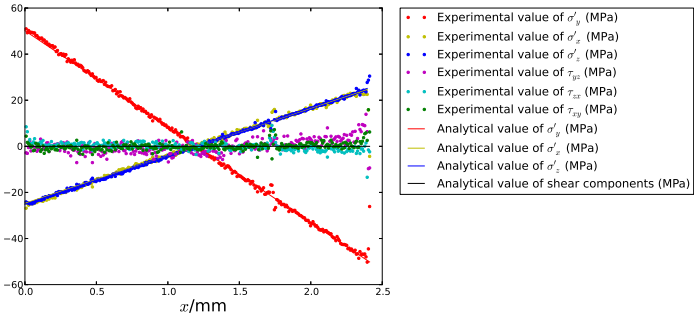

(a) Standard Laue treatment

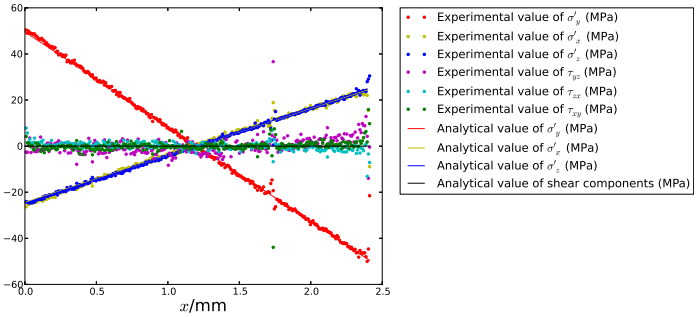

(b) Original Laue-DIC

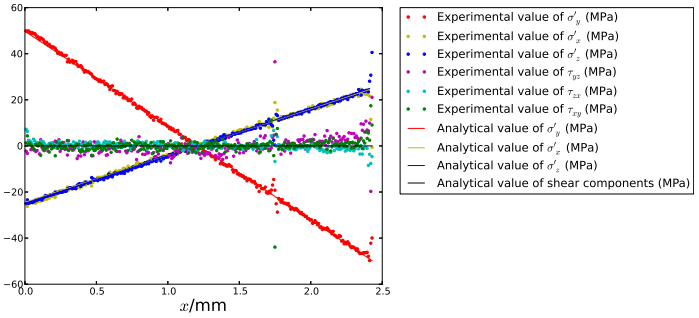

(c) Enhanced Laue-DIC

Figure 4.19: Stress profile of Ge sample at the loading of 140.35 N with distance 59.83 mm.

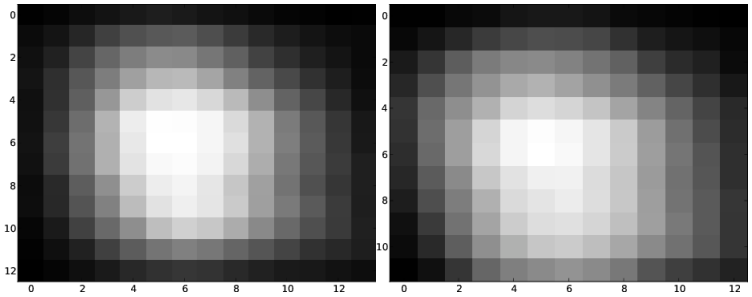

Figure 4.20: Spots in diffraction image of Ge.

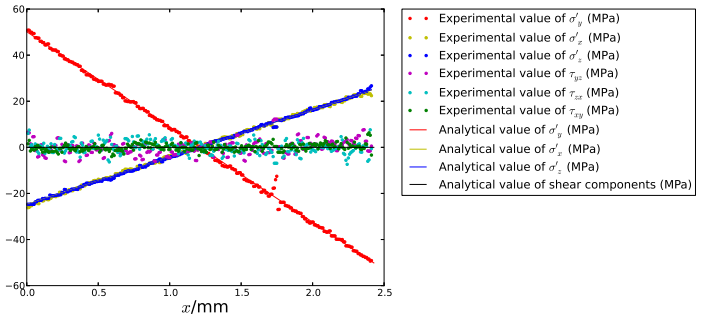

(a) At the distance 101.97 mm, by enhanced Laue-DIC

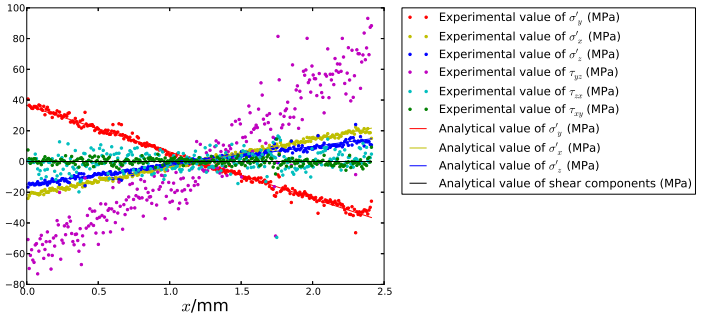

(b) At the distance 143.77 mm, by original Laue-DIC

Figure 4.21: Stress profile of Ge sample at the loading of 140.35 N with distance 101.97 mm and 143.77 mm.

Comment We can draw several conclusions from figures and tables above:

- Standard Laue treatment, original Laue-DIC, and enhanced Laue-DIC give very similar stress profile. This is because the Laue spots of Ge sample have more elliptical shapes than those of Si samples so that analytical fitting of spots can give reasonable estimation of diffraction peaks.

- The stress profile taken at a higher detector-sample distance invariably exhibits more fluctuation as in the case of Si sample.

- For stress profiles at the loading of 140.35 N taken at 143.77 mm (see Fig. 4.21b), we observed that the profile of stress components seemed deviating from analytical profile, especially for the τ_{yz} component, which was supposed to be zero. The reason for this abnormality is not known so far.

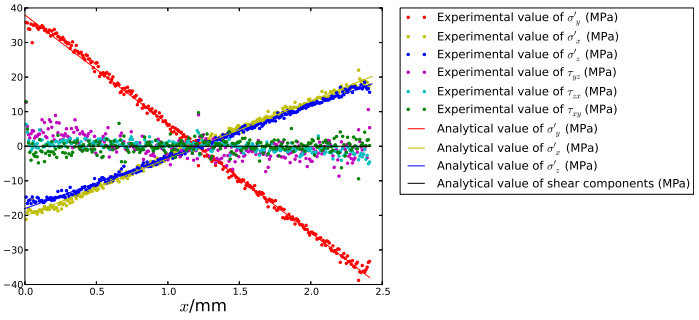

(a) At the distance 59.83 mm, by enhanced Laue-DIC

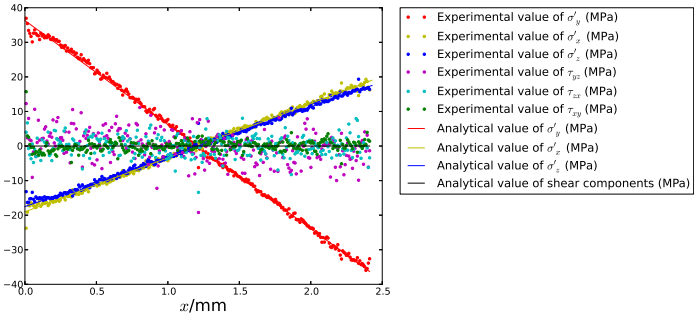

(b) At the distance 101.97 mm, by enhanced Laue-DIC

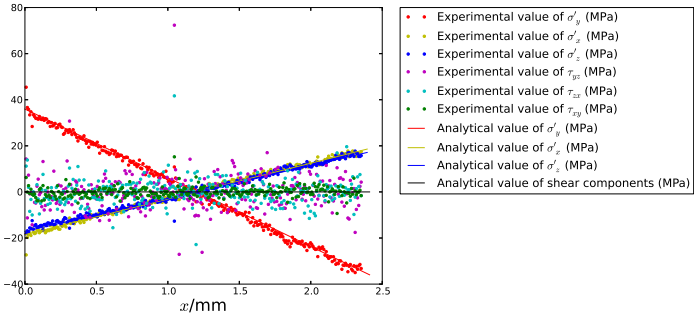

(c) At the distance 143.77 mm, by original Laue-DIC

Figure 4.22: Stress profile of Ge sample at the loading of 99.69 N.

4.5.3 316L sample

We examined the stress distribution at the load of 1.00 N, 2.01 N, 3.00 N, 4.01 N, 4.98 N, 5.99 N, 6.50 N with a detector-sample distance of 59.80 mm, and for the load of 3.00 N, we scanned the central line with an additional very short detector-sample distances: 38.83 mm. For the images taken at the distance 59.80 mm, the number of spots considered is ~ 15, and for the images taken at the distance 38.83 mm, the number of spots considered is ~ 25.

In Fig. 4.23, we plotted the results by the three methods at the loading of 3.00 N and the distance 38.83 mm, and in Fig. 4.24, we plotted the results by the three methods at the loading of 3.00 N and the distance 59.80 mm. Again, from visual impression, we found that the stress profiles taken at the distance 38.83 mm exhibited less fluctuations than those taken at the distance 59.80 mm. We also found that the results of the three methods gave similar results as in §4.5.2, and if we compared the shapes of spots diffracted from 316L (see Fig. 4.25) with those diffracted from Si sample (see Fig. 2.2), it was obvious that the spots diffracted from 316L sample were more elliptically shaped than those from Si sample, therefore the introduction of DIC would not improve significantly. Perhaps, if we further loaded the sample, the misorientation within it would become more pronounced and spots would become streaked or even splitted, as indicated in [Hofmann 2011].

Given the similarities of the results by the three methods, we will only plot the results by enhanced Laue-DIC for the rest of loading in Fig. 4.26, 4.27, 4.28, 4.29, 4.30, and 4.31, corresponding to the loading of 1.00 N, 2.01 N, 4.01 N, 4.98 N, 5.99 N, 6.50 N respectively. We can see that the sample begins to yield at the loading 4.01 N. As the loading was further applied incrementally, the τ_{zx} component gradually deviated from zero (see Fig. 4.29, 4.30, and 4.31). However, our FEM simulation failed to predict this phenomenon, and it might be due to the isotropic elasticity and plasticity that we assumed in the simulation (Tab. 4.4) which did not fit reality.

Comment For the figures above, we can draw several conclusions:

- At the loading of 3.00 N, we scanned the sample at the distance of 38.83 mm and 59.80 mm, and collected ~ 25 and ~ 15 spots respectively. And we have found that

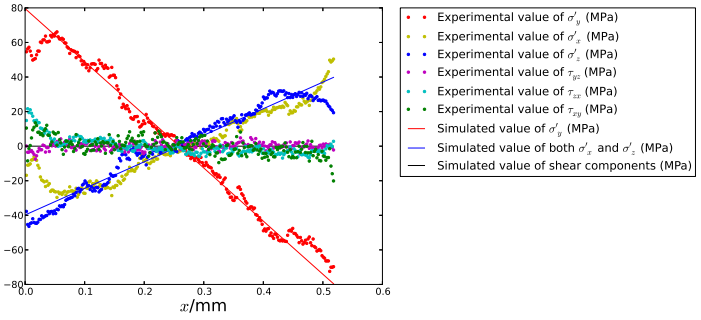

(a) Standard Laue treatment

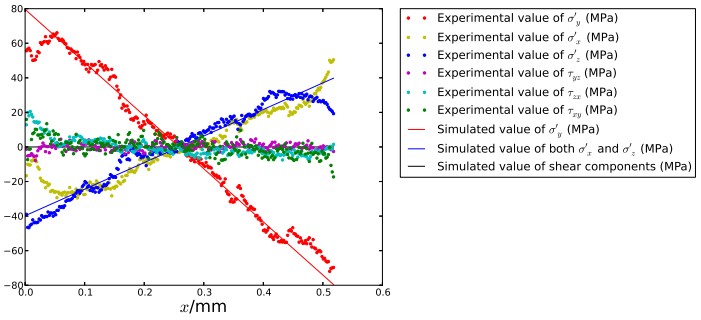

(b) Original Laue-DIC

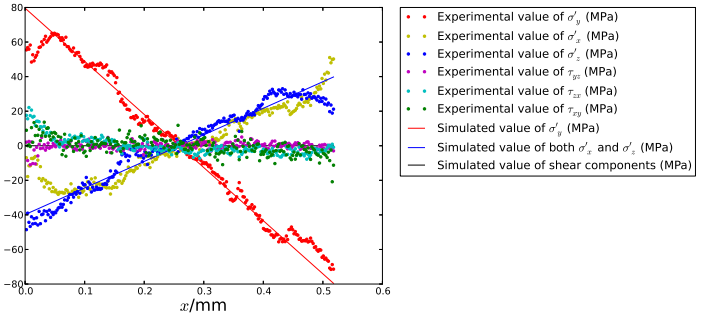

(c) Enhanced Laue-DIC

Figure 4.23: Stress profile of 316L sample at the loading of 3.00 N and the distance of 38.83 mm.

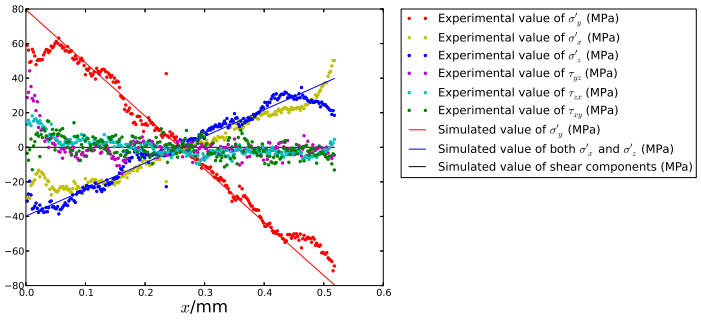

(a) Standard Laue treatment

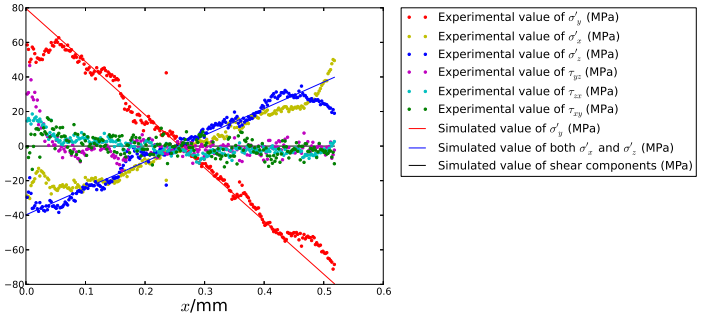

(b) Original Laue-DIC

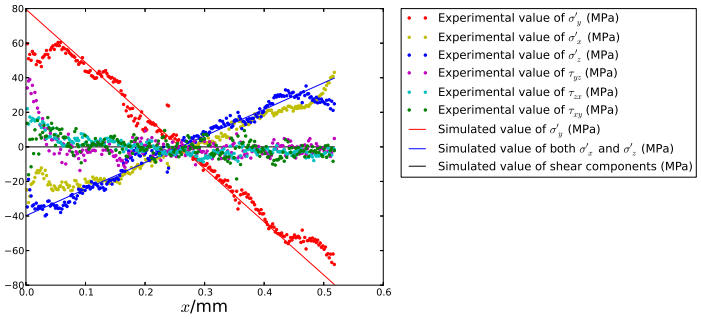

(c) Enhanced Laue-DIC

Figure 4.24: Stress profile of 316L sample at the loading of 3.00 N and the distance of 59.80 mm.

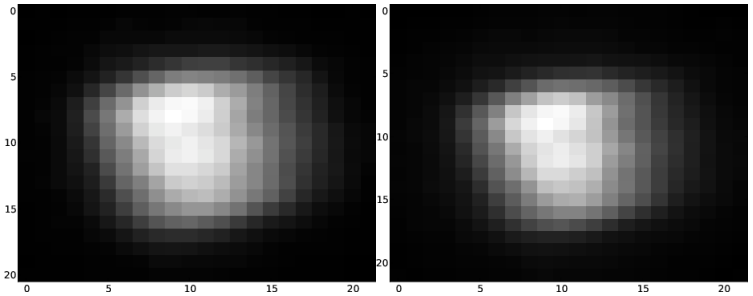

Figure 4.25: Spots in diffraction image of 316L.

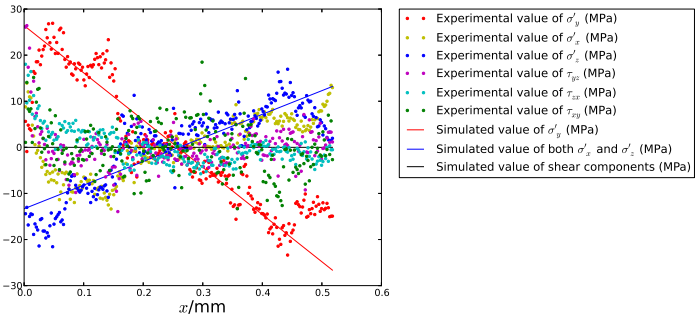

Figure 4.26: Stress profile of 316L sample at the loading of 1.00 N.

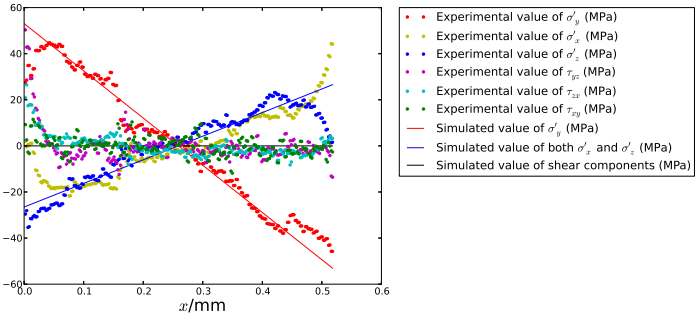

Figure 4.27: Stress profile of 316L sample at the loading of 2.01 N.

reducing the number of spots would increase the fluctuations of stress profiles.

- Standard Laue treatment, original Laue-DIC, and enhanced Laue-DIC give very similar stress profile. This is because the Laue spots of 316L sample have more elliptical shapes than those of Si samples so that analytical fitting of spots can give reasonable estimation of diffraction peaks as in the cases of Ge sample (§4.5.2).

- The yield occurred at the load of 4.01 N.

4.6 Error Analysis based on Numerical Tests

In last section, we observed that the calculated stress profiles were more or less fluctuated. In this section, we run the same numerical tests as in §2.5.2 and §3.3.1 to calculate the error bars of stress profiles and investigate whether the calculated error bar match the observed fluctuation of curve.

The error bar is calculated by the following procedure:

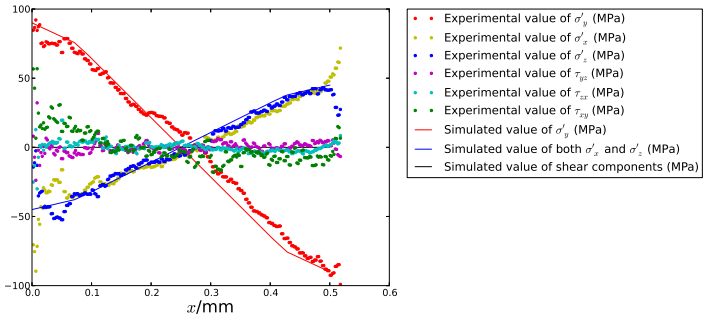

Figure 4.28: Stress profile of 316L sample at the loading of 4.01 N.

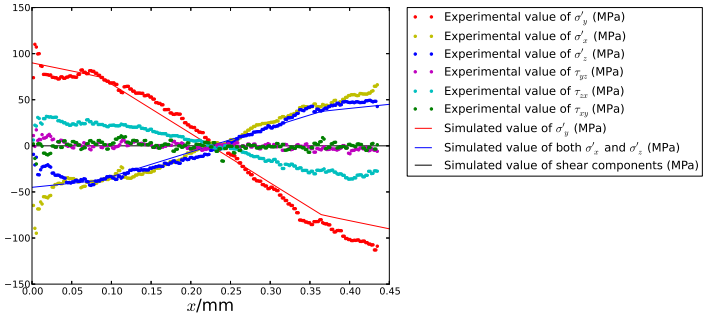

Figure 4.29: Stress profile of 316L sample at the loading of 4.98 N.

1. Fit each spot to get their parameters of Eqn. 2.18: A, r_X, r_Y, and θ.

2. For each spot, use those fitted parameters in the last step to fabricate an artificial spot, and perform statistical tests as in §2.5.1.4 to calculate the systematic and random error of the displacement of the spot. The imposed displacement for the spot is the one measured by DIC in real images, and the sample size of the statistical test is 100.

3. For all spots, add to their displacements measured by DIC from real image Gaussian noises, whose means and deviations are the corresponding systematic and random errors estimated from the last step, and perform statistical tests to calculate the fluctuation of deviatoric stress components, and hence the error bar. The sample size of the statistical tests is 100.

Of all the scanning sequence of elastic sample (Si and Ge) we have treated, we analyzed the error distribution of Si sample III at the loading of 200 N and at detector-sample distance of 101.73 mm and plotted the error bar in Fig. 4.32, because at such condition,

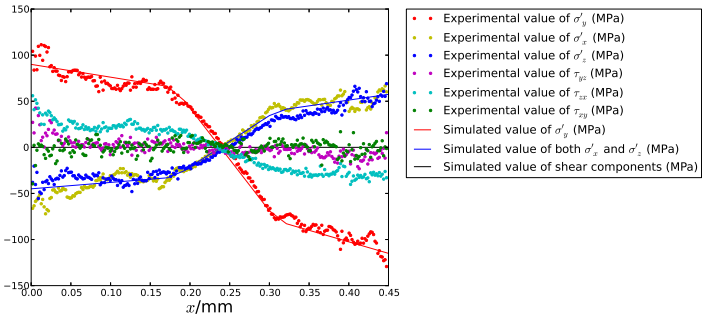

Figure 4.30: Stress profile of 316L sample at the loading of 5.99 N.

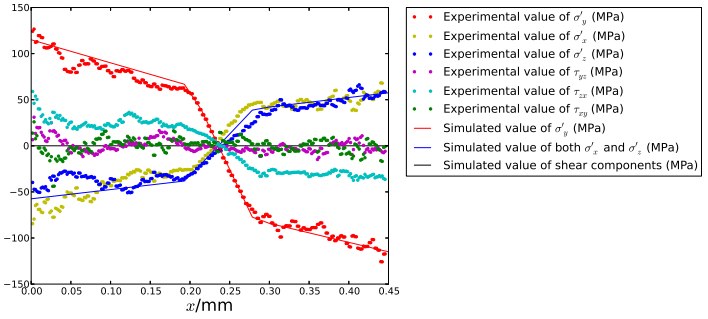

Figure 4.31: Stress profile of 316L sample at the loading of 6.50 N.

the stress profiles by both original and enhanced Laue-DIC (see Fig. 4.17b and 4.17c) exhibit the largest deviation from analytical results compared to other stress profiles. Of all the scanning sequence of elastoplastic sample (316L) we have treated, we analyzed the error distribution of 316L sample at the loading of 5 N and plotted the error bar in Fig. 4.33, because (i) at such condition, the stress profiles by both original and enhanced Laue-DIC (see Fig. 4.29) exhibit the largest deviation from simulated results compared to other stress profiles; (ii) compared to stress profiles at other loadings, the sample begins to deform plastically at the loading of 5 N.

In Fig. 4.32 and 4.33, we plotted the error bars at $\frac{1}{5}$, $\frac{2}{5}$, $\frac{3}{5}$, $\frac{4}{5}$ of the scanning distance, in which the numbers of spots considered are about $14 \sim 18$. From Fig. 4.32 and 4.33, we found that error bars calculated by the proposed procedure could well describe the fluctuations of stress profiles. Note that in Fig. 4.32b and 4.33b, two error bars are presented at each location, this is because that enhanced Laue-DIC calculates the stresses of two configurations.

To gain a more quantitative impression about the fluctuations of each components of

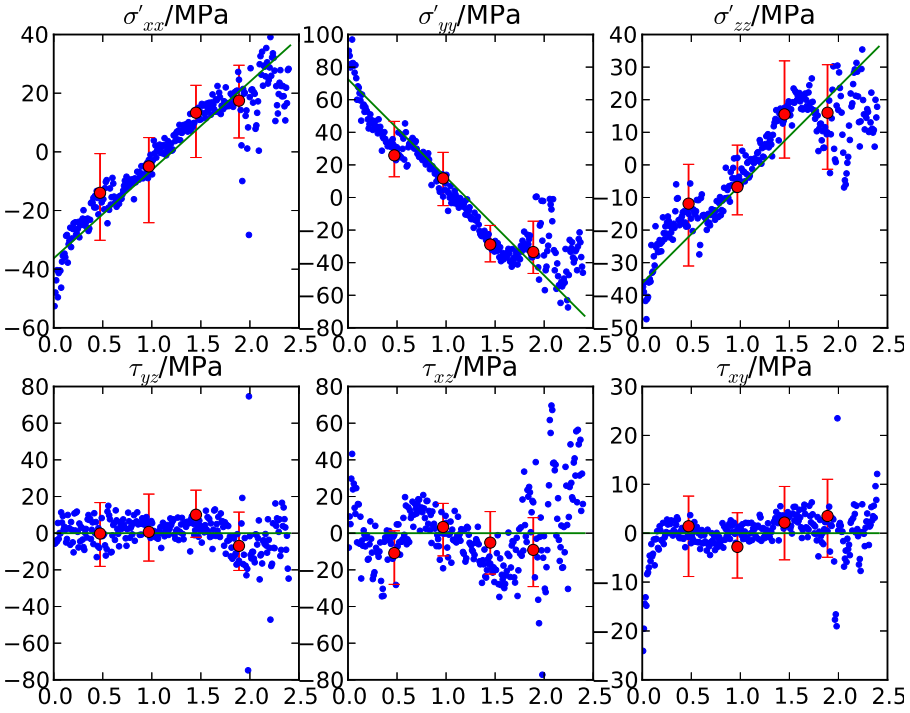

(a) Error bar of original Laue-DIC

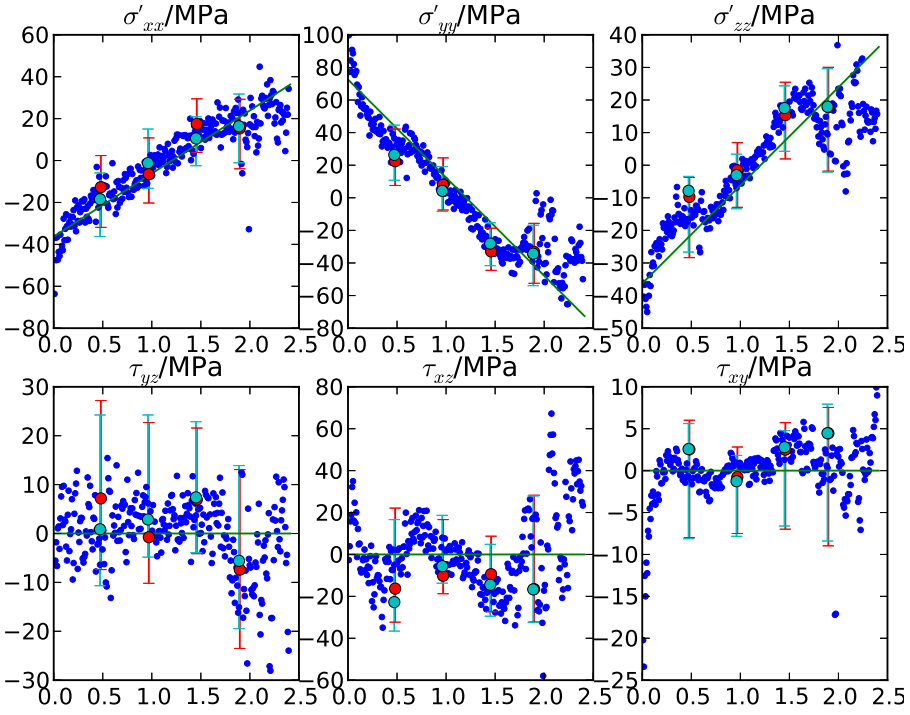

(b) Error bar of enhanced Laue-DIC

Figure 4.32: Error bar of stress profile of Si sample III.

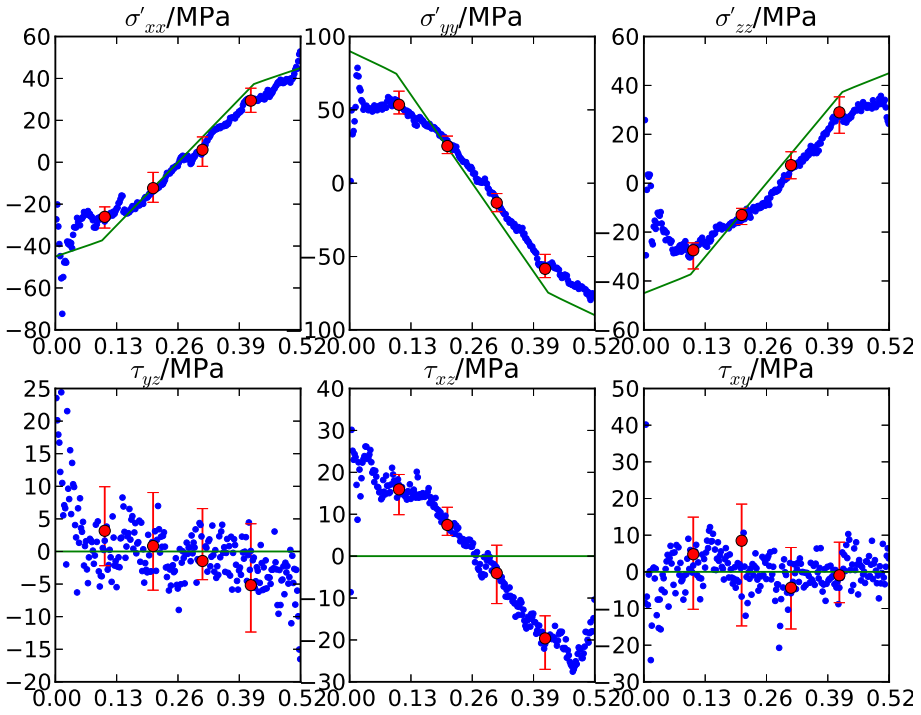

(a) Error bar of original Laue-DIC

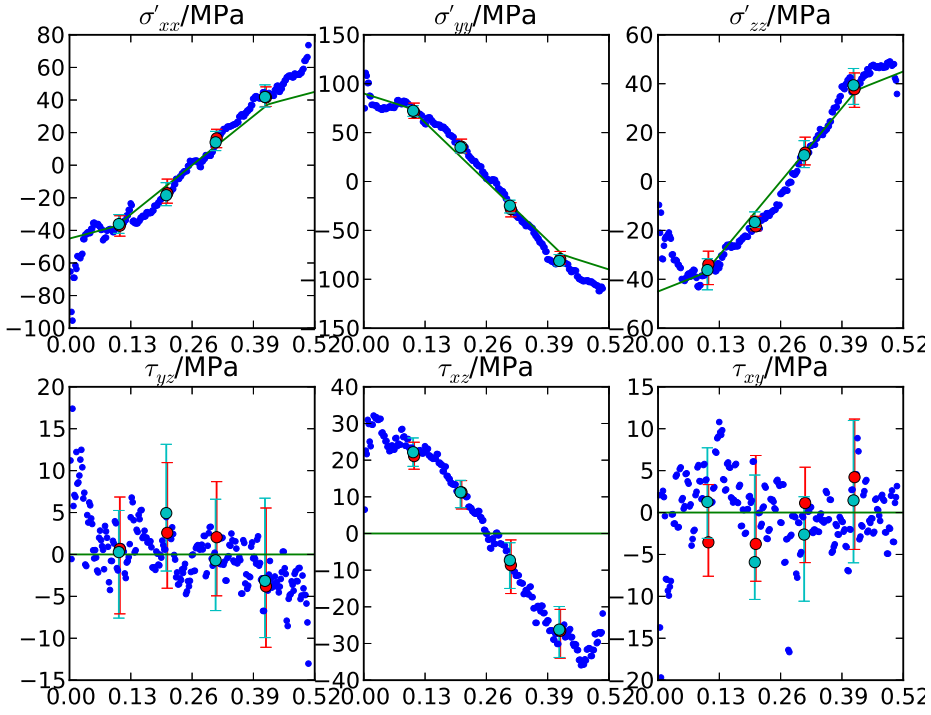

(b) Error bar of enhanced Laue-DIC

Figure 4.33: Error bar of stress profile of 316L sample.

stress, we tabulated the average length of error bars for each component of stress in Tab. 4.11. And it is found that the fluctuations of the shear components usually are of the same magnitude as those of the normal ones. This is a bit different from the conclusion of [Poshadel et al. 2012]: the shear components should exhibit larger fluctuations than normal ones. This difference be attributed to the orientation of crystal: at certain orientation, the spots' positions may be more sensitive to shear stress, while at other orientation, they may be more or equally sensitive to normal stress.

	σ'_{xx}	σ'_{yy}	σ'_{zz}	τ_{yz}	τ_{xz}	τ_{xy}
Fig. 4.32a	27.0	30.3	28.6	32.2	32.4	15.2
Fig. 4.32b	29.9	31.7	24.0	31.7	45.8	13.1
Fig. 4.33a	12.5	13.9	10.8	13.7	10.7	24.3
Fig. 4.33b	12.7	12.8	11.2	14.6	10.6	13.5

Table 4.11: Average length of error bars for each component of stress (unit: MPa)

4.7 Summary

In this chapter, we applied the standard Laue treatment, original Laue-DIC, and enhanced Laue-DIC to three materials: Si, Ge, and 316 stainless steel. We prepared cuboid samples for these material, and performed in situ four point bending tests. For each sample, we scanned the central line and used standard Laue treatment, original Laue-DIC, and enhanced Laue-DIC to obtain the stress profile. We have two main conclusions:

- For Si sample, the stress profiles by either original Laue-DIC or enhanced Laue-DIC exhibit less fluctuations than those by standard Laue treatment, and the results of original Laue-DIC and enhanced Laue-DIC are very similar. However, for Ge and 316L sample, the results of the three methods were very similar due to the fact that their spots (see Fig. 4.20 and 4.25) were more elliptically shaped than those of Si samples (see Fig. 2.2) hence analytically fitting could give reasonable estimation of diffraction direction.

- By comparing the stress profiles taken at different sample-detector distance, we found that the stress profiles taken at the closest distance demonstrated the least fluctua-

tion. This was due to the fact that the area detector could collect more spots at a closer sample-detector distance. Although spots taken at a larger distance would have better resolutions, they come at a cost of reducing the number of spots considered, and the improvement in spots' resolutions would not compensate for the reduction of the number of spots considered.

In §4.6 we proposed a procedure to estimate the uncertainties of stress evaluations, which traced the source of uncertainties from the uncertainties of the measurement of displacements by DIC. The calculated error bars turned out to be fit for the fluctuations of stress profiles.

Chapter 5

Conclusions and Perspectives

The characterization of intragranular elastic strain/stress by Laue microdiffraction has been well-established and implemented in several academic codes, e.g. LaueTool, XMAS, etc. However, the standard method used in these codes may lose its precision when fitting non-elliptical Laue spot to get the diffraction peak, because the analytical functions used for fitting implicitly assume the ellipticity of Laue spot. In the work presented here, we sought to improve the precision of elastic strain/stress characterization by applying digital image correlation (DIC) into diffraction image treatment, since DIC is insensitive to spot's shape. Compared to analytical fitting of spots, DIC does not measure peaks' 2D position, but rather peaks' displacements between two configurations by taking advantage of spots' resemblances, which can be quantified by the so-called "correlation coefficient".

A previous attempt of combining Laue microdiffraction and DIC has been shown to improve the intragranular elastic strain/stress evaluation, and the new method is called Laue-DIC. In this approach, we first locate a position within the crystal whose orientation and elastic strain are known in advance, and label it as reference configuration. Then, we treat the position within the crystal whose orientation and elastic strain are under investigation as current configuration, and measure the displacements of spots between reference and current configurations by DIC. Finally, we use, for example, least square method to calculate the relative deformation gradient between the two configurations.

Despite the success of Laue-DIC, it still suffers from two insufficiency: (i) it is difficult to locate a reference configuration whose elastic strain and orientation are known; (ii) when

the illumination of X-ray is shifted from reference configuration to current configuration, it is difficult to maintain the calibration parameters constant due to factors such as the imprecision of experimental machine, specimen's roughness, etc. To solve this problem, we proposed an enhanced version of Laue-DIC. The novelty of enhanced Laue-DIC compared with the original one rests in treating both the lattice matrices of reference configuration and calibration parameters as unknowns. The procedure of enhanced Laue-DIC can be explained by Fig. 3.1: (i) index each spot and measure the displacement of spot between two configurations; (ii) use, for example, standard Laue treatment, to calculate the lattice matrices and calibration parameters of two configurations, and use them as initial guess to minimize the discrepancy between measured spots' displacements and theoretical ones. The feasibility of enhanced Laue-DIC depends on the rank of Jacobian matrix of Eqn. 3.2: if it is full ranked, then with the displacements of 12 spots, we can obtain the lattice matrices and calibration parameters of two configurations which consists of a total of 24 unknowns. Enhanced Laue-DIC excels original Laue-DIC in two aspects: (i) it solves the deviatoric lattice matrices rather than their increment; (ii) it takes calibration parameters into consideration, therefore it is more robust against any errors in calibration parameters.

We applied the standard method, original Laue-DIC, and enhanced Laue-DIC to the treatment of image sequence of scanning bent monocrystals (Si, Ge, and 316L steel). It was found that: for Ge, 316L samples, whose spots' shapes appeared close to elliptic, the three methods gave similar curves, while for Si samples, whose spots were elongated, both original and enhanced Laue-DIC gave better match to the reference solutions than standard method.

Aside from the formulation of enhanced Laue-DIC, we also developed a procedure of statistically estimating the errors of elastic strain/stress resulted from DIC errors. Prior to that procedure, we need to characterize the noise of diffraction image in the first place. In our approach, the noise is described by a classical model: Poissonian-Gaussian noise model. This model is validated by collecting stacks of 100 image under the same condition and hence its parameters are obtained by linear regression.

With the noise model and its parameters, we are able to estimate the errors of original and enhanced Laue-DIC. This is accomplished in two steps: (i) synthesize artificial spot

image, add noise to each pixel, and perform numerical tests to investigate the distributions of DIC errors; (ii) add DIC errors to spots' displacements, and perform numerical tests to investigate the distributions of the results of original and enhanced Laue-DIC. Main conclusions of these numerical tests include that: (i) increasing the number of spots can decrease the errors; (ii) the random errors are usually larger than systematic errors; (iii) enhanced Laue-DIC is more robust against the errors of calibration parameters than original Laue-DIC.

Given the work presented above, in future, it is possible to expand the work in the following aspects:

1. find a more efficient algorithm to minimize the cost function Eqn. 3.6. The algorithm adopted in §3.3.1 can probably be further optimized in terms of efficiency.

2. develop another version of enhanced Laue-DIC. In my opinion, it is also possible to measure the lattice matrix of one illumination position by taking two diffraction images under different sets of calibration parameters. In that case, we have 16 unknowns to be optimized: 8 for the lattice matrix, and the rest for the calibration parameters.

3. explore the possibility of applying enhanced Laue-DIC to scanning the sample with rough surface. In current Laue microdiffraction, it is imperative to prepare sample with smooth surface in order to maintain calibration parameters. However, enhanced Laue-DIC is more robust against variation of calibration parameters.

4. Both original and enhanced Laue-DIC consist of two steps: (i) use DIC to obtain spots' displacements; (ii) use spots' displacements to calculate deformation gradient in original Laue-DIC or lattice matrices and calibration parameters in enhanced Laue-DIC. However, it would be worth a try to combine the two steps into one single step, more specifically, instead of correlating spots' images individually, we formulate one single cost function, whose input is all spots' images, and the output is no longer spots' displacements but the parameters under investigation. We could call this approach global Laue-DIC.

Bibliography

J. Abanto-Bueno and J. Lambros. Investigation of crack growth in functionally graded materials using digital image correlation. *Eng. Fract. Mech.*, 69:1695 – 1711, 2002. 58

F. Amiot, M. Bornert, P. Doumalin, J. C. Dupré, M. Fazzini, J. J. Orteu, C. Poilâne, L. Robert, R. Rotinat, E. Toussaint, B. Wattrisse, and J. S. Wienin. Assessment of digital image correlation measurement accuracy in the ultimate error regime: Main results of a collaborative benchmark. *Strain*, 49:483–496, 2013. 55, 57, 59, 82, 84, 99, 138

U. W. Arndt and D. J. Gilmore. X-ray television area detectors for macromolecular structural studies with synchrotron radiation sources. *J. Appl. Cryst.*, 12:1–9, 1979. 71

J. Bach, H.W. Höppel, M. Prell, and M. Göken. Crack initiation mechanisms in {AA6082} fatigued in the vhcf-regime. *Int. J. Fatigue*, 60:23 – 27, 2014. 21

R. Barabash, G. E. Ice, B. C. Larson, G. M. Pharr, K.-S. Chung, and W. Yang. White microbeam diffraction from distorted crystals. *Appl. Phys. Lett.*, 79:749–751, 2001. 54

S. Basolo, J. F. Bérar, N. Boudet, P. Breugnon, B. Chantepie, J. C. Clémens, P. Delpierre, B. Dinkespiler, S. Hustache, K. Medjoubi, M. Ménouni, C. Morel, P. Pangaud, and E. Vigeolas. A 20kpixels cdte photon-counting imager using xpad chip. *Nucl. Instrum. Methods Phys. Res. A*, 589:268 – 274, 2008. 65

S. Belouettar, A. Abbadi, Z. Azari, R. Belouettar, and P. Freres. Experimental investigation of static and fatigue behaviour of composites honeycomb materials using four point bending tests. *Compos. Struct.*, 87:265 – 273, 2009. 131

S Bergonnier, F Hild, and S Roux. Digital image correlation used for mechanical tests on crimped glass wool samples. *J. Strain Anal. Eng. Des.*, 40:185–197, 2005. 58

P.R. Bevington and D.K. Robinson. Uncertainties in Measurements. In *Data reduction and error analysis for the physical sciences*, chapter 1. McGraw-Hill, 2003. 69

M. Bornert, F. Brémand, P. Doumalin, J.-C. Dupré, M. Fazzini, M. Grédiac, F. Hild, S. Mistou, J. Molimard, J.-J. Orteu, L. Robert, Y. Surrel, P. Vacher, and B. Wattrisse. Assessment of digital image correlation measurement errors: Methodology and results. *Exp. Mech.*, 49:353–370, 2009. 55, 57, 84, 99

J. Boulanger, C. Kervrann, P. Bouthemy, P. Elbau, J.-B. Sibarita, and J. Salamero. Patch-based nonlocal functional for denoising fluorescence microscopy image sequences. *IEEE Trans. Med. Imag.*, 29:442–454, 2010. 65

D. Bouscaud, A. Morawiec, R. Pesci, S. Berveiller, and E. Patoor. Strain resolution of scanning electron microscopy based Kossel microdiffraction. *J. Appl. Cryst.*, 47:1699–1707, 2014. 25

T.B. Britton, C. Maurice, R. Fortunier, J.H. Driver, A.P. Day, G. Meaden, D.J. Dingley, K. Mingard, and A.J. Wilkinson. Factors affecting the accuracy of high resolution electron backscatter diffraction when using simulated patterns. *Ultramicrosc.*, 110:1443 – 1453, 2010. 24

R. Byrd, R. Schnabel, and G. Shultz. A trust region algorithm for nonlinearly constrained optimization. *SIAM J. Numer. Anal.*, 24:1152–1170, 1987. 112

R. Byrd, P. Lu, J. Nocedal, and C. Zhu. A limited memory algorithm for bound constrained optimization. *SIAM J. Sci. Comput.*, 16:1190–1208, 1995. 112

J.-S. Chung and G. E. Ice. Automated indexing for texture and strain measurement with broad-bandpass x-ray microbeams. *J. Appl. Phys.*, 86:5249–5255, 1999. 38, 48, 49

A.M. Cuitiño and M. Ortiz. Three-dimensional crack-tip fields in four-point-bending copper single-crystal specimens. *J. Mech. Phys. Solids*, 44:863 – 904, 1996. 131

B. D. Cullity. Diffraction I: The Directions of Diffracted Beams. In *Elements Of X Ray Diffraction*, chapter 3, pages 78–103. 1956a. 39, 40

B. D. Cullity. Diffraction II: The Intensities of Diffracted Beams. In *Elements Of X Ray Diffraction*, chapter 4, pages 104–137. 1956b. 23, 28, 40

L. Desgranges, H. Palancher, M. Gamaléri, J.S. Micha, V. Optasanu, L. Raceanu, T. Montesin, and N. Creton. Influence of the u3o7 domain structure on cracking during the oxidation of uo2. *J. Nucl. Mater.*, 402:167 – 172, 2010. 128

P. Doumalin and M. Bornert. Micromechanical Applications of Digital Image Correlation Techniques. In P. Jacquot and J.-M. Fournier, editors, *Interferometry in Speckle Light*, pages 67–74. Springer Berlin Heidelberg, 2000. 21, 82, 84

H. Faraji and W. MacLean. Ccd noise removal in digital images. *IEEE Trans. Imag. Process.*, 15:2676–2685, 2006. 65

A. Foi, M. Trimeche, V. Katkovnik, , and K. Egiazarian. Practical poissonian-gaussian noise modeling and fitting for single-image raw-data. *IEEE Trans. Imag. Process.*, 17: 1737–1754, 2008. 65

G. Gaucherin, F. Hofmann, J. P. Belnoue, and A. M. Korsunsky. Crystal plasticity and hardening: A dislocation dynamics study. *Procedia Eng.*, 1:241 – 244, 2009. 17

X. Gonze, J.-M. Beuken, R. Caracas, F. Detraux, M. Fuchs, G.-M. Rignanese, L. Sindic, M. Verstraete, G. Zerah, F. Jollet, M. Torrent, A. Roy, M. Mikami, Ph. Ghosez, J.-Y. Raty, and D.C. Allan. First-principles computation of material properties: the {ABINIT} software project. *Comput. Mater. Sci.*, 25:478 – 492, 2002. 16

V. K. Gupta and S. R. Agnew. Indexation and misorientation analysis of low-quality Laue diffraction patterns. *J. Appl. Cryst.*, 42:116–124, 2009. 47

B. He. X-ray Source and Optics. In *Two-Dimensional X-Ray Diffraction*, chapter 3, pages 51–84. John Wiley & Sons, Inc., 2009a. 26, 37, 128

B. He. X-Ray Detectors. In *Two-Dimensional X-Ray Diffraction*, chapter 4, pages 85–132. John Wiley & Sons, Inc., 2009b. 66, 67, 70

B. He. Goniometer and Sample Stages. In *Two-Dimensional X-Ray Diffraction*, chapter 5, pages 133–150. John Wiley & Sons, Inc., 2009c. 36

B. Henrich, A. Bergamaschi, C. Broennimann, R. Dinapoli, E.F. Eikenberry, I. Johnson, M. Kobas, P. Kraft, A. Mozzanica, and B. Schmitt. Pilatus: A single photon counting pixel detector for x-ray applications. *Nucl. Instrum. Methods Phys. Res. A*, 607:247 – 249, 2009. 65

E. Héripré, M. Dexet, J. Crépin, L. Gélébart, A. Roos, M. Bornert, and D. Caldemaison. Coupling between experimental measurements and polycrystal finite element calculations for micromechanical study of metallic materials. *Int. J. Plast.*, 23:1512 – 1539, 2007. 18, 21

F. Hild and S. Roux. Measuring stress intensity factors with a camera: Integrated digital image correlation (I-DIC). *C. R. Mec.*, 334:8 – 12, 2006. 21

T. Hoc, J. Crépin, L. Gélébart, and A. Zaoui. A procedure for identifying the plastic behavior of single crystals from the local response of polycrystals. *Acta Mater.*, 51:5477 – 5488, 2003. 17

F. Hofmann. *Probing the Deformation of Ductile Polycrystals by Synchrotron X-ray Micro-diffraction*. PhD thesis, Oxford University, 2011. 64, 152

F. Hofmann, S. Eve, J. Belnoue, J.-S. Micha, and A. M. Korsunsky. Analysis of strain error sources in micro-beam laue diffraction. *Nucl. Instrum. Methods Phys. Res. A*, 660: 130 – 137, 2011. 81, 128

F. Hofmann, X. Song, B. Abbey, T.-S. Jun, and A. M. Korsunsky. High-energy transmission Laue micro-beam X-ray diffraction: a probe for intra-granular lattice orientation and elastic strain in thicker samples. *J. Synchrotron Rad.*, 19:307–318, 2012. 39

G. W. Hollenberg, G. R. Terwilliger, and R. S. Gordon. Calculation of stresses and strains in four-point bending creep tests. *J. Am. Ceram. Soc.*, 54:196–199, 1971. 131

J. M. Holton. A beginner's guide to radiation damage. *J. Synchrotron Rad.*, 16:133–142, 2009. 40

G. E. Ice. Microbeam-forming methods for synchrotron radiation. *X-Ray Spectrom.*, 26: 315–326, 1997. 26

G. E. Ice, J.-S. Chung, J. Z. Tischler, A. Lunt, and L. Assoufid. Elliptical x-ray microprobe mirrors by differential deposition. *Rev. Sci. Instrum.*, 71:2635–2639, 2000. 26

G. E. Ice, J. W. L. Pang, B. C. Larson, J. D. Budai, J. Z. Tischler, J.-Y. Choi, W. Liu, C. Liu, L. Assoufid, D. Shu, and A. Khounsary. At the limit of polychromatic microdiffraction. *Mater. Sci. Eng. A*, 524:3 – 9, 2009. 40, 128

G.E. Ice. Reflective optics for microdiffraction. *Nucl. Instrum. Methods Phys. Res. A*, 582: 129 – 131, 2007. 26

G.E. Ice, J.W.L. Pang, R.I. Barabash, and Y. Puzyrev. Characterization of three-dimensional crystallographic distributions using polychromatic x-ray microdiffraction. *Scr. Mater.*, 55:57 – 62, 2006. 40

J. D. Jackson. Radiation by Moving Charges. In *Classical Electrodynamics*, chapter 14, pages 661–707. John Wiley & Sons, Inc., 1999. 26, 27

Z. Y. Jin and Z. S. Cui. Investigation on dynamic recrystallization using a modified cellular automaton. *Comput. Mater. Sci.*, 63:249 – 255, 2012. 17

C. Kirchlechner, D. Kiener, C. Motz, S. Labat, N. Vaxelaire, O. Perroud, J.-S. Micha, O. Ulrich, O. Thomas, G. Dehm, and J. Keckes. Dislocation storage in single slip-oriented cu micro-tensile samples: new insights via x-ray microdiffraction. *Philos. Mag.*, 91:1256–1264, 2011. 128

S. Labat, O. Robach, and V. Chamard. Local strain measurements : X-ray micro-laue and bragg coherent diffraction techniques. In S. Forest, A. Ponchet, and O. Thomas, editors, *Mechanics of nano-objects*, pages 189–209. Les Presses des Mines, 2011. 46, 47

LaueTools. URL `http://sourceforge.net/projects/lauetools/`. 42, 105

C. Le Bourlot, P. Landois, S. Djaziri, P.-O. Renault, E. Le Bourhis, P. Goudeau, M. Pinault, M. Mayne-L'Hermite, B. Bacroix, D. Faurie, O. Castelnau, P. Launois, and S. Rouzière. Synchrotron X-ray diffraction experiments with a prototype hybrid pixel detector. *J. Appl. Cryst.*, 45:38–47, 2012. 65

A. G. W. Leslie. Integration of macromolecular diffraction data. *Acta Cryst. D*, 55:1696–1702, 1999. 72

H.W. Li, H. Yang, and Z.C. Sun. A robust integration algorithm for implementing rate dependent crystal plasticity into explicit finite element method. *Int. J. Plast.*, 24:267 – 288, 2008. 17

W. Liu, G. E. Ice, J. Z. Tischler, A. Khounsary, C. Liu, L. Assoufid, and A. T. Macrander. Short focal length kirkpatrick-baez mirrors for a hard x-ray nanoprobe. *Rev. Sci. Instrum.*, 76(11), 2005. 26

W. K. Liu, H. S. Park, D. Qian, E. G. Karpov, H. Kadowaki, and G. J. Wagner. Bridging scale methods for nanomechanics and materials. *Comput. Methods Appl. Mech. Eng.*, 195:1407 – 1421, 2006. 17

Q. Ma. A four-point bending technique for studying subcritical crack growth in thin films and at interfaces. *J. Mater. Res.*, 12:840–845, 1997. 131

E. Macherauch. X-ray stress analysis. *Exp. Mech.*, 6:140–153, 1966. 37

K.R. Magid, J.N. Florando, D.H. Lassila, M.M. LeBlanc, N. Tamura, and J.W. Morris. Mapping mesoscale heterogeneity in the plastic deformation of a copper single crystal. *Philos. Mag.*, 89:77–107, 2009. 17, 55

E.N. Maslen. X-ray absorption. In E. Prince, editor, *International Tables for Crystallography*, volume C, pages 599–608. Springer Netherlands, 2004. 129

C. Maurice and R. Fortunier. A 3d hough transform for indexing ebsd and kossel patterns. *J. Microsc.*, 230:520–529, 2008. 25

C. Maurice, J. H. Driver, and R. Fortunier. On solving the orientation gradient dependency of high angular resolution {EBSD}. *Ultramicrosc.*, 113:171 – 181, 2012. 24

D. L. McDowell. Materials design: a useful research focus for inelastic behavior of structural metals. *Theor. Appl. Fract. Mech.*, 37:245 – 259, 2001. 16

D. L. McDowell. A perspective on trends in multiscale plasticity. *Int. J. Plast.*, 26:1280 – 1309, 2010. 16

W. A. Paciorek, M. Meyer, and G. Chapuis. Geometric distortion corrections for fiber-optic tapers in X-ray charge-coupled-device detectors. *J. Appl. Cryst.*, 32:11–14, 1999. 70

M. Palengat, G. Chagnon, D. Favier, H. Louche, C. Linardon, and C. Plaideau. Cold drawing of 316l stainless steel thin-walled tubes: Experiments and finite element analysis. *Int. J. Mech. Sci.*, 70:69 – 78, 2013. 136

W. H. Peters and W. F. Ranson. Digital imaging techniques in experimental stress analysis. *Opt. Eng.*, 21:213427–213427, 1982. 58

J. Petit, M. Bornert, F. Hofmann, O. Robach, J.S. Micha, O. Ulrich, C. Le Bourlot, D. Faurie, A.M. Korsunsky, and O. Castelnau. Combining laue microdiffraction and digital image correlation for improved measurements of the elastic strain field with micrometer spatial resolution. *Procedia {IUTAM}*, 4:133 – 143, 2012. 55, 56, 60, 64

J. Petit, O. Castelnau, M. Bornert, F. G. Zhang, F. Hofmann, A. M. Korsunsky, D. Faurie, C. Le Bourlot, J. S. Micha, O. Robach, and O. Ulrich. Laue-DIC: a new method for improved stress field measurements at the micron scale. *J. Synchrotron Rad.*, 2015. Accepted. 55, 56, 60

C. Ponchut. Characterization of X-ray area detectors for synchrotron beamlines. *J. Synchrotron Rad.*, 13:195–203, 2006. 66, 67, 70

C. Ponchut, J. Clément, J.-M. Rigal, E. Papillon, J. Vallerga, D. LaMarra, and B. Mikulec. Photon-counting x-ray imaging at kilohertz frame rates. *Nucl. Instrum. Methods Phys. Res. A*, 576:109 – 112, 2007. 65

A. Poshadel, P. Dawson, and G. Johnson. Assessment of deviatoric lattice strain uncertainty for polychromatic X-ray microdiffraction experiments. *J. Synchrotron Rad.*, 19: 237–244, 2012. 54, 55, 81, 94, 107, 147, 160

M. J. D. Powell. An efficient method for finding the minimum of a function of several variables without calculating derivatives. *Comput. J.*, 7:155–162, 1964. 112

D. Raabe. Molecular Dynamics. In *Computational Materials Science*, chapter 7, pages 87–110. Wiley-VCH Verlag GmbH & Co. KGaA, 2004. 17

O. Rand and V. Rovenski. Beams of general anisotropy. In *Analytical Methods in Anisotropic Elasticity*, chapter 6, pages 215–248. Birkhäuser Boston, 2005. 64, 134, 142

O. Robach, J.-S. Micha, O. Ulrich, and P. Gergaud. Full local elastic strain tensor from Laue microdiffraction: simultaneous Laue pattern and spot energy measurement. *J. Appl. Cryst.*, 44:688–696, 2011. 39, 44, 103

M. D. Sangid. The physics of fatigue crack initiation. *Int. J. Fatigue*, 57:58 – 72, 2013. 21

H. W. Schreier and M. A. Sutton. Systematic errors in digital image correlation due to undermatched subset shape functions. *Exp. Mech.*, 42:303–310, 2002. 138

L. H. Schwartz and J. B. Cohen. Properties of Radiation Useful for Studying the Structure of Materials. In *Diffraction from Materials*, chapter 3, pages 77–158. Springer Berlin Heidelberg, 1987a. 40

L. H. Schwartz and J. B. Cohen. The Dynamical Theory of Diffraction. In *Diffraction from Materials*, chapter 8, pages 469–537. Springer Berlin Heidelberg, 1987b. 30

L. St-Pierre, E. Héripré, M. Dexet, J. Crépin, G. Bertolino, and N. Bilger. 3d simulations of microstructure and comparison with experimental microstructure coming from o.i.m analysis. *Int. J. Plast.*, 24:1516 – 1532, 2008. 21

M. Stanton, W. C. Phillips, Y. Li, and K. Kalata. The detective quantum efficiency of CCD and vidicon-based detectors for X-ray crystallographic applications. *J. Appl. Cryst.*, 25: 638–645, 1992. 71

P. Suquet, H. Moulinec, O. Castelnau, M. Montagnat, N. Lahellec, F. Grennerat, P. Duval, and R. Brenner. Multi-scale modeling of the mechanical behavior of polycrystalline ice under transient creep. *Procedia {IUTAM}*, 3:76 – 90, 2012. 17

M. A. Sutton, J.-J. Orteu, and H. W. Schreier. Introduction. In *Image Correlation for Shape, Motion and Deformation Measurements*, chapter 1, pages 1–12. Springer US, 2009a. 58

M. A. Sutton, J.-J. Orteu, and H. W. Schreier. Digital Image Correlation (DIC). In *Image Correlation for Shape, Motion and Deformation Measurements*, chapter 5, pages 81–118. Springer US, 2009b. 21, 87

M. A. Sutton, J.-J. Orteu, and H. W. Schreier. Stereo-vision System Applications. In *Image Correlation for Shape, Motion and Deformation Measurements*, chapter 7, pages 175–208. Springer US, 2009c. 60

M. A. Sutton, J.-J. Orteu, and H. W. Schreier. Volumetric Digital Image Correlation (VDIC). In *Image Correlation for Shape, Motion and Deformation Measurements*, chapter 8, pages 209–224. Springer US, 2009d. 60

A. Tatschl and O. Kolednik. A new tool for the experimental characterization of microplasticity. *Mater. Sci. Eng. A*, 339:265 – 280, 2003. 21

C. Teodosiu. Fundamentals of the Theory of Elasticity. In *Elastic Models of Crystal Defects*, pages 11–97. Springer Berlin Heidelberg, 1982. 135

C. Teyssier, J. Bouchami, F. Dallaire, J. Idárraga, C. Leroy, S. Pospísil, J. Solc, O. Scallon, and Z. Vykydal. Performance of the medipix and timepix devices for the recognition of electron-gamma radiation fields. *Nucl. Instrum. Methods Phys. Res. A*, 650:92 – 97, 2011. 65

W. Tong. An evaluation of digital image correlation criteria for strain mapping applications. *Strain*, 41:167–175, 2005. 59, 76, 82

K. Z. Troost, P. van der Sluis, and D. J. Gravesteijn. Microscale elastic strain determination by backscatter kikuchi diffraction in the scanning electron microscope. *Appl. Phys. Lett.*, 62:1110–1112, 1993. 41

O. Ulrich, X. Biquard, P. Bleuet, O. Geaymond, P. Gergaud, J. S. Micha, O. Robach, and F. Rieutord. A new white beam x-ray microdiffraction setup on the bm32 beamline at

the european synchrotron radiation facility. *Rev. Sci. Instrum.*, 82(3), 2011. 127, 128, 130

B. C. Valek. *X-ray microdiffraction studies of mechanical behavior and electromigration in thin film structures*. PhD thesis, Stanford University, 2003. 42, 82

VHR. URL `http://www.photonic-science.com/products/PDF/X-ray_VHR_arrays.pdf`. 133

J. Villanova, O. Sicardy, R. Fortunier, J.-S. Micha, and P. Bleuet. Determination of global and local residual stresses in sofc by x-ray diffraction. *Nucl. Instrum. Methods Phys. Res. B*, 268:282 – 286, 2010. 128

S. Villert, C. Maurice, C. Wyon, and R. Fortunier. Accuracy assessment of elastic strain measurement by ebsd. *J. Microsc.*, 233:290–301, 2009. 41

Y. Wang and A. M. Cuitiño. Full-field measurements of heterogeneous deformation patterns on polymeric foams using digital image correlation. *Int. J. Solids Struct.*, 39:3777 – 3796, 2002. 58

Y. Q. Wang, M. A. Sutton, H. A. Bruck, and H. W. Schreier. Quantitative error assessment in pattern matching: Effects of intensity pattern noise, interpolation, strain and image contrast on motion measurements. *Strain*, 45:160–178, 2009. 65, 87

Y. Waseda, E. Matsubara, and K. Shinoda. Scattering and Diffraction. chapter 3, pages 67–106. 2011. 29

David Waterman and Gwyndaf Evans. Estimation of errors in diffraction data measured by CCD area detectors. *J. Appl. Cryst.*, 43:1356–1371, 2010. 69, 71, 72

B. Wattrisse, A. Chrysochoos, J.-M. Muracciole, and M. N.-G. Analysis of strain localization during tensile tests by digital image correlation. *Experimental Mechanics*, 41:29–39, 2001. 58

H. R. Wenk, F. Heidelbach, D. Chateigner, and F. Zontone. Laue Orientation Imaging. *J. Synchrotron Rad.*, 4:95–101, 1997. 47

E. M. Westbrook and I. Naday. [17] charge-coupled device-based area detectors. In Jr. Charles Carter, editor, *Macromolecular Crystallography Part A*, volume 276, pages 244 – 268. Academic Press, 1997. 65

B. Widrow, I. Kollar, and M. C. Liu. Statistical theory of quantization. *IEEE Trans. Instrum. Meas.*, 45:353–361, 1996. 72

A. J. Wilkinson. Measurement of elastic strains and small lattice rotations using electron back scatter diffraction. *Ultramicrosc.*, 62:237 – 247, 1996. 41

A. J. Wilkinson, G. Meaden, and D. J. Dingley. High-resolution elastic strain measurement from electron backscatter diffraction patterns: New levels of sensitivity. *Ultramicrosc.*, 106:307 – 313, 2006. 41

M. M. Woolfson. The Scattering of X-rays. In *An Introduction to X-ray Crystallography*, chapter 2, pages 32–49. 1997. 29

H. Yan and I. C. Noyan. Measurement of stress/strain in single-crystal samples using diffraction. *J. Appl. Cryst.*, 39:320–325, 2006. 54

W.G. Yang, B.C. Larson, J.Z. Tischler, G.E. Ice, J.D. Budai, and W. Liu. Differential-aperture x-ray structural microscopy: a submicron-resolution three-dimensional probe of local microstructure and strain. *Micron*, 35:431 – 439, 2004. 40

D. Zhang, N. F. Enke, and B. I. Sandor. Thermographic stress analysis of composite materials. *Exp. Mech.*, 30:68–73, 1990. 22

H. M. Zhang, X. H. Dong, Q. Wang, and Z. Zeng. An effective semi-implicit integration scheme for rate dependent crystal plasticity using explicit finite element codes. *Comput. Mater. Sci.*, 54:208 – 218, 2012. 17

K.S. Zhang, M.S. Wu, and R. Feng. Simulation of microplasticity-induced deformation in uniaxially strained ceramics by 3-d voronoi polycrystal modeling. *Int. J. Plast.*, 21:801 – 834, 2005. 21

Appendix

Appendix A

Gradient and Hessian Matrix of Objective Function Eqn. 3.6

A.1 Objective function

Eqn. 3.6 can be written into:

$$\begin{aligned}\Pi = & \sum_{s=1}^{n} W_x^{(s)}(d\theta_x^{(s)} - D\Theta_x^{(s)} + \Delta x_{\mathrm{c}} - \Delta x_{\mathrm{DIC}}^{(s)})^2 \\ & + \sum_{s=1}^{n} W_y^{(s)}(d\theta_y^{(s)} - D\Theta_y^{(s)} + \Delta y_{\mathrm{c}} - \Delta y_{\mathrm{DIC}}^{(s)})^2,\end{aligned} \tag{A.1}$$

where

$$\begin{aligned}\theta_x^{(s)} &\doteq \frac{\xi_i^{(s)} t_{1i}}{\xi_i^{(s)} t_{3i}} \\ \theta_y^{(s)} &\doteq \frac{\xi_i^{(s)} t_{2i}}{\xi_i^{(s)} t_{3i}} \\ \Theta_x^{(s)} &\doteq \frac{\Xi_i^{(s)} T_{1i}}{\Xi_i^{(s)} T_{3i}} \\ \Theta_y^{(s)} &\doteq \frac{\Xi_i^{(s)} T_{2i}}{\Xi_i^{(s)} T_{3i}}\end{aligned} \tag{A.2}$$

$$\begin{aligned}t_{\frac{\beta}{2}} &\doteq \tan\frac{\beta}{2}, \\ t_{\frac{B}{2}} &\doteq \tan\frac{B}{2}, \\ t_{\frac{\gamma}{2}} &\doteq \tan\frac{\gamma}{2}, \\ t_{\frac{\Gamma}{2}} &\doteq \tan\frac{\Gamma}{2}.\end{aligned} \tag{A.3}$$

$$\begin{aligned}\xi_i^{(s)} &\doteq l_{kp}^* h_p^{(s)} l_{kq}^* h_q^{(s)} \delta_{2i} - 2 l_{2k}^* h_k^{(s)} l_{ij}^* h_j^{(s)} \\ \Xi_i^{(s)} &\doteq L_{kp}^* h_p^{(s)} L_{kq}^* h_q^{(s)} \delta_{2i} - 2 L_{2k}^* h_k^{(s)} L_{ij}^* h_j^{(s)}\end{aligned} \tag{A.4}$$

and

$$\underset{\sim}{h}^{(s)} \doteq [h^{(s)}, k^{(s)}, l^{(s)}]^{\mathrm{T}}. \tag{A.5}$$

A.2 Gradient

$$\begin{aligned}\frac{\partial \Pi}{\partial d} = \; & 2\sum_{s=1}^{n} W_x^{(s)}(d\theta_x^{(s)} - D\Theta_x^{(s)} + \Delta x_{\mathrm{c}} - \Delta x^{(s)})\theta_x^{(s)} \\ & +2\sum_{s=1}^{n} W_y^{(s)}(d\theta_y^{(s)} - D\Theta_y^{(s)} + \Delta y_{\mathrm{c}} - \Delta y^{(s)})\theta_y^{(s)},\end{aligned} \tag{A.6}$$

$$\begin{aligned}\frac{\partial \Pi}{\partial D} = \; & -2\sum_{s=1}^{n} W_x^{(s)}(d\theta_x^{(s)} - D\Theta_x^{(s)} + \Delta x_{\mathrm{c}} - \Delta x^{(s)})\Theta_x^{(s)} \\ & -2\sum_{s=1}^{n} W_y^{(s)}(d\theta_y^{(s)} - D\Theta_y^{(s)} + \Delta y_{\mathrm{c}} - \Delta y^{(s)})\Theta_y^{(s)},\end{aligned} \tag{A.7}$$

$$\frac{\partial \Pi}{\partial \Delta x_{\mathrm{c}}} = 2\sum_{s=1}^{n} W_x^{(s)}(d\theta_x^{(s)} - D\Theta_x^{(s)} + \Delta x_{\mathrm{c}} - \Delta x^{(s)}), \tag{A.8}$$

$$\frac{\partial \Pi}{\partial \Delta y_{\mathrm{c}}} = 2\sum_{s=1}^{n} W_y^{(s)}(d\theta_y^{(s)} - D\Theta_y^{(s)} + \Delta y_{\mathrm{c}} - \Delta y^{(s)}), \tag{A.9}$$

$$\begin{aligned}\frac{\partial \Pi}{\partial t_{\frac{\beta}{2}}} = \; & 2\sum_{s=1}^{n} W_x^{(s)}(d\theta_x^{(s)} - D\Theta_x^{(s)} + \Delta x_{\mathrm{c}} - \Delta x^{(s)})d\frac{\partial \theta_x^{(s)}}{\partial t_{\frac{\beta}{2}}} \\ & +2\sum_{s=1}^{n} W_y^{(s)}(d\theta_y^{(s)} - D\Theta_y^{(s)} + \Delta y_{\mathrm{c}} - \Delta y^{(s)})d\frac{\partial \theta_y^{(s)}}{\partial t_{\frac{\beta}{2}}},\end{aligned} \tag{A.10}$$

$$\begin{aligned}\frac{\partial \Pi}{\partial t_{\frac{\gamma}{2}}} = \; & 2\sum_{s=1}^{n} W_x^{(s)}(d\theta_x^{(s)} - D\Theta_x^{(s)} + \Delta x_{\mathrm{c}} - \Delta x^{(s)})d\frac{\partial \theta_x^{(s)}}{\partial t_{\frac{\gamma}{2}}} \\ & +2\sum_{s=1}^{n} W_y^{(s)}(d\theta_y^{(s)} - D\Theta_y^{(s)} + \Delta y_{\mathrm{c}} - \Delta y^{(s)})d\frac{\partial \theta_y^{(s)}}{\partial t_{\frac{\gamma}{2}}},\end{aligned} \tag{A.11}$$

$$\begin{aligned}\frac{\partial \Pi}{\partial t_{\frac{B}{2}}} = \; & -2\sum_{s=1}^{n} W_x^{(s)}(d\theta_x^{(s)} - D\Theta_x^{(s)} + \Delta x_{\mathrm{c}} - \Delta x^{(s)})D\frac{\partial \Theta_x^{(s)}}{\partial t_{\frac{B}{2}}} \\ & -2\sum_{s=1}^{n} W_y^{(s)}(d\theta_y^{(s)} - D\Theta_y^{(s)} + \Delta y_{\mathrm{c}} - \Delta y^{(s)})D\frac{\partial \Theta_y^{(s)}}{\partial t_{\frac{B}{2}}},\end{aligned} \tag{A.12}$$

$$\begin{aligned}\frac{\partial \Pi}{\partial t_{\frac{\Gamma}{2}}} = \; & -2\sum_{s=1}^{n} W_x^{(s)}(d\theta_x^{(s)} - D\Theta_x^{(s)} + \Delta x_{\mathrm{c}} - \Delta x^{(s)})D\frac{\partial \Theta_x^{(s)}}{\partial t_{\frac{\Gamma}{2}}} \\ & -2\sum_{s=1}^{n} W_y^{(s)}(d\theta_y^{(s)} - D\Theta_y^{(s)} + \Delta y_{\mathrm{c}} - \Delta y^{(s)})D\frac{\partial \Theta_y^{(s)}}{\partial t_{\frac{\Gamma}{2}}},\end{aligned} \tag{A.13}$$

where

$$\begin{aligned}
\frac{\partial\theta_x^{(s)}}{\partial t_{\frac{\beta}{2}}} &= \frac{\xi_i^{(s)}\frac{\partial t_{1i}}{\partial t_{\frac{\beta}{2}}}\xi_j^{(s)}t_{3j} - \xi_i^{(s)}t_{1i}\xi_j^{(s)}\frac{\partial t_{3j}}{\partial t_{\frac{\beta}{2}}}}{(\xi_i^{(s)}t_{3i})^2} \\
\frac{\partial\theta_x^{(s)}}{\partial t_{\frac{\gamma}{2}}} &= \frac{\xi_i^{(s)}\frac{\partial t_{1i}}{\partial t_{\frac{\gamma}{2}}}\xi_j^{(s)}t_{3j} - \xi_i^{(s)}t_{1i}\xi_j^{(s)}\frac{\partial t_{3j}}{\partial t_{\frac{\gamma}{2}}}}{(\xi_i^{(s)}t_{3i})^2} \\
\frac{\partial\theta_y^{(s)}}{\partial t_{\frac{\beta}{2}}} &= \frac{\xi_i^{(s)}\frac{\partial t_{2i}}{\partial t_{\frac{\beta}{2}}}\xi_j^{(s)}t_{3j} - \xi_i^{(s)}t_{2i}\xi_j^{(s)}\frac{\partial t_{3j}}{\partial t_{\frac{\beta}{2}}}}{(\xi_i^{(s)}t_{3i})^2} \\
\frac{\partial\theta_y^{(s)}}{\partial t_{\frac{\gamma}{2}}} &= \frac{\xi_i^{(s)}\frac{\partial t_{2i}}{\partial t_{\frac{\gamma}{2}}}\xi_j^{(s)}t_{3j} - \xi_i^{(s)}t_{2i}\xi_j^{(s)}\frac{\partial t_{3j}}{\partial t_{\frac{\gamma}{2}}}}{(\xi_i^{(s)}t_{3i})^2}
\end{aligned} \tag{A.14}$$

$$\begin{aligned}
\frac{\partial\Theta_x^{(s)}}{\partial t_{\frac{B}{2}}} &= \frac{\Xi_i^{(s)}\frac{\partial T_{1i}}{\partial t_{\frac{B}{2}}}\Xi_j^{(s)}T_{3j} - \Xi_i^{(s)}T_{1i}\Xi_j^{(s)}\frac{\partial T_{3j}}{\partial t_{\frac{B}{2}}}}{(\Xi_i^{(s)}T_{3i})^2} \\
\frac{\partial\Theta_x^{(s)}}{\partial t_{\frac{\Gamma}{2}}} &= \frac{\Xi_i^{(s)}\frac{\partial T_{1i}}{\partial t_{\frac{\Gamma}{2}}}\Xi_j^{(s)}T_{3j} - \Xi_i^{(s)}T_{1i}\Xi_j^{(s)}\frac{\partial T_{3j}}{\partial t_{\frac{\Gamma}{2}}}}{(\Xi_i^{(s)}T_{3i})^2} \\
\frac{\partial\Theta_y^{(s)}}{\partial t_{\frac{B}{2}}} &= \frac{\Xi_i^{(s)}\frac{\partial T_{2i}}{\partial t_{\frac{B}{2}}}\Xi_j^{(s)}T_{3j} - \Xi_i^{(s)}T_{2i}\Xi_j^{(s)}\frac{\partial T_{3j}}{\partial t_{\frac{B}{2}}}}{(\Xi_i^{(s)}T_{3i})^2} \\
\frac{\partial\Theta_y^{(s)}}{\partial t_{\frac{\Gamma}{2}}} &= \frac{\Xi_i^{(s)}\frac{\partial T_{2i}}{\partial t_{\frac{\Gamma}{2}}}\Xi_j^{(s)}T_{3j} - \Xi_i^{(s)}T_{2i}\Xi_j^{(s)}\frac{\partial T_{3j}}{\partial t_{\frac{\Gamma}{2}}}}{(\Xi_i^{(s)}T_{3i})^2}
\end{aligned} \tag{A.15}$$

$$\begin{aligned}
\frac{\partial\Pi}{\partial l_{ij}^*} = \; & 2\sum_{s=1}^{n} W_x^{(s)}(d\theta_x^{(s)} - D\Theta_x^{(s)} + \Delta x_{\mathrm{c}} - \Delta x^{(s)})d\frac{\partial\theta_x^{(s)}}{\partial l_{ij}^*} \\
& +2\sum_{s=1}^{n} W_y^{(s)}(d\theta_y^{(s)} - D\Theta_y^{(s)} + \Delta y_{\mathrm{c}} - \Delta y^{(s)})d\frac{\partial\theta_y^{(s)}}{\partial l_{ij}^*},
\end{aligned} \tag{A.16}$$

$$\begin{aligned}
\frac{\partial\Pi}{\partial L_{ij}^*} = \; & -2\sum_{s=1}^{n} W_x^{(s)}(d\theta_x^{(s)} - D\Theta_x^{(s)} + \Delta x_{\mathrm{c}} - \Delta x^{(s)})D\frac{\partial\Theta_x^{(s)}}{\partial L_{ij}^*} \\
& -2\sum_{s=1}^{n} W_y^{(s)}(d\theta_y^{(s)} - D\Theta_y^{(s)} + \Delta y_{\mathrm{c}} - \Delta y^{(s)})D\frac{\partial\Theta_y^{(s)}}{\partial L_{ij}^*}.
\end{aligned} \tag{A.17}$$

where

$$\begin{aligned}
\frac{\partial\theta_x^{(s)}}{\partial l_{ij}^*} &= \frac{\frac{\partial\xi_p^{(s)}}{\partial l_{ij}^*}t_{1p}\xi_q^{(s)}t_{3q} - \xi_p^{(s)}t_{1p}\frac{\partial\xi_q^{(s)}}{\partial l_{ij}^*}t_{3q}}{(\xi_r^{(s)}t_{3r})^2} \\
\frac{\partial\theta_y^{(s)}}{\partial l_{ij}^*} &= \frac{\frac{\partial\xi_p^{(s)}}{\partial l_{ij}^*}t_{2p}\xi_q^{(s)}t_{3q} - \xi_p^{(s)}t_{2p}\frac{\partial\xi_q^{(s)}}{\partial l_{ij}^*}t_{3q}}{(\xi_r^{(s)}t_{3r})^2} \\
\frac{\partial\Theta_x^{(s)}}{\partial L_{ij}^*} &= \frac{\frac{\partial\Xi_p^{(s)}}{\partial L_{ij}^*}T_{1p}\Xi_q^{(s)}T_{3q} - \Xi_p^{(s)}T_{1p}\frac{\partial\Xi_q^{(s)}}{\partial L_{ij}^*}T_{3q}}{(\Xi_r^{(s)}T_{3r})^2} \\
\frac{\partial\Theta_y^{(s)}}{\partial L_{ij}^*} &= \frac{\frac{\partial\Xi_p^{(s)}}{\partial L_{ij}^*}T_{2p}\Xi_q^{(s)}T_{3q} - \Xi_p^{(s)}T_{2p}\frac{\partial\Xi_q^{(s)}}{\partial L_{ij}^*}T_{3q}}{(\Xi_r^{(s)}T_{3r})^2}
\end{aligned} \tag{A.18}$$

$$\begin{aligned}
\frac{\partial\xi_p^{(s)}}{\partial l_{ij}^*} &= 2h_j^{(s)}(\delta_{2p}l_{ir}^*h_r^{(s)} - \delta_{2i}l_{pr}^*h_r^{(s)} - \delta_{pi}l_{2r}^*h_r^{(s)}), \\
\frac{\partial\Xi_p^{(s)}}{\partial L_{ij}^*} &= 2h_j^{(s)}(\delta_{2p}L_{ir}^*h_r^{(s)} - \delta_{2i}L_{pr}^*h_r^{(s)} - \delta_{pi}L_{2r}^*h_r^{(s)})
\end{aligned} \tag{A.19}$$

A.3 Hessian Matrix

$$\frac{\partial^2\Pi}{\partial d^2} = 2\sum_{s=1}^{n}W_x^{(s)}(\theta_x^{(s)})^2 + 2\sum_{s=1}^{n}W_y^{(s)}(\theta_y^{(s)})^2 \tag{A.20}$$

$$\frac{\partial^2\Pi}{\partial D^2} = 2\sum_{s=1}^{n}W_x^{(s)}(\Theta_x^{(s)})^2 + 2\sum_{s=1}^{n}W_y^{(s)}(\Theta_y^{(s)})^2 \tag{A.21}$$

$$\frac{\partial^2\Pi}{\partial d\partial D} = -2\sum_{s=1}^{n}W_x^{(s)}\theta_x^{(s)}\Theta_x^{(s)} - 2\sum_{s=1}^{n}W_y^{(s)}\theta_y^{(s)}\Theta_y^{(s)} \tag{A.22}$$

$$\begin{aligned}
\frac{\partial^2\Pi}{\partial d\partial t_{\frac{\beta}{2}}} = \; & 2\sum_{s=1}^{n}W_x^{(s)}\left[(d\theta_x^{(s)} - D\Theta_x^{(s)} + \Delta x_{\mathrm{c}} - \Delta x^{(s)}) + d\theta_x^{(s)}\right]\frac{\partial\theta_x^{(s)}}{\partial t_{\frac{\beta}{2}}} \\
& +2\sum_{s=1}^{n}W_y^{(s)}\left[(d\theta_y^{(s)} - D\Theta_y^{(s)} + \Delta y_{\mathrm{c}} - \Delta y^{(s)}) + d\theta_y^{(s)}\right]\frac{\partial\theta_y^{(s)}}{\partial t_{\frac{\beta}{2}}}
\end{aligned} \tag{A.23}$$

$$\begin{aligned}
\frac{\partial^2\Pi}{\partial d\partial t_{\frac{\gamma}{2}}} = \; & 2\sum_{s=1}^{n}W_x^{(s)}\left[(d\theta_x^{(s)} - D\Theta_x^{(s)} + \Delta x_{\mathrm{c}} - \Delta x^{(s)}) + d\theta_x^{(s)}\right]\frac{\partial\theta_x^{(s)}}{\partial t_{\frac{\gamma}{2}}} \\
& +2\sum_{s=1}^{n}W_y^{(s)}\left[(d\theta_y^{(s)} - D\Theta_y^{(s)} + \Delta y_{\mathrm{c}} - \Delta y^{(s)}) + d\theta_y^{(s)}\right]\frac{\partial\theta_y^{(s)}}{\partial t_{\frac{\gamma}{2}}}
\end{aligned} \tag{A.24}$$

$$\frac{\partial^2\Pi}{\partial d\partial t_{\frac{B}{2}}} = -2D\left[\sum_{s=1}^{n}W_x^{(s)}\theta_x^{(s)}\frac{\partial\Theta_x^{(s)}}{\partial t_{\frac{B}{2}}} + \sum_{s=1}^{n}W_y^{(s)}\theta_y^{(s)}\frac{\partial\Theta_y^{(s)}}{\partial t_{\frac{B}{2}}}\right] \tag{A.25}$$

$$\frac{\partial^2\Pi}{\partial d\partial t_{\frac{\Gamma}{2}}} = -2D\left[\sum_{s=1}^{n} W_x^{(s)}\theta_x^{(s)}\frac{\partial\Theta_x^{(s)}}{\partial t_{\frac{\Gamma}{2}}} + \sum_{s=1}^{n} W_y^{(s)}\theta_y^{(s)}\frac{\partial\Theta_y^{(s)}}{\partial t_{\frac{\Gamma}{2}}}\right] \tag{A.26}$$

$$\frac{\partial^2\Pi}{\partial D\partial t_{\frac{\beta}{2}}} = -2d\left[\sum_{s=1}^{n} W_x^{(s)}\frac{\partial\theta_x^{(s)}}{\partial t_{\frac{\beta}{2}}}\Theta_x^{(s)} + \sum_{s=1}^{n} W_y^{(s)}\frac{\partial\theta_y^{(s)}}{\partial t_{\frac{\beta}{2}}}\Theta_y^{(s)}\right], \tag{A.27}$$

$$\frac{\partial^2\Pi}{\partial D\partial t_{\frac{\gamma}{2}}} = -2d\left[\sum_{s=1}^{n} W_x^{(s)}\frac{\partial\theta_x^{(s)}}{\partial t_{\frac{\gamma}{2}}}\Theta_x^{(s)} + \sum_{s=1}^{n} W_y^{(s)}\frac{\partial\theta_y^{(s)}}{\partial t_{\frac{\gamma}{2}}}\Theta_y^{(s)}\right], \tag{A.28}$$

$$\begin{aligned}\frac{\partial^2\Pi}{\partial D\partial t_{\frac{B}{2}}} = & -2\sum_{s=1}^{n} W_x^{(s)}\left[(d\theta_x^{(s)} - D\Theta_x^{(s)} + \Delta x_{\mathrm{c}} - \Delta x^{(s)}) - D\Theta_x^{(s)}\right]\frac{\partial\Theta_x^{(s)}}{\partial t_{\frac{B}{2}}} \\ & -2\sum_{s=1}^{n} W_y^{(s)}\left[(d\theta_y^{(s)} - D\Theta_y^{(s)} + \Delta y_{\mathrm{c}} - \Delta y^{(s)}) - D\Theta_y^{(s)}\right]\frac{\partial\Theta_y^{(s)}}{\partial t_{\frac{B}{2}}}\end{aligned} \tag{A.29}$$

$$\begin{aligned}\frac{\partial^2\Pi}{\partial D\partial t_{\frac{\Gamma}{2}}} = & -2\sum_{s=1}^{n} W_x^{(s)}\left[(d\theta_x^{(s)} - D\Theta_x^{(s)} + \Delta x_{\mathrm{c}} - \Delta x^{(s)}) - D\Theta_x^{(s)}\right]\frac{\partial\Theta_x^{(s)}}{\partial t_{\frac{\Gamma}{2}}} \\ & -2\sum_{s=1}^{n} W_y^{(s)}\left[(d\theta_y^{(s)} - D\Theta_y^{(s)} + \Delta y_{\mathrm{c}} - \Delta y^{(s)}) - D\Theta_y^{(s)}\right]\frac{\partial\Theta_y^{(s)}}{\partial t_{\frac{\Gamma}{2}}}\end{aligned} \tag{A.30}$$

$$\begin{aligned}\frac{\partial^2\Pi}{\partial d\partial l_{ij}^*} = & \ 2\sum_{s=1}^{n} W_x^{(s)}\left[(d\theta_x^{(s)} - D\Theta_x^{(s)} + \Delta x_{\mathrm{c}} - \Delta x^{(s)}) + d\theta_x^{(s)}\right]\frac{\partial\theta_x^{(s)}}{\partial l_{ij}^*} \\ & +2\sum_{s=1}^{n} W_y^{(s)}\left[(d\theta_y^{(s)} - D\Theta_y^{(s)} + \Delta y_{\mathrm{c}} - \Delta y^{(s)}) + d\theta_y^{(s)}\right]\frac{\partial\theta_y^{(s)}}{\partial l_{ij}^*}\end{aligned} \tag{A.31}$$

$$\frac{\partial^2\Pi}{\partial d\partial L_{ij}^*} = -2D\left[\sum_{s=1}^{n} W_x^{(s)}\theta_x^{(s)}\frac{\partial\Theta_x^{(s)}}{\partial L_{ij}^*} + \sum_{s=1}^{n} W_y^{(s)}\theta_y^{(s)}\frac{\partial\Theta_y^{(s)}}{\partial L_{ij}^*}\right] \tag{A.32}$$

$$\frac{\partial^2\Pi}{\partial D\partial l_{ij}^*} = -2d\left[\sum_{s=1}^{n} W_x^{(s)}\frac{\partial\theta_x^{(s)}}{\partial l_{ij}^*}\Theta_x^{(s)} + \sum_{s=1}^{n} W_y^{(s)}\frac{\partial\theta_y^{(s)}}{\partial l_{ij}^*}\Theta_y^{(s)}\right] \tag{A.33}$$

$$\begin{aligned}\frac{\partial^2\Pi}{\partial D\partial L_{ij}^*} = & -2\sum_{s=1}^{n} W_x^{(s)}\left[(d\theta_x^{(s)} - D\Theta_x^{(s)} + \Delta x_{\mathrm{c}} - \Delta x^{(s)}) - D\Theta_x^{(s)}\right]\frac{\partial\Theta_x^{(s)}}{\partial L_{ij}^*} \\ & -2\sum_{s=1}^{n} W_y^{(s)}\left[(d\theta_y^{(s)} - D\Theta_y^{(s)} + \Delta y_{\mathrm{c}} - \Delta y^{(s)}) - D\Theta_y^{(s)}\right]\frac{\partial\Theta_y^{(s)}}{\partial L_{ij}^*},\end{aligned} \tag{A.34}$$

$$\begin{aligned}\frac{\partial^2\Pi}{\partial l_{ij}^*\partial l_{pq}^*} = & \ 2\sum_{s=1}^{n} W_x^{(s)}\left[(d\theta_x^{(s)} - D\Theta_x^{(s)} + \Delta x_{\mathrm{c}} - \Delta x^{(s)})d\frac{\partial^2\theta_x^{(s)}}{\partial l_{ij}^*\partial l_{pq}^*} + d^2\frac{\partial\theta_x^{(s)}}{\partial l_{ij}^*}\frac{\partial\theta_x^{(s)}}{\partial l_{pq}^*}\right] \\ & +2\sum_{s=1}^{n} W_y^{(s)}\left[(d\theta_y^{(s)} - D\Theta_y^{(s)} + \Delta y_{\mathrm{c}} - \Delta y^{(s)})d\frac{\partial^2\theta_y^{(s)}}{\partial l_{ij}^*\partial l_{pq}^*} + d^2\frac{\partial\theta_y^{(s)}}{\partial l_{ij}^*}\frac{\partial\theta_y^{(s)}}{\partial l_{pq}^*}\right],\end{aligned} \tag{A.35}$$

$$\frac{\partial^2\Pi}{\partial L^*_{ij}\partial L^*_{pq}} = -2\sum_{s=1}^{n} W_x^{(s)}\left[(d\theta_x^{(s)} - D\Theta_x^{(s)} + \Delta x_c - \Delta x^{(s)})D\frac{\partial^2\Theta_x^{(s)}}{\partial L^*_{ij}\partial L^*_{pq}} - D^2\frac{\partial\Theta_x^{(s)}}{\partial L^*_{ij}}\frac{\partial\Theta_x^{(s)}}{\partial L^*_{pq}}\right] -2\sum_{s=1}^{n} W_y^{(s)}\left[(d\theta_y^{(s)} - D\Theta_y^{(s)} + \Delta y_c - \Delta y^{(s)})D\frac{\partial^2\Theta_y^{(s)}}{\partial L^*_{ij}\partial L^*_{pq}} - D^2\frac{\partial\Theta_y^{(s)}}{\partial L^*_{ij}}\frac{\partial\Theta_y^{(s)}}{\partial L^*_{pq}}\right]. \tag{A.36}$$

$$\frac{\partial^2\Pi}{\partial l^*_{ij}\partial L^*_{pq}} = -2dD\left[\sum_{s=1}^{n} W_x^{(s)}\frac{\partial\theta_x^{(s)}}{\partial l^*_{ij}}\frac{\partial\Theta_x^{(s)}}{\partial L^*_{pq}} + \sum_{s=1}^{n} W_y^{(s)}\frac{\partial\theta_y^{(s)}}{\partial l^*_{ij}}\frac{\partial\Theta_y^{(s)}}{\partial L^*_{pq}}\right], \tag{A.37}$$

$$\frac{\partial^2\theta_x^{(s)}}{\partial l^*_{ij}\partial l^*_{mn}} = \frac{\frac{\partial^2\xi_p^{(s)}}{\partial l^*_{ij}\partial l^*_{mn}}t_{1p}\xi_q^{(s)}t_{3q} - \xi_p^{(s)}t_{1p}\frac{\partial^2\xi_q^{(s)}}{\partial l^*_{ij}\partial l^*_{mn}}t_{3q} - \frac{\partial\xi_p^{(s)}}{\partial l^*_{ij}}t_{1p}\frac{\partial\xi_q^{(s)}}{\partial l^*_{mn}}t_{3q} - \frac{\partial\xi_p^{(s)}}{\partial l^*_{mn}}t_{1p}\frac{\partial\xi_q^{(s)}}{\partial l^*_{ij}}t_{3q}}{(\xi_r^{(s)}t_{3r})^2} +2\frac{\xi_p^{(s)}t_{1p}\frac{\partial\xi_q^{(s)}}{\partial l^*_{ij}}t_{3q}\frac{\partial\xi_k^{(s)}}{\partial l^*_{mn}}t_{3k}}{(\xi_r^{(s)}t_{3r})^3} \tag{A.38}$$

$$\frac{\partial^2\theta_y^{(s)}}{\partial l^*_{ij}\partial l^*_{mn}} = \frac{\frac{\partial^2\xi_p^{(s)}}{\partial l^*_{ij}\partial l^*_{mn}}t_{2p}\xi_q^{(s)}t_{3q} - \xi_p^{(s)}t_{2p}\frac{\partial^2\xi_q^{(s)}}{\partial l^*_{ij}\partial l^*_{mn}}t_{3q} - \frac{\partial\xi_p^{(s)}}{\partial l^*_{ij}}t_{2p}\frac{\partial\xi_q^{(s)}}{\partial l^*_{mn}}t_{3q} - \frac{\partial\xi_p^{(s)}}{\partial l^*_{mn}}t_{2p}\frac{\partial\xi_q^{(s)}}{\partial l^*_{ij}}t_{3q}}{(\xi_r^{(s)}t_{3r})^2} +2\frac{\xi_p^{(s)}t_{2p}\frac{\partial\xi_q^{(s)}}{\partial l^*_{ij}}t_{3q}\frac{\partial\xi_k^{(s)}}{\partial l^*_{mn}}t_{3k}}{(\xi_r^{(s)}t_{3r})^3} \tag{A.39}$$

$$\frac{\partial^2\Theta_x^{(s)}}{\partial L^*_{ij}\partial L^*_{mn}} = \frac{\frac{\partial^2\Xi_p^{(s)}}{\partial L^*_{ij}\partial L^*_{mn}}T_{1p}\Xi_q^{(s)}T_{3q} - \Xi_p^{(s)}T_{1p}\frac{\partial^2\Xi_q^{(s)}}{\partial L^*_{ij}\partial L^*_{mn}}T_{3q} - \frac{\partial\Xi_p^{(s)}}{\partial L^*_{ij}}T_{1p}\frac{\partial\Xi_q^{(s)}}{\partial L^*_{mn}}T_{3q} - \frac{\partial\Xi_p^{(s)}}{\partial L^*_{mn}}T_{1p}\frac{\partial\Xi_q^{(s)}}{\partial L^*_{ij}}T_{3q}}{(\Xi_r^{(s)}T_{3r})^2} +2\frac{\Xi_p^{(s)}T_{1p}\frac{\partial\Xi_q^{(s)}}{\partial L^*_{ij}}T_{3q}\frac{\partial\Xi_k^{(s)}}{\partial L^*_{mn}}T_{3k}}{(\Xi_r^{(s)}T_{3r})^3} \tag{A.40}$$

$$\frac{\partial^2\Theta_y^{(s)}}{\partial L^*_{ij}\partial L^*_{mn}} = \frac{\frac{\partial^2\Xi_p^{(s)}}{\partial L^*_{ij}\partial L^*_{mn}}T_{2p}\Xi_q^{(s)}T_{3q} - \Xi_p^{(s)}T_{2p}\frac{\partial^2\Xi_q^{(s)}}{\partial L^*_{ij}\partial L^*_{mn}}T_{3q} - \frac{\partial\Xi_p^{(s)}}{\partial L^*_{ij}}T_{2p}\frac{\partial\Xi_q^{(s)}}{\partial L^*_{mn}}T_{3q} - \frac{\partial\Xi_p^{(s)}}{\partial L^*_{mn}}T_{2p}\frac{\partial\Xi_q^{(s)}}{\partial L^*_{ij}}T_{3q}}{(\Xi_r^{(s)}T_{3r})^2} +2\frac{\Xi_p^{(s)}T_{2p}\frac{\partial\Xi_q^{(s)}}{\partial L^*_{ij}}T_{3q}\frac{\partial\Xi_k^{(s)}}{\partial L^*_{mn}}T_{3k}}{(\Xi_r^{(s)}T_{3r})^3} \tag{A.41}$$

$$\frac{\partial^2\xi_p^{(s)}}{\partial l^*_{ij}\partial l^*_{mn}} = \frac{\partial^2\Xi_p^{(s)}}{\partial L^*_{ij}\partial L^*_{mn}} = 2h_j^{(s)}h_n^{(s)}(\delta_{2p}\delta_{im} - \delta_{2i}\delta_{pm} - \delta_{pi}\delta_{2m}) \tag{A.42}$$

$$\frac{\partial^2\Pi}{\partial t_{\frac{\beta}{2}}\partial l^*_{ij}} = 2\sum_{s=1}^{n} W_x^{(s)}\left[(d\theta_x^{(s)} - D\Theta_x^{(s)} + \Delta x_c - \Delta x^{(s)})d\frac{\partial^2\theta_x^{(s)}}{\partial t_{\frac{\beta}{2}}\partial l^*_{ij}} + d^2\frac{\partial\theta_x^{(s)}}{\partial t_{\frac{\beta}{2}}}\frac{\partial\theta_x^{(s)}}{\partial l^*_{ij}}\right] +2\sum_{s=1}^{n} W_y^{(s)}\left[(d\theta_y^{(s)} - D\Theta_y^{(s)} + \Delta y_c - \Delta y^{(s)})d\frac{\partial^2\theta_y^{(s)}}{\partial t_{\frac{\beta}{2}}\partial l^*_{ij}} + d^2\frac{\partial\theta_y^{(s)}}{\partial t_{\frac{\beta}{2}}}\frac{\partial\theta_y^{(s)}}{\partial l^*_{ij}}\right] \tag{A.43}$$

$$\frac{\partial^2\Pi}{\partial t_{\frac{\gamma}{2}}\partial l^*_{ij}} = 2\sum_{s=1}^{n} W_x^{(s)}\left[(d\theta_x^{(s)} - D\Theta_x^{(s)} + \Delta x_c - \Delta x^{(s)})d\frac{\partial^2\theta_x^{(s)}}{\partial t_{\frac{\gamma}{2}}\partial l^*_{ij}} + d^2\frac{\partial\theta_x^{(s)}}{\partial t_{\frac{\gamma}{2}}}\frac{\partial\theta_x^{(s)}}{\partial l^*_{ij}}\right] +2\sum_{s=1}^{n} W_y^{(s)}\left[(d\theta_y^{(s)} - D\Theta_y^{(s)} + \Delta y_c - \Delta y^{(s)})d\frac{\partial^2\theta_y^{(s)}}{\partial t_{\frac{\gamma}{2}}\partial l^*_{ij}} + d^2\frac{\partial\theta_y^{(s)}}{\partial t_{\frac{\gamma}{2}}}\frac{\partial\theta_y^{(s)}}{\partial l^*_{ij}}\right] \tag{A.44}$$

$$\frac{\partial^2\Pi}{\partial t_{\frac{\beta}{2}}\partial L^*_{ij}} = -2dD\left[\sum_{s=1}^{n} W_x^{(s)}\frac{\partial\theta_x^{(s)}}{\partial t_{\frac{\beta}{2}}}\frac{\partial\Theta_x^{(s)}}{\partial L^*_{ij}} + \sum_{s=1}^{n} W_y^{(s)}\frac{\partial\theta_y^{(s)}}{\partial t_{\frac{\beta}{2}}}\frac{\partial\Theta_y^{(s)}}{\partial L^*_{ij}}\right] \tag{A.45}$$

$$\frac{\partial^2\Pi}{\partial t_{\frac{\gamma}{2}}\partial L^*_{ij}} = -2dD\left[\sum_{s=1}^{n} W_x^{(s)}\frac{\partial\theta_x^{(s)}}{\partial t_{\frac{\gamma}{2}}}\frac{\partial\Theta_x^{(s)}}{\partial L^*_{ij}} + \sum_{s=1}^{n} W_y^{(s)}\frac{\partial\theta_y^{(s)}}{\partial t_{\frac{\gamma}{2}}}\frac{\partial\Theta_y^{(s)}}{\partial L^*_{ij}}\right] \tag{A.46}$$

$$\frac{\partial^2\Pi}{\partial t_{\frac{B}{2}}\partial l^*_{ij}} = -2dD\left[\sum_{s=1}^{n} W_x^{(s)}\frac{\partial\theta_x^{(s)}}{\partial l^*_{ij}}\frac{\partial\Theta_x^{(s)}}{\partial t_{\frac{B}{2}}} + \sum_{s=1}^{n} W_y^{(s)}\frac{\partial\theta_y^{(s)}}{\partial l^*_{ij}}\frac{\partial\Theta_y^{(s)}}{\partial t_{\frac{B}{2}}}\right] \tag{A.47}$$

$$\frac{\partial^2\Pi}{\partial t_{\frac{\Gamma}{2}}\partial l^*_{ij}} = -2dD\left[\sum_{s=1}^{n} W_x^{(s)}\frac{\partial\theta_x^{(s)}}{\partial l^*_{ij}}\frac{\partial\Theta_x^{(s)}}{\partial t_{\frac{\Gamma}{2}}} + \sum_{s=1}^{n} W_y^{(s)}\frac{\partial\theta_y^{(s)}}{\partial l^*_{ij}}\frac{\partial\Theta_y^{(s)}}{\partial t_{\frac{\Gamma}{2}}}\right] \tag{A.48}$$

$$\frac{\partial^2\Pi}{\partial t_{\frac{B}{2}}\partial L^*_{ij}} = -2\sum_{s=1}^{n} W_x^{(s)}\left[(d\theta_x^{(s)} - D\Theta_x^{(s)} + \Delta x_c - \Delta x^{(s)})D\frac{\partial^2\Theta_x^{(s)}}{\partial t_{\frac{B}{2}}\partial L^*_{ij}} - D^2\frac{\partial\Theta_x^{(s)}}{\partial t_{\frac{B}{2}}}\frac{\partial\Theta_x^{(s)}}{\partial L^*_{ij}}\right] -2\sum_{s=1}^{n} W_y^{(s)}\left[(d\theta_y^{(s)} - D\Theta_y^{(s)} + \Delta y_c - \Delta y^{(s)})D\frac{\partial^2\Theta_y^{(s)}}{\partial t_{\frac{B}{2}}\partial L^*_{ij}} - D^2\frac{\partial\Theta_y^{(s)}}{\partial t_{\frac{B}{2}}}\frac{\partial\Theta_y^{(s)}}{\partial L^*_{ij}}\right], \tag{A.49}$$

$$\frac{\partial^2\Pi}{\partial t_{\frac{\Gamma}{2}}\partial L^*_{ij}} = -2\sum_{s=1}^{n} W_x^{(s)}\left[(d\theta_x^{(s)} - D\Theta_x^{(s)} + \Delta x_c - \Delta x^{(s)})D\frac{\partial^2\Theta_x^{(s)}}{\partial t_{\frac{\Gamma}{2}}\partial L^*_{ij}} - D^2\frac{\partial\Theta_x^{(s)}}{\partial t_{\frac{\Gamma}{2}}}\frac{\partial\Theta_x^{(s)}}{\partial L^*_{ij}}\right] -2\sum_{s=1}^{n} W_y^{(s)}\left[(d\theta_y^{(s)} - D\Theta_y^{(s)} + \Delta y_c - \Delta y^{(s)})D\frac{\partial^2\Theta_y^{(s)}}{\partial t_{\frac{\Gamma}{2}}\partial L^*_{ij}} - D^2\frac{\partial\Theta_y^{(s)}}{\partial t_{\frac{\Gamma}{2}}}\frac{\partial\Theta_y^{(s)}}{\partial L^*_{ij}}\right], \tag{A.50}$$

$$\frac{\partial^2\theta_x^{(s)}}{\partial t_{\frac{\beta}{2}}\partial l^*_{ij}} = \frac{\frac{\partial\xi_p^{(s)}}{\partial l^*_{ij}}\frac{\partial t_{1p}}{\partial t_{\frac{\beta}{2}}}\xi_q^{(s)}t_{3q} - \frac{\partial\xi_p^{(s)}}{\partial l^*_{ij}}t_{1p}\xi_q^{(s)}\frac{\partial t_{3q}}{\partial t_{\frac{\beta}{2}}} - \xi_p^{(s)}\frac{\partial t_{1p}}{\partial t_{\frac{\beta}{2}}}\frac{\partial\xi_q^{(s)}}{\partial l^*_{ij}}t_{3q} - \xi_p^{(s)}t_{1p}\frac{\partial\xi_q^{(s)}}{\partial l^*_{ij}}\frac{\partial t_{3q}}{\partial t_{\frac{\beta}{2}}}}{(\xi_r^{(s)}t_{3r})^2} +2\frac{\xi_p^{(s)}t_{1p}\xi_q^{(s)}\frac{\partial t_{3q}}{\partial t_{\frac{\beta}{2}}}\frac{\partial\xi_k^{(s)}}{\partial l^*_{ij}}t_{3k}}{(\xi_r^{(s)}t_{3r})^3} \tag{A.51}$$

$$\frac{\partial^2\theta_x^{(s)}}{\partial t_{\frac{\gamma}{2}}\partial l_{ij}^*} = \frac{\frac{\partial\xi_p^{(s)}}{\partial l_{ij}^*}\frac{\partial t_{1p}}{\partial t_{\frac{\gamma}{2}}}\xi_q^{(s)}t_{3q} - \frac{\partial\xi_p^{(s)}}{\partial l_{ij}^*}t_{1p}\xi_q^{(s)}\frac{\partial t_{3q}}{\partial t_{\frac{\gamma}{2}}} - \xi_p^{(s)}\frac{\partial t_{1p}}{\partial t_{\frac{\gamma}{2}}}\frac{\partial\xi_q^{(s)}}{\partial l_{ij}^*}t_{3q} - \xi_p^{(s)}t_{1p}\frac{\partial\xi_q^{(s)}}{\partial l_{ij}^*}\frac{\partial t_{3q}}{\partial t_{\frac{\gamma}{2}}}}{(\xi_r^{(s)}t_{3r})^2} + 2\frac{\xi_p^{(s)}t_{1p}\xi_q^{(s)}\frac{\partial t_{3q}}{\partial t_{\frac{\gamma}{2}}}\frac{\partial\xi_k^{(s)}}{\partial l_{ij}^*}t_{3k}}{(\xi_r^{(s)}t_{3r})^3} \tag{A.52}$$

$$\frac{\partial^2\theta_y^{(s)}}{\partial t_{\frac{\beta}{2}}\partial l_{ij}^*} = \frac{\frac{\partial\xi_p^{(s)}}{\partial l_{ij}^*}\frac{\partial t_{2p}}{\partial t_{\frac{\beta}{2}}}\xi_q^{(s)}t_{3q} - \frac{\partial\xi_p^{(s)}}{\partial l_{ij}^*}t_{2p}\xi_q^{(s)}\frac{\partial t_{3q}}{\partial t_{\frac{\beta}{2}}} - \xi_p^{(s)}\frac{\partial t_{2p}}{\partial t_{\frac{\beta}{2}}}\frac{\partial\xi_q^{(s)}}{\partial l_{ij}^*}t_{3q} - \xi_p^{(s)}t_{2p}\frac{\partial\xi_q^{(s)}}{\partial l_{ij}^*}\frac{\partial t_{3q}}{\partial t_{\frac{\beta}{2}}}}{(\xi_r^{(s)}t_{3r})^2} + 2\frac{\xi_p^{(s)}t_{2p}\xi_q^{(s)}\frac{\partial t_{3q}}{\partial t_{\frac{\beta}{2}}}\frac{\partial\xi_k^{(s)}}{\partial l_{ij}^*}t_{3k}}{(\xi_r^{(s)}t_{3r})^3} \tag{A.53}$$

$$\frac{\partial^2\theta_y^{(s)}}{\partial t_{\frac{\gamma}{2}}\partial l_{ij}^*} = \frac{\frac{\partial\xi_p^{(s)}}{\partial l_{ij}^*}\frac{\partial t_{2p}}{\partial t_{\frac{\gamma}{2}}}\xi_q^{(s)}t_{3q} - \frac{\partial\xi_p^{(s)}}{\partial l_{ij}^*}t_{2p}\xi_q^{(s)}\frac{\partial t_{3q}}{\partial t_{\frac{\gamma}{2}}} - \xi_p^{(s)}\frac{\partial t_{2p}}{\partial t_{\frac{\gamma}{2}}}\frac{\partial\xi_q^{(s)}}{\partial l_{ij}^*}t_{3q} - \xi_p^{(s)}t_{2p}\frac{\partial\xi_q^{(s)}}{\partial l_{ij}^*}\frac{\partial t_{3q}}{\partial t_{\frac{\gamma}{2}}}}{(\xi_r^{(s)}t_{3r})^2} + 2\frac{\xi_p^{(s)}t_{2p}\xi_q^{(s)}\frac{\partial t_{3q}}{\partial t_{\frac{\gamma}{2}}}\frac{\partial\xi_k^{(s)}}{\partial l_{ij}^*}t_{3k}}{(\xi_r^{(s)}t_{3r})^3} \tag{A.54}$$

$$\frac{\partial^2\Theta_x^{(s)}}{\partial t_{\frac{B}{2}}\partial L_{ij}^*} = \frac{\frac{\partial\Xi_p^{(s)}}{\partial L_{ij}^*}\frac{\partial T_{1p}}{\partial t_{\frac{B}{2}}}\Xi_q^{(s)}T_{3q} - \frac{\partial\Xi_p^{(s)}}{\partial L_{ij}^*}T_{1p}\Xi_q^{(s)}\frac{\partial T_{3q}}{\partial t_{\frac{B}{2}}} - \Xi_p^{(s)}\frac{\partial T_{1p}}{\partial t_{\frac{B}{2}}}\frac{\partial\Xi_q^{(s)}}{\partial L_{ij}^*}T_{3q} - \Xi_p^{(s)}T_{1p}\frac{\partial\Xi_q^{(s)}}{\partial L_{ij}^*}\frac{\partial T_{3q}}{\partial t_{\frac{B}{2}}}}{(\Xi_r^{(s)}T_{3r})^2} + 2\frac{\Xi_p^{(s)}T_{1p}\Xi_q^{(s)}\frac{\partial T_{3q}}{\partial t_{\frac{B}{2}}}\frac{\partial\Xi_k^{(s)}}{\partial L_{ij}^*}T_{3k}}{(\Xi_r^{(s)}T_{3r})^3} \tag{A.55}$$

$$\frac{\partial^2\Theta_x^{(s)}}{\partial t_{\frac{\Gamma}{2}}\partial L_{ij}^*} = \frac{\frac{\partial\Xi_p^{(s)}}{\partial L_{ij}^*}\frac{\partial T_{1p}}{\partial t_{\frac{\Gamma}{2}}}\Xi_q^{(s)}T_{3q} - \frac{\partial\Xi_p^{(s)}}{\partial L_{ij}^*}T_{1p}\Xi_q^{(s)}\frac{\partial T_{3q}}{\partial t_{\frac{\Gamma}{2}}} - \Xi_p^{(s)}\frac{\partial T_{1p}}{\partial t_{\frac{\Gamma}{2}}}\frac{\partial\Xi_q^{(s)}}{\partial L_{ij}^*}T_{3q} - \Xi_p^{(s)}T_{1p}\frac{\partial\Xi_q^{(s)}}{\partial L_{ij}^*}\frac{\partial T_{3q}}{\partial t_{\frac{\Gamma}{2}}}}{(\Xi_r^{(s)}T_{3r})^2} + 2\frac{\Xi_p^{(s)}T_{1p}\Xi_q^{(s)}\frac{\partial T_{3q}}{\partial t_{\frac{\Gamma}{2}}}\frac{\partial\Xi_k^{(s)}}{\partial L_{ij}^*}T_{3k}}{(\Xi_r^{(s)}T_{3r})^3} \tag{A.56}$$

$$\frac{\partial^2\Theta_y^{(s)}}{\partial t_{\frac{B}{2}}\partial L_{ij}^*} = \frac{\frac{\partial\Xi_p^{(s)}}{\partial L_{ij}^*}\frac{\partial T_{2p}}{\partial t_{\frac{B}{2}}}\Xi_q^{(s)}T_{3q} - \frac{\partial\Xi_p^{(s)}}{\partial L_{ij}^*}T_{2p}\Xi_q^{(s)}\frac{\partial T_{3q}}{\partial t_{\frac{B}{2}}} - \Xi_p^{(s)}\frac{\partial T_{2p}}{\partial t_{\frac{B}{2}}}\frac{\partial\Xi_q^{(s)}}{\partial L_{ij}^*}T_{3q} - \Xi_p^{(s)}T_{2p}\frac{\partial\Xi_q^{(s)}}{\partial L_{ij}^*}\frac{\partial T_{3q}}{\partial t_{\frac{B}{2}}}}{(\Xi_r^{(s)}T_{3r})^2} + 2\frac{\Xi_p^{(s)}T_{2p}\Xi_q^{(s)}\frac{\partial T_{3q}}{\partial t_{\frac{B}{2}}}\frac{\partial\Xi_k^{(s)}}{\partial L_{ij}^*}T_{3k}}{(\Xi_r^{(s)}T_{3r})^3} \tag{A.57}$$

$$\frac{\partial^2\Theta_y^{(s)}}{\partial t_{\frac{\Gamma}{2}}\partial L_{ij}^*} = \frac{\frac{\partial\Xi_p^{(s)}}{\partial L_{ij}^*}\frac{\partial T_{2p}}{\partial t_{\frac{\Gamma}{2}}}\Xi_q^{(s)}T_{3q} - \frac{\partial\Xi_p^{(s)}}{\partial L_{ij}^*}T_{2p}\Xi_q^{(s)}\frac{\partial T_{3q}}{\partial t_{\frac{\Gamma}{2}}} - \Xi_p^{(s)}\frac{\partial T_{2p}}{\partial t_{\frac{\Gamma}{2}}}\frac{\partial\Xi_q^{(s)}}{\partial L_{ij}^*}T_{3q} - \Xi_p^{(s)}T_{2p}\frac{\partial\Xi_q^{(s)}}{\partial L_{ij}^*}\frac{\partial T_{3q}}{\partial t_{\frac{\Gamma}{2}}}}{(\Xi_r^{(s)}T_{3r})^2} + 2\frac{\Xi_p^{(s)}T_{2p}\Xi_q^{(s)}\frac{\partial T_{3q}}{\partial t_{\frac{\Gamma}{2}}}\frac{\partial\Xi_k^{(s)}}{\partial L_{ij}^*}T_{3k}}{(\Xi_r^{(s)}T_{3r})^3} \tag{A.58}$$

$$\frac{\partial^2\Pi}{\partial t_{\frac{\beta}{2}}^2} = 2\sum_{s=1}^{n}W_x^{(s)}\left[(d\theta_x^{(s)} - D\Theta_x^{(s)} + \Delta x_c - \Delta x^{(s)})d\frac{\partial^2\theta_x^{(s)}}{\partial t_{\frac{\beta}{2}}^2} + d^2\left(\frac{\partial\theta_x^{(s)}}{\partial t_{\frac{\beta}{2}}}\right)^2\right] + 2\sum_{s=1}^{n}W_y^{(s)}\left[(d\theta_y^{(s)} - D\Theta_y^{(s)} + \Delta y_c - \Delta y^{(s)})d\frac{\partial^2\theta_y^{(s)}}{\partial t_{\frac{\beta}{2}}^2} + d^2\left(\frac{\partial\theta_y^{(s)}}{\partial t_{\frac{\beta}{2}}}\right)^2\right], \tag{A.59}$$

$$\frac{\partial^2\Pi}{\partial t_{\frac{\gamma}{2}}^2} = 2\sum_{s=1}^{n}W_x^{(s)}\left[(d\theta_x^{(s)} - D\Theta_x^{(s)} + \Delta x_c - \Delta x^{(s)})d\frac{\partial^2\theta_x^{(s)}}{\partial t_{\frac{\gamma}{2}}^2} + d^2\left(\frac{\partial\theta_x^{(s)}}{\partial t_{\frac{\gamma}{2}}}\right)^2\right] + 2\sum_{s=1}^{n}W_y^{(s)}\left[(d\theta_y^{(s)} - D\Theta_y^{(s)} + \Delta y_c - \Delta y^{(s)})d\frac{\partial^2\theta_y^{(s)}}{\partial t_{\frac{\gamma}{2}}^2} + d^2\left(\frac{\partial\theta_y^{(s)}}{\partial t_{\frac{\gamma}{2}}}\right)^2\right], \tag{A.60}$$

$$\frac{\partial^2\Pi}{\partial t_{\frac{B}{2}}^2} = -2\sum_{s=1}^{n}W_x^{(s)}\left[(d\theta_x^{(s)} - D\Theta_x^{(s)} + \Delta x_c - \Delta x^{(s)})D\frac{\partial^2\Theta_x^{(s)}}{\partial t_{\frac{B}{2}}^2} - D^2\left(\frac{\partial\Theta_x^{(s)}}{\partial t_{\frac{B}{2}}}\right)^2\right] - 2\sum_{s=1}^{n}W_y^{(s)}\left[(d\theta_x^{(s)} - D\Theta_x^{(s)} + \Delta x_c - \Delta x^{(s)})D\frac{\partial^2\Theta_y^{(s)}}{\partial t_{\frac{B}{2}}^2} - D^2\left(\frac{\partial\Theta_y^{(s)}}{\partial t_{\frac{B}{2}}}\right)^2\right], \tag{A.61}$$

$$\frac{\partial^2\Pi}{\partial t_{\frac{\Gamma}{2}}^2} = -2\sum_{s=1}^{n}W_x^{(s)}\left[(d\theta_x^{(s)} - D\Theta_x^{(s)} + \Delta x_c - \Delta x^{(s)})D\frac{\partial^2\Theta_x^{(s)}}{\partial t_{\frac{\Gamma}{2}}^2} - D^2\left(\frac{\partial\Theta_x^{(s)}}{\partial t_{\frac{\Gamma}{2}}}\right)^2\right] - 2\sum_{s=1}^{n}W_y^{(s)}\left[(d\theta_x^{(s)} - D\Theta_x^{(s)} + \Delta x_c - \Delta x^{(s)})D\frac{\partial^2\Theta_y^{(s)}}{\partial t_{\frac{\Gamma}{2}}^2} - D^2\left(\frac{\partial\Theta_y^{(s)}}{\partial t_{\frac{\Gamma}{2}}}\right)^2\right], \tag{A.62}$$

$$\frac{\partial^2\Pi}{\partial t_{\frac{B}{2}}\partial t_{\frac{\beta}{2}}} = -2dD\left[\sum_{s=1}^{n}W_x^{(s)}\frac{\partial\theta_x^{(s)}}{\partial t_{\frac{\beta}{2}}}\frac{\partial\Theta_x^{(s)}}{\partial t_{\frac{B}{2}}} + \sum_{s=1}^{n}W_y^{(s)}\frac{\partial\theta_y^{(s)}}{\partial t_{\frac{\beta}{2}}}\frac{\partial\Theta_y^{(s)}}{\partial t_{\frac{B}{2}}}\right] \tag{A.63}$$

$$\frac{\partial^2\Pi}{\partial t_{\frac{\Gamma}{2}}\partial t_{\frac{\gamma}{2}}} = -2dD\left[\sum_{s=1}^{n}W_x^{(s)}\frac{\partial\theta_x^{(s)}}{\partial t_{\frac{\gamma}{2}}}\frac{\partial\Theta_x^{(s)}}{\partial t_{\frac{\Gamma}{2}}} + \sum_{s=1}^{n}W_y^{(s)}\frac{\partial\theta_y^{(s)}}{\partial t_{\frac{\gamma}{2}}}\frac{\partial\Theta_y^{(s)}}{\partial t_{\frac{\Gamma}{2}}}\right] \tag{A.64}$$

$$\frac{\partial^2\theta_x^{(s)}}{\partial t_{\frac{\beta}{2}}^2} = \frac{\xi_i^{(s)}\frac{\partial^2 t_{1i}}{\partial t_{\frac{\beta}{2}}^2}\xi_j^{(s)}t_{3j} - 2\xi_i^{(s)}\frac{\partial t_{1i}}{\partial t_{\frac{\beta}{2}}}\xi_j^{(s)}\frac{\partial t_{3j}}{\partial t_{\frac{\beta}{2}}} - \xi_i^{(s)}t_{1i}\xi_j^{(s)}\frac{\partial^2 t_{3j}}{\partial t_{\frac{\beta}{2}}^2}}{(\xi_r^{(s)}t_{3r})^2} + 2\frac{\xi_i^{(s)}t_{1i}\xi_j^{(s)}\frac{\partial t_{3j}}{\partial t_{\frac{\beta}{2}}}\xi_k^{(s)}\frac{\partial t_{3k}}{\partial t_{\frac{\beta}{2}}}}{(\xi_r^{(s)}t_{3r})^3} \tag{A.65}$$

$$\frac{\partial^2\theta_x^{(s)}}{\partial t_{\frac{\gamma}{2}}^2} = \frac{\xi_i^{(s)}\frac{\partial^2 t_{1i}}{\partial t_{\frac{\gamma}{2}}^2}\xi_j^{(s)}t_{3j} - 2\xi_i^{(s)}\frac{\partial t_{1i}}{\partial t_{\frac{\gamma}{2}}}\xi_j^{(s)}\frac{\partial t_{3j}}{\partial t_{\frac{\gamma}{2}}} - \xi_i^{(s)}t_{1i}\xi_j^{(s)}\frac{\partial^2 t_{3j}}{\partial t_{\frac{\gamma}{2}}^2}}{(\xi_r^{(s)}t_{3r})^2} + 2\frac{\xi_i^{(s)}t_{1i}\xi_j^{(s)}\frac{\partial t_{3j}}{\partial t_{\frac{\gamma}{2}}}\xi_k^{(s)}\frac{\partial t_{3k}}{\partial t_{\frac{\gamma}{2}}}}{(\xi_r^{(s)}t_{3r})^3} \tag{A.66}$$

$$\frac{\partial^2\theta_y^{(s)}}{\partial t_{\frac{\beta}{2}}^2} = \frac{\xi_i^{(s)}\frac{\partial^2 t_{2i}}{\partial t_{\frac{\beta}{2}}^2}\xi_j^{(s)}t_{3j} - 2\xi_i^{(s)}\frac{\partial t_{2i}}{\partial t_{\frac{\beta}{2}}}\xi_j^{(s)}\frac{\partial t_{3j}}{\partial t_{\frac{\beta}{2}}} - \xi_i^{(s)}t_{2i}\xi_j^{(s)}\frac{\partial^2 t_{3j}}{\partial t_{\frac{\beta}{2}}^2}}{(\xi_r^{(s)}t_{3r})^2} + 2\frac{\xi_i^{(s)}t_{2i}\xi_j^{(s)}\frac{\partial t_{3j}}{\partial t_{\frac{\beta}{2}}}\xi_k^{(s)}\frac{\partial t_{3k}}{\partial t_{\frac{\beta}{2}}}}{(\xi_r^{(s)}t_{3r})^3} \tag{A.67}$$

$$\frac{\partial^2\theta_y^{(s)}}{\partial t_{\frac{\gamma}{2}}^2} = \frac{\xi_i^{(s)}\frac{\partial^2 t_{2i}}{\partial t_{\frac{\gamma}{2}}^2}\xi_j^{(s)}t_{3j} - 2\xi_i^{(s)}\frac{\partial t_{2i}}{\partial t_{\frac{\gamma}{2}}}\xi_j^{(s)}\frac{\partial t_{3j}}{\partial t_{\frac{\gamma}{2}}} - \xi_i^{(s)}t_{2i}\xi_j^{(s)}\frac{\partial^2 t_{3j}}{\partial t_{\frac{\gamma}{2}}^2}}{(\xi_r^{(s)}t_{3r})^2} + 2\frac{\xi_i^{(s)}t_{2i}\xi_j^{(s)}\frac{\partial t_{3j}}{\partial t_{\frac{\gamma}{2}}}\xi_k^{(s)}\frac{\partial t_{3k}}{\partial t_{\frac{\gamma}{2}}}}{(\xi_r^{(s)}t_{3r})^3} \tag{A.68}$$

$$\frac{\partial^2\Theta_x^{(s)}}{\partial t_{\frac{B}{2}}^2} = \frac{\Xi_i^{(s)}\frac{\partial^2 T_{1i}}{\partial t_{\frac{B}{2}}^2}\Xi_j^{(s)}T_{3j} - 2\Xi_i^{(s)}\frac{\partial T_{1i}}{\partial t_{\frac{B}{2}}}\Xi_j^{(s)}\frac{\partial T_{3j}}{\partial t_{\frac{B}{2}}} - \Xi_i^{(s)}T_{1i}\Xi_j^{(s)}\frac{\partial^2 T_{3j}}{\partial t_{\frac{B}{2}}^2}}{(\Xi_r^{(s)}T_{3r})^2} + 2\frac{\Xi_i^{(s)}T_{1i}\Xi_j^{(s)}\frac{\partial T_{3j}}{\partial t_{\frac{B}{2}}}\Xi_k^{(s)}\frac{\partial T_{3k}}{\partial t_{\frac{B}{2}}}}{(\Xi_r^{(s)}T_{3r})^3} \tag{A.69}$$

$$\frac{\partial^2\Theta_x^{(s)}}{\partial t_{\frac{\Gamma}{2}}^2} = \frac{\Xi_i^{(s)}\frac{\partial^2 T_{1i}}{\partial t_{\frac{\Gamma}{2}}^2}\Xi_j^{(s)}T_{3j} - 2\Xi_i^{(s)}\frac{\partial T_{1i}}{\partial t_{\frac{\Gamma}{2}}}\Xi_j^{(s)}\frac{\partial T_{3j}}{\partial t_{\frac{\Gamma}{2}}} - \Xi_i^{(s)}T_{1i}\Xi_j^{(s)}\frac{\partial^2 T_{3j}}{\partial t_{\frac{\Gamma}{2}}^2}}{(\Xi_r^{(s)}T_{3r})^2} + 2\frac{\Xi_i^{(s)}T_{1i}\Xi_j^{(s)}\frac{\partial T_{3j}}{\partial t_{\frac{\Gamma}{2}}}\Xi_k^{(s)}\frac{\partial T_{3k}}{\partial t_{\frac{\Gamma}{2}}}}{(\Xi_r^{(s)}T_{3r})^3} \tag{A.70}$$

$$\frac{\partial^2\Theta_y^{(s)}}{\partial t_{\frac{B}{2}}^2} = \frac{\Xi_i^{(s)}\frac{\partial^2 T_{2i}}{\partial t_{\frac{B}{2}}^2}\Xi_j^{(s)}T_{3j} - 2\Xi_i^{(s)}\frac{\partial T_{2i}}{\partial t_{\frac{B}{2}}}\Xi_j^{(s)}\frac{\partial T_{3j}}{\partial t_{\frac{B}{2}}} - \Xi_i^{(s)}T_{2i}\Xi_j^{(s)}\frac{\partial^2 T_{3j}}{\partial t_{\frac{B}{2}}^2}}{(\Xi_r^{(s)}T_{3r})^2} + 2\frac{\Xi_i^{(s)}T_{2i}\Xi_j^{(s)}\frac{\partial T_{3j}}{\partial t_{\frac{\beta}{2}}}\Xi_k^{(s)}\frac{\partial T_{3k}}{\partial t_{\frac{B}{2}}}}{(\Xi_r^{(s)}T_{3r})^3} \tag{A.71}$$

$$\frac{\partial^2\Theta_y^{(s)}}{\partial t_{\frac{\Gamma}{2}}^2} = \frac{\Xi_i^{(s)}\frac{\partial^2 T_{2i}}{\partial t_{\frac{\Gamma}{2}}^2}\Xi_j^{(s)}T_{3j} - 2\Xi_i^{(s)}\frac{\partial T_{2i}}{\partial t_{\frac{\Gamma}{2}}}\Xi_j^{(s)}\frac{\partial T_{3j}}{\partial t_{\frac{\Gamma}{2}}} - \Xi_i^{(s)}T_{2i}\Xi_j^{(s)}\frac{\partial^2 T_{3j}}{\partial t_{\frac{\Gamma}{2}}^2}}{(\Xi_r^{(s)}T_{3r})^2} + 2\frac{\Xi_i^{(s)}T_{2i}\Xi_j^{(s)}\frac{\partial T_{3j}}{\partial t_{\frac{\beta}{2}}}\Xi_k^{(s)}\frac{\partial T_{3k}}{\partial t_{\frac{\Gamma}{2}}}}{(\Xi_r^{(s)}T_{3r})^3} \tag{A.72}$$

$$\begin{aligned}\frac{\partial^2\Pi}{\partial t_{\frac{\beta}{2}}\partial t_{\frac{\gamma}{2}}} = \; & 2\sum_{s=1}^{n} W_x^{(s)}\left[(d\theta_x^{(s)} - D\Theta_x^{(s)} + \Delta x_c - \Delta x^{(s)})d\frac{\partial^2\theta_x^{(s)}}{\partial t_{\frac{\beta}{2}}\partial t_{\frac{\gamma}{2}}} + d^2\frac{\partial\theta_x^{(s)}}{\partial t_{\frac{\beta}{2}}}\frac{\partial\theta_x^{(s)}}{\partial t_{\frac{\gamma}{2}}}\right] \\ & +2\sum_{s=1}^{n} W_y^{(s)}\left[(d\theta_y^{(s)} - D\Theta_y^{(s)} + \Delta y_c - \Delta y^{(s)})d\frac{\partial^2\theta_y^{(s)}}{\partial t_{\frac{\beta}{2}}\partial t_{\frac{\gamma}{2}}} + d^2\frac{\partial\theta_y^{(s)}}{\partial t_{\frac{\beta}{2}}}\frac{\partial\theta_y^{(s)}}{\partial t_{\frac{\gamma}{2}}}\right],\end{aligned} \tag{A.73}$$

$$\frac{\partial^2\Pi}{\partial t_{\frac{\beta}{2}}\partial t_{\frac{\Gamma}{2}}} = -2dD\left[\sum_{s=1}^{n} W_x^{(s)}\frac{\partial\theta_x^{(s)}}{\partial t_{\frac{\beta}{2}}}\frac{\partial\Theta_x^{(s)}}{\partial t_{\frac{\Gamma}{2}}} + \sum_{s=1}^{n} W_y^{(s)}\frac{\partial\theta_y^{(s)}}{\partial t_{\frac{\beta}{2}}}\frac{\partial\Theta_y^{(s)}}{\partial t_{\frac{\Gamma}{2}}}\right] \tag{A.74}$$

$$\frac{\partial^2\Pi}{\partial t_{\frac{B}{2}}\partial t_{\frac{\gamma}{2}}} = -2dD\left[\sum_{s=1}^{n} W_x^{(s)}\frac{\partial\theta_x^{(s)}}{\partial t_{\frac{\gamma}{2}}}\frac{\partial\Theta_x^{(s)}}{\partial t_{\frac{B}{2}}} + \sum_{s=1}^{n} W_y^{(s)}\frac{\partial\theta_y^{(s)}}{\partial t_{\frac{\gamma}{2}}}\frac{\partial\Theta_y^{(s)}}{\partial t_{\frac{B}{2}}}\right] \tag{A.75}$$

$$\begin{aligned}\frac{\partial^2\Pi}{\partial t_{\frac{B}{2}}\partial t_{\frac{\Gamma}{2}}} = \; & -2\sum_{s=1}^{n} W_x^{(s)}\left[(d\theta_x^{(s)} - D\Theta_x^{(s)} + \Delta x_c - \Delta x^{(s)})D\frac{\partial^2\Theta_x^{(s)}}{\partial t_{\frac{B}{2}}\partial t_{\frac{\Gamma}{2}}} - D^2\frac{\partial\Theta_x^{(s)}}{\partial t_{\frac{B}{2}}}\frac{\partial\Theta_x^{(s)}}{\partial t_{\frac{\Gamma}{2}}}\right] \\ & -2\sum_{s=1}^{n} W_y^{(s)}\left[(d\theta_y^{(s)} - D\Theta_y^{(s)} + \Delta y_c - \Delta y^{(s)})D\frac{\partial^2\Theta_y^{(s)}}{\partial t_{\frac{B}{2}}\partial t_{\frac{\Gamma}{2}}} - D^2\frac{\partial\Theta_y^{(s)}}{\partial t_{\frac{B}{2}}}\frac{\partial\Theta_y^{(s)}}{\partial t_{\frac{\Gamma}{2}}}\right]\end{aligned} \tag{A.76}$$

$$\begin{aligned}\frac{\partial^2\theta_x^{(s)}}{\partial t_{\frac{\beta}{2}}\partial t_{\frac{\gamma}{2}}} = \; & \frac{\xi_i^{(s)}\frac{\partial^2 t_{1i}}{\partial t_{\frac{\beta}{2}}\partial t_{\frac{\gamma}{2}}}\xi_j^{(s)}t_{3j} - \xi_i^{(s)}\frac{\partial t_{1i}}{\partial t_{\frac{\beta}{2}}}\xi_j^{(s)}\frac{\partial t_{3j}}{\partial t_{\frac{\gamma}{2}}} - \xi_i^{(s)}\frac{\partial t_{1i}}{\partial t_{\frac{\gamma}{2}}}\xi_j^{(s)}\frac{\partial t_{3j}}{\partial t_{\frac{\beta}{2}}} - \xi_i^{(s)}t_{1i}\xi_j^{(s)}\frac{\partial^2 t_{3j}}{\partial t_{\frac{\beta}{2}}\partial t_{\frac{\gamma}{2}}}}{(\xi_r^{(s)}t_{3r})^2} \\ & +2\frac{\xi_i^{(s)}t_{1i}\xi_j^{(s)}\frac{\partial t_{3j}}{\partial t_{\frac{\beta}{2}}}\xi_k^{(s)}\frac{\partial t_{3k}}{\partial t_{\frac{\gamma}{2}}}}{(\xi_r^{(s)}t_{3r})^3}\end{aligned}$$

$$\begin{aligned}\frac{\partial^2\theta_y^{(s)}}{\partial t_{\frac{\beta}{2}}\partial t_{\frac{\gamma}{2}}} = \; & \frac{\xi_i^{(s)}\frac{\partial^2 t_{2i}}{\partial t_{\frac{\beta}{2}}\partial t_{\frac{\gamma}{2}}}\xi_j^{(s)}t_{3j} - \xi_i^{(s)}\frac{\partial t_{2i}}{\partial t_{\frac{\beta}{2}}}\xi_j^{(s)}\frac{\partial t_{3j}}{\partial t_{\frac{\gamma}{2}}} - \xi_i^{(s)}\frac{\partial t_{2i}}{\partial t_{\frac{\beta}{2}}}\xi_j^{(s)}\frac{\partial t_{3j}}{\partial t_{\frac{\gamma}{2}}} - \xi_i^{(s)}t_{2i}\xi_j^{(s)}\frac{\partial^2 t_{3j}}{\partial t_{\frac{\beta}{2}}\partial t_{\frac{\gamma}{2}}}}{(\xi_r^{(s)}t_{3r})^2} \\ & +2\frac{\xi_i^{(s)}t_{2i}\xi_j^{(s)}\frac{\partial t_{3j}}{\partial t_{\frac{\beta}{2}}}\xi_k^{(s)}\frac{\partial t_{3k}}{\partial t_{\frac{\gamma}{2}}}}{(\xi_r^{(s)}t_{3r})^3}\end{aligned}$$

$$\begin{aligned}\frac{\partial^2\Theta_x^{(s)}}{\partial t_{\frac{B}{2}}\partial t_{\frac{\Gamma}{2}}} = \; & \frac{\Xi_i^{(s)}\frac{\partial^2 T_{1i}}{\partial t_{\frac{B}{2}}\partial t_{\frac{\Gamma}{2}}}\Xi_j^{(s)}T_{3j} - \Xi_i^{(s)}\frac{\partial T_{1i}}{\partial t_{\frac{B}{2}}}\Xi_j^{(s)}\frac{\partial T_{3j}}{\partial t_{\frac{\Gamma}{2}}} - \Xi_i^{(s)}\frac{\partial T_{1i}}{\partial t_{\frac{\Gamma}{2}}}\Xi_j^{(s)}\frac{\partial T_{3j}}{\partial t_{\frac{B}{2}}} - \Xi_i^{(s)}T_{1i}\Xi_j^{(s)}\frac{\partial^2 T_{3j}}{\partial t_{\frac{B}{2}}\partial t_{\frac{\Gamma}{2}}}}{(\Xi_r^{(s)}T_{3r})^2} \\ & +2\frac{\Xi_i^{(s)}T_{1i}\Xi_j^{(s)}\frac{\partial T_{3j}}{\partial t_{\frac{B}{2}}}\Xi_k^{(s)}\frac{\partial T_{3k}}{\partial t_{\frac{\Gamma}{2}}}}{(\Xi_r^{(s)}T_{3r})^3}\end{aligned}$$

$$\begin{aligned}\frac{\partial^2\Theta_y^{(s)}}{\partial t_{\frac{B}{2}}\partial t_{\frac{\Gamma}{2}}} = \; & \frac{\Xi_i^{(s)}\frac{\partial^2 T_{2i}}{\partial t_{\frac{B}{2}}\partial t_{\frac{\Gamma}{2}}}\Xi_j^{(s)}T_{3j} - \Xi_i^{(s)}\frac{\partial T_{2i}}{\partial t_{\frac{B}{2}}}\Xi_j^{(s)}\frac{\partial T_{3j}}{\partial t_{\frac{\Gamma}{2}}} - \Xi_i^{(s)}\frac{\partial T_{2i}}{\partial t_{\frac{B}{2}}}\Xi_j^{(s)}\frac{\partial T_{3j}}{\partial t_{\frac{\Gamma}{2}}} - \Xi_i^{(s)}T_{2i}\Xi_j^{(s)}\frac{\partial^2 T_{3j}}{\partial t_{\frac{B}{2}}\partial t_{\frac{\Gamma}{2}}}}{(\Xi_r^{(s)}T_{3r})^2} \\ & +2\frac{\Xi_i^{(s)}T_{2i}\Xi_j^{(s)}\frac{\partial T_{3j}}{\partial t_{\frac{B}{2}}}\Xi_k^{(s)}\frac{\partial T_{3k}}{\partial t_{\frac{\Gamma}{2}}}}{(\Xi_r^{(s)}T_{3r})^3}\end{aligned} \tag{A.77}$$

Détermination du champ de contraintes dans les matériaux cristallins par microdiffraction Laue

RÉSUMÉ : La microdiffraction Laue permet l'estimation des déformations élastiques à l'échelle du micron. La procédure d'analyse standard, bien établie, utilisée pour extraire les déformations élastiques des images de Laue est limitée par deux sources d'erreurs : la détermination de la positions des taches de Laue sur le détecteur, et la sensibilité aux paramètres de calibration du montage. Pour améliorer la procédure, nous avons développé une procédure appelée Laue-DIC qui utilise la très bonne résolution de la technique de corrélation d'images numériques (DIC). Cette méthode utilise, pour la détermination de l'incrément de déformation élastique et de rotation, le déplacement des pics entre deux configurations mécaniques, estimé par DIC, au lieu de leur position. Nous montrons que cette méthode donne un profil de contrainte en meilleur accord avec les solutions analytiques et numériques, pour des échantillons monocristallins déformés en flexion 4-points. Nous proposons également une méthode Laue-DIC améliorée, dans laquelle les paramètres de calibration sont estimés à chaque point de mesure, simultanément à la déformation élastique.

En parallèle à la formulation de la méthode Laue-DIC (améliorée), nos efforts ont porté sur l'estimation de l'incertitude obtenue sur les déformations élastiques. Nous avons développé un modèle de bruit pour les images de Laue mesurées en rayonnement synchrotron, qui a été validé sur des séries de données, et qui nous a permis d'estimer les erreurs statistiques de la DIC, à partir d'images de Laue synthétiques. Ces erreurs ont ensuite été propagées dans la méthode Laue-DIC afin d'estimer les incertitudes sur les déformations élastiques, que l'on trouve en bon accord avec la fluctuation des contraintes locales estimées.

Mots clés : Microdiffraction Laue, corrélation d'images numériques, rayonnement synchrotron, analyse d'erreurs, essai mécanique *in situ*.

Determination of the stress field in crystalline materials by Laue microdiffraction

ABSTRACT: Laue microdiffraction is a powerful technique to characterize the intragranular elastic strain field at the scale of micrometer. Although a standard procedure extracting elastic strain and crystal orientation from Laue image has been well-established, it can suffer from two sources of uncertainties: the determination of peaks' positions and the sensitivity to calibration parameters. In light of the high accuracy of digital image correlation (DIC), we developed the so-called Laue-DIC method which used the peaks' displacements measured by DIC instead of peaks' positions to determine the elastic strain increment and rotation between two mechanical configurations. This method has been proved more efficient than the standard procedure in terms of stress profiles of bended beam. We also developed the enhanced version of Laue-DIC. By using the term "enhanced", we mean that we attempt to obtain both lattice matrices and calibration parameters of two configurations rather than solely the elastic strain increment and rotation from peaks' displacements.

Aside from the formulation of Laue-DIC, we also developed a procedure of statistically estimating the errors of elastic strain/stress resulted from DIC errors and calibration accuracy. We have first validated a classical noise model, Poissonian-Gaussian model, from diffraction images acquired at synchrotron radiation facility. With the noise model, we could statistically estimate the DIC errors by synthesizing artificial spots. The estimated DIC errors were further transmitted into the errors of Laue-DIC through statistical tests.

Keywords : Laue microdiffraction, digital image correlation, synchrotron radiation, error analysis, *in situ* mechanical test.

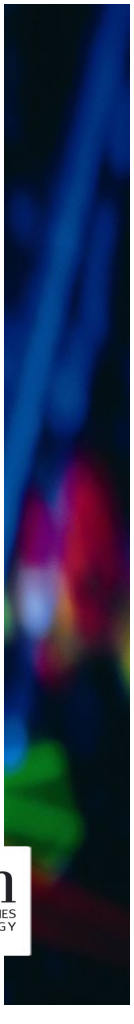

ARTS ET MÉTIERS ParisTech

ParisTech INSTITUT DES SCIENCES ET TECHNOLOGIES PARIS INSTITUTE OF TECHNOLOGY